Adsorption of organic friction modifiers at static and sheared interfaces

Alexander Joseph Armstrong

Wolfson College

University of Cambridge

August 2021

A thesis presented for the degree of
Doctor of Philosophy

Declaration

This thesis is the result of my own work and includes nothing which is the outcome of work done in collaboration except as declared in the preface and specified in the text. It is not substantially the same as any work that has already been submitted before for any degree or other qualification except as declared in the preface and specified in the text. This thesis does not exceed the prescribed word limit for the Engineering Degree Committee.

Alexander Armstrong
August 2021

Abstract

Adsorption of organic friction modifiers at static and sheared interfaces

Alexander Joseph Armstrong

Organic friction modifiers (OFMs) are additives that can be added to engine oils to reduce friction between rubbing surfaces. OFMs are thought to reduce friction by adsorbing at engine surfaces, producing films that are conventionally thought to be one molecule thick. Although established, the adsorption structure and the mechanism by which OFMs operate is far from proven. In this thesis, the adsorption and film structure of glycerol monooleate (GMO), an industrially relevant OFM, at the iron oxide-dodecane interface is investigated under static conditions and under applied shear. The study of the interface under applied shear is facilitated by the use of a novel sample environment, referred to as the tribometer, for neutron reflectometry (NR) and X-ray reflectometry (XRR). The tribometer can apply shear to an interface at rates of up to 3.8×10^3 s^{-1} and the thicknesses of thin films adsorbed at the interface can be determined via NR or XRR. The details of the tribometer are described in Chapter 2.

Chapter 3 investigates the aggregation of GMO in dodecane with pendant drop tensiometry and small angle neutron scattering. Additionally, the iron oxide surfaces used in the reflectometry studies are characterised through X-ray photoelectron spectroscopy, XRR and NR. Interestingly, a region of solvent depletion was found at the iron oxide-dodecane interface, which was approximately 1 nm thick. This is postulated to arise from the presence of adsorbed gases and depleted solvent.

Chapter 4 examines the adsorption of GMO at the iron oxide-dodecane interface under static conditions. The adsorption behaviour has been explored using depletion isotherms and NR. The former technique was used to study the adsorption of GMO as a function of bulk concentration and temperature. The adsorption behaviour was found to be Langmuir-like, indicating the formation of a monolayer film. In agreement, the thickness of the GMO adsorbate film was found to be less than the length of a GMO molecule. NR was then used to investigate the adsorption of GMO at the iron oxide-dodecane interface in the presence of water. Water was found to be present alongside GMO at the interface at 25 and 60 °C, although the film was found to alter from a mixed layer of GMO and water at 25 °C to a distinct bilayer of water and GMO at 60 °C.

Chapter 5 focusses on modelling NR and XRR data collected with the tribometer. An NR model is presented that combines conventional reflectivity theory with the summation of reflected intensities to describe reflectivity from thicker films. This model was used to describe the reflectivity of GMO adsorbed at the iron oxide-dodecane interface under shear at 7.0×10^2 s^{-1}. The film thickness was found to be equivalent to the film thickness determined when under static conditions, indicating that any changes to the film structure under this particular shear rate were not resolvable using the tribometer and NR. Finally, a model which describes the XRR data of GMO adsorbed at the iron oxide-dodecane interface at 3.0×10^3 s^{-1} is presented.

Acknowledgements

I would firstly like to thank Alex whose knowledge, support and enthusiasm has been invaluable during my study. I am extremely grateful for your supervision and time spent reviewing many megabytes of my work. I'd also like to thank Tom McCoy for being a source of unending knowledge and entertainment. I promise at some point I will drive you around instead.

I would like to thank Infineum UK and EPSRC for the funding. I'd especially like to thank Pete Dowding, Beatrice Cattoz and Colin Willis from Infineum UK, who offered much-needed support and enthusiasm throughout my PhD. Thanks to Rui Apòstolo and Philip Camp of the School of Chemistry, University of Edinburgh, whose simulations and analysis have been extremely insightful. Thanks to Elizabeth Willneff, Andrew Britton and Sven Schroeder at the School of Chemical and Process Engineering, University of Leeds, for providing assistance and expertise during the XPS experiments. I would also like to thank Robert Barker who provided much-needed guidance and assistance during the neutron experiments and while analysing the reflectometry data.

Many thanks to Becky Welbourne at ISIS and Philip Gutfruend at the ILL for offering their patience, expertise and humour during our neutron experiments. Thanks to Jonathan Rawle at Diamond Light Source for the expertise and assistance during our X-ray experiments.

Working at the BP Institute has been a privilege, and I would like to thank my office mates Nikzad Falahati, Bohao Wu, Izaak Jephson, Ahmed Othman and honorary member David Brossault for the camaraderie and laughs. Special thanks to all the people that are or were part of the Routh Group during my time at Cambridge, and many thanks to the wider BPI community.

I'd like to thank my parents and brother who have always been very supportive during my study. Last, and of course not least, I'd like to pay special thanks to Becca who has put up living with the PhD lifestyle, or lack thereof, for the past four years. I would not have been able to do this without you.

Publications and talks

Publications

Armstrong, A. J., McCoy, T. M., Welbourn, R. J. L., Barker, R., Rawle, J. L., Cattoz, B., Dowding, P. J., Routh, A. F., Towards a neutron and X-ray reflectometry environment for the study of solid–liquid interfaces under shear, *Sci. Rep.*, **11**, 9713; 10.1038/s41598-021-89189-1 (2021).

Talks

Armstrong, A. J, "Neutron reflectometry reveals the structure of glycerol monooleate at the iron oxide-dodecane interface", CEB Graduate Conference, Department of Chemical Engineering & Biotechnology, University of Cambridge, Jun 25$^{\text{th}}$, 2021.

Armstrong, A. J, "Studying Organic Friction Modifiers in Tribological Contacts with Neutron and X-ray Reflectometry", BP Institute Seminar, BP Institute, University of Cambridge, Oct 29$^{\text{th}}$, 2020.

Armstrong, A. J, "Measuring the conformation of organic friction modifiers under shear", Edwards Centre mini-conference, Department of Chemical Engineering & Biotechnology, University of Cambridge, Jan 10$^{\text{th}}$, 2020.

Contents

Chapter 1

Introduction

1.1 Friction and lubrication

The reaction force that acts counter to the movement of an object against another is known as friction, which arises via the dissipation of the objects' kinetic energies to heat. Over the 15–18$^{\text{th}}$ centuries empirical laws of friction were established by da Vinci, Amontons and Coulomb.[1,2] These laws have been consolidated and are generally referred to as Amontons' laws of friction. They state: (**I**) the frictional force between two objects, $F_{\parallel}$, is proportional to the applied normal load, $F_{\perp}$, (**II**) the frictional force is independent of the apparent contact area, A, between two objects and (**III**) friction arising between objects under steady motion is independent of the objects' tangential velocity, which is often attributed to Coulomb's work.[3] As a consequence of the first law, the friction between two bodies is often quantified by the coefficient of friction, μ, which is the ratio of the frictional force to the applied normal force as shown in Equation 1.1.

$$\mu = \frac{F_{\parallel}}{F_{\perp}} \tag{1.1}$$

Friction can be viewed as the energy dissipated due to elastic and plastic deformations in contacting objects, where plastic deformations lead to the wear of materials. Therefore, as the applied load increases, deformation increases and more energy is dissipated.

The second law may appear strange if considering sliding objects of different sizes over a much larger surface. However, as these objects will have some roughness, only a small fraction of the objects' surfaces will be in contact through protrusions referred to as asperities. Therefore, A is larger than the true area of contact, A_{R}, as depicted in Figure 1.1. The real area of contact is understood to be directly proportional to the applied load, since with greater loads, more asperities are brought into contact and those already in contact deform to give larger contacting areas.[4] The measured friction is then the sum of the friction arising between individual asperities. At a given load, objects with smaller surfaces that have a lower number of asperities will undergo greater asperity deformation compared to objects with larger apparent areas of

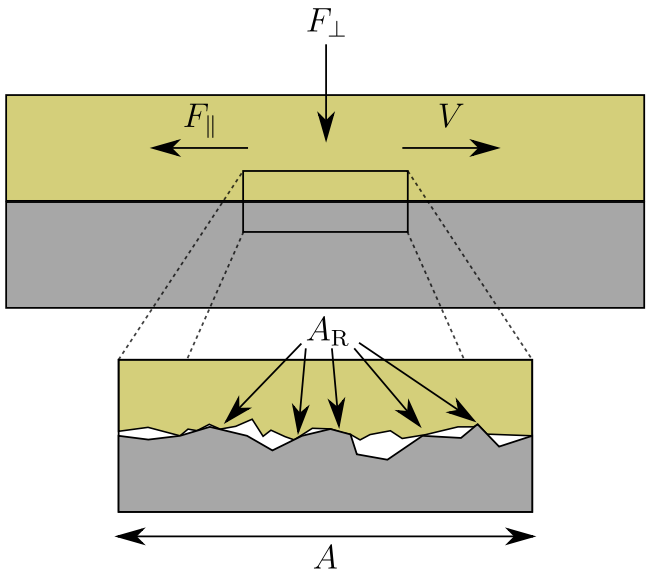

Figure 1.1: A schematic of an object that is moving with a velocity, V, across the surface of another stationary object. The upper object is also loaded by a force, $F_\perp$, acting in the normal direction. The frictional force acts in the opposite direction to the lateral movement. A magnified perspective of the contact region is shown below, where the surfaces no longer appear smooth.

contact. If the first law holds, then the lower number of contacts is offset by the greater friction that arises between contacting asperities due to greater loads through these junctions. It then follows that the apparent area of contact does not influence friction. The third law separates kinetic friction, the frictional force operating on two objects under motion, from static friction, which is the frictional force when accelerating from a stationary state. The latter is generally greater than the former.

The use of the word law conveys a false sense of universality; it is known that these frictional laws only apply to certain dry systems. Rigorously clean metal surfaces are a particularly good example of where the relationship between $F_\parallel$ and $F_\perp$ may deviate from the simple linear expression above. In this case, strong metallic bonding between two clean metal surfaces in contact can dominate over small applied loads in determining the static friction. Hence, it is more appropriate to model $F_\parallel$ by Equation 1.2.

$$F_\parallel = \mu F_\perp + \sigma A_\mathrm{R} \tag{1.2}$$

Here, σ is the shear stress that must be applied to break any adhesive bonds between the contacting asperities, known as the yield stress. As such, σ can be viewed as the interaction strength between the contacting surfaces, which can span from weak van der Waal attractions through to strong metallic bonds. The term σA_R is sometimes referred to as the Derjaguin offset.[5]

Clean surfaces which are placed under ambient atmospheric conditions become contaminated rapidly by the adsorption of atmospheric gases such as O_2, CO_2 and H_2O. These adsorbed

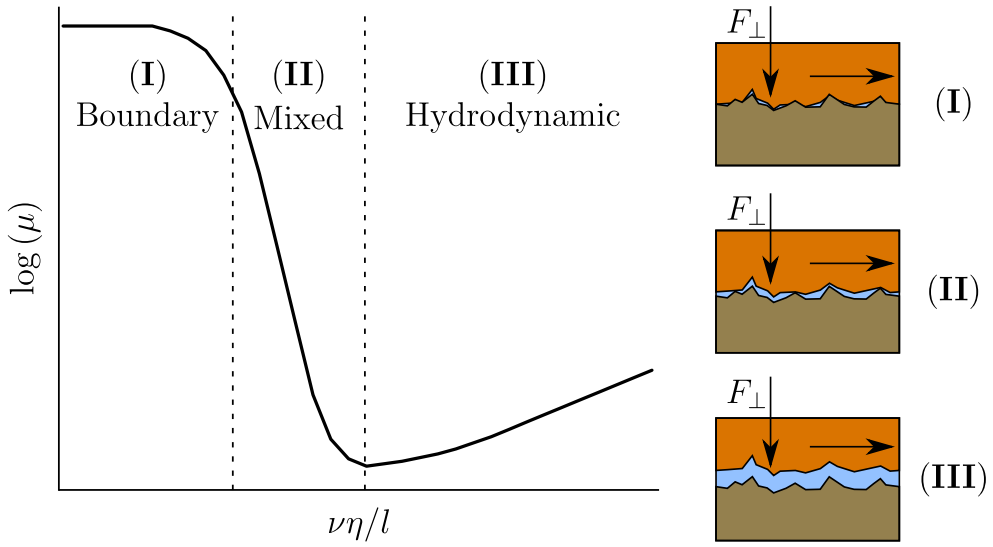

Figure 1.2: The Stribeck curve and typical friction regimes. The schematics on the right depict the contacts encountered in the three regimes for two surfaces under load, where the blue material represents liquid lubricant.

molecules are understood to significantly screen the attractive interactions of surfaces in their clean state; for metals such as tungsten and nickel, adsorbed gases can reduce μ by a factor of ~ 4.[6] It is understood that the attractive forces between adsorbed species is generally much weaker than clean metals and thus, less force is required to induce shear between them. Therefore, most surfaces are passively lubricated when exposed to the atmosphere.

Lubrication can be easily extended through the direct application of liquids to contacts, which can result in distinct regimes of friction. The variation of a steady-state coefficient of friction across various regimes is well documented in journal bearings and is depicted in the Stribeck curve, Figure 1.2, as a function of the dimensionless Hersey number, $\nu\eta/l$.[7–9] Here, ν is the angular velocity of the shaft, η is the dynamic viscosity of the lubricating liquid and l is the load applied per projected unit area.

At low Hersey numbers the boundary friction regime is encountered, where the hydrodynamic pressure generated in the liquid is small and the oil film cannot sustain the applied load. Consequently, a high fraction of the surface asperities are in contact, leading to high friction as a large proportion of asperities are elastically or plastically deformed. Furthermore, adhesive junctions can form between contacting asperities, which must be broken before lateral movement can occur. Unsurprisingly, the value of μ in the boundary regime is significantly reduced by the presence of molecules adsorbed at the surfaces.

As the Hersey number increases, the fluid film thickens and thus, the contact area between the surfaces decreases throughout the mixed regime. The stress required to shear liquids is, in general, lower than that required to shear solid junctions, so that friction arising from the non-contacting portion of the interface is typically low. Therefore, the macroscopic coefficient of friction decreases rapidly with Hersey number. As the Hersey number increases further, the solid surfaces become completely separated and the friction reaches a minimum at the

start of the hydrodynamic regime. This is due to the thin nature of the oil layer. Within the hydrodynamic regime, friction rises slowly with the Hersey number as viscous losses increase with greater oil film thicknesses.

These regimes are applicable to conformal surfaces, where the apparent contact area is typically a high proportion of the total surface area of two surfaces. However, for non-conformal surfaces, where the geometries of two surfaces do not compliment each other, hydrodynamic friction is only sustained at very light loads. As the Hersey number decreases towards the mixed regime, the pressure propagating over the contacting surfaces will be high due to the small contact area. This leads to the elastic deformation of the surfaces, and can also raise the viscosity of the lubricating liquid. This is called elastohydrodynamic friction.[10]

Friction arising solely within the engine of an average passenger car from the year 2000 has been estimated to account for ~ 12 % of the total fuel energy.[11] The various mechanical components of an engine are engineered with different geometries, working loads and operating velocities; this leads to a range of lubrication regimes throughout the engine. For example, during normal operation the engine bearings and pistons are thought to operate under the hydrodynamic regime, whereas the non-conformal Cam-follower systems in the engine valve-train operate under boundary conditions.[12] Conditions closer to boundary lubrication are also found when starting the engine, which has become more frequent with start/stop technology.[13] The friction arising in the hydrodynamic regime can be minimised by optimising the oil viscosity, which, conversely, has minimal impact on the friction in the boundary regime. In order to minimise frictional loses in the mixed and boundary regimes, additives can be used that operate at solid-liquid interfaces; these additives decrease the shear stress required to induce or continue lateral movement of two bodies in contact. In general, these additives are known as friction modifiers, and are included in engine lubricants. Friction modifiers are commonly classed into three distinct groups: organic friction modifiers (OFMs), inorganic friction modifiers and polymeric friction modifiers.[14]

1.2 Engine surfaces

Engine components are subject to different stresses and temperatures, and hence, must meet particular requirements. While aluminium, magnesium and titanium alloys are used for some high performance components, steel is most commonly used to manufacture the moving components within an engine.[15] Steel is a broad term for the alloys of iron formed with a low, $<$ 2 wt%, carbon content, and different steel phases can be formed depending on the temperature and carbon content as shown by the iron-carbon phase diagram in Figure 1.3. The two most abundant phases are ferric, α, and austentic, γ. The ferric phase has a body-centred cubic (BCC) structure, whereas the austentic phase has a face-centred cubic structure (FCC). Schematics of the unit cells for these structures are shown in Figure 1.4. Carbon is solubilised in the iron structure by occupying the space between the iron atoms, known as interstitial sites. This is possible as carbon atoms are considerably smaller than the iron atoms. The occupation

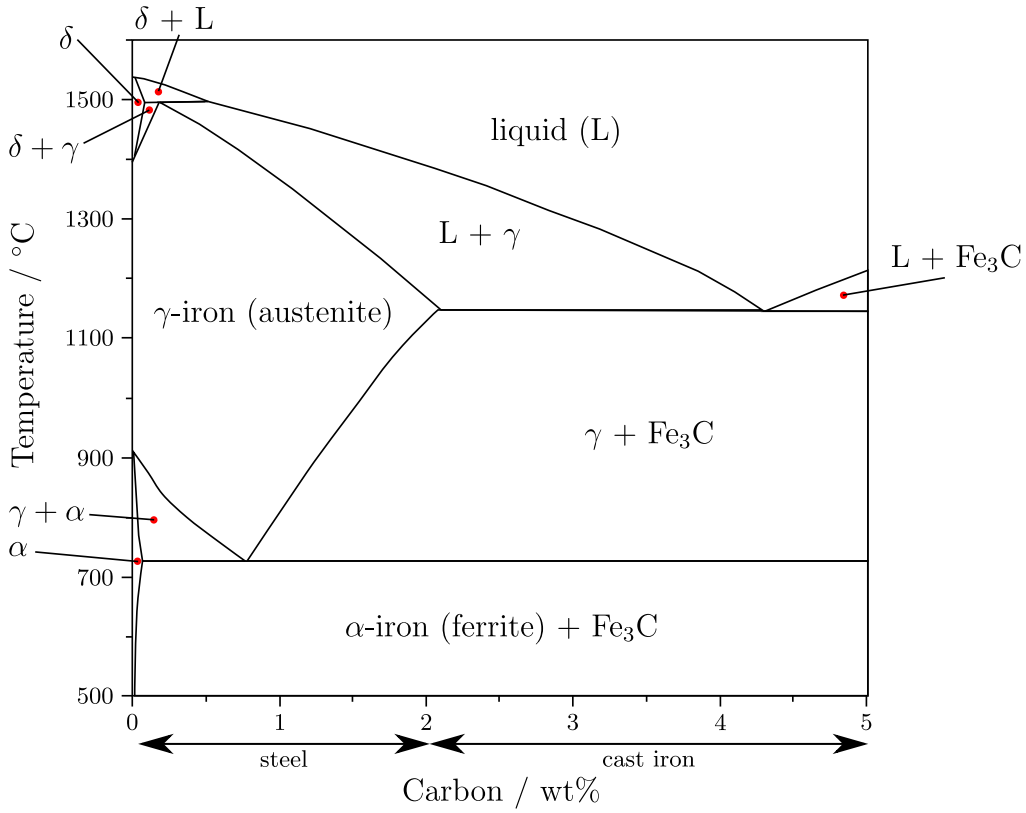

Figure 1.3: The iron-carbon phase diagram shows the equilibrium phase behaviour of iron alloyed with carbon, adapted from the cited work.[16] Fe_3C is known as cementite and is a ceramic material in its pure form. The mixed phases or microstructures formed in the regions where two phases coexist, such as pearlite which is formed with ferric and cementite, are not shown. The term cast iron relates to alloys with > 2 wt% carbon.

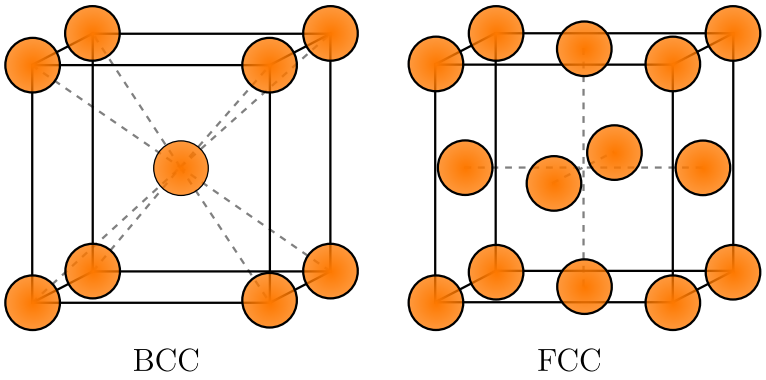

Figure 1.4: The unit cells of body-centred cubic and face-centred cubic lattices. The orange spheres depict the iron atoms. The full black lines do not depict chemical bonds but the bounds of the unit cell. The grey dashed lines are to assist the eye, and do not depict chemical bonds.

of interstitial sites leads to distortions in the crystal structure, which strengthens the steel.

The alloys of steel can be extended by the inclusion of transition metal elements such as molybdenum, nickel and chromium among others. These elements are of similar size to iron and hence do not occupy interstitial sites but substitute into the lattice structure. When incorporated into steels, elements such as manganese and nickel promote the formation of austentite steels. If these elements are included in high concentrations, the γ phase can be

formed as a stable alloy at room temperature. On the other hand, the formation of ferritic phases over a wider range of composition can be achieved by the inclusion elements such as chromium and molybdenum among some p-block elements like aluminium and silicon. Beyond altering the phase, these elements can also inhibit oxidative and corrosive processes. Stainless steels, which are those that contain $\gtrsim 11$ wt% chromium, are particularly resistant to corrosion.

Engines components are made from a variety of steels to meet the required strengths and durability required in different regions of the engine. However, it is the surfaces of the materials that dictate their frictional behaviour. Combustion engine surfaces are often engineered to have surface roughnesses on the µm scale.[17] When the lubricating oil film is on the same length scale or thinner, asperity contact occurs giving rise to high friction coefficients and wear as associated with the boundary lubrication regime. Here, the most significant factor is the chemical composition of the steel surface. This not only determines the strength of junctions formed between contacting steel surfaces, but also dictates the chemistry of surface-active components within the bulk oil. Unlike iron, the passivating oxide films of steel can contain alloying elements. For instance, stainless steels are known to contain a substantial amount of chromium oxide, which decreases in concentration with depth into the bulk material.[18] Iron oxides are also present at the surface, which constitute a significant proportion of the surface. These are thought to be a mixture of Fe(II) and Fe(III) oxides and hydroxides, and are common to all steel surfaces.[19,20]

1.3 Organic friction modifiers

Organic friction modifiers are amphiphiles with polar head groups and non-polar tail groups, as shown in Figure 1.5. Their tail groups are typically over 10 carbons long, differentiating them from other shorter-chain surfactants and imparting solubility in hydrocarbon solvents. The conventional understanding is that OFMs adsorb from solution at metallic engine surfaces due to their amphiphilic nature, where the polar head group interacts with the hydrophilic engine surface and the hydrophobic alkyl chain extends into the bulk hydrocarbon solvent. It is thought that compact surface layers are formed as a result of van der Waals attractions between adjacent adsorbate molecules, which form regions of low shear moduli when brought into contact on opposing moving surfaces. As a result, the friction is lower than that arising between clean, dry surfaces.[14,21] Fatty acids and their ability to reduce friction have been studied extensively, as discussed below. However, due to their corrosive action on some metals in hydrocarbon solvents, OFMs based on amines, alcohols, and esters among other polar functional groups have been developed that are milder in terms of corrosive ability.[21,22] A brief review of the OFM friction reduction mechanism is laid out below.

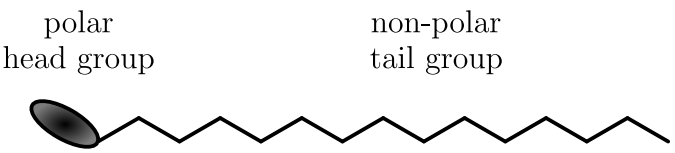

Figure 1.5: The general structure of an OFM. OFMs are not restricted to one head group or one tail group, as depicted here.

1.3.1 Foundations of boundary lubrication

The mechanistic understanding laid out above was developed over the 20$^{\text{th}}$ century, where researchers used tribometer tests and adsorption studies to infer the structure of OFMs. Notably, Hardy *et al.* found that the deposition of pure fatty acids and alcohols onto glass and steel surfaces reduced the friction when sliding under boundary conditions.[23] Smaller droplets of lubricant were found to be as effective as larger doses; as such, it was argued that only a thin layer of lubricant was responsible for the reduction of friction, and it was postulated to be a monolayer. Friction reduction was also found to improve monotonically with increasing acid/alcohol chain length, which was explained via the formation of a slip plane between the terminal groups of alkyl chains of contacting monolayers. Small quantities of fatty acids were later shown to reduce friction in boundary contacts when dissolved in hydrocarbon solvents, which cannot reduce friction as effectively when used independently.[24] Evidence of friction reduction via fatty acid monolayers has been shown using the Langmuir-Blodgett deposition technique on glass and steel surfaces.[25,26] Both works reported that friction could be effectively reduced for longer sliding durations if a greater number of fatty acid layers were deposited. This led to the suggestion that sustained friction modification relies on the continuous replenishment of the additive at the interface due to the removal of adsorbate when asperity contact, and subsequent wear, occurs. Therefore, the theory that self-assembled additive monolayers are responsible for the reduction in friction in the boundary regime begun to propagate as the principal theory.[27] A schematic of the boundary lubrication via monolayers is shown in Figure 1.6.

This lubrication mechanism was later supported by adsorption isotherm studies conducted on a variety of surfaces such as steel and iron oxide in hydrocarbon solvents. These studies found that the majority of additives showed Langmuir-type adsorption, indicating the formation of monolayers.[28–30] Later tribological tests were found to align well with the suggestion of monolayer lubrication, as μ was found to rapidly decrease as the additive concentration increased at very low concentrations until a plateau was reached at higher additive concentrations.[31–33]

The model proposed by Bowden[27] makes a distinction between the friction arising from asperity-asperity contact and the friction arising between monolayer films or monolayer-asperity contacts. This implies that the adsorbate films have some ability to withstand the applied load, which was later ascribed to the adsorption strength of the additive to the surface and the cohesion between adsorbate molecules.[34] The former relates to the distinction of chemical adsorption, or chemisorption, from physical adsorption, or physisorption, while cohesion can be viewed as the strength of the van der Waals forces between adsorbate molecules. Chemisorp-

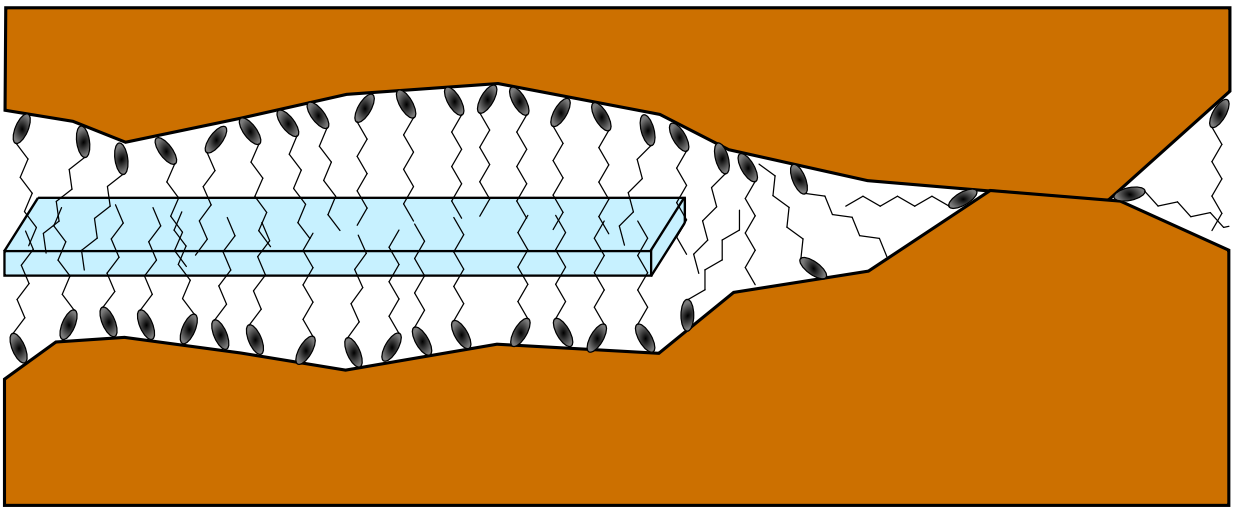

Figure 1.6: A depiction of the conventional OFM mechanism of friction reduction. The light blue cuboid depicts the slip plane formed between the terminal groups of the OFM alkyl chains. To the right, full asperity contact is depicted, where the adsorbate film cannot be sustained.

tion arises from the formation of chemical bonds between adsorbate and adsorbent, leading to relatively large changes of the enthalpy of adsorption, ΔH, where $\Delta H < -40$ kJ mol^{-1}.[35] This leads to irreversible adsorption. Chemisorption is stronger than physisorption, where the latter is facilitated through intermolecular forces between the adsorbate and adsorbent. The typical values for ΔH via physisorption are between -40 and 0 kJ mol^{-1}. Hence, physisorption is considered as reversible adsorption.

Increasing the temperature of loaded steel surfaces lubricated by oils, thought to contain polar molecules, was found to increase friction.[36] This was found to be reversible by cooling the system and hence, it was suggested that the increase in friction arose from disorientation or desorption of the adsorbate film. The temperature at which these transitions occurred were suggested to depend on the adsorption strength of the additive. These transition temperatures were later explored by Frewing, who found transitions at lower temperatures for systems lubricated by alcohols compared to fatty acids and their esters.[37,38] It was also found that additives dissolved in hydrocarbon solvents displayed lower transition temperatures with decreasing concentration; this was later confirmed by other tribological studies.[31,33] Two transition temperatures would later be identified. The first transition was marked by an increasing variability in μ while the second transition was identified by the onset of an exponential increase in μ.[39] The former observation was proposed to result from the loss of order in the molecular film, which has been observed by electron diffraction studies to be reversible.[40] The latter observation was suggested to arise from the partial desorption of the lubricating film, where it is thought that the remaining adsorbed molecules cannot support the high loads, resulting in a greater area of contact, and hence higher friction.

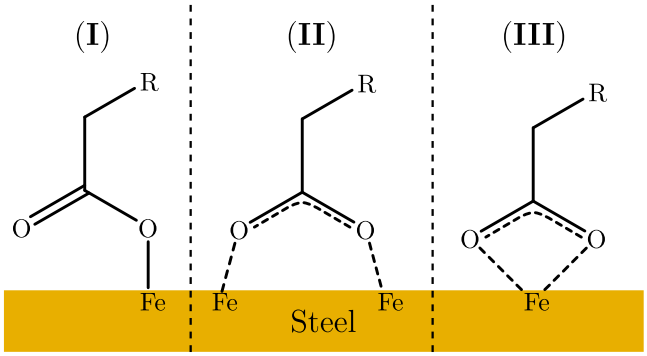

Figure 1.7: Three possible carboxylate modes at steel surfaces, which are named the following: (**I**) monodentate, (**II**) bidentate bridging, and (**III**) bidentate chelating.

1.3.2 Current understanding of boundary lubrication

The adsorption mechanisms of fatty acids at steel/iron oxide surfaces are the most thoroughly investigated. Reflection IR spectroscopy has been used to detail the adsorption of fatty acids from hydrocarbon solution onto steel substrates, where the adsorption is suggested to arise through a number of modes.[41,42] It was found that a portion of the adsorbed acid formed iron carboxylates through the dissociation of the carboxylic hydrogen; Figure 1.7 shows three carboxylate binding modes that have been proposed.[43] At the same time, carboxylic acid was also detected at the interface. By washing the substrate with heptane, some carboxylic acid was removed while some remained at the interface. This was suggested to arise from the presence of physisorbed and chemisorbed acid at the interface, which is supported by similar findings through molecular dynamics[42] (MD) and density functional theory[44] (DFT) simulations. Polarised neutron reflectometry also showed that only partial desorption of a self-assembled oleic acid film at the iron oxide-dodecane interface could be induced by washing the interface with neat solvent.[45] Similarly, evidence for amine adsorption via a mixture of physisorption and chemisorption is offered by a number of studies; X-ray photoelectron spectroscopy of dried hexadecylamine on iron oxide surfaces indicate the presence of chemisorbed amine[46], while temperature-dependant depletion isotherms of hexadecylamine adsorption at the hematite-dodecane interface suggest physisorption.[47] In addition, quartz crystal microbalance studies of di- and tri-fatty amines at steel-hexadecane interfaces have shown that a significant amount of the adsorbed additives can be washed off upon rinsing with additional solvent, indicating physisorption.[48] However, substantial amounts of the amine additives were also found to remain at the interface, indicating that some of the amines were chemisorbed at the interface. DFT simulations have also indicated that molecules with ester head groups can adsorb via chemisorption.[44] However, quartz crystal microbalance studies have shown that the majority of a self-assembled film of glycerol monooleate adsorbed at the steel-hexadecane interface can be removed by solvent rinsing, strongly indicating physisorption.[49]

The friction arising from contacting monolayer films has been investigated in so-called nanotribology studies. Surface-force apparatus have been used to study the friction between monolayers on mica surfaces as a function of surface coverage and temperature among other variables.[50,51]

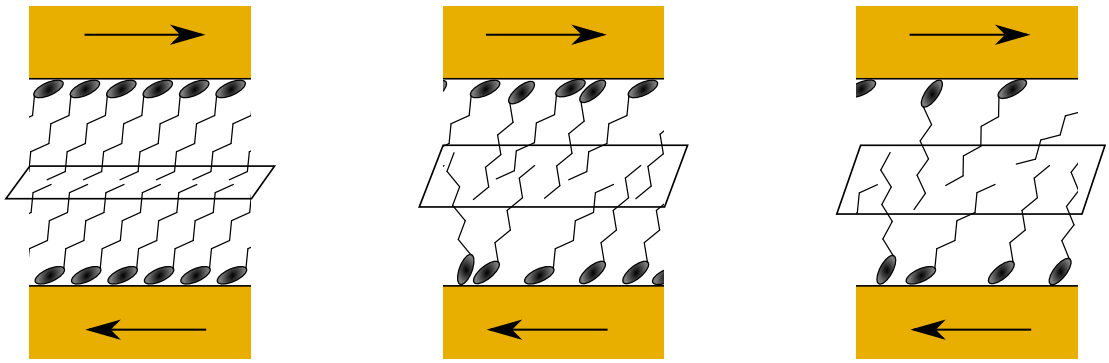

Figure 1.8: A schematic of the solid-like, amorphous and liquid-like adsorbate layers on moving surfaces. The region of contact between the monolayers is highlighted by the box between the layers.

The effect of these variables was found to collapse onto a general phase diagram, where friction is low when the monolayers are described as solid-like or liquid-like: that is, when the temperatures and the packing of the molecules of the monolayer are such that disorder is low or high. Between these states, the friction was found to reach a maximum, where the layer was described as amorphous and contains a degree of disorder but less so than the liquid-like layer. Depictions of the film structures are shown in Figure 1.8.

These results agree with MD simulations of sliding iron oxide surfaces that are coated by OFM monolayers.[52,53] The behaviour of friction over these states was described as arising from the extent of interdigitation of the monolayer alkyl chains. The interdigitation was argued to be low when the films are solid-like, so that attractive van der Waals forces between the monolayers are small. This leads to weak adhesion energy between the monolayers, and thus only small amounts of energy are dissipated between the monolayers. As disorder increases, so does the interdigitation of the alkyl chains, which strengthens the attractive interactions between the monolayer films, leading to greater friction. Additionally, it is expected that interdigitated chains will have to adopt specific conformations in order to move past one another when the density of alkyl chains is high. The energy required to force conformations that enable slip between alkyl chains is expected to be another source of dissipation. As the disorder of the monolayer grows, the space between interdigitated chains increases, lowering the strength of attractive interactions between adjacent alkyl chains while the energy dissipated at any one moment due to chain conformation rearrangement is lowered. By simulating surfaces with nanoscale roughnesses, it has been suggested that films are less ordered on rougher surfaces, leading to greater friction.[54] It should be noted that friction does not solely arise from the interactions of the surface layers; for instance, friction with liquid-like films has been reported to be greater than that arising from more solid-like films from tribometer tests.[33] This difference was proposed to arise from the lower surface coverage relating to a greater extent of asperity-asperity contact. Simulations of OFM-coated iron oxide surfaces under confinement show that the surfaces are squeezed closer together when the film density is lower.[52] Therefore, it is

possible that the low friction reported for liquid-like films is not apparent when surfaces have a roughness that extends beyond the length of the film.

Another source of friction has been suggested to arise from the forced-tilting of adsorbate molecules when sharp asperities indent against them, as studied by atomic force microscopy (AFM).[55,56] This is known as ploughing, and is thought to increase with greater normal forces due to the greater extent at which molecules must be perturbed in order for the asperity to move along the surface.[57,58] Simulations suggest that as surface coverage increases, the friction arising from sharp tipped asperities increases as they indent further into the surface film, thus increasing the extent of ploughing.[59] This mechanism of energy dissipation would perhaps be encountered less in a macroscopic tribological contact than the friction arising from interdigitation as sharp asperities will be worn early on after the onset of sliding.

It has been observed that friction arising under boundary lubrication increases logarithmically as a function of sliding velocity for some self-assembled or deposited monolayers.[60–63] This behaviour was originally described by Briscoe and Evans, who found this relationship for deposited films of stearic acid on molecularly smooth mica surfaces.[64] Additionally, friction was found to increase linearly with increasing pressure and decreasing temperature. It was postulated that in order to facilitate motion of one coated surface over the other, an energy barrier must be overcome. Drawing on similarities to Erying's[65] activated slip model for the description of liquid viscosity, a thermal-activated slip model was proposed by Briscoe and Evans that included a pressure term to model increasing activation energies with greater pressures. By assuming the sliding velocity, V, was equal to the average molecular velocity of the deposited monolayers, the velocity could be related to the shear strength, τ, of the monolayers via Equation 1.3.

$$V = 2V_0 e^{[-(E+p\Omega)/k_\mathrm{B}T]} \sinh\left(\frac{\phi\tau}{k_\mathrm{B}T}\right) \tag{1.3}$$

Here, V_0 is a velocity constant, E is the activation energy required to overcome the energy barrier, p is the hydrostatic pressure, Ω is the pressure activation volume and ϕ is the stress activation volume. The Ω term was suggested to be the volume increase required to enable motion between the monolayers and the ϕ term was later ascribed to the product of the area over which shear stress acts multiplied by an activation distance.[66] The activation distance is the distance parallel to the surface between the minimum and maximum energies when sliding one monolayer over another, which is depicted in Figure 1.9. The shear strength of the monolayers was calculated by dividing the measured frictional force by the contact area determined via optical interferometry. When the shear strength is high, so that $e^{\phi\tau} \gg e^{-\phi\tau}$, the sinh term can be approximated as $\exp(\phi\tau/k_\mathrm{B}T)$ and Equation 1.3 can be rearranged to:

$$\begin{gathered} V = V_0 e^{[(\phi\tau - E - p\Omega)/k_\mathrm{B}T]} \\ \text{or } \tau = \frac{k_\mathrm{B}T}{\phi} \ln\frac{V}{V_0} + \frac{1}{\phi}(E + p\Omega) \end{gathered} \tag{1.4}$$

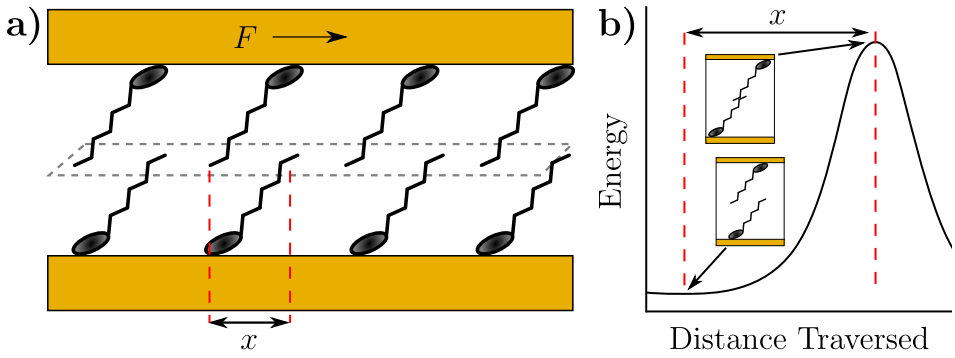

Figure 1.9: **a)** Depiction of the stress activation volume, where the grey dashed box shows the area over which shear stress acts. The activation length, x, is half the spacing between OFM molecules. **b)** The energy diagram for the process of sliding a surface over another with a monolayer of adsorbate. The increase in energy between these states is the activation energy towards sliding the upper surface over the bottom surface. The insets show depictions of the OFM molecules at the lowest and highest energy states.

where it follows that shear strength, and thus, friction is linearly dependant on temperature and pressure while logarithmically dependant on sliding velocity. Similar trends have been reported in computational studies of boundary contacts lubricated by monolayers.[67–70] Computational work has also suggested that interdigitation between the adsorbate film and any remaining solvent confined between two compressed, sliding surfaces may also lead to similar rises in friction with the logarithm of sliding speed.[52,69]

It is quite surprising that similar behaviour is noted between the experimental and theoretical results, as the latter are restricted to the study of nanoscale contacts, where roughnesses are at most nanoscopic and the interfaces are subject to very high shear rates (on the order of 10^9 s^{-1}). On the other hand, macroscopic systems, as studied experimentally with tribometers, consist of a distribution of contacts with different local pressures and shear rates. This is expected to lead to different levels of interdigitation between the films, and thus give rise to macroscopic friction which is the result of all contacts. Furthermore, wear of surfaces is an incontrovertible result of boundary lubrication of sliding surfaces, which is not accounted for in simulations and is thought to be a significant energy dispersive event compared to the elastic/plastic deformation of monolayer films. Whilst run-in periods were conducted in the tribometer experiments before average friction coefficients were measured, it is likely that the experimental trends found through tribological tests contain further dissipative events that could be as, if not more, significant as the thermal-activation stress model as shown in Equation 1.4.

The increase in friction with the logarithm of sliding speed is not a universal feature of boundary lubrication. High or low surface coverage films have been found to either vary only weakly with sliding velocity or to be completely independent of sliding velocity.[52,71] Friction independent of sliding speed was noted for steel surfaces lubricated by hexadecane solutions that contain oleic acid, the *cis* unsaturated (C_9-C_{10}) counterpart of stearic acid.[62] Oleic acid was argued to form less ordered films than those formed by stearic acid and elaidic acid, the *trans* analogue of oleic acid, due to the packing constraints imposed by the non-linear *cis* double bond. This

is supported by the lower surface excess, and hence lower packing density, reported for oleic acid in comparison to stearic acid at the iron oxide-dodecane interface.[45] Consequently, self-assembled oleic acid films resemble liquid-like films that give rise to poorer lubrication; these liquid-like films display no frictional dependence on sliding speed.[33,72,73] Linoleic acid was found to have a lower surface excess still, suggesting that increasing the *cis* unsaturation decreases packing density. In a similar manner, molecules that contain hydroxy groups in the alkyl tail group show lower friction compared to additives that have non-functionalised alkyl tail groups; this is suggested to arise from hydrogen bonds between tail groups, leading to greater cohesive strength between adsorbate molecules and a greater packing density.[33]

Specialised tribometers equipped with interferometric microscopes have been used to characterise the *in-situ* formation of OFM monolayer films in tribological contacts.[74] However, these experiments have also revealed film thicknesses beyond monolayer length scales for self-assembled fatty acids at steel surfaces.[75,76] Furthermore, it has been shown that fatty acids dispersed in organic solvent with trace amounts of water can form films thicker than monolayers at steel surfaces.[77] Similarly, there is some evidence that three stacked monolayers of behenic acid, a fatty acid, on mica can withstand extended sliding in similar conditions as monitored through an optical interferometry.[64] AFM results suggest that stearic and oleic acids can adsorb at the quartz-hexadecane interface when rubbed against steel.[78] Interestingly, these layers range in thickness from 2–4 nm for stearic acid and up to 20 nm for oleic acid. These experiments were conducted *ex-situ*, so it is possible that the time or process taken between rubbing the quartz surfaces to placement in an AFM liquid cell changed the interface, or perhaps that wear particles are captured in the AFM images. Nonetheless, findings such as these indicate that friction-reducing film structures are not limited to monolayers and indeed, the suggestion of thicker boundary films has been debated previously.[79] Whilst it is established that deposited monolayer structures can reduce friction between flat surfaces, there is less evidence to suggest that self-assembled OFM interfacial structures are monolayers. Despite the plethora of conducted research, there is still much to discover regarding the adsorption and self-assembly of OFMs other than fatty acids, especially regarding the adsorbate structures formed under boundary lubrication conditions. The fundamental mechanism behind friction modification can be elucidated by understanding how OFMs self-assemble at interfaces and how their surface structure varies with applied tribological conditions.

1.4 Aims

The primary aim of this study was to investigate the adsorption of glycerol monooleate (GMO), an industrially relevant OFM, from dodecane solutions onto iron oxide surfaces under static conditions and under applied shear. Iron oxide was chosen as the representative surface as it is common to all steel surfaces and presents a well-defined model surface to study. The structure of GMO is shown in Figure 1.10. Experiments under static conditions were conducted to investigate the effects of bulk concentration, temperature and water content on the structure of

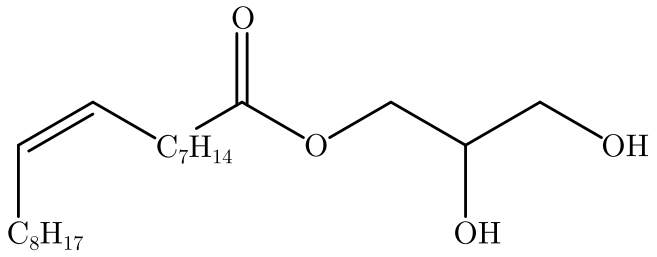

Figure 1.10: The molecular structure of glycerol monooleate (GMO).

adsorbed GMO. The self-assembly of GMO at the interface under applied shear was investigated using a novel rig, referred to as the tribometer, that provides a suitable neutron and X-ray reflectometry environment for *in-situ* structural characterisation.

The details of the experimental techniques used in this work are discussed in Chapter 2. After, the bulk self-assembly of GMO dissolved in dodecane is investigated in Chapter 3. As part of this chapter, the nature of the interfaces provided by the reflectometry substrates are also characterised. Next, the findings of the adsorption experiments conducted under static conditions are presented in Chapter 4. The experiments conducted under shear with the tribometer are then presented in Chapter 5. Finally, Chapter 6 concludes the presented work and discusses possible avenues for future work.

Chapter 2

Experimental

The background and general details of the main experimental techniques used throughout the project are laid out in this chapter. Specific experimental detail can be found in later chapters.

2.1 Pendant drop tensiometry

Pendant drop tensiometry is a technique that primarily enables the determination of surface and interfacial tensions at gas-liquid and liquid-liquid interfaces. These result from the depletion in cohesive forces between molecules across interfaces of immiscible liquids, where the forces act to minimise the surface area of the interface. In this manner, interfacial tensions also represent the energies required to create further area between two immiscible liquids. Interfacial energy is a key parameter when engineering wetting and spreading phenomena, and is also important when designing colloidal systems such as foams and emulsions.

Beyond understanding the forces between immiscible liquids, pendant drop tensiometry can be used to infer the chemical composition of interfacial layers when, for example, surfactants are included in one phase. Most commonly, a single component is dissolved into the liquid phase at low concentration and the surface or interfacial tension is measured as a function of the concentration. Using the Gibbs adsorption isotherm, the variation in interfacial tension with concentration can be used to characterise the adsorption of the surfactant.

2.1.1 Theory

The pendant drop technique relies on the gravitational deformation of a liquid droplet, which if held in an immiscible fluid follows the Young-Laplace equation, given in Equation 2.1, at equilibrium.[80]

$$\gamma \left(\frac{1}{R_1} + \frac{1}{R_2} \right) = \Delta P \equiv \Delta P_0 - \Delta \rho g z \tag{2.1}$$

Here, γ is the interfacial tension, and R_1 and R_2 are the two principal radii of curvature for the surface of given pendant drop. The pressure drop across the interface, ΔP, is referred to as the Laplace pressure. This can be re-expressed as the pressure difference at the apex of the droplet, ΔP_0. To relate the pressure difference across the pendant drop apex to the Laplace pressure at all vertical positions, z, the hydrostatic pressure must be included with a positive density difference, $\Delta\rho$, which occurs when the droplet phase has a greater density than the surrounding fluid. Gravitational acceleration is denoted as g.

By assuming the pendant droplets are axisymmetric about the z axis, Equation 2.1 can be rewritten as three first-order differential equations as a function of the pendant drop silhouette arc length s. This is achieved by using the cylindrical coordinates z and r with the angle, ϕ, between the horizontal and the local tangent of the droplet. The length scales are nondimensionalised by R_0, the radius of curvature at the apex ($\bar{z} = z/R_0$, $\bar{r} = r/R_0$, $\bar{s} = s/R_0$). The three coupled differential equations are shown in Equation 2.2.

$$\frac{\mathrm{d}\bar{r}}{\mathrm{d}\bar{s}} = \cos\phi \qquad \frac{\mathrm{d}\bar{z}}{\mathrm{d}\bar{s}} = \sin\phi \qquad \frac{\mathrm{d}\phi}{\mathrm{d}\bar{s}} = 2 - B_0\bar{z} - \frac{\sin\phi}{\bar{r}} \tag{2.2}$$

The above equations are subject to the following boundary conditions; $\bar{z} = 0$, $\bar{r} = 0$, $\phi = 0$ at $\bar{s} = 0$. B_0 is the Bond number defined as

$$B_0 = \frac{\Delta\rho \times g \times R_0^2}{\gamma}\,. \tag{2.3}$$

For a given droplet, it then follows that B_0 is dependant on the shape, which can be determined by geometrical analysis of the silhouette. The schematic in Figure 2.1a shows the above variables imposed on a standard droplet shape, with Figure 2.1b showing an example pendant drop. The analysis of the droplet shape requires numerical methods to fit the recorded silhouette image, where data points of the outline are fit. Details of the minimisation methods are not covered here but can be found elsewhere.[81] Once B_0 is determined, γ can be calculated.

Gibbs adsorption isotherm

The variation in surface/interfacial tension may be used to characterise the adsorption behaviour of surfactants. Specifically, if a solution contains i different components, the surface excess of the i^{th} component, Γ_i, is defined as the difference in the amount of that component at the interface compared to the bulk solution divided by the area of the interface. The differential form of the Gibbs adsorption isotherm, derivable from thermodynamic expressions for open systems[35], is

$$\mathrm{d}\gamma = -\sum_i \Gamma_i \mathrm{d}\mu_i \tag{2.4}$$

where μ_i is the chemical potential of the i^{th} component; this expression holds at constant temperature. A simple solution of surfactant dissolved in a solvent will only have two components

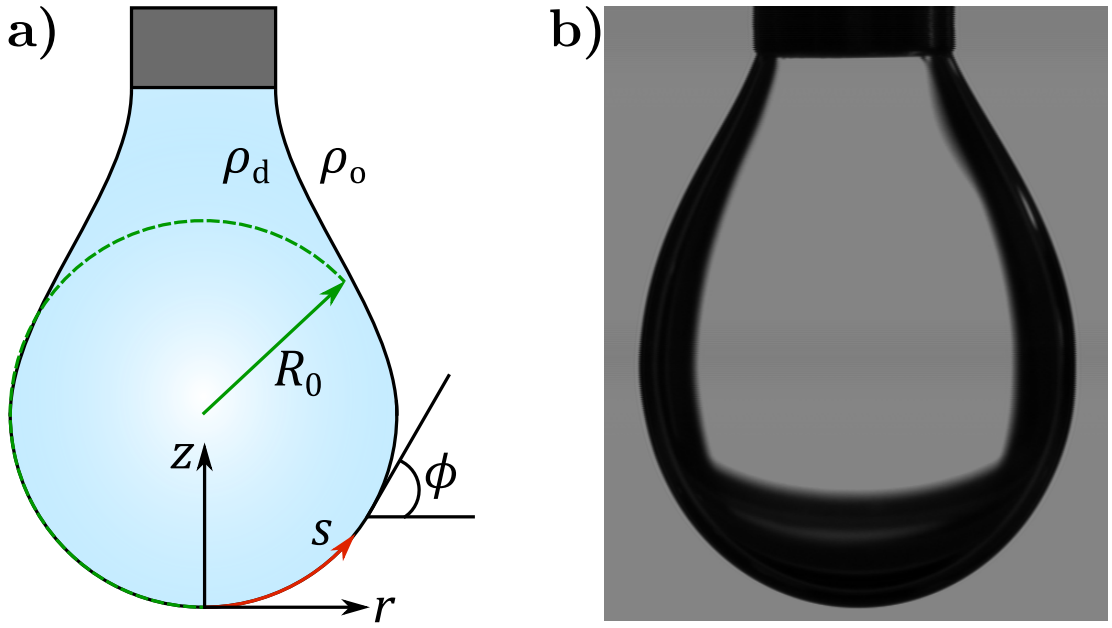

Figure 2.1: **a)** Schematic of a pendant droplet with variables used in the calculation of the interfacial tension. Here, ρ_d and ρ_o are the densities of the droplet and the surrounding fluid. **b)** Image of a typical pendant drop suspended on a blunt-ended needle.

that contribute to the surface/interfacial tension. It is common to set the surface excess of the solvent to zero, $\Gamma_{solv} = 0$, enabling the surface excess of the surfactant component, Γ_{surf}, to be expressed as

$$\Gamma_{surf} = -\left(\frac{d\gamma}{d\mu_{surf}}\right) . \tag{2.5}$$

The differential chemical potential can be expressed as $d\mu_i = RT d\ln a_i$, where R is the universal gas constant, T is the temperature of the system and a_i is the activity, defined as $a_i = C_i\alpha_i$, where C_i is the concentration and α_i is the activity coefficient. Hence, Equation 2.5 can be written as

$$\Gamma_{surf} = -\frac{a_{surf}}{RT}\left(\frac{d\gamma}{da_{surf}}\right) \tag{2.6}$$

where the logarithmic term $d\ln a_{surf}$ has been expressed as $d\ln a_{surf} = (1/a_{surf})\, da_{surf}$. By studying solutions of low surfactant concentration, one can assume the solutions behave as ideal solutions where the activity coefficient of the surfactant is ~ 1. The variation in the surface/interfacial tension at equilibrium as a function of C_{surf} can then be related to Γ_{surf} through the Gibbs adsorption isotherm as shown in Equation 2.7.

$$\Gamma_{surf} = -\frac{C_{surf}}{RT}\left(\frac{d\gamma}{dC_{surf}}\right) \tag{2.7}$$

It follows that if the surface/interfacial tension decreases between solutions of increasing C_{surf}, the surface excess of the surfactant increases, and hence a positive adsorption of surfactant at the interface has occurred. Equation 2.7 is often re-expressed using the natural logarithm

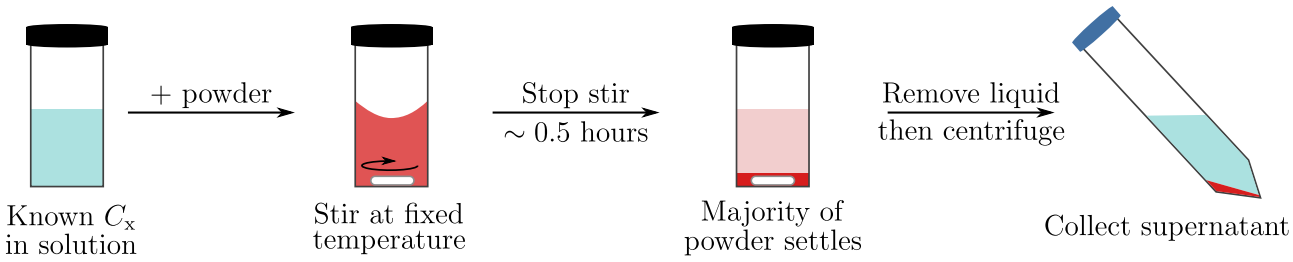

Figure 2.2: The general process of a depletion isotherm. The concentration of the surface-active compound x is denoted as C_x. The white bar in the stirring solution is a magnetic stirrer flea.

of C_{surf} to simplify fitting as the data typically adopts either linear or low-order polynomial behaviour. This is expressed in Equation 2.8.

$$\Gamma_{surf} = -\frac{1}{RT}\left(\frac{d\gamma}{d\ln(C_{surf})}\right) \tag{2.8}$$

2.1.2 Experimental

Pendant drop tensiometry was carried out on a Krüss DSA 100, using the DSA 1 software to capture and analyse the droplet images. The needles used were blunt-ended with diameters of either 1.83 or 0.53 mm. The correct choice of needle was necessary in order to achieve Bond numbers between 0.4–0.6, which are the suggested values for reliable tension measurements. The larger needle was used when studying solutions pertaining to high interfacial tensions and the smaller needle for those solutions with low interfacial tensions.

2.2 Depletion isotherms

Depletion isotherms are a class of adsorption isotherm that can be used to study the adsorption of surface-active compounds at solid-liquid interfaces. The general process is depicted in Figure 2.2. A known mass of the solid of interest, typically a powder, is added to a solution with a known initial concentration of adsorbate. The mixture is then left to equilibrate for a number of hours while under agitation at a fixed temperature. The solid is then removed and the concentration of the remaining molecule of interest is determined. The difference in concentration before and after mixing with the solid is related to the amount of the surface-active compound adsorbed at the solid-liquid interface. Hence, if the surface area of the solid is known, a surface excess of the adsorbate, Γ, can be established.

By studying the adsorption of surface-active compounds as a function of concentration, an understanding of the adsorption and adsorbate structure can be developed. In the most basic manner it is possible to determine if the adsorbed interfacial structure is composed of a single depth of molecules, or if the interfacial layer is a multilayer. The former is usually identified by a plateau in the adsorbed amount as concentration increases, while the latter is characterised by a continual increase in the amount adsorbed.

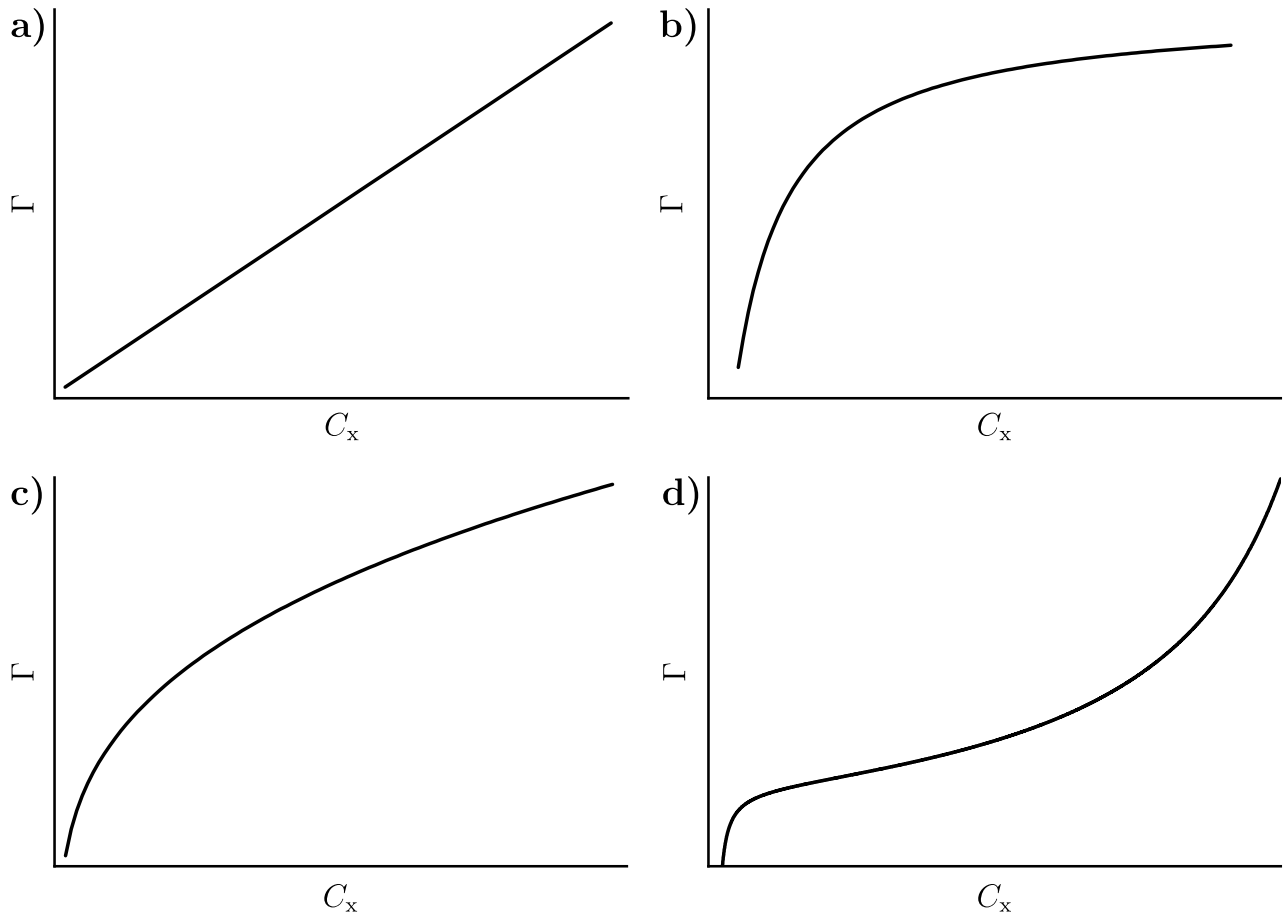

Figure 2.3: General shapes of the: **a)** Henry isotherm, **b)** Langmuir isotherm, **c)** Freundlich isotherm, **d)** BET isotherm. Note that the general trends presented here are only select cases, and various behaviours are possible, especially for the more complex BET isotherm.

For quantitative information, models must be used to infer specific information about the adsorbate, such as the area occupied at the interface by each individual molecule. Many different adsorption behaviours have been observed, which result from the specific interactions between solvent, adsorbate and the adsorbent. Therefore, in an effort to parametrise, a large number of models have been proposed.[82] A full discussion is not presented here but a small number of common isotherm models are shown in Figure 2.3 and will be discussed in the next section.

2.2.1 Models

The following isotherm models were originally developed to parametrise the adsorption of gases at solid-gas interfaces. While comparable behaviour can be found for adsorption at solid-liquid interfaces, it is worth noting that the solvent will interact with both the adsorbate and the solid surface. When an adsorbent is first introduced to a solution, the surface will be surrounded by solvent molecules due to their greater number. Therefore, adsorption of the solute can only occur by displacement of the solvent molecules from the solid surface and hence, interactions of comparable strength between solvent-adsorbent and solute-adsorbent pairs can lead to competitive adsorption. As such, the adsorption behaviour of a solute is dependant on

the solvent.

Henry isotherm

The Henry isotherm is the simplest example of an adsorption isotherm, where the surface excess is a linear function of the equilibrium concentration of the adsorbate in solution. The Henry isotherm is given as

$$\Gamma = K_{\mathrm{H}} C_{\mathrm{x}} \,, \tag{2.9}$$

where C_{x} is the equilibrium concentration of the adsorbate species x and K_{H} is the Henry equilibrium constant. The constant K_{H} can be interpreted as the ratio of the rate constants associated with the adsorption process, k_{a}, and the desorption process, k_{d}, of the adsorbate. In many isotherms, it is often found that the data at low concentrations follows the Henry isotherm but deviates at higher concentrations.

Langmuir isotherm

The Langmuir isotherm is a widely used model to characterise the adsorption of species at solid-gas and solid-liquid interfaces. It was derived in the early 20$^{\mathrm{th}}$ century from kinetics, where the adsorption and desorption processes of the adsorbate species are a function of the number of available sites at the interface.[83] The rate of adsorption and desorption, r_{a} and r_{d} respectively, are described as

$$r_{\mathrm{a}} = k_{\mathrm{a}} C_{\mathrm{x}} \epsilon_{\mathrm{v}} \qquad \text{and} \qquad r_{\mathrm{d}} = k_{\mathrm{d}} \epsilon_{\mathrm{o}} \,, \tag{2.10}$$

where ϵ_{v} is the number of vacant sites and ϵ_{o} is the number of occupied sites. When equilibrium is reached the rates of reaction are equivalent, and thus:

$$\frac{\epsilon_{\mathrm{o}}}{\epsilon_{\mathrm{tot}}} = \frac{C_{\mathrm{x}} k_{\mathrm{a}}}{k_{\mathrm{d}} + C_{\mathrm{x}} k_{\mathrm{a}}} \tag{2.11}$$

where ϵ_{tot}, the total number of sites on the surface, is given as $\epsilon_{\mathrm{v}} + \epsilon_{\mathrm{o}}$. The fractional surface coverage is defined as $\epsilon_{\mathrm{o}}/\epsilon_{\mathrm{tot}}$ and can be defined in terms of the surface excess compared to a theoretical maximum surface excess when the whole surface is covered by adsorbate, Γ_{m}. The Langmuir equilibrium constant, K_{L} is defined as $k_{\mathrm{a}}/k_{\mathrm{d}}$. Therefore it is possible to define the Langmuir isotherm as

$$\Gamma = \frac{\Gamma_{\mathrm{m}} K_{\mathrm{L}} C_{\mathrm{x}}}{1 + K_{\mathrm{L}} C_{\mathrm{x}}} \,. \tag{2.12}$$

This approach assumes three key features about the adsorption process. The first assumption is that adsorption only occurs at certain sites on the adsorbent and each site behaves identically. The second assumption is that the interaction between the adsorbate and the adsorbent is independent of the surface excess, and hence no interaction occurs between adjacent adsorbate

molecules. The final assumption is that only one site can be occupied by a molecule, and hence when all sites are occupied the surface excess reaches a plateau and a monolayer is formed. These assumptions are not physical for many practical systems, but the Langmuir isotherm does mimic the adsorption behaviour of a surprising number of systems.[84,85]

Freundlich isotherm

The Freundlich isotherm is an empirical isotherm which does not follow the Henry isotherm at low C_{x} and does not show an adsorption plateau. It is argued that adsorption follows the Freundlich isotherm when the surface behaves heterogeneously. The model is given by:

$$\Gamma = K_{\mathrm{F}} C_{\mathrm{x}}^{1/n} \,. \tag{2.13}$$

Here, K_{F} is the Freundlich equilibrium constant and n is a number > 1. The former is suggested to describe the adsorbent capacity and the latter describes the degree of heterogeneity of the surface sites.[86] Both constants are empirical and, as a result, the isotherm is only typically considered when other models do not describe data satisfactorily. The lack of a plateau suggests the build up of multiple adsorbate layers. Therefore, interactions between neighbouring adsorbate molecules must influence the adsorption, and will no doubt impact the values of K_{F} and n.

BET isotherm

The Brunauer, Emmett and Teller (BET) isotherm is an extension of the Langmuir isotherm and was derived when studying the adsorption of gas molecules onto solid surfaces which form multilayers.[87] At low pressures, it is assumed a single layer of gas will adsorb at the interface with a homogeneous heat of adsorption, q_1. As the pressure increases, gas will begin to adsorb at the monolayer, and a multilayer structure will begin to form. This process is assumed to have a different heat of adsorption to the monolayer formation, but the heat of adsorption for the peripheral layers, q_{L}, is assumed to be identical. The BET isotherm is given by

$$V = \frac{V_{\mathrm{m}} K_{\mathrm{BET}} P}{(P_{\mathrm{s}} - P)\left[1 + (K_{\mathrm{BET}} - 1)\left(\dfrac{P}{P_{\mathrm{s}}}\right)\right]} \tag{2.14}$$

where V is the volume of the adsorbed gas which is determinable through the ideal gas law upon exposure to the solid powder and V_{m} is the volume of the gas when a full monolayer is adsorbed at the interface. The ratio, K_{BET}, is the equilibrium constant for adsorption directly at the interface to the equilibrium constant for adsorption in the peripheral layers, and Γ_{m} is the surface excess of the gas required to form a complete monolayer. The pressure of the gas at equilibrium is P and P_{s} is the saturation pressure of the gas at a given temperature. It is possible to approximate K_{BET} as a function of q_1 and q_{L}, $K_{\mathrm{BET}} = e^{(q_1 - q_{\mathrm{L}})/RT}$. The BET isotherm is often used to find the surface area of a solid per unit mass, S, by using the pre-

determined cross-sectional area per molecule, A_{PM}, of a particular gas and the mass of the solid, M, in conjunction with Equation 2.15. Nitrogen gas is often used at a temperature of 77 K, which has an $A_{\mathrm{PM}} = 16.2$ Å^2.

$$S = \frac{\left(\frac{V_{\mathrm{m}}}{V^{\mathrm{m}}}\right) N_{\mathrm{A}} A_{\mathrm{PM}}}{M} \tag{2.15}$$

Here, V^{m} is the molar volume of an ideal gas and N_{A} is the Avogadro constant.

The BET isotherm can also be applied to liquid systems, where the pressure is replaced by the concentration of the adsorptive species in solution and the volume is substituted for the analogous surface excess by taking into account the specific surface area:

$$\Gamma = \frac{\Gamma_{\mathrm{m}} K_{\mathrm{BET}} C_{\mathrm{x}}}{(C_{\mathrm{x}}^{\mathrm{s}} - C_{\mathrm{x}}) \left[1 + (K_{\mathrm{BET}} - 1)\left(\frac{C_{\mathrm{x}}}{C_{\mathrm{x}}^{\mathrm{s}}}\right)\right]}\,. \tag{2.16}$$

Here, $C_{\mathrm{x}}^{\mathrm{s}}$ is the solution property that is an analogue of the saturation pressure. There is some debate as to what property $C_{\mathrm{x}}^{\mathrm{s}}$ should represent. Some researchers use the solubility limit of the adsorptive species in solution, while others have chosen to fit the parameter and make the isotherm empirical.[88,89]

2.2.2 Experimental

Solutions of known concentration were prepared and masses of ~ 0.5 g of powdered samples were added to the solutions along with a magnetic flea. These solutions were stirred for at least 5 hours to ensure equilibrium. The solutions were then left to stand for approximately 30 minutes to enable the majority of the powder to settle out. After, approximately 7 ml of the liquid from the top of the sample was removed and centrifuged at 10,000 rpm to settle out the remaining powder from the suspension. The supernatant was collected and the concentration was determined by Fourier transform infra-red (FTIR) spectroscopy, using a PerkinElmer Spectrum 100 spectrometer with a liquid N_2-cooled mercury-cadmium-telluride detector. A PIKE liquid transmission cell with CaF_2 windows seperated by a 1 mm spacer was used to contain the samples while the transmission of IR radiation was determined.

2.3 Neutron reflectometry

Neutron reflectometry (NR) is an elastic scattering technique that utilises the reflection of neutrons across boundaries of differing neutron optical indices in order to determine the properties of thin films. Reflection can be measured in various directions from the interface, with the two main modes of reflectivity known as specular and off-specular. Specular reflectivity is primarily used to determine the thickness and atomic densities of thin films.

Owing to the penetration depth of neutrons, they can be used to study buried solid-liquid interfaces, which are less accessible with electromagnetic radiation. Furthermore, as the elements do not scatter neutrons in a homogeneous way, thin films can be highlighted by selecting materials comprised of different elements or isotopes. One useful example of this is the difference in scattering between the two lightest isotopes of hydrogen, ^{1}H and ^{2}H. By enriching the amount of ^{2}H in a compound, it is possible to distinguish between layers that have a high concentration of ^{1}H or ^{2}H.

Neutron reflectometry involves the measurement of the reflected intensity of neutrons from the interface of interest, and suffers the loss of phase information similar to other diffraction and scattering techniques. Consequently, the collected data cannot be directly inverted for interpretation, and a representative model must be fit to the data in order to extract quantitative information. A basic description of neutron reflectometry theory is laid out so that work presented later can be interpreted. More detailed descriptions of neutron reflectometry can be found elsewhere.[90–93]

2.3.1 Theory

The time-independent Schrödinger equation describes the wavefunction, Ψ, for a neutron propagating over space as shown in Equation 2.17.

$$\left[-\frac{\hbar^2}{2m_\mathrm{n}}\nabla^2 + V(\boldsymbol{r})\right]\Psi = E\Psi \tag{2.17}$$

Here, m_n is the mass of a neutron, E is the total energy of the neutron, $V(\boldsymbol{r})$ is the neutron interaction potential and the Laplacian, ∇^2, in Cartesian coordinates is given by

$$\nabla^2 = \frac{\partial^2}{\partial x^2} + \frac{\partial^2}{\partial y^2} + \frac{\partial^2}{\partial z^2}\,, \tag{2.18}$$

where x, y, z are a orthogonal coordinate system. A neutron propagating through a free-space vacuum has an energy

$$E = \frac{|\hbar\boldsymbol{k}_0|^2}{2m_\mathrm{n}}\,, \tag{2.19}$$

where $\boldsymbol{k}_0$ is the neutron wavevector in a vacuum. The magnitude of the wavevector, $k_0 = |\boldsymbol{k}_0|$, is related to the neutron wavelength, λ, through $k_0 = 2\pi/\lambda$. The wavelength is related to the linear momentum, p, as described by the de Brogile relation, $\lambda = h/p$ where the linear momentum of a neutron can be defined in terms of the neutron velocity, v_n, as $p = m_\mathrm{n}v_\mathrm{n}$.

When a neutron propagates through a material, $V(\boldsymbol{r})$ will be non-zero. There are two main scattering interactions between neutrons and matter; the strong interaction between a neutron and a nucleus of a material, and a magnetic interaction between the neutron spin and the magnetic field produced by unpaired electrons of magnetic atoms.

Neutron interactions with nuclei

The strong interaction between an individual nuclei and neutron is considered to be point-like. In a medium containing many individual nuclei, $V(\boldsymbol{r})$ can be considered as the interaction between the neutron and the distribution of nuclei. If this distribution is homogeneous, the interaction potential can be described by

$$V_{\mathrm{n}}(\boldsymbol{r}) = \left(\frac{2\pi\hbar^2}{m_{\mathrm{n}}}\right) Nb\,. \tag{2.20}$$

Here, N is the number density of the nuclei within the material and b is the scattering length of the material nuclei. The scattering length is a complex number, $b = b' + ib''$, with real, b', and imaginary, b'', components. The imaginary number, i, is defined as $\sqrt{-1}$. The scattering component is described by b', which varies across the chemical elements and isotopes of the periodic table without a distinct pattern as shown for the first 26 elements in Figure 2.4.

The total rate of scattering, ω_{scat}, from a non-magnetic nuclei can be described as $\omega_{\mathrm{scat}} = I_0 \times \sigma_{\mathrm{scat}}$, where $\sigma_{\mathrm{scat}} = 4\pi b'^2$, which is known as the total scattering cross-section, and I_0 is the intensity of neutrons incident onto the sample nuclei. The total scattering cross-section of a nuclei can be considered as the sum of the coherent scattering cross-section, σ_{coh}, and the incoherent scattering cross-section, σ_{incoh}. The former cross-section describes the amount of scattering from a nuclei that leads to a discernible scattered neutron intensity profile, whereas σ_{incoh} describes the amount of scatter that has little to no structure in the neutron intensity profile. As such, it is possible to regard the bound coherent scattering length, b'_{coh}, and bound incoherent scattering length, b'_{incoh}, for individual nuclei following Equation 2.21.

$$b'_{\mathrm{coh}} = \sqrt{\frac{4\pi}{\sigma_{\mathrm{coh}}}} \qquad\qquad b'_{\mathrm{incoh}} = \sqrt{\frac{4\pi}{\sigma_{\mathrm{incoh}}}} \tag{2.21}$$

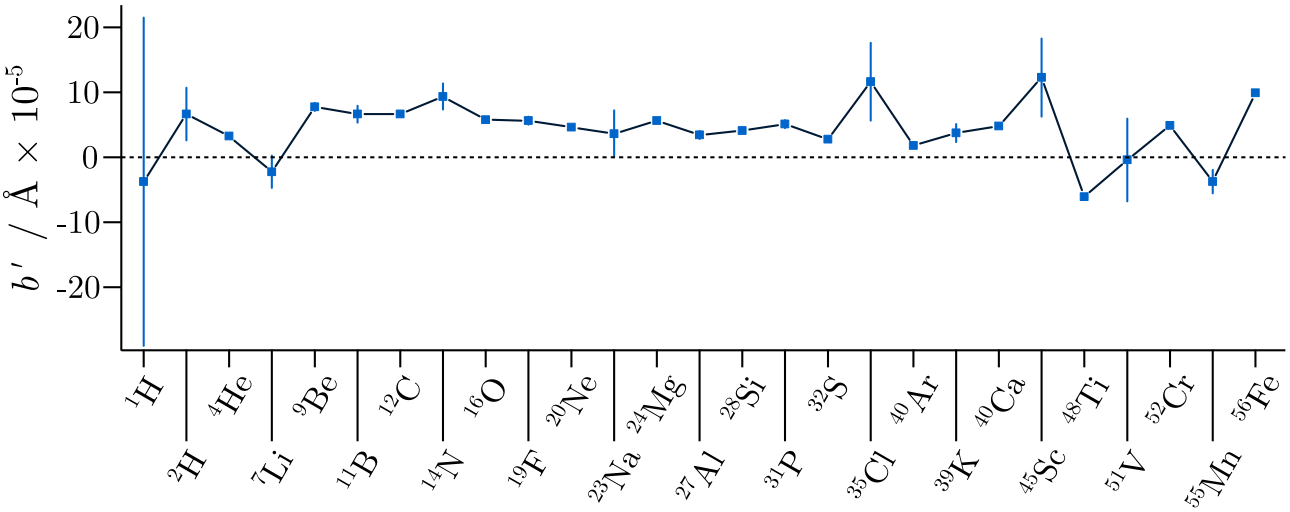

Figure 2.4: The real component of the scattering length, b', for the first 26 elements.[94] Each point is the value of b'_{coh} while the bar at each point corresponds to the bound incoherent scattering length b'_{incoh}. The lines between data points are interpolations to guide the eye.

The imaginary component of the scattering length describes the absorption of neutrons by sample nuclei, where the absorption cross-section, σ_{abs}, can be defined as $\sigma_{\text{abs}} = (4\pi/k_0)b''$. The attenuation of a beam of neutrons in a particular forward direction by absorption and scattering can then be described by Beer's law in Equation 2.22.

$$I = I_0 \mathrm{e}^{-\mu L} \tag{2.22}$$

Here, μ is the attenuation coefficient and is defined as $\mu = N \times \sigma_{\text{tot}}$, where $\sigma_{\text{tot}} = \sigma_{\text{coh}} + \sigma_{\text{incoh}} + \sigma_{\text{abs}}$, and L is the path length of the neutron beam within a material.

The combination of the number density and the scattering length of a material is referred to as the nuclear scattering length density, $\beta_{\text{n}} = Nb$, where the real component describes the scattering power and the imaginary component describes the absorption power of a material's nuclei. In general, the nuclear scattering length density of a material containing i different nuclei can be described following Equation 2.23. For the remainder of this thesis, the nuclear scattering length density will refer specifically to the coherent contribution of β_{n}, with the incoherent and absorption terms neglected unless specifically mentioned.

$$\beta_{\text{n}} = N \sum_i b_i \tag{2.23}$$

Neutron interactions with magnetic materials

Neutrons possess a magnetic moment, $\boldsymbol{\mu}_{\text{m}}$, which is defined as $\boldsymbol{\mu}_{\text{m}} = \gamma \mu_{\text{N}} \boldsymbol{\sigma}$, where $\gamma = -1.913$, $\mu_{\text{N}} = 5.050 \times 10^{-27}$ A m^2 and $\boldsymbol{\sigma}$ are the Pauli matrices. If a neutron enters a region of space with a magnetic field, the neutron interaction potential will be altered by the magnetic flux density, $\boldsymbol{B}(\boldsymbol{r})$, as shown in Equation 2.24.

$$V_{\text{m}}(\boldsymbol{r}) = -\boldsymbol{\mu}_{\text{m}} \cdot \boldsymbol{B}(\boldsymbol{r}) \tag{2.24}$$

Atoms with unpaired electrons can induce a $\boldsymbol{B}(\boldsymbol{r})$, and hence cause a scattering interaction with a neutron. As neutrons are spin 1/2 particles, neutrons can either be aligned with or against the magnetic field within a material, where the former alignment is referred to as spin-up(+) and the latter is termed spin-down(−). The total interaction potential is then the combination of the nuclear and magnetic interactions, $V(\boldsymbol{r}) = V_{\text{n}}(\boldsymbol{r}) \mp V_{\text{m}}(\boldsymbol{r})$. The magnetic scattering length density, β_{m}, for a magnetic material can be defined as

$$\beta_{\text{m}} = \frac{-m_{\text{n}}}{2\pi\hbar^2} \boldsymbol{\mu}_{\text{m}} \cdot \boldsymbol{B}(\boldsymbol{r})\,. \tag{2.25}$$

It is possible to express $\beta_{\text{m}} = CN\mu_{\text{mat}}$, where μ_{mat} is the magnetic moment per formula unit of a material in bohr magneton, μ_{B}, and C is a constant of 2.699×10^{-5} Å μ_{B}^{-1}. Specifically, μ_{mat} is the component of the material's magnetic moment in the plane of the sample. The total scattering length density for spin-up, β_{++}, and spin-down, β_{--}, neutrons are defined in

Equation 2.26.

$$\beta_{++} = \beta_{\mathrm{n}} + \beta_{\mathrm{m}} \qquad \beta_{--} = \beta_{\mathrm{n}} - \beta_{\mathrm{m}} \tag{2.26}$$

Reflection with neutrons

A schematic of a simple reflection experiment is shown in Figure 2.5a, where a beam of neutrons with the wavevector, $\boldsymbol{k}_{\mathrm{i}}$, is incident onto a perfectly flat interface between two homogeneous media at a grazing angle, θ_{i}. As the neutrons strike the interface, neutrons are either reflected at the specular angle, where $\theta_{\mathrm{r}} = \theta_{\mathrm{i}}$, or transmitted into the medium at an angle θ_{t}. The specular reflectivity, R, is defined as $R = I_{\mathrm{R}}/I_0$, where I_{R} is the intensity of reflected neutrons and I_0 is the incident intensity of neutrons onto the sample.

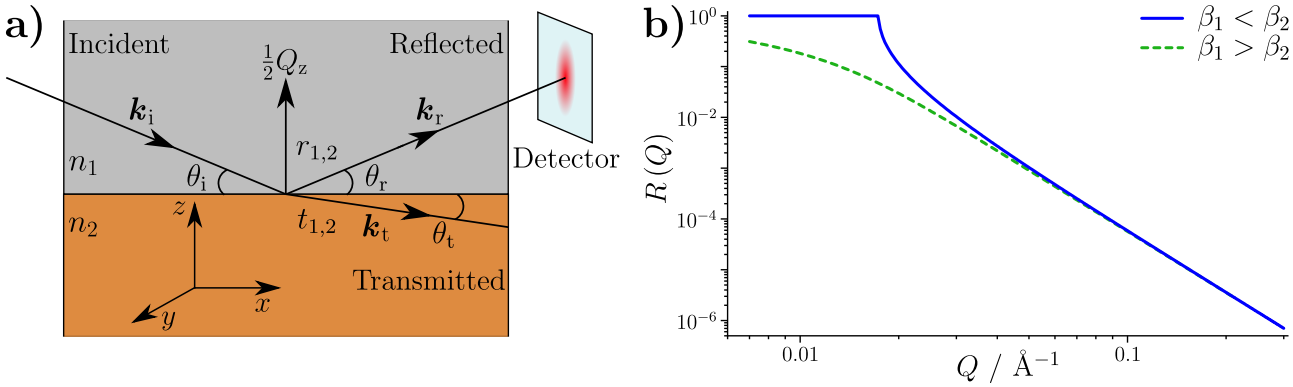

Figure 2.5: **a)** Schematic of specular reflection from an ideal interface between two media with neutron refractive indices n_1 and n_2. The reflected beam has a wavevector $\boldsymbol{k}_{\mathrm{r}}$ with an amplitude of $r_{1,2}$. The transmitted beam has the wavevector $\boldsymbol{k}_{\mathrm{t}}$ with an amplitude of $t_{1,2}$. **b)** Simulated reflectivity, $R\,(Q)$, from ideal interfaces as a function of Q. The difference in β between the two layers is 6×10^{-6} Å^{-2}. The profile simulated where $\beta_1 < \beta_2$ exhibits total reflection at the interface when $Q < 0.017$ Å^{-1}. This is not observed in the profile where $\beta_1 > \beta_2$.

The reflectivity can also be expressed as a function of the Fresnel reflection coefficient, r, by

$$R = \left| \frac{r}{\psi_{\mathrm{i}}} \right|^2 . \tag{2.27}$$

The reflection coefficient describes the amplitude of the reflected wave, and ψ_{i} describes the amplitude of the incident wave, which is usually defined as $\psi_{\mathrm{i}} = 1$ for convenience. To determine the value of the Fresnel reflection coefficient, the wavefunction of the incident, reflected and transmitted neutrons must be considered. Due to the nature of layered samples, $V(\boldsymbol{r})$ will only vary in the z-direction; therefore, the Schrödinger equation is reduced to a one-dimensional

equation,

$$\frac{-\hbar^2}{2m_\mathrm{n}}\frac{\mathrm{d}^2\Psi}{\mathrm{d}z^2} + V(\boldsymbol{r})\Psi = E\Psi$$

$$\left[\frac{\mathrm{d}^2}{\mathrm{d}z^2} + k_\pm^2\right]\Psi = 0 \tag{2.28}$$

$$k_\pm^2 = \frac{2m_\mathrm{n}}{\hbar^2}\left(E - V(\boldsymbol{r})\right) .$$

Here, $k_\pm$ is the spin-dependant wavenumber of the neutron within a material, which can be expressed as a function of the wavenumber within a vacuum, $k_\pm = \sqrt{k_0^2 - 4\pi\left(\beta_\mathrm{n} \pm \beta_\mathrm{m}\right)}$. The general solution for the wavefunction in the first medium, ψ_1, is given as

$$\psi_1 = \psi_\mathrm{i} e^{-ik_1 \sin\theta_\mathrm{i} z} + re^{ik_1 \sin\theta_\mathrm{i} z}, \tag{2.29}$$

where the incident wave propagates in the $-z$ direction and the reflected wave propagates in the $+z$ direction. It is possible to describe the wavefunction using a singular wavenumber and angle as $|\boldsymbol{k}_\mathrm{i}| = k_i = k_r = k_1$ and $\theta_\mathrm{i} = \theta_\mathrm{r}$. The wavefunction for the transmitted neutron wave in the second medium is given as

$$\psi_2 = te^{-ik_2 \sin\theta_\mathrm{t} z} \tag{2.30}$$

where t is the amplitude of the transmitted neutron wave in the second medium. The continuity of the wavefunction, and its first derivative, at the interface (where $z = 0$) requires that $1+r = t$ and $k_1 \sin\theta_\mathrm{i}(1 - r) = tk_2 \sin\theta_\mathrm{t}$. These equations are simultaneous equations, and thus, it is possible to express r and t as

$$t = \frac{2k_1 \sin\theta_\mathrm{i}}{k_2 \sin\theta_\mathrm{t} + k_1 \sin\theta_\mathrm{i}} \qquad \text{and} \qquad r = \frac{k_1 \sin\theta_\mathrm{i} - k_2 \sin\theta_\mathrm{t}}{k_1 \sin\theta_\mathrm{i} + k_2 \sin\theta_\mathrm{t}} . \tag{2.31}$$

where it is evident that the reflectivity will be dependant on θ_i and λ of the incident neutrons. The momentum change of the reflected neutrons is given as $\boldsymbol{Q} = \boldsymbol{k}_\mathrm{r} - \boldsymbol{k}_\mathrm{i}$. For specular reflection the scattering vector is exclusively in the z-direction so that $\boldsymbol{Q} = Q_\mathrm{z}$, which is referred to as Q and can be defined in terms of θ_i and λ as

$$Q = \frac{4\pi \sin\theta_\mathrm{i}}{\lambda} . \tag{2.32}$$

The reflectivity from two ideal interfaces as a function of Q has been simulated and is shown in Figure 2.5b. The reflectivity profile simulated where $\beta_1 < \beta_2$ displays total reflection at low Q. This phenomenon can be understood by considering the angle adopted by the transmitted beam through Snell's law, where $n_{\pm,1} \cos\theta_\mathrm{i} = n_{\pm,2} \cos\theta_\mathrm{t}$. Here, $n_\pm$ are the neutron refractive

indices of each material, where $n_{\pm}^2$ can be defined as shown in Equation 2.33.

$$n_{\pm}^2 = \frac{k_{\pm}^2}{k_0^2} = 1 - \frac{\lambda^2}{\pi}\left(\beta_{\mathrm{n}} \pm \beta_{\mathrm{m}}\right) \tag{2.33}$$

For many materials $\left|n_{\pm}^2 - 1\right|$ is typically $< 10^{-3}$ and so $n_{\pm}$ can be approximated as

$$n_{\pm} \approx 1 - \frac{\lambda^2}{2\pi}\left(\beta_{\mathrm{n}} \pm \beta_{\mathrm{m}}\right) \tag{2.34}$$

by considering the first two terms of the Taylor series of $\sqrt{1+x}$, where $x = \left(n_{\pm}^2 - 1\right)$. When $n_{\pm,1} > n_{\pm,2}$ and θ_{i} is small so that $\cos\theta_{\mathrm{i}} \sim 1$,

$$\frac{n_{\pm,1}\cos\theta_{\mathrm{i}}}{n_{\pm,2}} > 1\,. \tag{2.35}$$

Therefore, θ_{t} is purely imaginary with a real component equal to zero. This corresponds to zero transmission of intensity into the second medium; therefore, the neutrons are completely reflected. This is the case until $\theta_{\mathrm{i}} > \cos^{-1}\left(n_{\pm,2}/n_{\pm,1}\right)$, where the reflectivity will begin to fall with increasing Q. The sudden drop in reflectivity just beyond the region of total reflection is known as the critical edge and the associated Q value at the critical edge is $Q_{\mathrm{c}} = 4\sqrt{\pi\left(\beta_2 - \beta_1\right)}$. At higher Q, far beyond the critical edge, the reflectivity falls away following $R \propto 1/Q^4$.

Reflection from samples with thin films

When the sample contains a thin layer between two media, multiple reflections can occur between the first two interfaces as depicted in Figure 2.6a. The numerous reflections combine either constructively or destructively as a function of Q, forming an interference pattern in the measured reflectivity. An example of this has been simulated in Figure 2.6b, where clear interference fringes are visible. These are referred to as Kiessig fringes, where the Q spacing between the fringes, ΔQ, is inversely related to the thickness of the thin film, d, through $\Delta Q = 2\pi/d$.

In order to account for multiple reflections from samples with thin films, it is necessary to consider the combined reflection and transmission amplitudes from each layer. The total reflectivity can then be calculated using the combined reflection amplitude, r_{tot}, in conjunction with Equation 2.27. For the case shown in Figure 2.6a, we can consider r_{tot} as the infinite sum shown in Equation 2.36.

$$\begin{aligned} r_{\mathrm{tot}} &= r_{1,2} + t_{1,2}r_{2,3}t_{2,1}e^{-i2\phi} + t_{1,2}r_{2,3}^2 r_{2,1}t_{2,1}e^{-i4\phi} + \cdots \\ r_{\mathrm{tot}} &= r_{1,2} + t_{1,2}r_{2,3}t_{2,1}e^{-i2\phi}\left[1 + r_{2,3}r_{2,1}e^{-i2\phi} + r_{2,3}^2 r_{2,1}^2 e^{-i4\phi} + \cdots\right] \end{aligned} \tag{2.36}$$

The product of transmission and reflection amplitudes originate from the path taken before reflection towards the detector. The exponential factor is known as the phase offset between

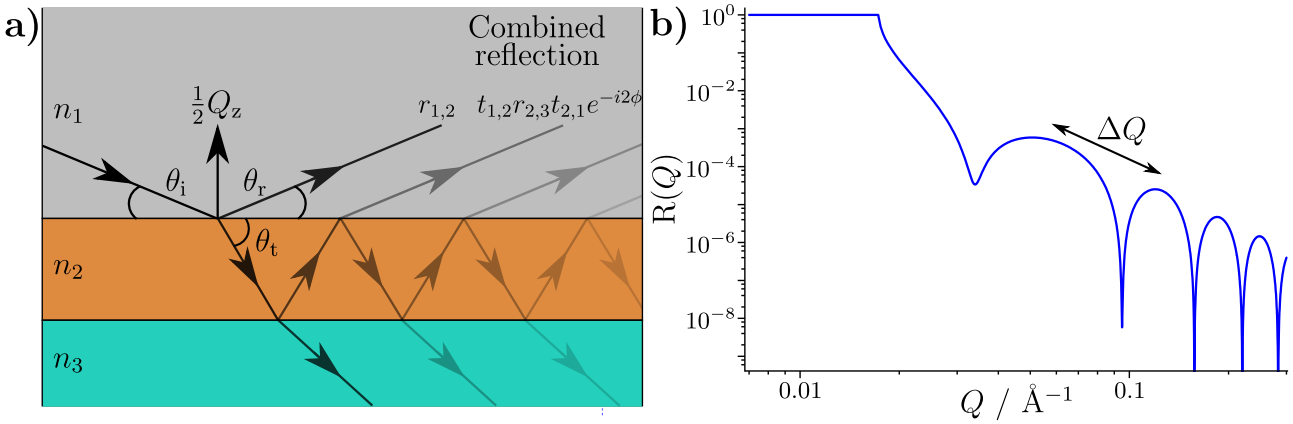

Figure 2.6: **a)** Specular reflection from a layered sample, where reflection occurs from both the interface between the first two layers and the interface between the middle and last interface. The amplitudes of the first two reflected neutron waves propagating towards the detector are labelled. **b)** Simulated reflectivity from layered samples as shown in **a)**, where β is equal to 6, 3 and 0×10^{-6} Å^{-2} for the media with n_1, n_2 and n_3 respectively. The thickness, d, of the thin film is 100 Å. Multiple reflections from the middle layer combine, leading to an interference pattern in the reflectivity data.

the reflected waves and ϕ is the phase difference as given in Equation 2.37.

$$\phi = \frac{2\pi}{\lambda} d\, n_2 \sin\theta_t \tag{2.37}$$

The sum in the square brackets of Equation 2.36 can be expressed as the sum of a geometric progression,

$$\sum_{j=0}^{n-1} a l^j = a\left(\frac{1-l^n}{1-l}\right), \tag{2.38}$$

where $l = r_{2,3}r_{2,1}e^{-i2\phi}$. Therefore, the sum in the square brackets is

$$\left[1 + r_{2,3}r_{2,1}e^{-i2\phi} + r_{2,3}^2 r_{2,1}^2 e^{-i4\phi} + \cdots\right] = \frac{1 - r_{2,3}^n r_{2,1}^n e^{-i2n\phi}}{1 - r_{2,3}r_{2,1}e^{-i2\phi}}. \tag{2.39}$$

The reflection coefficients will tend to zero after a large number of reflections, n, in the thin film. Therefore, the sum of the geometric progression can be simplified to

$$\left[1 + r_{2,3}r_{2,1}e^{-i2\phi} + r_{2,3}^2 r_{2,1}^2 e^{-i4\phi} + \cdots\right] = \frac{1}{1 - r_{2,3}r_{2,1}e^{-i2\phi}}. \tag{2.40}$$

The above expression can be substituted into Equation 2.36 to provide:

$$r_{\text{tot}} = r_{1,2} + t_{1,2}r_{2,3}t_{2,1}e^{-i2\phi}\left(\frac{1}{1 - r_{2,3}r_{2,1}e^{-i2\phi}}\right)$$

$$r_{\text{tot}} = r_{1,2} + \frac{t_{1,2}r_{2,3}t_{2,1}e^{-i2\phi}}{1 - r_{2,3}r_{2,1}e^{-i2\phi}} \tag{2.41}$$

$$r_{\text{tot}} = \frac{r_{1,2} + r_{1,2}^2 r_{2,3}e^{-i2\phi} + t_{1,2}r_{2,3}t_{2,1}e^{-i2\phi}}{1 + r_{1,2}r_{2,3}e^{-i2\phi}}$$

where the last equation is possible as $r_{\text{x,y}} = -r_{\text{y,x}}$. Using the identity $1 + r = t$, r_{tot} can be expressed solely with reflection coefficients as shown in Equation 2.42.

$$r_{\text{tot}} = \frac{r_{1,2} + r_{1,2}^2 r_{2,3}e^{-i2\phi} + (1 + r_{1,2})\, r_{2,3}\, (1 - r_{1,2})\, e^{-i2\phi}}{1 + r_{1,2}r_{2,3}e^{-i2\phi}} \tag{2.42}$$

$$r_{\text{tot}} = \frac{r_{1,2} + r_{2,3}e^{-i2\phi}}{1 + r_{1,2}r_{2,3}e^{-i2\phi}}$$

The reflectivity can be calculated using the complex conjugate of r_{tot}, r_{tot}^*:

$$R = \left|\frac{r_{\text{tot}}}{\psi_{\text{i}}}\right|^2 = r_{\text{tot}}r_{\text{tot}}^* = \frac{r_{1,2} + r_{2,3}e^{-i2\phi}}{1 + r_{1,2}r_{2,3}e^{-i2\phi}} \times \frac{r_{1,2} + r_{2,3}e^{+i2\phi}}{1 + r_{1,2}r_{2,3}e^{+i2\phi}}\,. \tag{2.43}$$

This process can be generalised for a sample with $m-1$ interfaces between m media of different β using the Abelés matrix method or the equivalent Parratt recursive formalism.[95] The former method is presented here, where a 2×2 matrix, $\mathbf{C}_m$, is assigned to each medium as shown in Equation 2.44.

$$\mathbf{C}_m = \begin{bmatrix} e^{i\phi_m} & r_{m,m+1}e^{i\phi_m} \\ r_{m,m+1}e^{-i\phi_m} & e^{-i\phi_m} \end{bmatrix} \tag{2.44}$$

The product of the m matrices leads to a final 2×2 matrix, $\mathbf{M}$:

$$\mathbf{M} = \prod_1^m \mathbf{C}_m = \begin{bmatrix} \mathrm{M}_{11} & \mathrm{M}_{12} \\ \mathrm{M}_{21} & \mathrm{M}_{22} \end{bmatrix}\,. \tag{2.45}$$

The exponential factor $e^{i\phi_m}$ for the first and last media are equal to one as $\phi_1 = 0$ and $\phi_m = 0$. The reflection coefficient, $r_{m,m+1}$, arising from the interface of the m^{th} and $m + 1^{\text{th}}$ media is zero. The total reflection amplitude, r_{tot}, can then be calculated using two elements of $\mathbf{M}$:

$$r_{\text{tot}} = \frac{\mathrm{M}_{21}}{\mathrm{M}_{11}}\,. \tag{2.46}$$

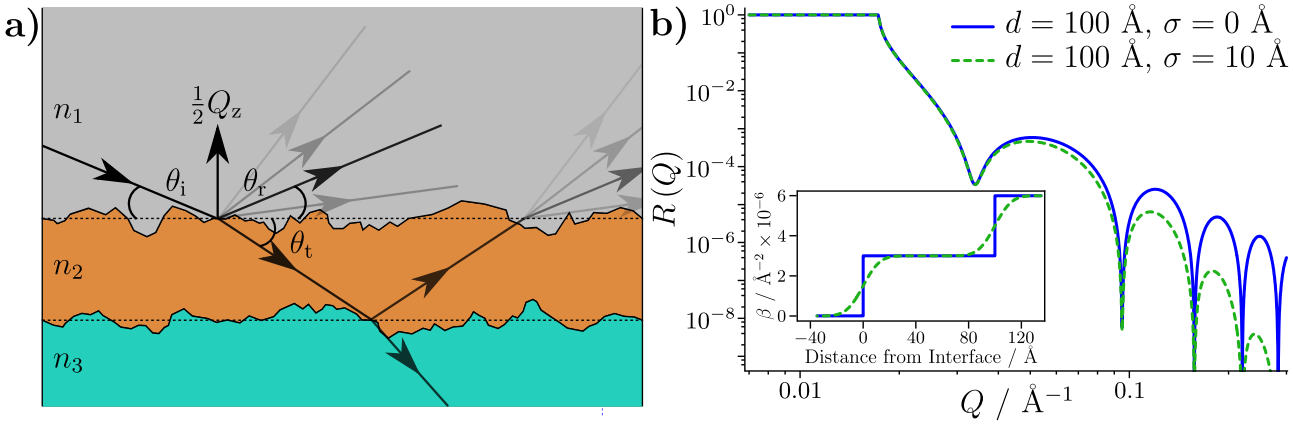

Figure 2.7: **a)** Reflection from a rough layered sample, with specular reflection shown as the darker arrows and off-specular reflection as the transparent arrows. Off-specular reflection from the second interface is not shown for clarity. The transmission angles for the second and third layers will also have distributions from the roughened interfaces, which are not shown for clarity. **b)** Comparison of specular reflectivity measured from two layered samples. The blue profile is that from Figure 2.6 and the dashed green profile is simulated for a system with the same layer thickness but with $\sigma = 10$ Å. The inset shows the β profile over the vertical distance from the first interface for both samples.

Surfaces and interfaces are never ideal and have some intrinsic roughness associated with them. The roughness of a surface decreases the specular reflection and increases the off-specular reflection compared to the idealised model of the surface as depicted in Figure 2.7. The reduction in specular reflection can be modelled by the Croce-Névot factor, which modifies the reflection amplitude calculated for an ideal interface as shown in Equation 2.47.

$$r_{\text{rough}} = r_{\text{flat}} e^{-2k_{z,m}k_{z,m+1}\sigma_m^2} \tag{2.47}$$

Here, $k_{z,m}$ is the component of the wavevector in the m^{th} medium in the z-direction, where $k_{z,m} = k_m \sin\theta_m$. The σ_m term is the root-mean-square, or RMS, roughness of the interface between the m^{th} and $m+1^{\text{th}}$ media, which can be defined as:

$$\sigma_m = \sqrt{\langle h^2 \rangle} \tag{2.48}$$

where h is the vertical deviation from the average height of the rough surface and the brackets, $\langle\rangle$, denote the macroscopic average of h^2 over the area of the sample. As the Croce-Névot factor models the variation of two materials over an interface with a Gaussian distribution, the value of σ_m must be considered carefully. A model will become increasingly non-physical as a layer's roughness approaches the value of the layer thickness, and models with layer roughnesses greater than their thicknesses should be viewed with scepticism. The roughness of a layer is often constrained to only adopt values which are, at most, half that of the layer thickness, inhibiting the adoption of non-physical values. This corresponds to at least 95 % of the negative vertical deviations from an interface falling within the average thickness of the layer, as estimated through the Gaussian probability density between the mean and 2σ.

2.3.2 Experimental

Neutron reflectometry experiments were conducted on INTER[96] at ISIS, UK and FIGARO[97] at the Institut Laue-Langevin (ILL), France. Both reflectometers operate on a time-of-flight (ToF) principle, where the incident neutron beam has a distribution of kinetic energies. In order to measure the reflectivity as a function of Q, the ToF technique is based upon timing how long it takes for a neutron to arrive at the detector over a known distance. By converting the time taken to arrive at the detector, the neutron wavelength can be determined through the de Brogile relation assuming that inelastic scattering is negligible. The reflectivity over a range of Q can then be collected simultaneously at one incident angle. Reflectivity profiles over a larger Q range can be collected by using two or three incident angles.

While both reflectometers operate on the same principal of detection, there are some distinct differences between the instruments. The most notable is the method of neutron production. Neutron reflectometry requires a substantial flux of neutron radiation, which must be produced from atomic nuclei. The two major sources of neutrons for experiments are nuclear reactors and neutron spallation sources. Neutrons produced by the former rely on nuclear fission of heavy elements, where heavy nuclei are split into two lighter nuclei, generating two or three neutrons as a by-product. As fission is a chain-reaction, neutrons are continuously produced through this method. The production of neutrons via spallation involves striking a target of tungsten or mercury with high energy protons, resulting in the ejection of neutrons from the target. Spallation is a pulsed source of neutrons, where short bursts of neutrons are produced multiple times a second. Neutrons are typically produced with a high kinetic energy by both methods, meaning that the neutron wavelengths are much smaller than the length scale of the objects under investigation. For favourable scattering interactions the neutron wavelength must be of the same order as the length scale of the objects under study and so neutrons are moderated to decrease the neutron energy. This is achieved by passing the neutrons through a light material, where inelastic collisions reduce the kinetic energy and hence increase λ. After the neutrons are moderated they are guided towards the instruments.

Beamlines

Simplified schematics of the INTER and FIGARO instruments are shown in Figure 2.8. Both instruments are non-polarised reflectometers, where the neutron beam contains an equivalent ratio of spin-up and spin-down neutrons. The chopper systems sit just beyond the neutron source at the beginning of the neutron beamlines. These systems are rotating disks that either block or admit neutrons, the latter of which is facilitated by an aperture. The choppers define the pulses of neutrons with a specific wavelength distribution while also defining the initial time for the ToF technique. The incident neutrons must also pass a frame overlap mirror either before or after the chopper systems. These are coated mirrors that only transmit neutrons with wavelengths lower than a pre-defined value. Without the frame overlap mirrors, neutrons with longer wavelengths that pass through the choppers can encroach upon successive pulses

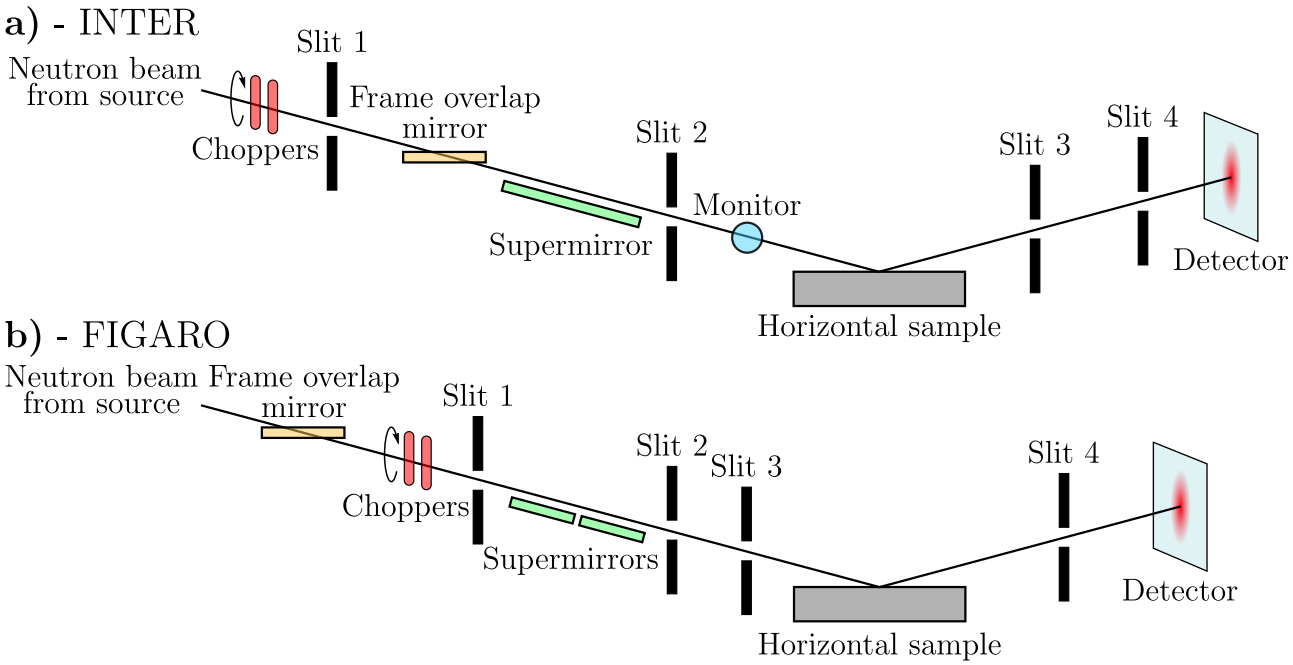

Figure 2.8: Simplified schematics of the **a)** INTER and **b)** FIGARO neutron reflectometers, which are based at ISIS, UK and the ILL, France, respectively. For both schematics, the incident neutron beam propagates from left to right.

of neutrons, compromising the ToF technique. The supermirrors can be used to define the incident angle of the beam towards the sample position. The monitor on INTER determines the incident flux of neutrons, which is required as the flux of a spallation source can be variable. A monitor is not required on FIGARO as the flux is taken to be constant due to the reactor source. The slits are used to collimate the beam, removing stray neutrons that deviate from the desired beam path. Slits placed before the sample also determine the total illuminated area on the sample. The detector on INTER is a point detector, filled with ^{3}He gas as the detecting medium. The detector on FIGARO is a 2D area detector, where the surface of the detector has pixels that can detect neutron intensity independently of the neighbouring pixels.

Substrates

Substrates provide the solid surface for use in NR, and must be as flat as possible in order to avoid significant off-specular reflectivity. Additionally, the substrates should not contain materials that are highly adsorbing of neutrons and nor should they contain materials that can become radioactive when irradiated by neutrons, such as steel. For this work, silicon was identified as a suitable substrate material as it has a particularly low absorption cross section and is relatively cheap. Substrates were purchased from Pi-Kem, UK, with two different dimensions: 80 × 50 × 15 mm (l × w × h) and 55 × 55 × 10 mm. These were polished to a 3 Å RMS roughness before being sputter-coated with an iron layer $\sim$ 200 Å thick. Sputter coating was carried out by Nano-optics Berlin, Germany or by Pi-Kem. An image of an example substrate is shown in Figure 2.9.

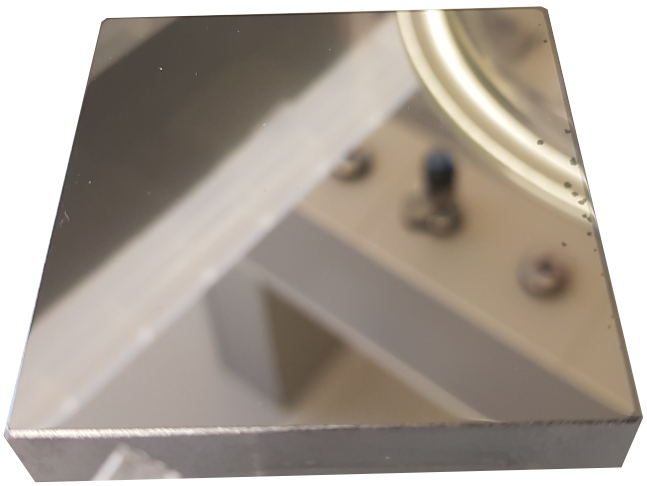

Figure 2.9: Image of an iron-coated silicon substrate. Some imperfections are noticeable on the edge of the substrate, which are thought to result from corrosion after exposure to the atmosphere for extended periods.

Data, error and resolution

The number of neutrons arriving at the detector in a particular time period, N, follows a Poisson distribution, where the distribution of counts around the average value can be described by the standard deviation, σ, given by

$$\sigma = \sqrt{N}\,. \tag{2.49}$$

By summing consecutive periods of counting, N and σ will be greater, but the fractional uncertainty σ/N decreases.

After a measurement has been made, the data is normalised by a transmission dataset, converting the counts to reflectivity. The transmission dataset is a direct beam-to-detector measurement that defines the incident beam intensity for each neutron wavelength. The instrument settings are kept the same as for the reflection measurement and the beam passes through the sample but does not reflect so that all additional scattering and adsorption are accounted for. The random uncertainty in the final reflectivity dataset is then the combined fractional uncertainty in the Poisson error for the reflection and transmission measurements.

A possible source of systematic error is misalignment of a sample with the incident neutron beam. Therefore, the sample interface must be aligned with the beam before measurement. A good indicator that alignment has not been achieved is an intensity that is below unity for reflection above the critical edge, and a Q_c that deviates from the expected value. In this work, every effort has been made to make sure all measurements were conducted with aligned samples.

The uncertainty in momentum transfer, $\mathrm{d}Q$, is defined by the angular divergence of the incident beam, $\mathrm{d}\theta$, and the spread of wavelengths, $\mathrm{d}\lambda$. The fractional uncertainty of Q can be calculated

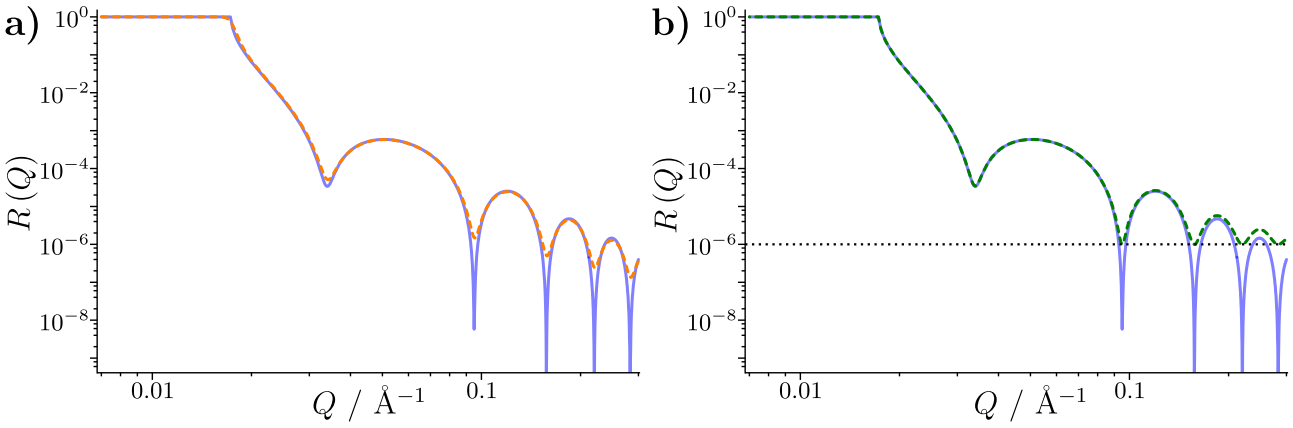

Figure 2.10: **a)** Simulation showing how resolution impacts the measured reflectivity. The ideal reflectivity from the ideal sample in Figure 2.6b is shown in pale blue, while the dashed orange reflectivity profile is the same simulation but with an applied 3 % standard deviation resolution. **b)** Comparison of reflectivity with and without an incoherent background. The reflectivity profile in pale blue is that shown in part **a)**, and the reflectivity in dashed green is the same but with an applied incoherent flat background at $R(Q) = 1 \times 10^{-6}$.

as shown in Equation 2.50.

$$\frac{\mathrm{d}Q}{Q} = \sqrt{\left(\frac{\mathrm{d}\lambda}{\lambda}\right)^2 + \left(\frac{\mathrm{d}\theta}{\theta}\right)^2} \tag{2.50}$$

The uncertainty in θ is determined by the collimation provided by the slits and $\mathrm{d}\lambda$ is determined by the width of each neutron pulse. The effect of $\mathrm{d}Q$ on the measured reflectivity is most apparent in data with Kiessig fringes, where the minima of the fringes appear smeared as shown in Figure 2.10.

Contrast with scattering length densities

There must be a substantial difference between the β of two different layers for their interfacial characteristics to be discernible by reflectometry; this difference is referred to as contrast. Therefore, layers can be highlighted or diminished by accentuating or reducing the difference in β between neighbouring layers, which is known as contrast-matching. This is a particularly useful tool when studying multiple layers comprised of organic media that contain a significant proportion of ^{1}H. By enriching the amount of D (^{2}H) in one of the layers, the contrast can be increased as H and D scatter differently (see Figure 2.4), distinguishing the adjacent layers. Furthermore, a series of reflectivity profiles can be collected using different contrasts for a particular layer. By analysing these profiles simultaneously, a more unique solution can be achieved.

Magnetic samples are more commonly studied on polarised neutron reflectometers, where neutrons can be polarised before and after reflection in order to infer a sample's magnetic structure. Magnetic scatter that occurs on a non-polarised neutron instrument, as used in this work, can be considered as the linear combination of the reflectivity from down- and up-spin neutrons.

This approach assumes the magnetic domains of the materials are greater than the in-plane coherence length of the neutron beam. The nuclear and magnetic scattering length densities of some common materials used throughout this work are shown in Table 2.1.

The incoherent scatter that arises naturally from nuclei introduces a flat background to the reflectivity, which often dominates the reflection at high Q as shown in Figure 2.10b. This can be thought of as a nuisance factor, and is particularly prominent when any media at the interface contain a significant quantity of ^{1}H.

Table 2.1: Number densities and scattering length densities at 25 °C for the materials used in this work.

Material	N / formula unit Å$^{-3} \times 10^{-2}$	β_n / Å$^{-2} \times 10^{-6}$	β_m / Å$^{-2} \times 10^{-6}$
Si	4.99	2.07	-
SiO_2	2.20	3.47	-
Fe	8.49	8.02	4.94
α-Fe_2O_3	1.98	7.20	-
γ-Fe_2O_3	1.84	6.67	1.06
Fe_3O_4	1.35	6.95	1.30
$C_{12}H_{26}$	0.26	−0.46	-
$C_{12}D_{26}$	0.26	6.70	-
H_2O	3.33	−0.56	-
D_2O	3.33	6.37	-
$C_{21}H_{40}O_4$	0.16	0.21	-
$C_{21}D_{18}H_{22}O_4$	0.16	3.21	-

2.3.3 Data analysis

As mentioned previously, the reflectivity data cannot be directly inverted for information on layer characteristics such as β_n, thickness and roughness. In order to extract quantitative information, a model of the sample must be constructed and the simulated reflectivity profile for the model is then fit to the data. The match between the data and the simulated profile is improved by iteratively varying the model parameters, enabling the characteristics of the sample layers to be inferred.

Inferring parameter values that are consistent with a particular dataset is equivalent to inferring the parameter probability distribution, which can be framed using Bayes' theorem:

$$P(\Theta|\mathrm{D},\mathrm{M}) = \frac{P(\mathrm{D}|\Theta,\mathrm{M}) \times P(\Theta|\mathrm{M})}{P(\mathrm{D}|\mathrm{M})} \tag{2.51}$$

where $P(\Theta|\mathrm{M})$ is referred to as the prior which encapsulates the probabilities, P, associated

with a set of parameter values, Θ, given a particular model, M, before any data analysis takes place. The symbol | denotes given. The likelihood function, $P(\mathrm{D}|\Theta,\mathrm{M})$, modifies the prior beliefs by taking into account the probability of obtaining a dataset, D, given a set of parameter values for a given model. The posterior distribution, $P(\Theta|\mathrm{D},\mathrm{M})$, is the probability distribution of a set of parameter values given a dataset and a particular model. The posterior distribution reflects the state of knowledge after fitting the data while considering the initial beliefs. The denominator is known as the evidence, and reflects the probability of a dataset given a model. The evidence does not need to be calculated when inferring parameter values such as the median and 95% confidence intervals as it is only a scaling factor. Therefore, it is possible to express the posterior distribution as a proportionality:

$$P(\Theta|\mathrm{D},\mathrm{M}) \propto P(\mathrm{D}|\Theta,\mathrm{M}) \times P(\Theta|\mathrm{M}) \ . \tag{2.52}$$

Fitting data

The best fit that can be achieved to a dataset is equivalent to maximising the likelihood function. In the case of NR a Gaussian distribution very closely approximates the underlying Poisson distribution for each reflectivity data point as the number of counts is high. Therefore, the likelihood function can be maximised by the minimisation of a least-squares χ^2 goodness-of-fit cost function as shown in Equation 2.53.

$$\chi^2 = \sum_{i=1}^{N} \left(\frac{R_i - S_i}{\sigma_i} \right)^2 \tag{2.53}$$

Here, R_i and σ_i are the reflectivity and reflectivity error at the i^{th} data point, while S_i is the simulated reflectivity at the same Q. When χ^2 is minimised the best fit parameter values can be extracted, and the uncertainty in the parameter values can be determined from the covariance matrix. However, this approach assumes the parameters have a Guassian distribution and can either under- or overestimate confidence intervals.[98] A different technique that can sample the posterior distribution without the previous assumption is Markov chain Monte Carlo (MCMC), following the Metropolis-Hastings algorithm. A thorough account of MCMC processes are available elsewhere but it is worthwhile to briefly lay out the general framework for a neutron reflectometry dataset.[99,100]

The algorithm starts with an initial set of parameter values, Θ_1, which fall within a given prior distribution. The likelihood function is evaluated with this set of parameter values, where the goodness-of-fit is χ^2_1. A new set of parameter values, Θ_2, is then required from the prior distribution, which can be achieved through perturbation of Θ_1. The simplest example, called a Metropolis update, follows:

$$\Theta_2 = \Theta_1 + s \times c \tag{2.54}$$

where c is a random number drawn from a symmetric distribution centred around zero, such as a Gaussian or Uniform distribution, and s is a scaling factor known as the step size. Following the generation of the new parameters, the likelihood function is evaluated with a goodness-of-fit χ^2_2. The new parameter values are kept if $a > 1$, where a is given by

$$a = \frac{P\left(\Theta_2|\mathrm{M}\right)}{P\left(\Theta_1|\mathrm{M}\right)} \times \exp\left(\frac{\chi^2_1 - \chi^2_2}{2}\right) . \tag{2.55}$$

However, if $a < 1$ then the new set of parameter values is only accepted with the probability of a. If the new set of parameter values are rejected, the parameter values are set back to Θ_1. The successive iteration then takes the original or new parameter value and repeats the above process.

The general behaviour at the beginning of the algorithm is to accept a large number of the proposed parameters as the likelihood function tends towards a maximum value. When the algorithm has reached an apparent maximum, the sampler has reached the region of parameter space where the posterior distribution is located. It is common to discard the parameter values from the beginning of the sampling process in an attempt to remove any dependence on the chosen starting parameter values. This is known as burn-in. After reaching the region of parameter space where the posterior distribution is located, the nature of both Equation 2.54 and Equation 2.55 ensures that parameter values from the posterior distribution are sampled according to their probability as determined by the likelihood and prior functions. The ideal scenario is to leave the sampling process to run for a very long time so that the posterior distribution is well approximated, which is known as convergence. Multiple chains for each parameter can be run simultaneously in an effort to speed up the process.

It is not trivial to know when convergence is achieved, and there are numerous diagnostics to suggest convergence has been met.[101] A convergence diagnostic devised by Gelman and Rubin has proven a popular choice because of its relative ease to implement and interpret.[102] The method assesses the variability of the parameter values, known as mixing, that are sampled in the region of the posterior distribution by the MCMC sampler. If the parameters are well mixed then the posterior distribution should be approximated suitably, but if only a handful of different parameter values have been explored the posterior distribution will not be well approximated. After running an MCMC sampler that has discarded all points deemed to be in the burn-in stage, there will be m chains, each containing n parameter values. The m chains are split at the midpoint so that the number of chains is $\hat{m} = 2m$ and the number of parameter samples in each split chain is $\hat{n} = n/2$. Each parameter value in the split chains is denoted $\psi_{i,j}$, where i is the number of the sample parameter in a split chain in a series up to $\hat{n}$ and j is the number of the chain in a series up to $\hat{m}$. For each parameter, the variance between each chain, B, is calculated as:

$$B = \frac{\hat{n}}{\hat{m} - 1} \sum_{j=1}^{\hat{m}} \left(\bar{\psi}_{.j} - \bar{\psi}_{..}\right)^2 \tag{2.56}$$

where

$$\bar{\psi}_{.j} = \frac{1}{\hat{n}} \sum_{i=1}^{\hat{n}} \psi_{i,j} \qquad \text{and} \qquad \bar{\psi}_{..} = \frac{1}{\hat{m}} \sum_{j=1}^{\hat{m}} \bar{\psi}_{.j} \,. \tag{2.57}$$

The average within-chain variance, W, for each parameter is calculated as

$$W = \frac{1}{\hat{m}} \sum_{j=1}^{\hat{m}} s_j^2, \qquad \text{where} \qquad s_j^2 = \frac{1}{\hat{n}-1} \sum_{i=1}^{\hat{n}} \left(\psi_{ij} - \bar{\psi}_{.j}\right)^2 . \tag{2.58}$$

The posterior variance for each parameter is estimated by a weighted sum of W and B:

$$\hat{\sigma}^2 = \frac{\hat{n}-1}{\hat{n}} W + \frac{1}{\hat{n}} B \,. \tag{2.59}$$

Finally, the ratio of the square-roots of $\hat{\sigma}^2$ and W is calculated:

$$\hat{R} = \sqrt{\frac{\hat{\sigma}^2}{W}} \tag{2.60}$$

where $\hat{R}$ is called the potential scale reduction factor. The value of $\hat{R} \to 1$ as $n \to \infty$, where W is the only significant factor. This behaviour is expected because $B \to 0$ with $n \to \infty$ as the chains should be centred about the posterior distribution with similar variances. Simultaneously, W will approach a stable finite value. If the burn-in stage was not removed sufficiently, then $\hat{R}$ will significantly deviate from one. This is the very reason for splitting the chains into two; by doing so, it is possible to assess if the sampled parameter values arise solely from the posterior distribution. It has been suggested that convergence is satisfactorily reached when $\hat{R} < 1.1$.[103] This value is arbitrary and is not based on statistical significance which has lead to some criticism.[104] In this work, it was attempted to reach convergence by using a large number of samples ($\sim 1 \times 10^6$) after reaching a steady likelihood value, and attempting to reduce $\hat{R} < 1.1$. In this manner, states that appear to be converged are reached, although it is not possible to absolutely state that convergence has been achieved.

The final consideration when terminating an MCMC sampler is the number of independent samples collected. To represent the posterior distribution of a particular parameter, θ, it is common to take an estimator, $E(\theta)$, of the posterior distribution, such as the mean or median. It is commonly assumed that the central limit theorem applies to MCMC samples[99], and thus the $(1-\alpha)$ confidence interval of the estimator, $E(\theta)_{\mathrm{CI}}$, is approximated by:

$$E(\theta)_{\mathrm{CI}} \approx f^* \frac{\bar{\sigma}}{\sqrt{n_{\mathrm{eff}}}} \tag{2.61}$$

where f^* is the appropriate factor for the $(1-\alpha)$ confidence interval (1.96 for a 95 % confidence interval), $\bar{\sigma}$ is the standard deviation of the sampled θ values and n_{eff} is the effective sample size of the posterior distribution. Therefore, when $\bar{\sigma} = 1$ it is necessary to acquire > 38000

independent samples to quote the 95 % confidence intervals to a precision of ± 0.01. An effective sample size must be used as the parameter values that are sampled in successive iterations are often correlated, which is to say that it takes a number of iterations for the parameter values to appear as if they are from different parts of the posterior distribution. It is possible to approximate n_{eff} for a given parameter by

$$n_{\text{eff}} = \frac{mn}{1 + 2\sum_{t=1}^{T} \hat{\rho}_t} \,. \tag{2.62}$$

Here, $\hat{\rho}_t$ is the approximated autocorrelation function for an offset t between each iteration, which can be calculated as

$$\hat{\rho}_t = 1 - \frac{V_t}{2\hat{\sigma}^2} \tag{2.63}$$

where V_t is given by

$$V_t = \frac{1}{m\,(n-t)} \sum_{j=1}^{m} \sum_{i=t+1}^{n} \left(\psi_{i,j} - \psi_{i-t,j}\right)^2 \,. \tag{2.64}$$

The sum to T in Equation 2.62 is used instead of a sum to ∞ as the autocorrelations become noisy when t becomes large. Therefore, T is taken when the sum of two consecutive estimated autocorrelations is negative,

$$T = t' \text{ when } \hat{\rho}_{t'-1} + \hat{\rho}_{t'} < 0\,; \tag{2.65}$$

this enables the estimation of the offset where the sample parameters are no longer correlated. In this work, sampling was only terminated when the number of independent samples per parameter was at least $\sim 10^4$. The lowest number of independent samples per fit and E_θ^{CI} are given for each MCMC fit.

When fitting the data collected with the tribometer, it was not possible to use an MCMC sampling scheme to estimate the uncertainty due to issues simulating the reflectivity within the sampler. Therefore, in order to estimate the uncertainty in the inferred parameter values, a bootstrap re-sampling routine was used. This involved using a custom python script (originally written by Dr Thomas Wood, STFC UK) to re-sample the datasets with replacement and then fit each re-sampled dataset via the `SciPy` differential evolution optimiser using the original model and cost function.[105] This procedure was repeated 500 times for each dataset, resulting in a distribution of parameter values, enabling the median and 95 % confidence interval values to be calculated. The 95 % confidence limits were calculated as the difference between the median and the $2.5^{\text{th}}/97.5^{\text{th}}$ percentiles of the parameter distributions. The bootstrap re-sampling mimics measuring the sample repeatedly, which should only have variations dictated by the random error associated with Poisson counting statistics.[106] Through fitting these re-sampled datasets, distributions for each parameter are formed, which have widths that are based upon

the stability of the fit and the random error associated with each data point. The former represents systematic error in the fit process, which becomes dominant when the model does not reproduce the data well. This can be minimised by only applying the bootstrap method to data that fit suitably.

Model selection

When fitting NR data, it is not clear which model should be fit to a dataset as multiple models can appear equally plausible. Bayes' theorem can be applied to the problem of model selection:

$$P\left(\mathrm{M}|\mathrm{D}\right) = \frac{P\left(\mathrm{D}|\mathrm{M}\right) \times P\left(\mathrm{M}\right)}{P\left(\mathrm{D}\right)} \tag{2.66}$$

where $P\left(\mathrm{D}|\mathrm{M}\right)$ is the evidence given a particular model as seen in Equation 2.51, and $P\left(\mathrm{M}\right)$ is the prior probability of M. $P\left(\mathrm{M}|\mathrm{D}\right)$ is the posterior of M given the data and $P\left(D\right)$ is the probability of obtaining the data. For brevity, the evidence of model i will be denoted by Z_i for the remainder of this work. The suitability of a particular model, M_2, to describe a dataset can be compared to another reference model, M_1, by comparing the ratios of the two model posteriors as shown in Equation 2.67.

$$\frac{P\left(\mathrm{M}_2|\mathrm{D}\right)}{P\left(\mathrm{M}_1|\mathrm{D}\right)} = \frac{\dfrac{Z_2 \times P\left(\mathrm{M}_2\right)}{P\left(\mathrm{D}\right)}}{\dfrac{Z_1 \times P\left(\mathrm{M}_1\right)}{P\left(\mathrm{D}\right)}} = \frac{Z_2 \times P\left(\mathrm{M}_2\right)}{Z_1 \times P\left(\mathrm{M}_1\right)} \tag{2.67}$$

If the posterior ratio is > 1, then M_2 is the preferable model to describe the data. If the two prior probabilities of two plausible models are equivalent, then the posterior ratio is only dependant on the ratio of the evidences:

$$\frac{P\left(\mathrm{M}_2|\mathrm{D}\right)}{P\left(\mathrm{M}_1|\mathrm{D}\right)} = \frac{Z_2}{Z_1} = B\,. \tag{2.68}$$

The ratio of the two evidences is known as the Bayes factor, B, which can be used to assess which model should be used when analysing data following the criteria laid out in Table 2.2. The evidence for a particular model can be written as:

$$Z = \iint_{\mathbf{R}} P\left(\mathrm{D}|\Theta, \mathrm{M}\right) P\left(\Theta|\mathrm{M}\right) \mathrm{d}^w\Theta \tag{2.69}$$

where w is the number of parameters in Θ and $\mathbf{R}$ is a matrix with dimensions $2 \times w$ defining the limits of integration. The bulk of the evidence is typically in a small region of the multidimensional integral where the likelihood and prior probabilities approach their maximum value. Typically, models with better fits to the data are strongly preferred. However, if models are similarly suited to match the data, then it falls upon the complexity of the models and the prior beliefs. In general, those models that are less complex but match the data well are favoured in a manner that follows Ockham's razor.[108] Alternatively, if models are equivalent or

Table 2.2: Interpretation of Bayes factors for model selection.[107]

$2 \ln B$	Evidence against M_1
0–2	Not worth a bare mention
2–6	Positive
6–10	Strong
> 10	Very strong

of similar complexity and match the data well, then models with tighter priors have a greater evidence. It has been suggested that a simple way of interpreting why one model has a greater evidence than another is to consider the ratio of the optimal parameter value to the prior range, which can be thought of as an average parameter value.[109] Therefore, the prior range of each parameter is of fundamental importance when calculating model evidences.

One approach to estimate the evidence is nested sampling, developed by Skilling.[110] The algorithm begins with n objects adopting random parameter values from $P(\Theta|\mathrm{M})$, after which the likelihood for each object is calculated, and sorted into ascending order. The object with the lowest likelihood is then removed, and is termed a dead point. A new object is generated with a set of parameter values drawn from $P(\Theta|\mathrm{M})$ where the values must be drawn so that the likelihood is greater than the likelihood of the dead point. This is achieved by randomly copying the values of one of the remaining original points and perturbing the parameter values by a small random amount. If this operation is repeated k times, k dead points will have been generated and n objects will remain in a region of parameter space with high likelihood and prior probabilities. When estimating the evidence it is convenient to rephrase the collective priors of every parameter in Θ as a multidimensional space called the prior volume, ε^*, as shown in Equation 2.70.

$$\varepsilon^* = \int \cdots \int_{\mathbf{R}} P(\Theta|\mathrm{M}) \, \mathrm{d}\Theta \tag{2.70}$$

After an iteration has proceeded, the prior volume is reduced to a smaller value, ε, as only those prior values that result in a likelihood greater than the lowest point are valid for the rest of the process. Following a number of iterations, the evidence can be estimated via the trapezoid rule:

$$Z = \sum_k A_k \tag{2.71}$$

where A_k is the evidence bounded by the k^{th} and $k - 1^{\text{th}}$ dead point:

$$A_k = \frac{1}{2} \left(P(\mathrm{D}|\Theta, \mathrm{M})_{k-1} + P(\mathrm{D}|\Theta, \mathrm{M})_k \right) \times h_k \tag{2.72}$$

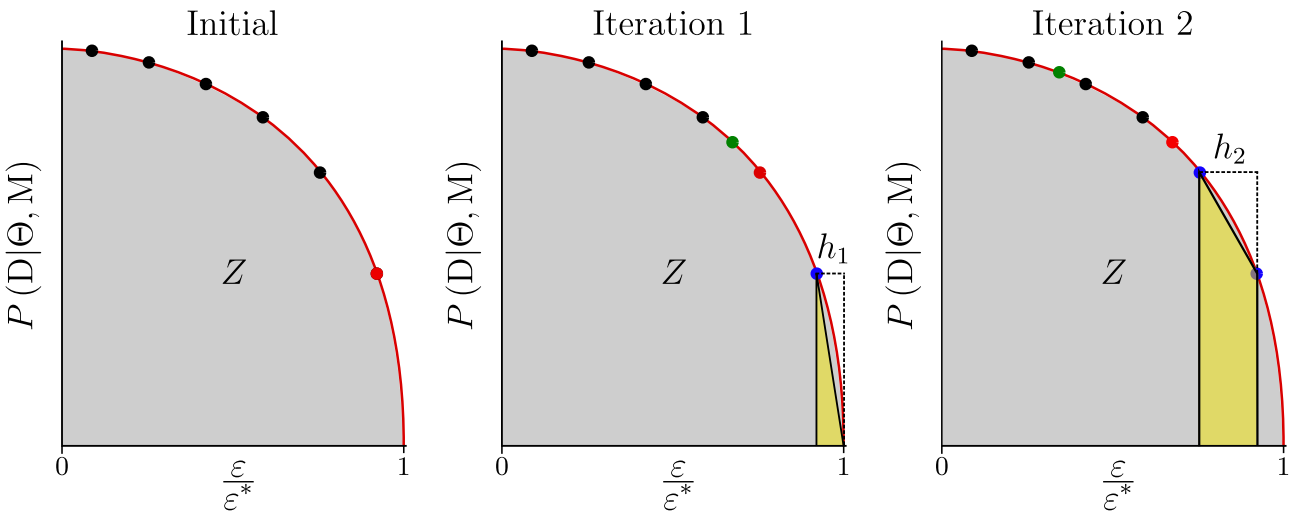

Figure 2.11: Schematic of the nested sampling process for the estimation of evidence, as shown by the grey area under the red curve. The fraction $\varepsilon/\varepsilon^*$ is the proportion of parameter values that have likelihoods above a given value. Six objects, shown as points, are used in this problem to estimate the evidence. They are assigned random parameter values from $P\,(\Theta|\mathrm{M})$, and the likelihoods sorted into ascending order in the initial phase. The red dot at the lowest likelihood is removed when proceeding to Iteration 1 and a new point is randomly generated as shown in green. The new lowest likelihood point is identified, also shown in red. The lowest likelihood point from the initial phase, as shown in blue, is used to determine the first area, A_1, as shown in yellow. Iteration 2 repeats the above process, where the next portion of the total area, A_2, is determined from the last two lowest likelihood points.

where h_k is

$$h_k = \frac{1}{\varepsilon^*}\left(\varepsilon_{k-1} - \varepsilon_k\right) . \tag{2.73}$$

Hence, after many iterations and a large n, the estimated evidence approaches the true value. This process is depicted in Figure 2.11 for $n = 6$.

In this work, nested sampling was terminated when the logarithmic ratio of the current estimated evidence, $\widehat{Z}$, to the estimated remaining evidence, $\Delta\widehat{Z}$, was less than some criteria κ defined by

$$\kappa \geq \ln\left(\widehat{Z} + \Delta\widehat{Z}\right) - \ln\left(\widehat{Z}\right) . \tag{2.74}$$

The criteria used in this work set $\kappa = 10^{-3}\,(n-1) + 10^{-2}$, which corresponds to a fraction of remaining evidence to the estimated evidence ~ 0.66 when $n = 500$. However, at termination $n-1$ points remain in a location of the highest likelihood. By cycling through a further $n-1$ integration steps without the replacement step, the percentage of the remaining evidence to the determined evidence falls to ~ 1 %.

A useful by-product of cycling through the full prior volume is that the posterior distribution

can be sampled using the evidences determined by each k^{th} dead point by

$$P\left(\Theta|\mathrm{D}_k, \mathrm{M}\right) \approx \frac{A_k}{Z}\,. \tag{2.75}$$

As the full prior range is explored, there is no possibility of being stuck in a local minimum, which is possible when fitting data via least-squares regression. As such, multi-modal posteriors can be explored.[111] However, the resolution achievable when sampling more simplistic posterior distributions is inferior to an MCMC sampling procedure during a given time frame; nonetheless, the posterior distribution determined via nested sampling is an extremely useful diagnostic tool when considering model selection.

Software

NR data analysis was conducted using three different pieces of software. GenX[112] 2.10 was used for producing simple best-fits using a differential evolution algorithm, and was used when fitting data collected with the tribometer. `Refl1D`[113] 0.8.13–0.8.14 was used for sampling the posterior distribution of data collected with solid-liquid cells; this was achieved using the DREAM[114] MCMC scheme provided in the `Refl1D` python package. A combination of the python packages `refnx`[115] 0.1.18 with `dynesty`[116] 1.0 were used to estimate model evidence via nested sampling.

An example problem

An example of data fitting and model selection is presented using simulated data of a theoretical sample structure. The sample structure is based on those used throughout the rest of the thesis, with a silicon substrate sputter coated with a 200 Å thick iron layer. A native silicon dioxide layer is typically found between the silicon and iron layer, and an iron oxide layer typically persists at the surface of the substrate. An adsorbed surfactant is simulated at the iron oxide surface with two layers, where the inner layer is densely packed with a thickness of 20 Å, while the outer layer is less dense with a thickness of 10 Å. The substrate structure is simulated as submerged in dodecane-d_{26}, which is a common solvent used in this work. The simulated data are shown in Figure 2.12a along with the β_{++} profile in Figure 2.12b, where the adsorbed surfactant layers are termed surf_{in} and surf_{out} for the inner and outer layers. The parameters used to simulated the data are shown in Table 2.3. The reflectivity error bar associated with each data point is a constant of 5 % $\mathrm{d}R/R$, and is assumed to be Gaussian in nature. Each data point is offset by a small random number drawn from the Gaussian distribution with a standard deviation defined by the error $\mathrm{d}R$. A constant error of 5 % is not representative of a true reflection measurement as all neutron sources have a non-uniform distribution of λ. However, this simple example serves as a good demonstration. A standard deviation $\mathrm{d}Q/Q$ resolution of 3 % was also used, which is a fairly typical resolution in the work conducted here.

A nested sampling analysis was conducted on the simulated data to find an appropriate number of interfacial layers to model. The initial parameter values and priors are shown in Appendix A,

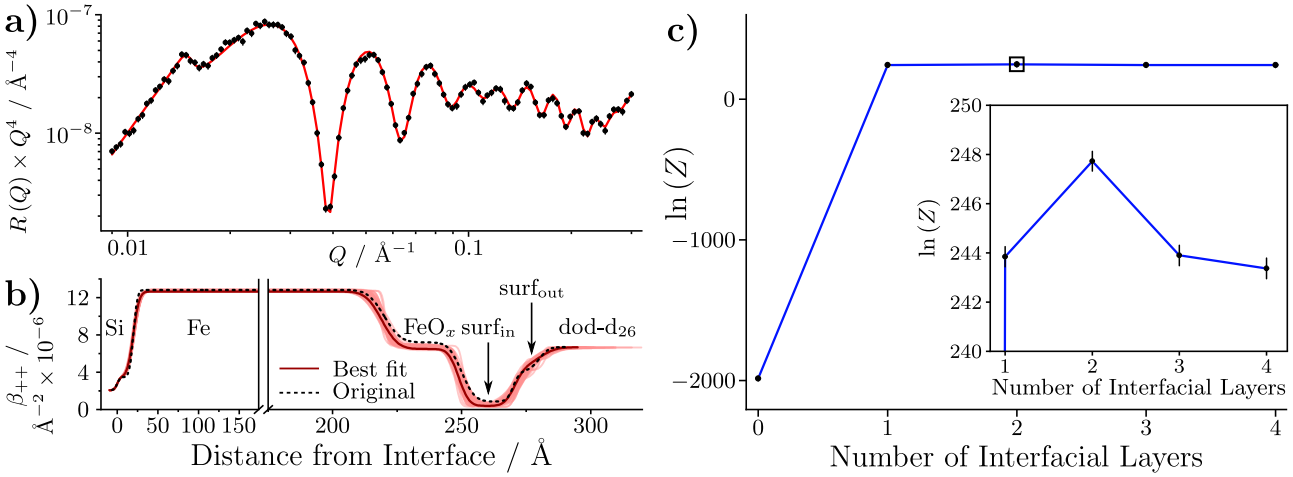

Figure 2.12: **a)** Simulated reflectivity of the theoretical sample structure. The best fit achieved by the MCMC sampling is shown by the red line. The reflectivity is scaled by Q^4 to aid comparison. **b)** The original and fitted β_{++} profiles from the simulated reflectivity data. The original profile was taken before any noise was added to the data. The light red traces show 50 random samples taken from the MCMC posterior distribution to indicate the extent of uncertainty across the sample. **c)** Nested sampling results for modelling the data with an increasing number of interfacial layers. The model with the greatest evidence is highlighted by the box. The inset shows the results for the four highest evidences. The lines are interpolations to guide the eye.

Table 2.3: Layer parameters used to simulate, and inferred from, the reflectivity profile shown in Figure 2.12a. Those parameters without uncertainties were held fixed in the fit process.

Layer	β_n / Å$^{-2} \times 10^{-6}$		β_m / Å$^{-2} \times 10^{-6}$		Thickness / Å		Roughness / Å	
	Original	Fitted	Original	Fitted	Original	Fitted	Original	Fitted
Si	2.07	2.07	-	-	∞	∞	3	3
SiO_2	3.47	3.47	-	-	20	$20.3^{+1.7}_{-1.6}$	4	$6.3^{+0.6}_{-0.7}$
Fe	8.02	$7.9^{+0.2}_{-0.1}$	4.81	$4.84^{+0.1}_{-0.2}$	200	199^{+1}_{-1}	5	$3.9^{+0.6}_{-0.7}$
FeO_x	7.00	$6.6^{+0.3}_{-0.3}$	0.2	$0.1^{+0.2}_{-0.1}$	30	$29.9^{+1.0}_{-0.1}$	4	$3.3^{+1.8}_{-2.2}$
$surf_{in}$	0.86	$0.4^{+0.4}_{-0.2}$	-	-	20	$21.9^{+2.7}_{-6.3}$	2	$4.3^{+7.6}_{-3.1}$
$surf_{out}$	4.10	$4.4^{+2.2}_{-4.1}$	-	-	10	$8.3^{+5.5}_{-3.2}$	3	$5.7^{+6.9}_{-4.3}$
dod-d_{26}	6.70	$6.7^{+0.1}_{-0.1}$	-	-	∞	∞	-	-

Table A1 and the estimated evidence associated with modelling 0–4 interfacial layers are shown in Figure 2.12c. The general trend in Figure 2.12c is similar to previous work[117,118], where the model with two layers represents the data better than the model with only one layer, but does not over fit the data with too many parameters such as the models with three and four layers. The highest evidence was found with 2 layers, where $\ln(Z) = 247.7 \pm 0.4$. The Bayes factor for selecting this model over the models with 1 and 3 layers is 7.8 ± 1.1 and 7.7 ± 1.2. Therefore, there is a strong preference for modelling the data with two layers when inferring parameter values.

Following the nested sampling results, an MCMC scheme was used to infer the parameter values for each layer in the model with 2 interfacial layers. The best fit to the data is shown as the red line in Figure 2.12a, and the corresponding β_{++} profile from the best fit is shown as the full maroon line. The determined parameter values are shown in Table 2.3. There is generally good agreement between the original parameters and the inferred parameter values for the substrate layers. However, the uncertainty in surfactant layers is much greater, which likely arises because there are numerous combinations of surfactant parameters that lead to a reasonable fit. It would be possible to improve the uncertainty by providing another contrast of the system, which, in this case, would be most easily achieved with the hydrogenated solvent, dodecane-h_{26}.

2.4 X-ray reflectometry

X-ray reflectometry follows the same principal as NR, and can also be used to determine atomic densities and thicknesses of thin films. However, the interactions of X-rays with matter are fundamentally different to those between neutrons and matter. X-rays interact with the electrons that surround atomic nuclei. As a result, X-rays are more strongly scattered from materials comprised of heavy, electron-rich elements.

A basic description of the main interactions involved in XRR are outlined here. The theory follows the same principals laid out in the NR theory section. Rigorous descriptions of X-ray scattering and reflectometry theory are available elsewhere.[90,91,93,119]

2.4.1 Theory

The X-ray refractive index of a material, n, is given as:

$$n = 1 - \delta - i\eta \tag{2.76}$$

where δ describes the scattering of the X-ray and η describes the adsorption. They are defined as:

$$\delta = \frac{\lambda^2}{2\pi} N r_e f_1 \qquad \text{and} \qquad \eta = \frac{\lambda^2}{2\pi} N r_e f_2 \,, \tag{2.77}$$

where λ is the wavelength of the X-ray, N is the number density of the sample material, r_e is a constant called the classic electron radius with a value of 2.81794×10^{-5} Å and the two terms denoted by f are the real and imaginary parts of the complex number referred to as the atomic form factor, $f = f_1 + if_2$. The X-ray wavelength is often interchanged with the photon energy, E, by relating it to Planck's constant, h, and the speed of light in a vacuum, c, as

$$E = \frac{hc}{\lambda}. \tag{2.78}$$

The atomic form factor is the Fourier transform of the electron density of the sample atom, and hence the components of f increase as the number of electrons increase across the periodic table. The atomic form factor also diminishes with decreasing λ and increasing scattering angle, θ. Values for each element in the periodic table measured over a range of λ are available in certain databases.[120] The scattering length, b, is the product of the atomic form factor and r_e, $b = fr_e$. Therefore, in a consistent manner to NR, the real component of the scattering length density, $\beta_{\text{X-ray}}$, can be defined using the real part of the atomic form factor as $\beta_{\text{X-ray}} = r_e N f_1$.

2.4.2 Experimental

XRR experiments were carried out on two different instruments. Hard XRR was carried out on I07, the X-ray diffractometer instrument at Diamond Light Source, UK.[121] I07 is a high-resolution diffractometer that uses a select wavelength of radiation to probe samples of interest. For the experiments presented herein, $\lambda = 0.496$ Å. As a result of using a fixed wavelength, the scattering angle must be increased in order to obtain higher values of Q. Specular XRR is achieved by placing the detector at an angle of 2θ from the incident beam at a set distance from the sample interface.

Diamond Light Source houses a number of instruments based around a photon source called a synchrotron, where electrons are accelerated up to velocities close to the speed of light with energies on the order of GeV. Electrons, like other charged particles, emit electromagnetic radiation when they accelerate or decelerate. By bending the electron beam within the loop, the electrons are accelerated and a distribution of photons is generated which propagate towards different beamline instruments. In other parts of the synchrotron, straight sections of the loop contain devices called wigglers and undulators. Both devices contain a series of magnets that oscillate the electron beam horizontally, accelerating the beam back-and-forth. As a result, electromagnetic radiation is emitted in the forward direction, and can be built-up over the length of the wiggler/undulator. Compared to wigglers, undulators are designed to produce a lower amplitude of perturbation to the electron beam, giving rise to a less divergent beam with a more well-defined wavelength of the resulting photons. The emitted photons then propagate to the adjacent beamline instrument.

A simple schematic of the I07 instrument is shown in Figure 2.13. I07 receives photons from an undulator in the storage ring, which provides a highly collimated X-ray beam. The photon

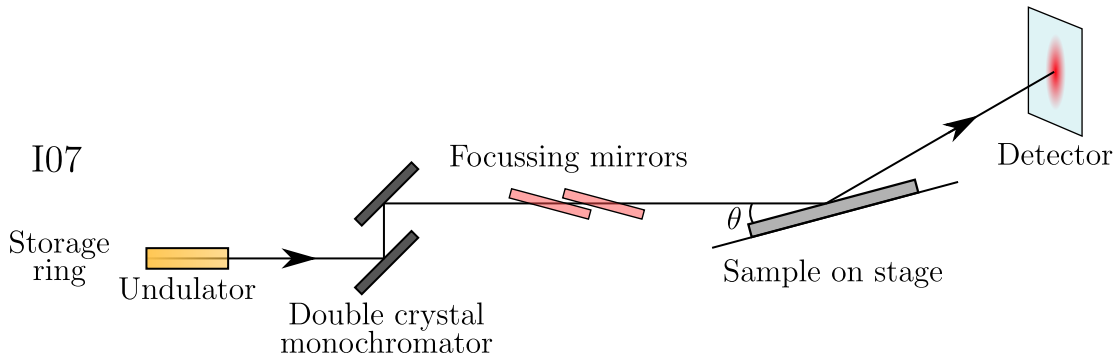

Figure 2.13: A simplified schematic of the I07 instrument beamline set up in a reflectometer geometry.

beam then passes through a double crystal monochromator, where two silicon blocks select a required beam energy in the range of 8–30 keV. This range of photon energies falls within the wavelength range of 0.413–1.550 Å, and thus all photons that pass the monochromator are X-rays. The beam then passes through focussing mirrors which can define the vertical and horizontal beam size, and also the downward and outward angle of the incident beam. Afterwards, the beam impinges onto the sample surface where the angle is defined by the angle of the stage that the sample is secured to. A hexapod is used to control the stage tilt and stage height. After reflection, the beam propagates in the specular direction and into a detector. I07 has a number of different detectors that can be used; in the work described here, the detector was a 2D Pilatus 100K detector, where individual square pixels with a length of 172 µm could measure the counts in a given time frame independently of other pixels.

The Q resolution of the beamline when set up in a reflection geometry follows Equation 2.50, where the resolution in the angle is the dominant factor. This is because the fractional energy resolution, as defined by the double crystal monochromator, is a constant at $\sim 2.5 \times 10^{-4}$ and the resolution of θ is $\sim 5 \times 10^{-3}$ degrees as defined by the detector pixel width and the distance to the detector. Therefore, the resulting uncertainty in the momentum transfer, dQ, was estimated to be 2.2×10^{-3} Å^{-1}.

Soft XRR was carried out on a Philips/Panalytical PW3050/65 X'Pert PRO HR horizontal diffractometer at the Department of Materials Science and Metallurgy, University of Cambridge. The general experimental setup is similar to I07, where the sample is tilted by an angle θ along the beam, and the detector is placed at an angle of 2θ to measure the specular reflection. A copper anode was used for the production of X-rays with a wavelength of $\lambda = 1.54$ Å. The horizontal width of the incident slit was 5 mm, defining the horizontal width of the beam footprint to be ~ 5 mm, and a divergence slit defined to give a divergence of 0.031° was used to collimate the incident beam at a distance of 220 mm from the substrate. This results in an approximate maximum footprint of 50 mm along the direction of the beam. A slit placed before the detector was set to have a vertical height of 0.3 mm. The detector used was a Xe proportional detector and was used as a point detector. The slit height before the detector defines the angular spread that reaches the detector, which is estimated to have a standard

deviation of 0.011° following the theory in section four of the cited work.[122] This value is an order of magnitude greater than the resolution of the goniometer used to define θ. Therefore, the standard deviation resolution, dQ, is estimated to be ~ 0.0016 Å^{-1}.

X-ray scattering length densities

The X-ray scattering form factors and scattering length densities of some common materials used in this work are shown in Table 2.4.

Table 2.4: X-ray scattering form factors and scattering length densities at 25 °C with a photon energy of 25 keV ($\lambda = 0.496$ Å) for the materials used in this work.

Material	N / formula unit Å^{-3} $\times 10^{-2}$	f_1 / formula unit^{-1}	$\beta_{\text{X-ray}}$ / Å^{-2} $\times 10^{-6}$
Si	4.99	14.0	19.8
SiO_2	2.20	30.0	18.6
Fe	8.49	26.3	62.8
α-Fe_2O_3	1.98	76.5	42.8
γ-Fe_2O_3	1.84	76.5	39.6
Fe_3O_4	1.35	110.8	42.1
$C_{12}H_{26}$	0.26	98.0	7.3
$C_{21}H_{40}O_4$	0.16	198.0	8.9

2.4.3 Data analysis

XRR data analysis was conducted using GenX 2.10 to produce best-fits using a differential evolution algorithm. Unlike the NR data analysis, a least-squares χ^2 minimisation was not conducted when fitting the XRR data. The reason a χ^2 minimisation was not used is because the cost function is weighted towards those data points with low error at low Q. Therefore, while a good fit can be achieved at low Q with a χ^2 minimisation, the fit at medium and high Q is poor as the residuals become small with increasing Q. Instead, a minimisation of the logarithm of the difference between the real and simulated reflectivity was used and is referred to as the figure-of-merit (FOM):

$$\text{FOM} = \sum_{i=1}^{N} |\log R_i - \log S_i| \ . \tag{2.79}$$

Here, R_i and S_i are the real and simulated reflectivity at each i^{th} Q point. It should be noted that this does not take into account the counting error associated with each data point. Bootstrap re-sampling was used to estimate the uncertainty in inferred parameters from XRR

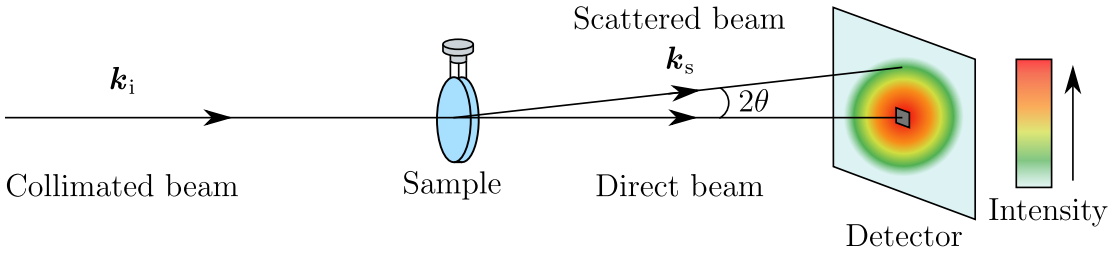

Figure 2.14: A schematic of a transmission SANS experiment, where an incident beam of collimated neutrons with the wavevector $\boldsymbol{k}_\mathrm{i}$ is scattered through a small angle of 2θ. The scattered beam has the wavevector $\boldsymbol{k}_\mathrm{s}$ and the momentum transfer can be described as $\boldsymbol{Q} = \boldsymbol{k}_\mathrm{s} - \boldsymbol{k}_\mathrm{i}$. The grey square placed at the centre of the detector is known as the beam stop and is designed to stop the non-scattered direct beam from damaging the detector when measuring scattering from samples.

data. As the counting error associated with each data point was ignored when fitting the data, the uncertainty presented for the parameters are associated with the stability of the fit.

2.5 Small angle neutron scattering

Small angle neutron scattering (SANS) is an elastic scattering technique that is used to study the structure of materials in the range of 1–100 nm. The typical SANS geometry is shown in Figure 2.14, which depicts a SANS instrument operating in transmission mode. Here, a neutron beam is guided towards a cell that contains a solution of the substance of interest. The neutron beam propagates through the solution in the cell and is scattered at small angles by structures in the nanometer range. The scattered intensity of neutrons is then detected at a set distance behind the sample using a position sensitive detector, and the intensity can be related to the structure of the scatterers. There are a number of interpretation methods with model fitting being the most common method to infer structural properties. A brief overview of the theory and analysis behind the SANS technique is presented here. Thorough descriptions of the theory can be found elsewhere.[91,123,124]

2.5.1 Theory

The same fundamental neutron-matter interactions found within subsection 2.3.1 are relevant for the discussion of SANS theory. Of particular relevance to SANS is the differential form of the elastic scattering cross-section, $(\mathrm{d}\sigma/\mathrm{d}\Omega)_\mathrm{el}$, which describes the number of elastically scattered neutrons per unit solid angle, Ω. Solid angles are directly related to the momentum transfer, $\boldsymbol{Q}$, of neutrons upon scattering and thus, the intensity measured at different positions across the detector, $I(\boldsymbol{Q})$, is related to $(\mathrm{d}\sigma/\mathrm{d}\Omega)_\mathrm{el}$ through

$$I(\boldsymbol{Q}) = \left[I_0(\lambda)\, \eta(\lambda)\, T(\lambda)\, \Delta\Omega \left(\frac{\mathrm{d}\sigma}{\mathrm{d}\Omega} \right)_\mathrm{el} \right] \otimes \mathrm{R}(\boldsymbol{Q}) + B(\boldsymbol{Q}) \ . \tag{2.80}$$

Here, I_0, η and T are the incident flux, the efficiency of the detector and the transmission function of the sample. The solid angle that a detector pixel subtends is given by $\Delta\Omega$ and can be related to $\boldsymbol{Q}$. The $\mathrm{R}(\boldsymbol{Q})$ term represents the resolution function which convolves the term in the square bracket as denoted by the $\otimes$ operator. Finally, the background signal, $B(\boldsymbol{Q})$, is added to the overall signal and is usually a flat function that only varies slowly with $\boldsymbol{Q}$. The background signal arises from the incoherent scattering of neutrons and is greatest when a large proportion of hydrogen is present in the sample.

When dealing with dilute samples, the number of neutrons that reach the detector can be radially averaged to result in a 1D intensity profile as a function of Q. This process also requires correction for a number of factors to ensure consistency between measurement time and instrumental factors. For instance, whilst I_0 and η are typically known for each individual instrument, T must be measured for each sample. This is done by measuring the intensity that arrives at the central pixels on the detector, relating to the unperturbed portion of the beam. Further corrections are made using the scattered intensity of an empty cell, a blocked beam and the neat solvent. The process for non-dilute samples is more complicated as some samples will display orientational structure, and hence the scattering will not be radially isotropic.

The elastic differential scattering cross-section at $Q = 0$ can be written as:

$$\left(\frac{\mathrm{d}\sigma}{\mathrm{d}\Omega}\right)_{\mathrm{el}}^{Q=0} = \left(\frac{N}{V}\right) V_{\mathrm{p}}^2 \left|\beta_{\mathrm{solu}} - \beta_{\mathrm{solv}}\right|^2 \tag{2.81}$$

where N is the number of scatterers and V is the scattering volume. As such, N/V is the concentration of scatterers in the sample solution. The scattering length density of the scatterer/solute is denoted as β_{solu}, and for the solvent as β_{solv}. Finally, V_{p} is the volume of scatterer and thus, the intensity is written in units of per unit distance, commonly framed in terms of cm^{-1}. The intensity of the direct beam at $Q = 0$ is not measured as the beam stop is placed in front of the detector at the central position during a scattering measurement. Hence, the value of the intensity at $Q = 0$ is not directly determinable, but the measured intensity as $Q \to 0$ is well approximated by Equation 2.81. It is also possible to relate $(\mathrm{d}\sigma/\mathrm{d}\Omega)_{\mathrm{el}}$ to the direct beam intensity by the Guinier approximation[125]:

$$\ln\left[\left(\frac{\mathrm{d}\sigma}{\mathrm{d}\Omega}\right)_{\mathrm{el}}^{Q\to 0}\right] \approx \ln\left[\left(\frac{N}{V}\right) V_{\mathrm{p}}^2 \left|\beta_{\mathrm{solu}} - \beta_{\mathrm{solv}}\right|^2\right] - \left(\frac{R_{\mathrm{g}}^2}{3}\right) Q^2 \,. \tag{2.82}$$

Here, R_{g} is the radius of gyration, which in a scattering circumstance relates to the root-mean-square radius of the scattering object. Therefore, through a linear fit to the natural logarithm of $I(Q)$ as a function of Q^2, a structural dimension can be determined. This relation should be linear in the region of $0 < Q \lesssim R_{\mathrm{g}}^{-1}$ if the sample is approximately monodisperse.

It is also possible to relate $(\mathrm{d}\sigma/\mathrm{d}\Omega)_{\mathrm{el}}$ to the shape, size and constitution of individual scattering structures along with the structural position of scattering objects in relation to one another. This is a more thorough analysis than the Guinier approximation, and it holds over a larger

range of Q. The characteristics of individual scatterers contributes a scattering function known as the form factor, $\mathrm{F}(Q)$. Specifically, $\mathrm{F}(Q)$, is the Fourier transform of the distribution of β_{solu}, and hence contains information on the length scales of the scatterer; for instance, a spherical form factor contains information on the radius over which the β_{solu} contrasts β_{solv}. As previously mentioned, the scattering cross section can be related to any structure that exists between the individual scatters, which will manifest when considerable correlation exists between positions of scatterers. The structural contribution is termed the structure factor, $\mathrm{S}(Q)$, and the relationship between the scattering cross section and both factors is given in Equation 2.83.

$$\left(\frac{\mathrm{d}\sigma}{\mathrm{d}\Omega}\right)_{\mathrm{el}} = \left|\mathrm{F}(Q)\right|^2 \mathrm{S}(Q) \tag{2.83}$$

As a result, Equation 2.80 for reduced 1D data of isotropic systems becomes:

$$I(Q) = \left[\left(\frac{N}{V}\right) V_{\mathrm{p}}^2 \left|\beta_{\mathrm{solu}} - \beta_{\mathrm{solv}}\right|^2 \langle\left|\mathrm{F}(Q)\right|^2\rangle \mathrm{S}(Q)\right] \otimes \mathrm{R}(Q) + B(Q) \tag{2.84}$$

where $\langle\left|\mathrm{F}(Q)\right|^2\rangle$ denotes the orientational average of the form factor intensity. The (N/V) term can be written in terms of the volume fraction of scattering particles, ϕ:

$$\frac{N}{V} = \frac{\phi}{V_{\mathrm{p}}} \qquad \text{as } N = \frac{\phi V}{V_{\mathrm{p}}}\,. \tag{2.85}$$

The volume fraction is often referred to as the scale factor, and this convention is followed herein. This factor is directly correlated with the difference in β. The structure factor for dilute, isotropic systems is equal to one.

2.5.2 Experimental

SANS was conducted on D11 at the ILL, France.[126,127] A neutron wavelength of 10 Å was selected by the velocity selector. The full width at half maximum neutron wavelength resolution, $\mathrm{d}\lambda/\lambda$, was 9 %, and defines the resolution function. Two sample detector distances of 1.4 and 8 m were used to collect high and low Q data. The data were reduced with the corrections as mentioned in the previous section and were stitched together to form a composite dataset. The final Q range was approximately 0.007–0.454 $\mathrm{Å}^{-1}$. Data were analysed using the python packages `sasmodels` 1.0.5[128] and `Bumps` 0.8.0[129], where the former is a variant of the popular small angle scattering fitting software SASview[130], and the latter is the optimiser engine behind `Refl1D`, used for fitting NR data.

2.6 X-ray photoelectron spectroscopy

X-ray photoelectron spectroscopy (XPS) is a method for the characterisation of the chemical composition of the outer surface of solid samples. The technique relies on the photoelectron

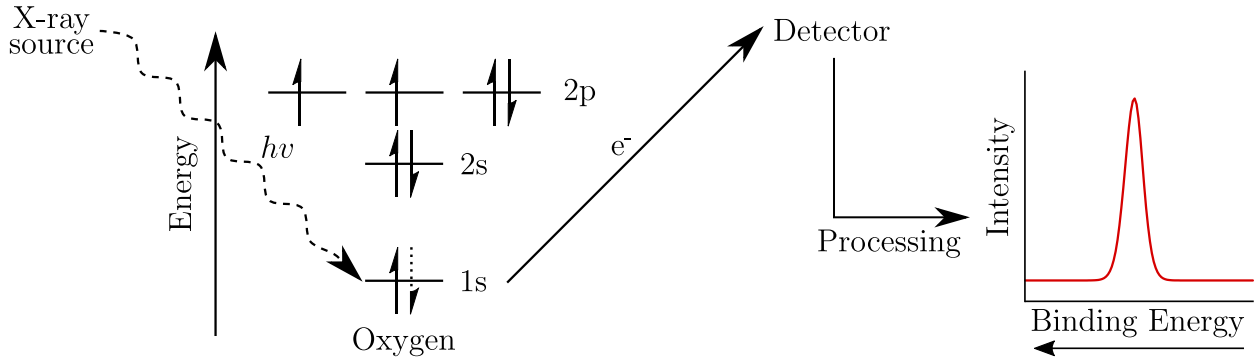

Figure 2.15: Schematic of the photoelectron effect with oxygen in a sample, where a 1s electron is excited and emitted as a photoelectron. The photoelectron will propagate outwards from the sample and towards a detector. A connected computer will quantise the number of counted electrons per unit energy, and return a spectrum of the number of counted electrons as a function of the binding energy. The convention for photoelectron spectra is to have the binding energy increasing from right to left.

effect, where electromagnetic radiation that falls upon a material can induce the emission of electrons. In the case of XPS, the emission of a photoelectron occurs by the excitation of a core-level electron, which in turn requires the incident radiation to have an energy in the X-ray region of the electromagnetic spectrum. This process is depicted for the exciation of an oxygen 1s electron in Figure 2.15.

By measuring the kinetic energy, KE, of an emitted electron, the binding energy, BE, can be determined through

$$KE = h\nu - \phi - BE\,, \tag{2.86}$$

where $h\nu$ is the energy of the incident photon, and ϕ is a constant called the work function, which is associated with the particular instrument in use. The binding energies of electrons relate to the attraction between an electron and nucleus; hence, BE is indicative of the electronic state of the emitted electron prior to ejection. As such, the particular chemical element from which the electron was ejected, and to a lesser extent the chemical environment of that element, can be inferred. The intensity of photoelectrons arriving at the detector is determined by the probability of the electron escaping the sample, and the probability of the emission of an electron following irradiation. Therefore, XPS can be used to quantify the elemental composition at the surface of a solid. The surface sensitivity arises from the high rate of inelastic scattering of the emitted electrons when escaping the sample; it is generally approximated that only the top 5–10 nm of a surface is probed. The high rate of inelastic scattering also requires that analysis must be carried out under some level of vacuum. A brief overview of the theory of XPS is laid out here. The theoretical and practical considerations of XPS are covered extensively elsewhere.[131]

2.6.1 Theory

The photoelectron effect and quantification

The goal of XPS is to identity chemical species and to quantify the atomic concentrations of species present at the surface of a given sample. The former is achieved by classification of core-level excitation peaks along a binding energy continuum that spans from the energy of the X-ray source to the sample's Fermi level, which is defined at 0 eV. Photoelectrons emitted from a particular electronic state of a given chemical element will give rise to a set of peaks that lie in the same region of the BE spectrum, regardless of the precise chemical species present. Therefore, the chemical elements present at the surface of a sample can be identified rapidly. On a finer scale, it is possible to detect small binding energy shifts in the typical element regions; these shifts are indicative of the chemical species present and can be used to infer the chemical environment of a given element, such as its oxidation state. This is most often achieved through comparison of peaks arising from a unknown sample compared to a known standard.

The latter objective of quantification is achieved by calculating the areas of excitation peaks. The atomic concentration of a given element is calculated with the determined peak areas and through the use of relative sensitivity factors, which account for the instrumental set-up and, importantly, the photoelectron cross section of each chemical element. The latter have been tabulated and describe the probability of photoelectron emission from specific electronic states, and hence, specific chemical elements.[132] The relative accuracy of the determined atomic concentrations is generally quoted to 10 %, and while it is possible to increase the accuracy through additional experimental steps, it is also necessary to account for all species present in the probed volume. This is particularly difficult if hydrogen is present, as the photoelectron cross section of hydrogen is very small compared to other elements, leading to a lack of discrete excitation peaks.[133] Consequently, it is much easier to determine relative concentrations, where the high precision of the experiment allows for minimal error in the relative ratios of chemical species.

Spin-orbit coupling

It is often the case that more than one excitation peak can arise from a given electronic state. Spin-orbit coupling is one particular mechanism whereby multiple peaks can arise in the XPS spectra. Here, orbitals with higher angular momenta, such as the p and d orbitals, can couple with the magnetic spin of the electron within these orbitals. When an excited electron is emitted from one of these orbitals, the coupling can give rise to a set of doublet peaks within the XPS spectra. The two possible states of total angular momenta for a given electron is given by the Clebsch-Gordan series. Those photoelectrons arising from a state of greater angular momentum have a lower binding energy and thus, it is typically possible to distinguish between the binding energies of the two states. The number of electrons within the two states leads to a set ratio for peaks arising from spin-orbit coupling. For example, a ground state Fe atom has a configuration of $2p^6$, where the spin-orbit coupling results in two states of total angular

momenta. The splitting of an iron doublet for the 2p region is $\sim$ 13 eV, and the ratio of the peak areas should then be 2:1 for the $2p_{3/2}$:$2p_{1/2}$ doublet peaks.[134]

Final state effects

Beyond spin-orbit coupling, additional peaks arise from so-called final state effects where the structure of the sample after the emission of a photoelectron influences the kinetic energy. Prominent examples of final state effects are known as shake-up satellites, which are resolvable peaks that arise at higher binding energies compared to a core-level excitation peak. These peaks arise from photoelectrons inelastically interacting with valence electrons upon emission. The photoelectrons lose kinetic energy and are thus observed as a peak at higher binding energies. Similarly, it is known that excitation peaks arising from metal species can display asymmetric shapes, with broader tails on the higher binding energy side of the peak.[135] The reason for the asymmetry is similar to the interaction that leads to satellite peaks but the splitting between the main peak and the satellite features are not resolvable.

Following the emission of a core-level electron, it is also possible for electrons in other, higher energy, orbitals to spontaneously fall in energy to fill the hole created by the emission of the photoelectron. Upon falling to the lower energy orbital, energy is transferred to another electron, leading to its emission, and hence a peak in the spectra. These photoelectrons are termed Auger electrons.

Other sources of peaks in XPS spectra are multiplet splitting and Plasmon loss features. The latter arises from the interaction of the emitted photoelectron with electrons in the conduction band, leading to distinguishable peaks for some elements. The former can arise from the coupling of magnetic fields induced by unpaired electrons. Two unpaired electrons can form if the chemical species contains an unpaired electron in the valence shell or through rearrangement can form an unpaired electron in the valence shell, and through the loss of a core-level electron. Consequently, a number of peaks arise from multiplet splitting that are often convoluted. Through theoretical work laid out in the 1970s[136,137], it has been shown that XPS spectra of known standards can be modelled.[138] However, it is common to represent the ensemble multiplet structure as one peak as the multiplet peaks can depend on the chemical environment of the element.

Background

The accurate determination of the area of a photoelectron resonance is key for meaningful quantification. This area is bounded by the background level of photoelectrons that arrive at the detector with higher or lower KE than a resonance peak. Unfortunately, the background intensity is not a simple function and is often significantly different either side of a resonance peak, resulting in an apparent step change to the background signal. Therefore, the quantification of a peak's area is strongly dependant on the method use to account for the background.

The nature of the background signal of an XPS spectrum is not precisely known.[139] For some

peaks, the background can appear flat at either side. In this case a simple linear function is suitable to describe the background; this is often the case for peaks arising from s orbitals. However, the linear model is not appropriate when accounting for step changes in background signal. A function frequently used when the background appears to step-change is the Shirley background.[140] This is an empirical model which considers the background intensity at a given BE is proportional to the area of the peak at lower binding energies. This results in a sloping background that increases as the peak area increases.

It is understood that a major factor in the background signal is the inelastic scattering of photoelectrons, where emitted electrons lose a proportion of energy before reaching the analyser and thus, do not reach the detector if the electrons do not have the correct energy to pass through the analyser. These inelastic effects can be modelled through the use of material-specific electron loss functions in a theory often referred to as the Tougaard background.[141] In leiu of known electron loss functions, two and three parameter empirical models can be used to account for inelastic photoelectron cross section of materials.[139]

In this work, a simple Shirley background has been used to correct for the background in peaks with a step change. While empirical in nature, it is understood to result in a reasonable approximation of the background, and is widely used in XPS analysis.

Charge correction

Emitted photoelectrons can leave a build up of positive charge on the sample surface, which reduces the KE of further emitted photoelectrons, shifting core-level peaks towards higher binding energies. This is most often found in insulator materials that do not remain in electrical contact with the spectrometer, where a current can not flow between the sample and spectrometer. To counter these effects, it is common to calibrate XPS spectra by forcing a particular peak arising from a known chemical species to a specific binding energy. A particularly common method is to define the aliphatic C 1s peak at 285.0–284.6 eV; this peak is ubiquitous owing to the presence of adsorbed carbonaceous species, known as adventitious carbon, at sample surfaces.[142] This peak persists in all but the most meticulously clean samples. It is also possible to assess if charge build up has occurred on the surface by assessing if the Fermi level of the sample is aligned at 0 eV. This technique relies on having a density of states at the Fermi level, and hence is only applicable to metallic samples. As the former technique relies on calibrating to an unknown carbonaceous material, it was instead chosen to calibrate the Fermi level to 0 eV as all samples contained metallic iron.

2.6.2 Experimental

The XPS data presented in this work was obtained with an enviroESCA spectrometer at the University of Leeds. The sample was loaded into the spectrometer and the atmosphere was reduced to a pressure of 10^{-6} mbar. The X-ray source used an aluminium anode, resulting in a photon energy of 1486.7 eV. The area of the impinging X-ray beam was 300 µm^2. The detector

was positioned at a normal angle from the sample surface, resulting in a 90° take-off angle for the photoelectrons. A pass energy of 100 eV with a step size of 1 eV was used for the collection of low resolution survey spectra. High resolution spectra were collected in finer energy regions where the pass energy was 30 eV and the step size was 0.1 eV. A dwell time of 0.2 s was used for both survey and high resolution spectra.

Data were analysed using CasaXPS, a peak fitting software that minimises the least-squares error between the model and observed data. CasaXPS includes a Monte Carlo (MC) approach to assess the parameter uncertainty for a given fit. Here, the observed data are perturbed by a random amount, proportional to the Poisson error associated with each data point, resulting in the formation of a simulated dataset that has all the statistical characteristics of the original dataset. If repeated enough times, it is possible to quantify the parameter uncertainty that arises from the Poisson error in the data. In this work, 200 simulated datasets were generated and fitted from a given observed dataset.

2.7 Beamline tribometer

The beamline tribometer was devised to provide a suitable reflectometry environment for the *in-situ* study of film structures under shear at solid-liquid interfaces. The tribometer, Figure 2.16, was commissioned by Infineum UK Ltd and was manufactured by Cambridge Reactor Design, UK. It was designed to fit on both the INTER and FIGARO neutron reflectometers and it was also designed to fit on the I07 X-ray diffraction instrument. A brief overview of the equipment is presented, followed by a description of the characteristics of the tribometer.

2.7.1 Equipment overview

At the centre of the tribometer an aluminium shaft holds a polyether ether ketone (PEEK) roller, with a radius of 25 mm, partially submerged in an oil bath. A belt transmission system, attached to a brushless motor (Maxon), can rotate the roller. A $55 \times 55 \times 10$ (l × w × h) mm substrate can be secured above the roller in a housing using two screws and a gib plate. The roller and motor sit on a rectangular aluminium plate that can be raised to either create a loaded contact or to form a specific gap between the roller and substrate. The former is facilitated by four pneumatic actuators that push the assembly plate upwards, producing a loaded contact between the roller and the substrate. The actuators are operated using compressed gas regulated between 0.3–4 bar, enabling varying loads through the contact of up to ~ 100 N. Alternatively, the roller can be raised to a specific distance from the substrate by tightening four screws on the assembly plate. Using two laser displacement sensors (micro-epsilon ILD 1420s) the roller-substrate gap can be calibrated with micrometer precision. A second motor (Maxon) drives the aluminium plate along two parallel rails, allowing the reciprocation of the roller over 34 mm of the substrate's surface. At the end of each reciprocating stroke the rotation of the roller is reversed to match the direction of horizontal travel. The oil bath and substrate

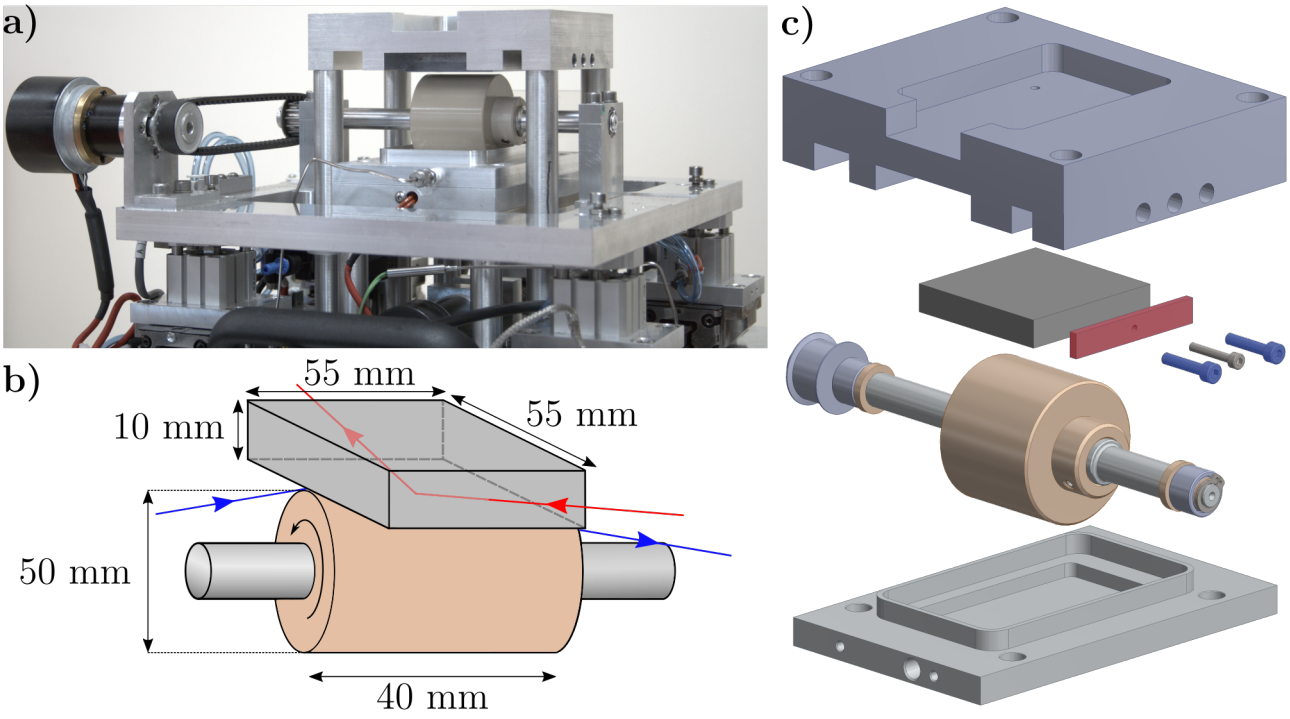

Figure 2.16: **a)** Diagonal view of the tribometer in the lowered position. **b)** A schematic of the roller and substrate at the centre of the tribometer. The red and blue arrows depict the approximate paths for the neutron and X-ray beams respectively. **c)** Exploded view of the centre of the tribometer. The two screws in the head unit force the gib strip against the substrate, securing it above the roller.

holder can be held at temperatures up to 120 °C. All the operating electronics are controlled via a Eurotherm Mini8 controller using analog inputs/outputs.

2.7.2 Roller movement

The angular velocity of the roller is controlled by the Mini8 controller which supplies a voltage between 0.3–3 V to the motor. The Eurotherm controller was pre-calibrated in this range so that the roller could be set to angular velocities of 50–500 rpm. However, the velocity of the shaft, and hence roller, was found to be lower than the pre-calibrated set point in the range of 75–400 rpm. The linearity in this range is shown by a linear fit to the measured roller RPM via one of the laser displacement sensors as shown in Figure 2.17a. The lasers were able to measure the angular velocity due to an oscillation in the aluminium shaft's distance from the sensor, which is believed to arise from movement in the bearing system. The angular velocities were also measured using a tachometer which could detect the rotational frequency of small white sticky label placed on the aluminium roller shaft. The tachometer data agree excellently with the speeds determined via the laser. The roller's diameter is 50 mm, and therefore, the accessible surface velocities are 1.4–9.8 $\times$ 10^{-1} m s^{-1} with angular velocities of 50–400 rpm. These velocities were determined while the roller was completely dry and not in contact with a surface. Thus, when entraining oil on to a substrate or when the roller is in contact with a substrate, the angular and surface velocities can be expected to be lower than the stated values.

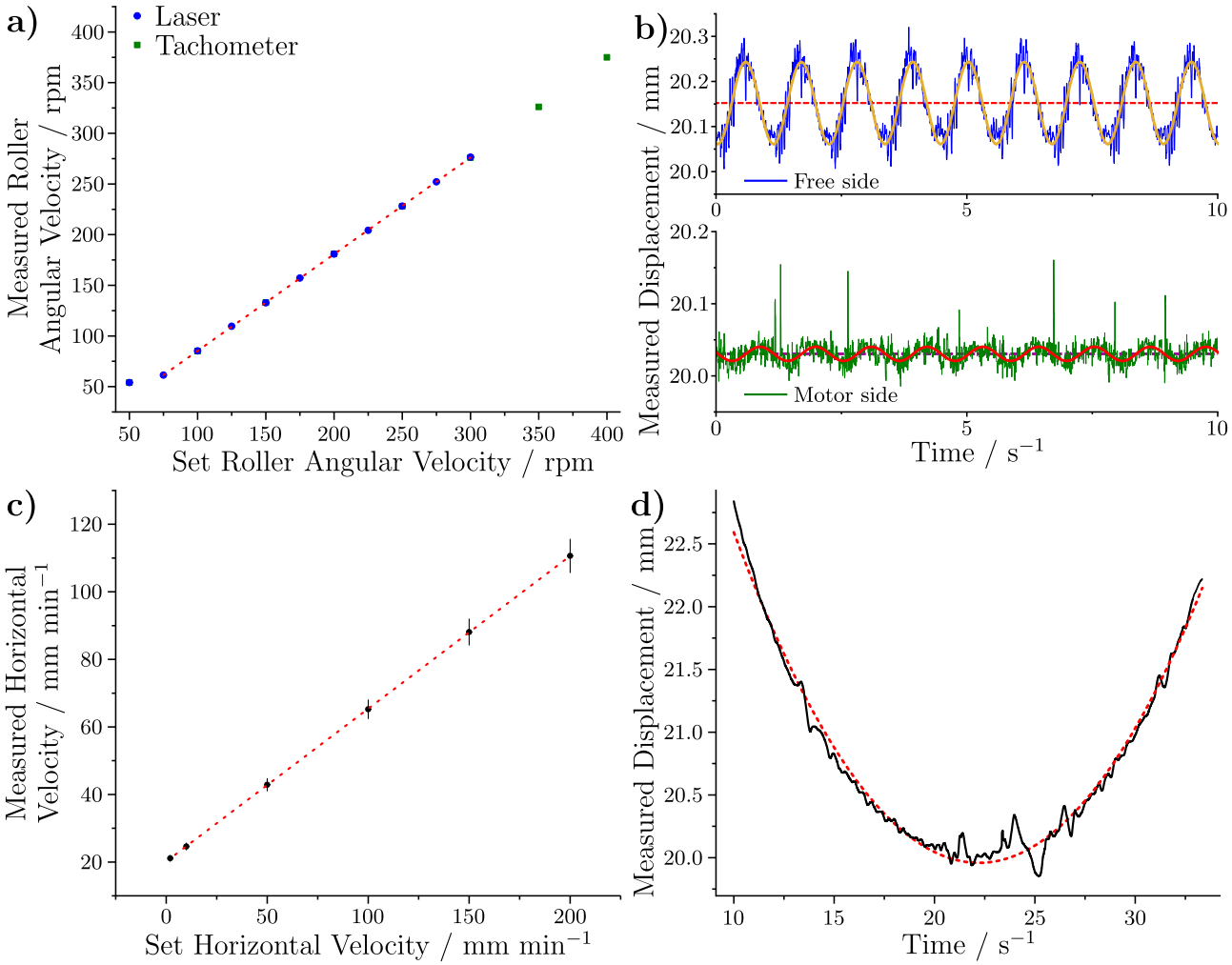

Figure 2.17: **a)** Measured angular velocities for the roller as a function of the pre-calibrated angular velocity range. Some of the tachometer results are not visible due to overlap with the laser data. **b)** The oscillation in the vertical deviation from the sensor to the aluminium shaft that holds the roller. The upper panel shows the oscillation on the side of the roller furthest away from the motor. The lower panel shows the oscillation on the same side as the motor. **c)** Measured horizontal velocities for the assembly plate as a function of the horizontal velocity set point. The dashed red lines show a weighted linear fit to the data. The error bars are propagated standard deviations for the horizontal velocities. **d)** Measured displacement as the roller traverses horizontally over the sensor. The minimum corresponds to the roller shaft sitting directly over the sensor. The red dashed line is a parabola fit to the data.

The oscillation in the roller shaft was found to be of greater magnitude on the side of the aluminium shaft that was furthest away from the motor. This side of the aluminium shaft is referred to as the free side, while the side closest to the motor is referred to as the motor side. The oscillation in the displacement from the lasers on both sides of the aluminium shaft is shown in Figure 2.17b. Here, the roller was set to rotate at 50 rpm. Note that these oscillations were not measured simultaneously, and so any apparent phase offset between these datasets is

not real. Both datasets were fit with the following wave function:

$$D = A\sin\left(Bx + \phi\right) + C \tag{2.87}$$

where D is the measured displacement, x is the elapsed time, A is the amplitude of the wave function and B relates to the time taken to complete one oscillation. Specifically, $B = 2\pi/T$ where T is the time taken to complete an oscillation of 2π radians. Finally, C is a constant offset from zero and represents the centre of the oscillation; these offsets are marked by the dashed lines in Figure 2.17b. The fitted oscillation amplitudes of the free side and motor side are 91 and 10 µm respectively, where the latter appears constant over an angular velocity range 50–400 rpm. However, it has been observed that the free side oscillation assumes a wider range of amplitudes, which are approximately 40–90 µm. As both lasers sense the displacement of the aluminium shaft from an equivalent distance from the centre of the substrate, the oscillation can be estimated to have a maximum amplitude of approximately 50 microns at the centre of the roller by taking the average of the two separate measured oscillations. This estimation serves as an approximate maximum to the oscillation at the centre of the roller as this calculation assumes that both separate oscillations are in-phase, and hence the oscillations of both sides combine constructively.

The horizontal traverse of the assembly plate, powered by the second motor, operates in a comparable manner to the roller motor with a pre-calibrated speed range of 0–200 mm min^{-1}. Similar to the roller angular velocities, the true horizontal velocities are lower than the pre-calibrated set points. The measured horizontal speeds are shown in Figure 2.17c, with the linearity shown by the fit. Thus, the accessible horizontal velocities are between 0.3–1.8 $\times 10^{-3}$ m s^{-1}. These velocities were determined by dividing the radius of the roller shaft, 6 $\pm$ 0.25 mm, by the time taken to traverse from the edge of the shaft to the centre. The centre of the shaft was approximated by fitting the measured displacement data, D, to the following parabola:

$$D = a + bx + cx^2 \tag{2.88}$$

where a, b and c are coefficients. The time at which the minimum of the parabola was reached, $x_{\min}$, was determined by setting the first derivative to zero and re-arranging to solve for $x_{\min}$:

$$\frac{\mathrm{d}D}{\mathrm{d}x} = b + 2cx = 0 \qquad \Rightarrow \qquad x_{\min} = \frac{-b}{2c}\,. \tag{2.89}$$

The error bars in the final measured horizontal velocity are the estimated standard deviations of the velocities. These were calculated via the propagation of error in the coefficients a and b, and the error in the diameter of the aluminium shaft, estimated to be $\pm$ 0.25 mm.

As the horizontal velocities are small compared to the angular velocities of the roller, the movement of the roller over the surface predominately translates to a sliding motion of the roller. This can be quantified using the slide-roll ratio, SRR, which is defined on a scale of 0–2 and calculated as $SRR = u_{\mathrm{s}}/U$ where $u_{\mathrm{s}} = |u_1 - u_2|$ and $U = (u_1 + u_2)/2$. Here, u_1 is

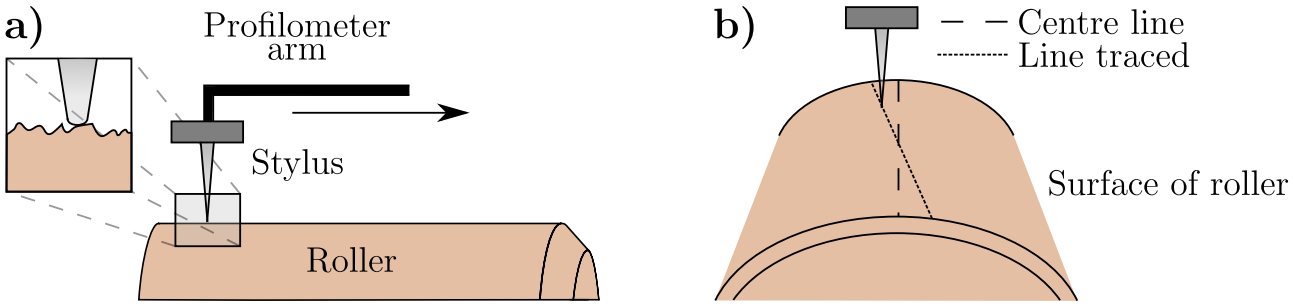

Figure 2.18: **a)** Concept of profilometery with the roller. The stylus is connected to the profilometer arm which travels across the roller surface in the direction of the arrow. During the traverse of the roller surface, the vertical displacement of the stylus is measured as a function of horizontal distance travelled. **b)** Due to the nature of the curved surface, the probed line of travel across the surface may not be the centre line of the roller.

the surface velocity of the roller and u_2 is the horizontal velocity of the roller. A $SRR = 0$ translates to pure rolling and a $SRR = 2$ translates to pure sliding. The maximum SRR for the tribometer is 2 when the horizontal velocity is zero and the roller is rotating; the SRR is also 2 at the end of each reciprocating stroke when the horizontal velocity is momentarily zero. The minimum achievable SRR is 1.95 at 54 rpm and 120 mm min^{-1}.

2.7.3 Roller roughness

The roller surface is visibly textured and as the XRR geometry requires the beam to pass through the roller, the roller's surface profile was characterised via contact profilometery. Profilometry was conducted using a Talysurf i120 stylus profilometer at the Department of Mechanical Engineering, University of Cambridge with the assistance of Tony Dennis. A schematic of the process of contact profilometery with the roller is shown in Figure 2.18a. The roller was placed onto a sample stage and was fixed into place using sticky tape. It was attempted to align the centre line of the roller with the line of travel of the profilometer (see Figure 2.18b), although in practice this could not be ensured as the roller has a curved surface. A stylus with a tip radii of 2 µm was attached to the end of the profilometer probe and a height-range gauge of 1 mm was used to set the limit in vertical deviation. The stylus was placed onto the roller's surface and then traversed approximately 37.0 mm over the roller's surface while measuring the vertical displacement every 1 µm of horizontal travel. This was done for three different positions over the roller.

The raw data for one position is shown in the upper panel of Figure 2.19a. The data for all three positions was found to have a significant gradient which could be indicative of waviness of the roller surface. However, as the roller has a curved surface and thorough alignment was not possible with the stylus, it is likely that this is due to the stylus deviating from the centre of the roller. As such, a parabola was fit to the surface profile and the raw data was corrected by subtracting the fitted line. This approach may have the drawback of removing differences in the radius of the roller over its length, but it was deemed an acceptable method for the

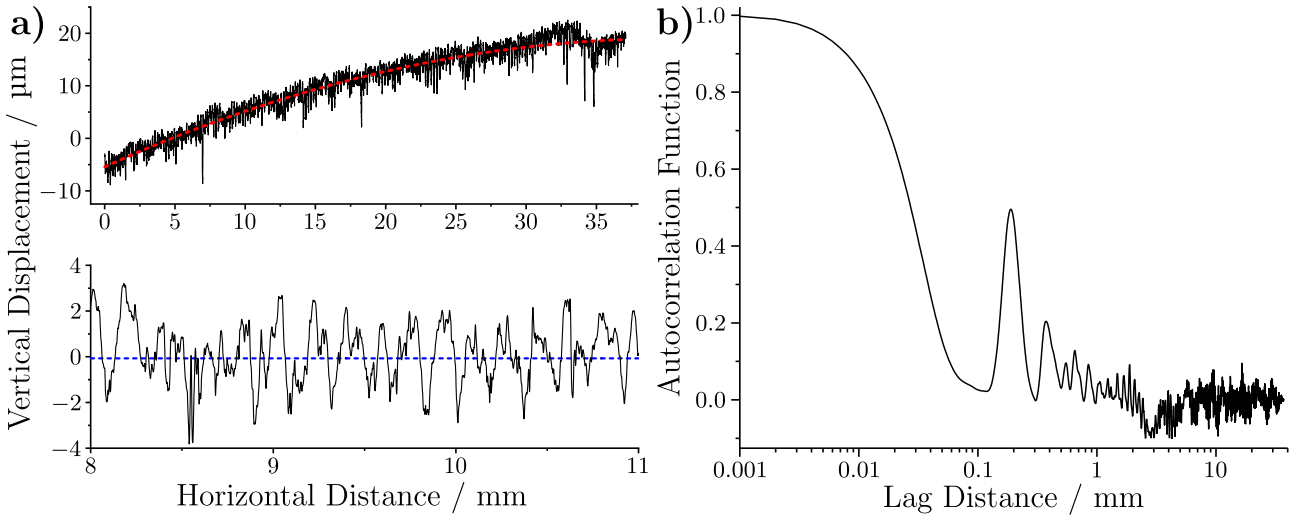

Figure 2.19: **a)** The upper panel shows the raw vertical displacement for one of the three roller positions measured by the profilometer. The red dashed line shows the fit of the parabola curve to the data. The lower panel shows the normalised data which was produced by subtracting the parabola curve from the raw data. The blue dashed line shows the arithmetic mean of the normalised vertical deviation over the whole horizontal range. **b)** The autocorrelation function shows the correlation between the vertical heights and distances over the surface. The peak at $\sim$ 0.2 mm in the autocorrelation function shows the primary distance between the vertical deviations.

purposes of inspecting the roughness on a micrometer scale.

From the normalised dataset, it is possible to calculate the RMS roughness of the roller surface, R_q. The square of R_q is calculated by taking the mean of the square of the vertical deviations, z, over the probed length, L, as given by

$$R_\mathrm{q}^2 = \frac{1}{L}\int_0^L z^2 \mathrm{d}x\,. \tag{2.90}$$

Here, x is the horizontal distance. The average RMS roughness for the three positions was found to be 1.6 µm, with a range of 1.6–1.7 µm between the three measurements. The average maximum difference in the three recorded deviations was found to be 20 µm, with a range of 16–26 µm across the measurements.

As these deviations are relatively small, the visible texture on the roller's surface is most likely not explained by vertical deviation. As can be seen in Figure 2.19a, the vertical deviations appear to have some step-like structure, which, if periodic will perhaps be visible. The lateral length scale over which these periodic step-like structures are found is perhaps easier to visualise with the autocorrelation function, $R\,(\tau)$, which can be defined as shown in Equation 2.91.

$$R\,(\tau) = \sum_{x=0}^{N} z(x) z\,(x-\tau) \tag{2.91}$$

Here, N is the length of the dataset and τ is a distance in the series between the minimum,

0.001 mm, and maximum, 37 mm, measured horizontal distances and is referred to as the lag distance. When $(x - \tau) < 0$, then zero is substituted for $z\,(x - \tau)$. The normalised $R\,(\tau)$ is shown in Figure 2.19b, where $R\,(\tau)$ is divided by the maximum value in order to scale the autocorrelation between -1 and 1. A peak is apparent at ~ 0.2 mm which relates to significant positive correlation of vertical deviations 0.2 mm apart. The peaks at greater distances appear to be multiples of the primary peak at 0.2 mm.

2.7.4 Contact

Loaded contact between the roller and a substrate is achieved by using compressed gas to force the actuator cylinders, and thus, the assembly plate and roller, upwards. The pressure of the gas applied to the actuators is regulated by an SMC ITV0050 regulator to an upper limit of 4.0 bar. As the actuators are double acting cylinders, extension and retraction is achieved by feeding compressed air into either the extension or retraction ports. This requires two compressed gas lines per actuator, which is achieved through a combination of a solenoid valve and two manifold valves. The solenoid valve splits the regulated compressed gas line into two separate lines, after which, two manifolds separate the two gas lines into four feeds each for either the extension or retraction ports on all of the actuators in parallel. Therefore, the lines that are connected to the actuators are at a maximum of 1.0 bar. The force produced upwards, F_{U}, by one actuator is calculated to be 31.4 N from

$$F_{\mathrm{U}} = P \times R_{\mathrm{act}}^2 \times \pi\,. \tag{2.92}$$

Here, P is the pressure and R_{act} is the radius of the actuator head, which is 10 mm. The total upwards force produced from all four actuators is 126 N. The mass of the assembly plate, including the roller and the roller motor, was determined to be 2.36 kg. Consequently, the total force upwards, F_{tot}, is calculated to be 102 N. This calculation does not account for a uneven mass distribution over the assembly, which is problematic as the motor is placed at one corner while the other three corners do not house additional components. Hence, this calculation should only be viewed as a first-order approximation. It has also been observed that some actuators do not extend at lower pressures despite a greater theoretical upward force than required to extend them. This is suggested to arise from a frictional force in the actuator motion, which must be overcome before the actuators can move.

Assuming the roller is raised so that it is flush in contact with the substrate and is loaded evenly across its width, an even pressure is applied to the substrate. The applied pressure assumes a parabolic distribution over the contact line and can be estimated following Hertzian contact theory.[143] The full width of the contact line, b, between the roller and substrate is estimated as:

$$b = 2\left[\frac{2F_{\mathrm{tot}}R}{W\pi E^*}\right]^{1/2} \tag{2.93}$$

where R is the radius of the roller (25 mm), W is the width of the roller (40.4 mm) and E^* is the contact modulus, defined as

$$E^* = \frac{E_\mathrm{R}}{(1-v_\mathrm{R}^2)} + \frac{E_\mathrm{S}}{(1-v_\mathrm{S}^2)}\,. \tag{2.94}$$

Here, v_R and v_S are the Poission ratios of the roller and substrate, and E_R and E_S are the Young's modulus for the roller and substrate. The Poission ratios and Young's moduli were estimated as those values for PEEK and silicon, where $v_\mathrm{R} = 0.38$, $v_\mathrm{S} = 0.27$, $E_\mathrm{R} = 3.85$ GPa and $E_\mathrm{S} = 170$ GPa. The contact region at the maximum applied gas pressure was calculated to be 192 µm. The peak pressure, P_0, within the contact region is calculated as:

$$P_0 = \left[\frac{F_\mathrm{tot}E^*}{W\pi R}\right]^{1/2} \tag{2.95}$$

and the mean contact pressure is defined as $P_\mathrm{m} = P_0\pi/4$. Therefore, for the maximum applied gas pressure of 4 bar, the mean and maximum Hertzian line contact pressures were calculated to be 9.4 and 11.9 MPa. These contact pressures are lower than the equivalent achievable in ball-on-plate and pin-on-disk tribometers, albeit with different materials (steel/aluminium).[144,145] However, a lower contact pressure is not surprising as the roller has a much wider contact area compared to these other tribometers.

When using the tribometer in loaded contact mode while entraining dodecane, substrates are worn rapidly. The wear of the substrates is a fundamental issue as reflectometry relies upon the underlying substrate structure remaining the same over the duration of an experiment. An image of two worn substrates, one standard iron-coated Si substrate and one steel substrate (polished to 300 Å), are shown in Figure 2.20. The iron-coated Si substrate was worn in three separate locations following two different experiments. In the first experiment, 10 ml of dodecane was placed into the oil bath and the roller was raised into contact using a pressure of 1 bar, where $F_\mathrm{tot} = 8$ N. The roller was set to an angular velocity of 50 rpm and fixed in one position for approximately 20 minutes. This is visible as the full dark line that extends from one side of the substrate to the other and is labelled by a white I label. The dark colour of the wear track is thought to arise from the removal of iron at the interface, as the roller was discoloured a dark grey colour. The roller was unloaded from the contact and repositioned along the substrate surface before reforming the contact with the substrate. The same experiment was repeated at the new position and the resulting wear scar is labelled by the white II label. This wear scar does not span the full roller width. The reason for this difference is not known but it was noted that due to friction in the actuators and the uneven load carried by each actuator, the cylinders on one side of the tribometer extended first and to a greater extent than those on the other side of the tribometer. This resulted in an uneven contact between the roller and the substrate, which led to an uneven applied load across the substrate.

The steel substrate was worn following a 20 minute run with a roller angular velocity of 84 rpm without a horizontal velocity. The produced wear scar is the most visible scar in the image.

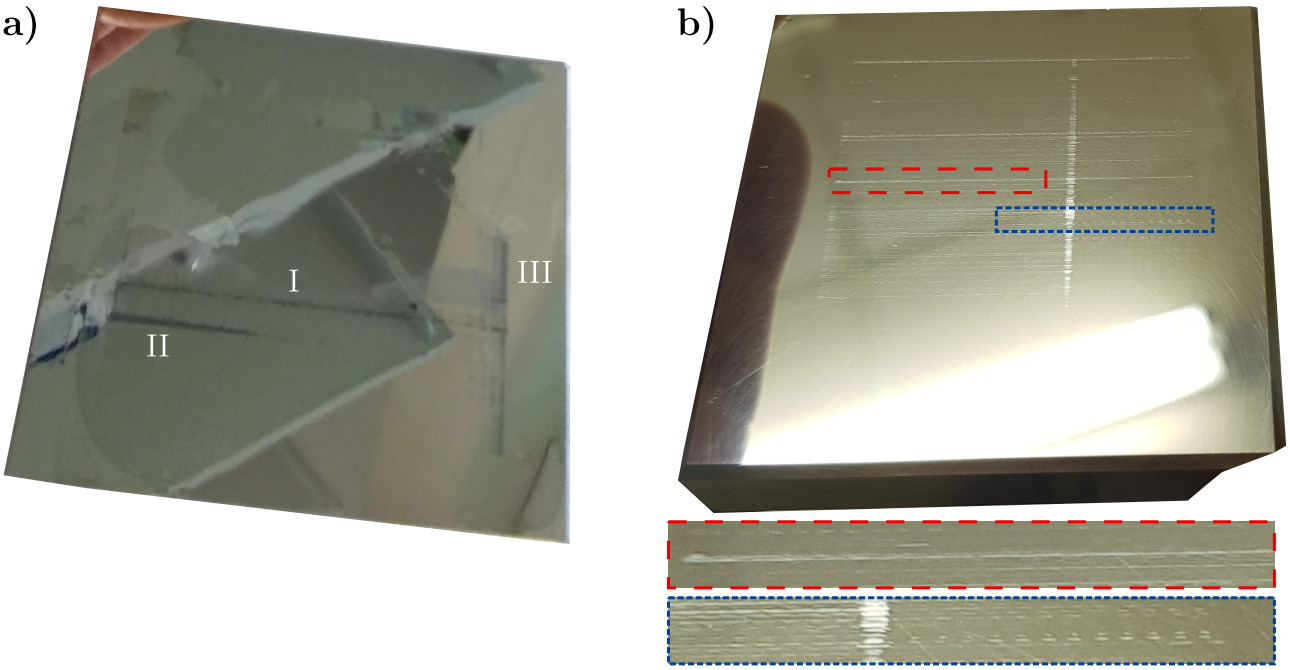

Figure 2.20: **a)** An image of a worn iron-coated Si substrate. This substrate was used multiple times. The black lines show the wear region, where it is thought the iron coating was either partially or fully removed through wear. The liquid on the surface is residual dodecane. The wear scar marked by the III label was unintentionally made and is not further discussed. **b)** A worn steel substrate following contact with the tribometer. The part of the substrate surface surrounded by the coloured dashed boxes are magnified at the bottom with the corresponding colours as a key.

After, a five minute run was conducted with the same angular velocity but with a horizontal velocity of 65 mm min^{-1}. The wear scar can be seen to extend over the full stroke length of the tribometer, with distinct wear patterns that appear over the surface. The full stroke length is 34 mm, and the distance between the wear scars is $\sim$ 0.8 mm. This corresponds to a time taken to traverse the wear spots of 0.7 seconds, which at 84 rpm translates to approximately 1 rotation of the roller between the wear spots. It is quite surprising that distinct patterns of wear are apparent as the roller rotation is not synchronised with the roller horizontal position, and furthermore, there is some variability in the amount of roller rotation at the end of each roller stroke. It is not clear why some of the other wear scars do not show a discernible pattern but instead show consistent wear over the full roller stroke, implying that the roller is constantly in contact with substrate. This could result from localised regions of a greater radius along the roller width; however, this was not detected from the profilometry analysis. It may be possible to draw similarities between the roller oscillatory motion in subsection 2.7.2. However, as the oscillatory motion is minimised on one side of the tribometer it would be expected that the distinct wear patterns would appear more on one side of the substrate, which does not appear to be consistent with the apparent wear pattern.

Wear on the substrates' surfaces suggests that the loaded roller is not supported by the entrained dodecane, and that surface-surface contact is occurring. This suggests that not enough force can be generated by the resulting hydrodynamic pressure as dodecane is forced through the

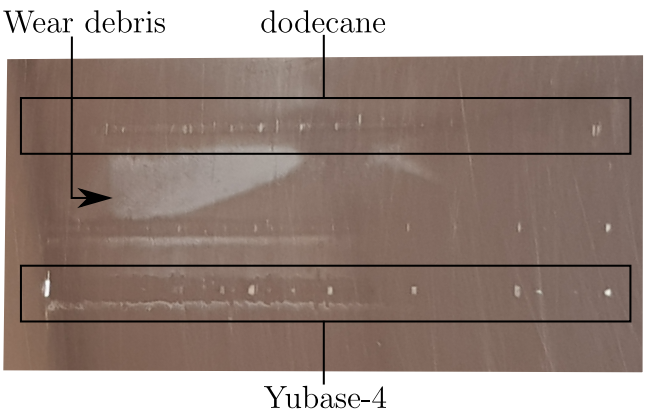

Figure 2.21: Comparison of the wear scars formed from rotating the roller in contact with a steel substrate loaded with 8 N of normal force. The wear scar in the middle of the two labelled wear scars resulted from a short run of approximately three minutes and was stopped as a judder was apparent on the rotation of the roller due to a loose screw on the bearing housing. This was tightened and the roller was moved across the surface, and the run restarted.

contact between the roller and the substrate. One possible reason that significant hydrodynamic pressure could not be generated is due to the low viscosity of dodecane, which is reported to be 1.38×10^{-3} Pa s at 25 °C.[146,147] To test this hypothesis the wear on a steel substrate was compared between 10 ml of dodecane and Yubase-4, which is a base oil with a dynamic viscosity of 2.21×10^{-2} Pa s as measured with a Kinexus Rheometer in a cone-plate geometry at 25 °C. Contact was formed between the substrate and the roller while it was rotating at 181 rpm in an attempt to reduce any dry contact between the substrate and the roller. The applied load was approximately 8 N and the angular velocity was kept at 181 rpm with zero horizontal velocity for both lubricating samples. The roller was run for 20 minutes, and then the substrate was dried and an image taken for both samples. Between running the tribometer with dodecane and Yubase-4, the roller was moved a few mm across the substrate surface.

Wear was produced on the substrate after 20 minutes with both lubricating samples as shown in Figure 2.21. It appears that the wear is more severe when running with dodecane, with a larger region of wear debris adjacent to the wear scar. The debris is thought to be small fragments of steel as the PEEK roller was discoloured during this test. However, the contact between the roller and the substrate may not be similar between the two runs due to the uneven action of the tribometer actuators. This may explain why wear scars on the right hand side of the substrate are visible in the scar formed with Yubase-4 but not visible when run with dodecane. Despite this, it is clear that wear still occurs at the substrate with the higher viscosity base oil. It is possible that a higher viscosity base oil may be able to maintain a hydrodynamic film, but it is suggested that the initial uneven lifting of the tribometer actuators is a more fundamental issue to producing a evenly loaded contact with similar lubrication regimes across the whole contact.

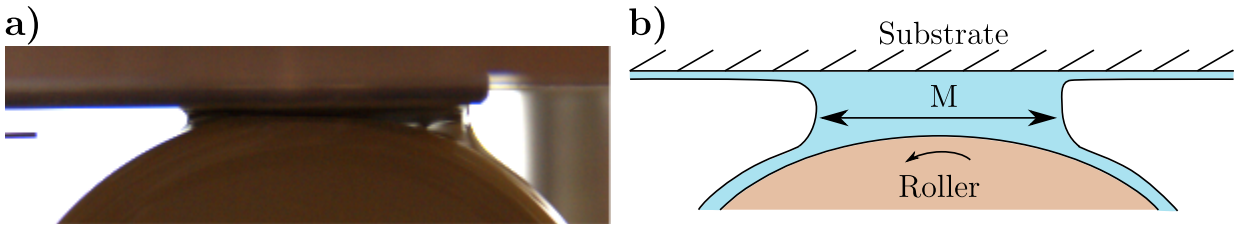

Figure 2.22: **a)** An image of the meniscus between the substrate and the roller with a calibrated gap of 200 µm and a roller angular velocity of 300 rpm. **b)** Schematic of the image in **a)**, where the roller is rotating counter-clockwise. The minimum meniscus width is the shortest distance between the two liquid-air interfaces. Not to scale.

2.7.5 Calibrated gap

The procedure for calibrating a gap between the roller and substrate is described here. Initially, the aluminium plate was lowered by loosening four screws connected to the actuators so that the plate was flush against the actuator heads. The roller shaft was then moved to sit over the laser displacement sensors and held in position without rotation. The aluminium plate was then raised so that the roller was in light contact with the substrate; this was achieved by tightening the four screws in succession by a half turn each. After each cycle of tightening the screws by a half turn, the aluminium plate was levelled by tightening or loosening screws where the aluminium plate was not level. When the roller was in contact with the substrate, it was made sure that the roller sat flush against the substrate. This could be evaluated by holding a light behind the roller, where, if light could pass between the roller and the substrate, the roller was not flush against the substrate. The displacement between the shaft and the lasers was then noted down and the required displacement calculated for a specific gap size. Screws on either side of the roller were then loosened by approximately the same amount to reach the required gap size. The displacement on either side was checked and altered in succession to make sure the gap size was equal on either side. Finally, four nuts that sit with the screws were tightened, stopping the screws from tightening or loosening any further.

2.7.6 Meniscus widths and flow within the meniscus

When the tribometer is set up with a calibrated gap between the roller and substrate, rotating the roller entrains a liquid sample onto the substrate's surface. The entrained liquid forms a meniscus between the upper part of the roller and the substrate, where the width of the meniscus increases in length with different angular velocities of the roller. An image of a meniscus between the roller and substrate at a gap of 200 µm is shown in Figure 2.22a, and a schematic showing the minimum meniscus width, M, is shown in Figure 2.22b. The meniscus width is of particular importance when using the tribometer for NR, as the beam footprint is typically extended as much as possible over the same direction as the meniscus width; this is done to decrease the counting time to a minimum. As such, a portion of the neutron footprint on the substrate will cover the region within the meniscus and the rest of the footprint will fall outside of the meniscus region.

To estimate the meniscus widths at set gap sizes and roller angular velocities, 10 ml of dodecane-h_{26} was placed into the oil bath and the roller was positioned 0.5, 0.4 and 0.2 mm from the substrate surface. The roller was rotated with angular velocities between 54–276 rpm and the position of the roller was held in a fixed horizontal position over the laser displacement sensors. The meniscus width when stationary was also determined by rotating the roller to entrain dodecane onto the substrate surface and then halting the rotation. Images of the meniscus were collected using a Canon 1000D camera with an $f/5.6$ aperture, ISO of 200 and an exposure time of $1/60^{\text{th}}$ of a second. The camera was coupled with the digiCamControl software to control the interval timing on the camera shutter. The camera was positioned on a Hama tripod, and placed so that the camera lens was centred down the roller shaft. The focus of the camera was shifted to the plane of the front of the roller to capture sharp images of the meniscus at the edge of the roller. A needle with a known diameter of 0.50 mm was positioned in the same focal plane so that the pixel width of the resulting images could be calibrated. A light box was placed behind the tribometer to increase the contrast between the meniscus and background. Thirty images were collected for each angular velocity at each calibrated gap; these images were collected with a one second interval between them.

The images were then processed using ImageJ 2.1.0 using a custom Java script to process the images in batches. The script converts the images into a grey scale 8-bit format, and then sets the colours to be strictly black or white depending on the light intensity. This process effectively reduces the images to the outlines of the meniscus and the needle. ImageJ then calibrates the pixel size by drawing a straight line across the outline of the needle, and calibrates the length of the line in pixels to 0.5 mm. A line is then drawn across the minimum width of the meniscus and the line's length is converted from pixels to mm.

The meniscus width data are shown in Figure 2.23a and four select images are shown in Figure 2.23b to highlight how the conditions affect the menisci shape. The error bars show the standard deviation of the meniscus widths from the 30 individual images taken for each angular velocity. In general, the meniscus width increases with the roller angular velocity, and increases $\sim$ 2 mm with gap sizes of 0.2 and 0.4 mm. Similarly, a smaller gap size also increases the meniscus width as more dodecane is entrained onto the substrate. An initial increase is seen for the meniscus width with a 0.5 mm gap, but at the highest angular velocity it was found that the meniscus width was smaller than the menisci at lower angular velocities, which is clear from the fourth image in Figure 2.23b. It is not expected that a greater angular velocity of the roller would decrease the amount of dodecane that reaches the meniscus and indeed, simulations of ink at similar rotational speeds suggests that the angular velocity only increases the amount of liquid reaching the upper part of a rotating roller.[148] These simulations also suggest that the inertial force of a roller dominate over gravitational, viscous and surface tension forces. Previous work has also indicated that two flow regimes exist in the meniscus between a roller and a flat surface when the position of the meniscus is close to the minimum roller-plate separation. The upper flow regime is a recirculating flow that does not appear to be well-mixed with the lower flow regime which is fast-moving and dominated by the motion of the roller.[149] Therefore, it is

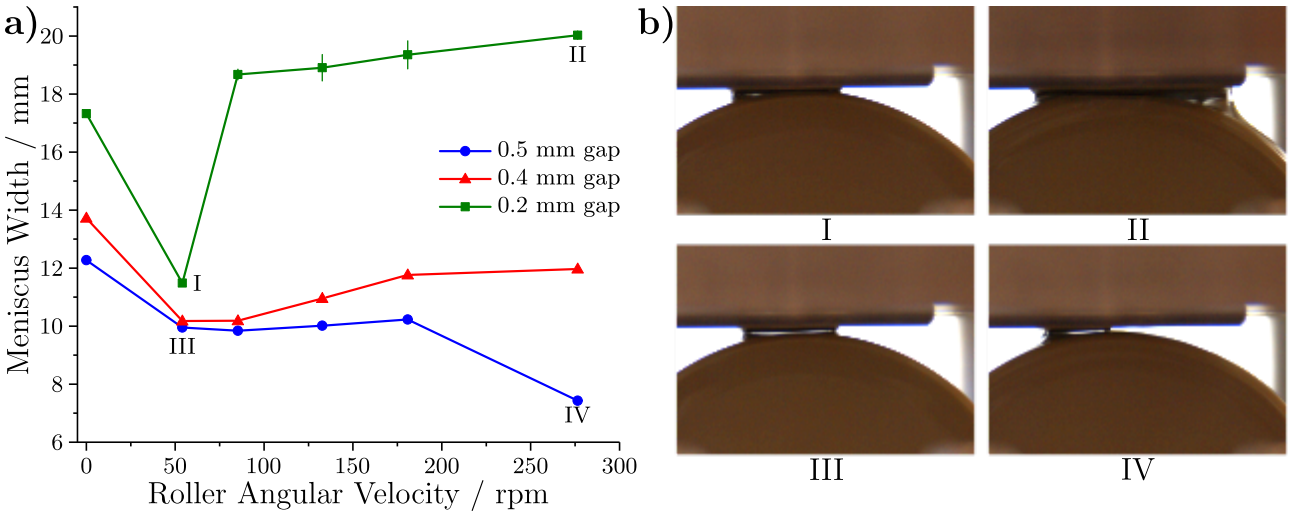

Figure 2.23: **a)** Data collected for the meniscus widths at three different calibrated gaps over a range of roller angular velocities. **b)** Four images which show the behaviour of the meniscus at different gap sizes and angular velocities.

suggested that a significant portion of the entrained dodecane is swept through the meniscus region and entrained back down into the oil bath. The inertial effect may explain why the meniscus appears shifted in the direction of the roller rotation.

Contrastingly at smaller roller-substrate gaps, more of the entrained dodecane will come into contact, and subsequently transfer momentum to the surface of the substrate or to the slower flowing dodecane already held in the meniscus. This transfer of momentum leads to a slower flow of dodecane through the meniscus and a bank of dodecane is consequently built up at the inlet side of the meniscus, increasing the width.

Chapter 3

Characterisation of glycerol monooleate aggregation and reflectometry substrates

3.1 Background

Glycerol monooleate is known to form reverse micelles when dissolved in non-polar solvents, such as *n*-alkanes.[150,151] Simulations have suggested that pre-formed reverse micelles of GMO in *n*-heptane can adsorb at confined mica surfaces under shear and remain intact.[152] These structures were found to show similar frictional behaviour to the films formed with non-aggregated monomers of GMO. Similar structures were also noted in simulations of GMO adsorption at perfectly flat, confined, sliding iron oxide surfaces.[153] While it is likely that both aggregates and monomers of GMO exist in bulk solution, the interplay between these species when adsorbed at the iron oxide-solution interface has received little attention and thus, the structure of the GMO adsorbate film is unclear. Therefore, understanding the aggregation of GMO in dodecane may provide insight into the adsorption of GMO at the iron oxide-dodecane interface as studied in Chapter 4.

In this chapter, the bulk behaviour of GMO in dodecane is investigated first. Pendant drop tensiometry has been used to infer the approximate onset of GMO aggregation in dodecane and SANS has been used to determine the structure of the aggregates formed in bulk solution. Additionally, the swelling of the GMO aggregates on addition of water has also been quantified through SANS. The substrates used in the NR experiments are then characterised using XPS, XRR and NR.

The GMO used throughout this chapter was purchased from Sigma Aldrich (1-Oleoyl-*rac*-glycerol, $>$ 99 %) and was stored below 0 °C where possible. The *rac* phrase in the name relates to the nature of the sample, which is a racemic (50:50) mixture of the two stereoisomers that arise from the stereocentre of the secondary alcohol of the GMO head group. Possible

structural isomers that may be found within a sample of GMO are considered to arise though the *trans* analogue of the double bond in the alkyl chain group, and through the formation of the ester bond with the secondary alcohol group of glycerol to form 2-Oleoylglycerol. While these isomers share similar structure with GMO, the different geometries of the head and tail groups may lead to different self-assembly behaviour. The GMO was used as-received and so it is not possible to rule out the presence of these isomers and other possible impurities, such as other monooleins with different alkyl chain lengths, within the sample.

Dodecane was used as the solvent throughout this chapter as the deuterated variant is one of the cheaper alkanes that can be found within typical lubricant base oils.[154] The cost becomes a significant factor for neutron scattering experiments, as the required mass of the solvent can exceed 100 g. Other molecules that are cheaper to deuterate such as aromatics are not suitable as they have a greater polarity than *n*-alkanes; this can alter the solution and adsorption behaviour of polar additives. *n*-Dodecane-h_{26} was purchased from Fisher (> 99 % purity, Acros Organics) and *n*-dodecane-d_{26} was obtained from Cambridge Isotopes, US (> 98 % deuterated, 98 % purity).

3.2 Bulk properties of glycerol monooleate dissolved in dodecane

3.2.1 Pendant drop tensiometry

Pendant drop tensiometry was used to study the adsorption of GMO at the dodecane-water interface. This can be viewed as a near-ideal interface, where the transition between water and dodecane is sharp, typically with a Å length scale.[155,156] Additionally, surface defects do not exist as experienced on solid surfaces. The adsorption of GMO was probed by measuring the equilibrium interfacial tension of individual water pendant droplets immersed in GMO-dodecane solutions in a glass curvette. Pendant droplets of ultra-pure water were formed using blunt-ended needles and a glass syringe, which along with the curvette were left to soak in aqueous Decon 90 solution overnight, and then washed thoroughly with ultra-pure water and dried in an oven before use. The cleaned curvette was filled with the sample solutions and placed onto a temperature controlled plate. The plate was controlled by a Julabo water bath and a Eurotherm controller temperature controller; the former was set to 37 °C while the Eurotherm was set to 27 °C. These temperature settings were tested with a blank dodecane solution, which was found to have a temperature of 25 ± 1 °C after an equilibration period of 30 minutes. While a temperature gradient is likely to be formed when only heating the curvette from the bottom, the gradient will be minimal as the temperature of the plate and the surrounding air had a maximum difference of 9 °C.

The interfacial tension of a blank solution of dodecane was measured using a 1.83 mm blunt-ended needle. A droplet with a size of 51.5 µm was formed, and allowed to equilibrate for 30

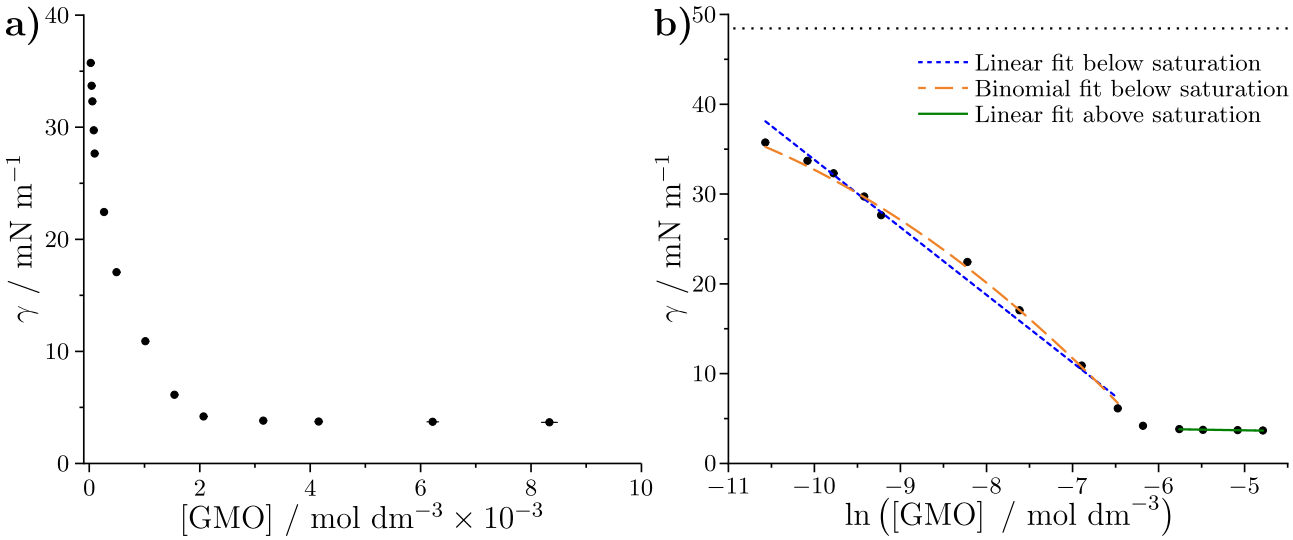

Figure 3.1: **a)** Interfacial tension of the dodecane-water interface as a function of the concentration of GMO in dodecane. There are error bars in both interfacial tension and in the concentration of GMO, but they are obscured by the data points. **b)** The interfacial tension as a function of the natural logarithm of the GMO concentration. The dotted line at the top shows the neat dodecane-water interfacial tension.

minutes prior to collection of 180 images of the pendant droplet, collected with a 10 second gap between each image. The outline of each pendant droplet image was fit, enabling the determination of γ using the densities of dodecane and water at 25 °C, which are 0.745 g cm^{-3} and 0.997 g cm^{-3} respectively.[146,147] The average interfacial tension was found to be 48.4 ± 0.2 mN m^{-1}, which is lower than a previously reported value for the dodecane-water interface of 52.6 mN m^{-1} at 25 °C.[157] The difference could be due to the presence of surface-active impurities in the dodecane; the solvent was used as received in the present work, but was purified multiple times with an alumina column in the cited work.

Solutions of GMO in dodecane (0.03–8.33 mM) were then loaded into the curvette from lowest to highest concentration and a fresh pendant droplet was formed in each solution. Care was taken to ensure only one water droplet was formed inside each sample. After a water droplet was formed, the droplet was left to equilibrate for 30 minutes on the heater plate before taking images. Measurements were taken until the determined γ value was stable for at least 30 minutes, after which the interfacial tensions for each image were averaged and the standard deviation of the distribution determined. The smaller blunt-ended needle was used for collecting the pendant drop images at GMO concentrations > 1 mM. The density of dodecane was taken as 0.745 g cm^{-3} for all the GMO solutions as the density difference between neat dodecane and the 8.33 mM GMO-dodecane solution was found to be 0.06 %, which was deemed negligible. The averaged γ as a function of the GMO concentration is shown in Figure 3.1a. The error bars for the interfacial tension are the calculated standard deviation of 180 images and the error bars in the concentration of GMO are the propagated weighing error.

The interfacial tension decreases as the concentration of GMO increases, indicating greater GMO adsorption at the water-dodecane interface. Adsorption of GMO is thought to occur

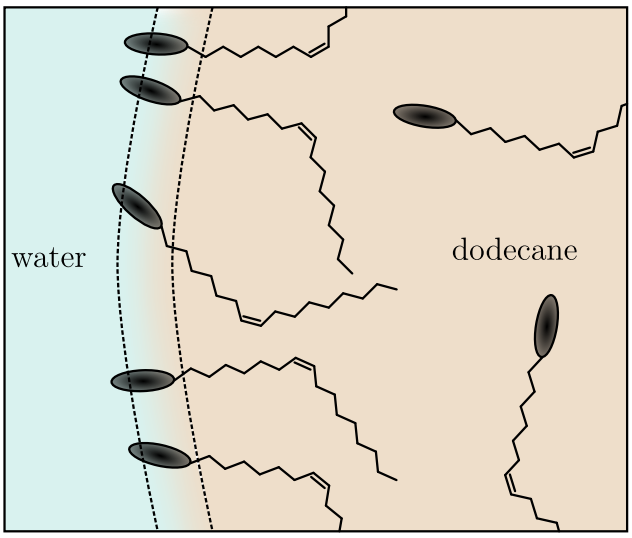

Figure 3.2: A schematic of GMO adsorbed at the dodecane-water interface, which is shown as the banded region. The GMO head group is shown as the oval shape; if the adsorbate GMO is predominately monomolecular, the head group will adsorb to the water-rich region of the interface. Monomers, and reverse micelles (not shown), will also be present in the bulk dodecane solution.

so the hydrophilic head group can maximise its molecular interactions when positioned with the head group within the water-rich part of the interface, while the hydrophobic alkyl chain extends into the dodecane-rich portion of the interface. A schematic of the interface with adsorbed GMO is shown in Figure 3.2. As the concentration of GMO increases, the gradient becomes less negative until a plateau is reached at $\gamma \sim 4$ mN m^{-1}, indicating that the surface excess of GMO reaches a maximum.

As GMO occupies more of the interface as the bulk concentration increases, GMO will accumulate in the bulk solution and begin to aggregate. Aggregation in non-aqueous solvents is driven by the maximisation of favourable interactions between the amphiphilic molecules themselves, and between the surfactant and solvent. Here, a reverse micelle structure is formed where the polar head groups orient themselves towards one another and interact through dipolar and/or hydrogen-bonding interactions. Meanwhile, the tail groups extend into the bulk solvent and interact with solvent molecules or other surfactant tail groups through weaker dispersion interactions. These interactions result in an enthalpic gain compared to an unordered isotropic solution, which contrasts the analogous formation of aggregates in aqueous solvents, which are driven by the entropic hydrophobic effect.[158] It is thought that the former process is less thermodynamically favourable, and thus, the concentration at which aggregation begins to occur, known as the critical micelle concentration (CMC), is less well-defined in non-polar solvents.[159,160]

The data were plotted using the natural logarithm of the concentration of GMO as shown in Figure 3.1b, and then fit with linear functions above and below the saturation of the interface to identify the point at which the onset of saturation occurs. This is a typical way of determining the CMC in aqueous systems, but it is expected that small aggregates may have already formed

by the onset of saturation at the interface.[161] As such, the determined CMC concentration may relate to an increase in the rate of change of the aggregate size as the concentration increases. By setting the two linear fits equal to one another, the concentration intersection was determined to be $2.4 \pm 0.2 \times 10^{-3}$ mol dm^{-3}. However, the linear model below the point of saturation has a relatively poor fit, and it could be argued that the data follow a parabolic trend, as has been found previously for other surfactant systems.[161,162] Therefore, the data was fit with a binomial model and the saturation concentration was determined to be $2.1 \pm 0.1 \times 10^{-3}$ mol dm^{-3}. The uncertainty for both determined concentrations was calculated following the propagation of error of the determined coefficients from the fits.

The surface excess of GMO was also determined following Equation 2.8. The gradient of the interfacial tension as a function of the logarithmic concentration, $\mathrm{d}\gamma/\mathrm{d}\ln(C_{\mathrm{surf}})$, is itself a function of $\ln(C_{\mathrm{surf}})$. Therefore, a concentration must be selected in order to calculate a surface excess. By using the determined concentration of $2.1 \pm 0.1 \times 10^{-3}$ mol dm^{-3} as the onset of saturation, the maximum surface excess was determined to be $4.1 \pm 0.3 \times 10^{-6}$ mol m^{-2}. The area occupied by each adsorbed GMO molecule, A_{PM}, is a minimum when the interface is saturated. Assuming a monolayer is formed upon adsorption, A_{PM} can be calculated following:

$$A_{\mathrm{PM}} = \frac{1}{\Gamma_{\mathrm{GMO}} \times N_{\mathrm{A}}} \tag{3.1}$$

where N_{A} is Avogadro's constant. Hence, the A_{PM} was determined to be 40.1 ± 2.6 Å^2, which is thought to be dictated by the alkyl tail group as it is larger than the polar head group. The assumption of a monolayer is based on the simple argument of maximising favourable intermolecular interactions for both tail and head groups with the polar and non-polar regions of the interface. However, it should be noted the adsorbed structure of GMO is not known and could be more complex.

3.2.2 Small angle neutron scattering

The data presented here was collected as part of a larger experiment planned and led by Dr Thomas McCoy, University of Cambridge, on D11 at the ILL. The author assisted with the preparation of the experiment and the collection of data. The analysis presented here was conducted individually.

SANS was conducted on two solutions of 20 mM GMO in dodecane-d_{26}, where one solution was prepared with the addition of H_2O so that the water-to-surfactant ratio, W = [water] / [GMO], was 5. The GMO concentration used was a factor of ~ 10 above the CMC determined via pendant drop tensiometry, suggesting that aggregates should be present within the bulk solution. The data were collected at 25 °C in quartz cells with 2 mm path lengths.

Guinier plots of the reduced data collected with the two solutions are shown in Figure 3.3a. Using linear fits to the data, the radii of gyration of the aggregated GMO with and without added water were determined to be 18.0 ± 0.1 and 16.4 ± 0.1 Å respectively. These dimensions

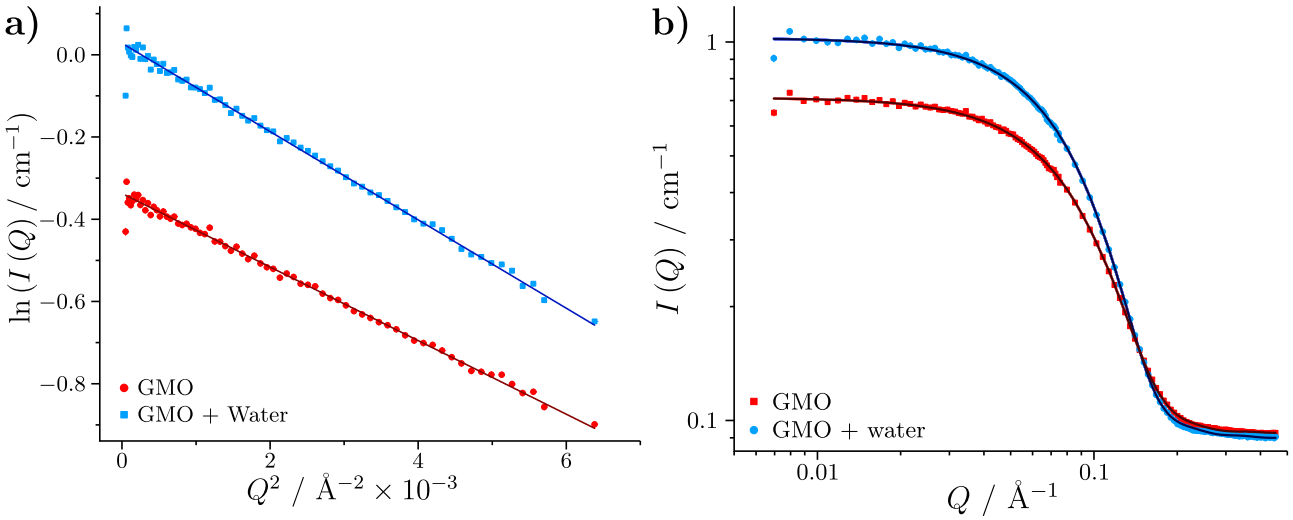

Figure 3.3: **a)** Guinier plots of the SANS data collected with the two solutions of 20 mM GMO in dodecane with and without additional water. **b)** Comparison of fits to the data collected with the 20 mM GMO-dodecane systems with and without water.

relate to the RMS radii of the aggregates formed by the GMO in solution, and the presence of water appears to swell the GMO aggregates. The greater intensity of scattering for the system containing water could be associated with a greater number of scatterers as it is expected that the presence of water within the solution promotes micellisation. However, as shown in Equation 2.84, the intensity could also be increased by the greater volume of the scattering objects when water is present, as implied by the greater R_{g}. Furthermore, the greater intensity could result from the presence of H_2O within the scattering objects, which will increase the contrast between the solvent and the scatterer as the β_{n} of H_2O is lower than that of GMO.

In order to infer the shape and dimensions of the aggregates, the data were modelled using Equation 2.84. A spheroid form factor, with equatorial radii, R_{e}, and a polar radius, R_{p}, was used to model the data. The linear behaviour of the Guinier plots suggest that the solutions are appropriately dilute to be modelled without a structure factor. The 1D average form factor for a spheroid, $\langle |\mathrm{F}(Q)|^2 \rangle$, is given in Equation 3.2.

$$\langle |\mathrm{F}(Q)|^2 \rangle = \int_0^1 F^2(Q, u)\, \mathrm{d}u$$

$$F(Q, u) = \frac{3(\sin QR - QR\cos QR)}{(QR)^3} \tag{3.2}$$

$$R = R_{\mathrm{e}} \left[1 + u^2 \left(\frac{R_{\mathrm{p}}^2}{R_{\mathrm{e}}^2} - 1 \right) \right]^{1/2}$$

The data were fit with an MCMC scheme, where the β_{n} of the solvent and GMO were fixed with their nominal values of 6.70×10^{-6} and 0.21×10^{-6} Å^{-2} respectively. These parameters

Table 3.1: Median and 95 % confidence interval values for the parameters used to the fit SANS data. The minimum effective number of independent samples for the GMO-dodecane and GMO-water-dodecane system are 992881 and 989528 respectively.

State	Background / $cm^{-1} \times 10^{-2}$	Scale Factor $\times 10^3$	R_e / Å	R_p / Å
Without H_2O	$9.23^{+0.00}_{-0.00}$	$3.76^{+0.01}_{-0.01}$	$26.10^{+0.03}_{-0.03}$	$13.72^{+0.04}_{-0.04}$
With H_2O	$8.96^{+0.01}_{-0.01}$	$4.54^{+0.01}_{-0.01}$	$27.41^{+0.03}_{-0.03}$	$15.54^{+0.04}_{-0.04}$

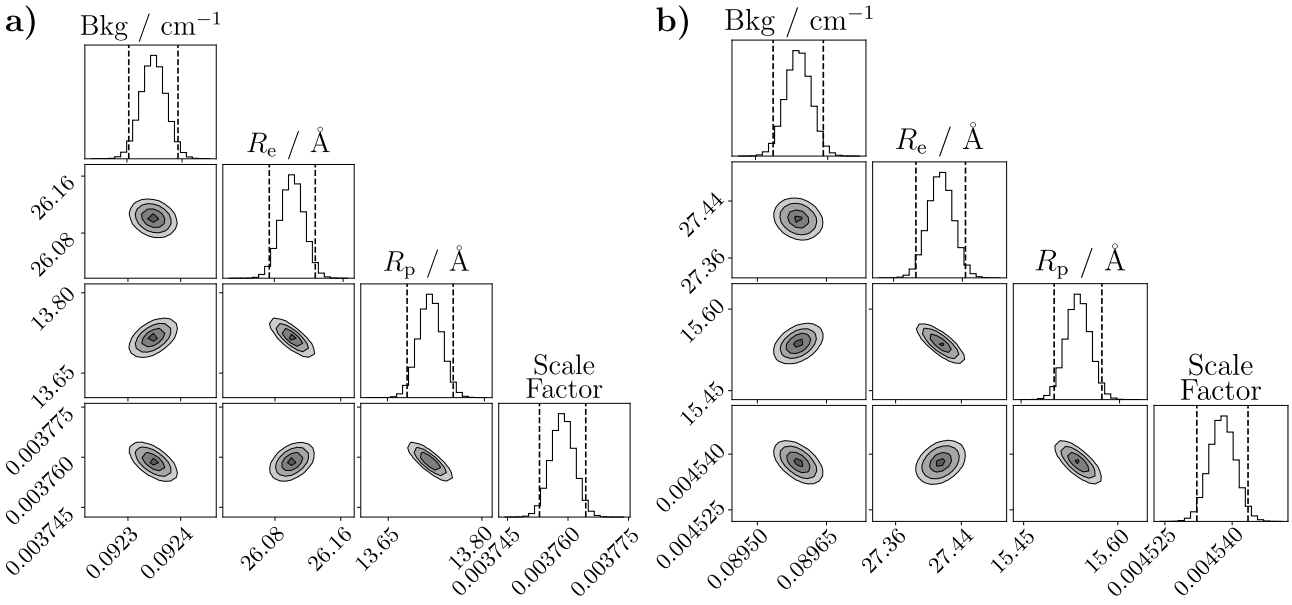

Figure 3.4: **a)** A corner plot of the parameter 1D and 2D histograms of the dry GMO system, showing the shape of the posterior distribution. **b)** The corner plot for the GMO/water system.

had to be fixed as the scale parameter was allowed to vary. Since the scale factor and contrast difference are perfectly correlated, inferring parameter distributions is not possible without assuming a fixed value for either one. It would be possible to fit the β_n of both GMO and the solvent if different contrasts of the system had been collected and fit simultaneously. The fits to the GMO and GMO/water systems are compared to the data in Figure 3.3b. The inferred parameter distributions are shown in Table 3.1 and the posterior distributions are shown through Figure 3.4.

The greater radii in the equatorial axes suggest the spheroids are oblate. Consistent with the Guinier analysis, the inferred radii of the spheroid are expanded in the presence of water. As such, the volume of the micelles, defined in Equation 3.3, are expanded when in the presence of water.

$$V_p = \frac{4}{3}\pi R_p R_e^2 \tag{3.3}$$

The calculated volume of the micelles in the GMO and GMO/water systems are $3.91^{+0.01}_{-0.01} \times 10^4$ and $4.89^{+0.01}_{-0.01} \times 10^4$ Å^3 respectively. It is expected that the water is contained within the micelle

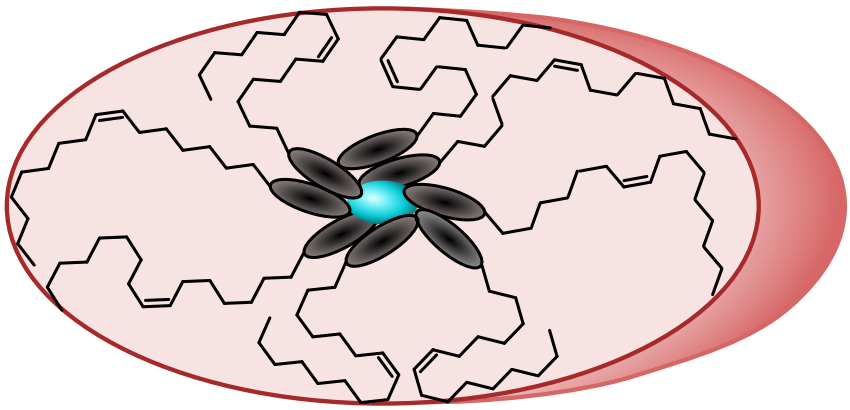

Figure 3.5: Depiction of the reverse micellar spheroids of the GMO and GMO/water systems. The schematic shows a cross section of the oblate spheroid. The blue ellipsoid at the centre depicts water contained within the micelle. The largest radius, R_e, is shared by the axis in the plane of page.

core, where it can hydrogen bond to the polar alcohol and carbonyl functional groups of GMO. As the number of water molecules increases with added water, the core of the micelle swells, increasing the volume of the micelle. It should be noted that the system without added water is expected to contain a trace amount of water as GMO and dodecane are reported to contain a small amount (< 1 %).[151] The equatorial radii are slightly greater than the extended length of a GMO molecule which is estimated to be 23.8 Å, while R_p is at least 8 Å smaller. This implies that alkyl chains aligned in the direction of polar axis have a greater number of gauche defects in comparison to those in the equatorial direction; this leads to a coiling effect of the alkyl chain. A schematic of the general shape of the GMO reverse micelles is shown in Figure 3.5.

Assuming the reverse micelle formed without added water is comprised solely of GMO and that the density of the micelle is that of bulk GMO, the aggregation number of the micelle can be estimated. As listed in Chapter 2, the number density of GMO is 0.0016 Å^{-3}, and hence the volume per molecule is $\sim$ 625 Å^3. Therefore, the average aggregation number is estimated to be 63. This value represents an approximate upper limit on the number of GMO molecules in an aggregate, and as discussed above, it is likely that water will account for some of this volume. Furthermore, the GMO density within an aggregate is likely to be lower than the bulk density due to solvent penetration into the micelles, increasing the volume per molecule, and hence, a lower aggregate number can be expected.

The upper limit is calculated to be at least double the aggregation number found by Bradley-Shaw *et al.* for 10 and 20 wt% GMO solutions in heptane via MD simulations.[150] The difference is even greater when compared to simulation results of 10 wt% GMO in squalene, where the calculated average aggregation number is 12 GMO molecules per reverse micelle.[153] These differences could arise from the difference in GMO concentration, as these simulations used concentrations $\gtrsim$ 10 times that used here ($\sim$ 0.85 wt%). However, the radius of gyration, which can be expected to scale with aggregation number, effectively remained constant for GMO in heptane over a concentration range of 1–10 wt%.[150] Therefore, it is expected that the

bulk concentration of GMO should not significantly alter the size nor the aggregation number of the aggregates. It is possible that the difference in solvent accounts for the discrepancy in the aggregation number, as the major axis of GMO micelles is reported to extend as the solvent molecular weight increases.[151] However, only a monotonic increase was reported, and thus, by extrapolation, it is not expected that squalene would have a lower aggregation number than dodecane. As the aggregates in the MD simulations did not include water, it is possible that this could account for the greater apparent aggregation number. Curiously, the addition of water to GMO in heptane ($W = 2$) via MD simulation was found to have no swelling effect on the micelle size.[163] On the other hand, SAXS studies suggest that only 0.3 wt% water can swell the major axis by up to 40 Å for a 5 wt% GMO/decane system.[151] This is inconsistent with the results presented here, where $\sim$ 0.2 wt% water only swelled the major axis by $\sim$ 1 Å.

3.3 Characterisation of reflectometry substrates

3.3.1 X-ray photoelectron spectroscopy

XPS was conducted on a fresh iron-coated silicon substrate in order to identify typical chemical species at the substrate's surface. The substrate was vacuum packed upon delivery, and was kept under vacuum in a desiccator. After collecting spectra of the fresh substrate, referred to as the native state, the substrate was cleaned with a UV/ozone cleaner (zoneSEM, Hitachi) for 20 minutes and the spectra were collected again. This was done to study how the chemical species at the interface altered after using the oxidative cleaning technique. The substrate surface was then completely wetted with dodecane-d_{26} and dried under a N_2 stream before being placed back into the spectrometer for analysis. These measurements were conducted to assess if the solvent used in the reflectometry studies influences the surface species. It is expected that the results shown here are typical of other iron-coated silicon substrates used throughout this work.

Survey spectra

The substrate was loaded into the spectrometer without a prior cleaning step. Initially, a low resolution survey spectra was collected with a BE range from -3 eV to $+1470$ eV, which is shown in Figure 3.6a. The presence of iron and oxygen are clear, where the latter is expected to be mostly in the form of iron oxides at the very outer region of the substrate. The C 1s peak also suggests the presence of carbon at the interface. Two additional survey spectra were collected at different locations across the substrate and are compared to the initial survey spectrum in Figure 3.6b. The survey spectra from three different spatial positions are alike, suggesting that the chemical species at the surface are similar across the substrate and are in approximately the same quantity over the different positions.

High resolution spectra were then collected for the C 1s, O 1s, Fe 2p and Fermi level regions at Position 1. These regions were also measured following UV/ozone cleaning of the substrate and after exposing the substrate to dodecane-d_{26}.

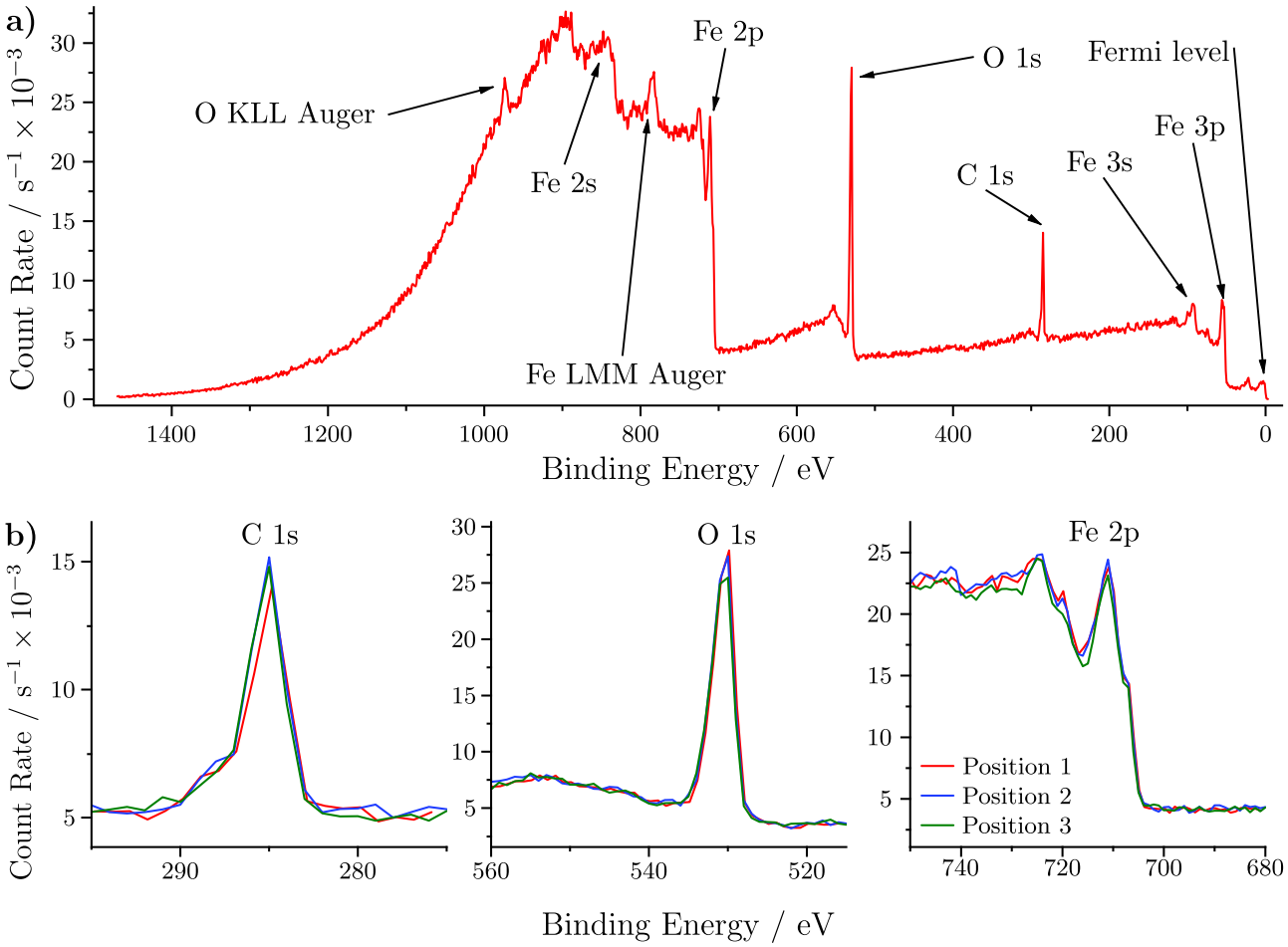

Figure 3.6: **a)** Survey spectrum of an iron-coated silicon substrate with the major peaks labelled with the appropriate transitions. **b)** Overlaid survey spectra of the C 1s, O 1s and Fe 2p regions for the three different substrate positions.

Carbon

A comparison of the C 1s spectra following these different treatments is shown in Figure 3.7a. The carbonaceous material is thought to be adsorbed at the interface following exposure to molecules present in the ambient atmosphere before and after vacuum packing. The presence of adventitious carbon on surfaces is a known phenomenon.[164] It is clear that UV/ozone treatment can reduce the amount of carbon at the interface, even when the substrate is exposed to the atmosphere before re-entering the spectrometer. The exposure of the substrate to dodecane-d_{26} appears to increase the amount of adsorbed carbonaceous material, although it is not clear from a qualitative interpretation if this is due to exposure to solvent or from further exposure to the atmosphere.

Through comparison with standards that contain particular functionalities, the different carbon species that comprise the C 1s peak can be quantified.[164] Following the constraints and peak shapes laid out by Biesinger *et al.*[138], the data from all three substrate states have been fit with a linear background as shown in Figure 3.7b. However, it was found that the four peak model laid out in the aforementioned work, with two separate peaks representing ketone and ester functionalities, could not fit the data and retain meaningful peak parameters. It was found

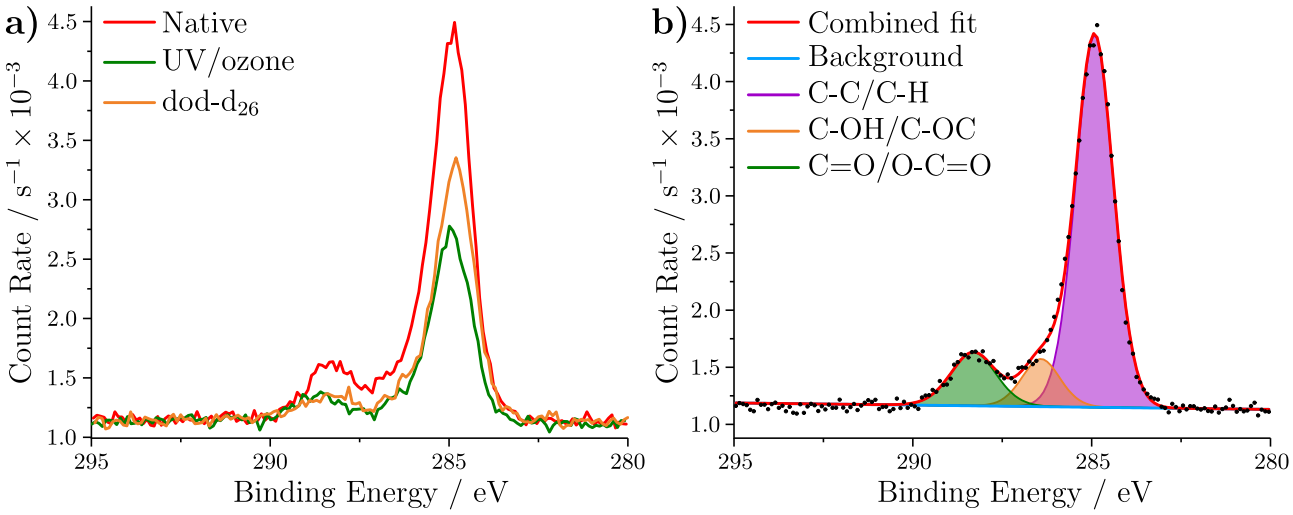

Figure 3.7: **a)** Overlaid XPS spectra of the C 1s region of the substrate in the native state, after a 20 minute UV/ozone clean, and after being exposed to dodecane-d_{26} and then dried. **b)** Fits to the C 1s region of the native substrate with a linear background.

Table 3.2: Median and 95 % confidence interval values for the peak parameters resulting from the MC fitting procedure to the C 1s data.

State	Species	*BE* / eV	Width (FWHM) / eV	Area / eV $s^{-1} \times 10^{-3}$	Relative Amount / %
Native	C-C/C-H	$284.9^{+0.0}_{-0.0}$	$1.2^{+0.0}_{-0.0}$	$4.4^{+0.1}_{-0.1}$	77^{+2}_{-2}
	C-OH/C-OC	$286.4^{+0.0}_{-0.0}$	$1.2^{+0.0}_{-0.0}$	$0.5^{+0.1}_{-0.1}$	10^{+1}_{-1}
	C=O/O-C=O	$288.3^{+0.1}_{-0.0}$	$1.5^{+0.2}_{-0.2}$	$0.7^{+0.1}_{-0.1}$	13^{+1}_{-2}
UV/ozone	C-C/C-H	$284.9^{+0.0}_{-0.0}$	$1.3^{+0.0}_{-0.0}$	$2.2^{+0.1}_{-0.1}$	77^{+4}_{-3}
	C-OH/C-OC	$286.4^{+0.0}_{-0.0}$	$1.3^{+0.0}_{-0.0}$	$0.3^{+0.1}_{-0.1}$	9^{+2}_{-2}
	C=O/O-C=O	$288.7^{+0.1}_{-0.1}$	$1.6^{+0.3}_{-0.4}$	$0.4^{+0.1}_{-0.1}$	14^{+3}_{-3}
dod-d_{26}	C-C/C-H	$284.8^{+0.0}_{-0.0}$	$1.3^{+0.0}_{-0.0}$	$2.9^{+0.1}_{-0.1}$	78^{+3}_{-3}
	C-OH/C-OC	$286.3^{+0.0}_{-0.0}$	$1.3^{+0.0}_{-0.0}$	$0.5^{+0.0}_{-0.1}$	9^{+1}_{-2}
	C=O/O-C=O	$288.4^{+0.1}_{-0.1}$	$2.0^{+1.1}_{-0.3}$	$0.5^{+0.3}_{-0.1}$	13^{+6}_{-3}

that a three peak model was more suitable and thus, the peak at $\sim$ 288 eV is expected to arise from a broad range of carbonyl species. The inferred parameter values from the fitting and MC error analysis are shown in Table 3.2. The total area of the carbon peak was found to be $5.7^{+0.2}_{-0.2} \times 10^3$ eV s^{-1} for the native state, $2.9^{+0.3}_{-0.2} \times 10^3$ eV s^{-1} for the UV/ozone cleaned state, and $3.8^{+0.3}_{-0.2} \times 10^3$ eV s^{-1} after exposure to dodecane-d_{26}, and thus that the amount of adventitious carbon can be approximately halved through UV/ozone treatment. It is noted that the relative amounts of the different carbon species remain unaltered after cleaning and after exposure to dodecane-d_{26}. It is expected that aliphatic species that solely contain C-C/C-H functionalities do not remain at the interface when under vacuum in significant quantity; this is reasoned as these molecules can only weakly adsorb at the interface through induction

and dispersion forces, and typically have low boiling points by definition of being present in the ambient atmosphere. However, it is clear that aliphatic carbon is present at the interface and thus, it is suggested that the C-C/C-H functionalities are present at the interface through oxygen containing functionalities that are more strongly adsorbed at the interface via dipolar, induction and dispersion forces. This could explain why UV/ozone removes carbon of the different environments homogeneously.

The increase in the amount of carbonaceous material at the interface after exposure to dodecane-d_{26} could suggest material within the solvent has adsorbed at the interface. However, the substrate was also exposed to the atmosphere while wetting the substrate, and it is possible that adsorption at the interface occurred from atmospheric carbonaceous species. Therefore, it is not possible to conclude from which source the additional carbon species arose, but it is suggested that it is more likely for the relative amounts to stay equivalent if adsorption from the atmosphere had taken place.

Oxygen

The high resolution O 1s spectra are shown in Figure 3.8a for the three different treatments. It is expected that ferrous, Fe(II), and ferric, Fe(III), iron oxide species will have grown on the surface from oxidation processes when exposed to the atmosphere. The O 1s resonances from these species are reported to arise at binding energies of approximately 530 eV, and hence the largest peak in all three spectra at 530 eV is assigned to lattice O^{2-} within the iron oxide species.[138,165,166] However, the signal at greater binding energies arises from a more ambiguous source. It is possible that the outer oxide layer becomes hydrated in the atmosphere and in turn forms iron hydroxide species, as previously suggested for iron oxide and other oxide species.[167,168] The O 1s resonance arising from OH^- species have been reported to have a BE in the region of 531.5 eV[165,166]. Further to hydroxide species, the presence of oxygen-containing carbonaceous material at the interface is strongly implied by the C 1s spectra. Through the study of known standards that contain oxygen containing functionalities, peaks arising from oxygen within carbonaceous material are expected to have a BE of 532.2 eV and above.[169] In addition, water has also been assigned to BEs of approximately 532 eV.[138] Consequently, it is expected that multiple species will give rise to the binding energies above those of the iron oxide species.

The increase in signal strength of the iron oxide lattice peak following UV/ozone treatment is thought to arise from the removal of adventitious carbon at the interface. This is rationalised as less photoelectrons will lose energy before reaching the detector when lower amounts of adventitious material are adsorbed at the interface. The loss of signal at BEs around 532 eV could be linked to the loss of carbonaceous material comprised of oxygen containing functionalities or to any other oxygenated species that can be removed via UV/ozone cleaning.

The data from all three states have been modelled using a Shirley background, and the fit to the data collected in the native state is shown in Figure 3.8b. A model with three peaks was used to

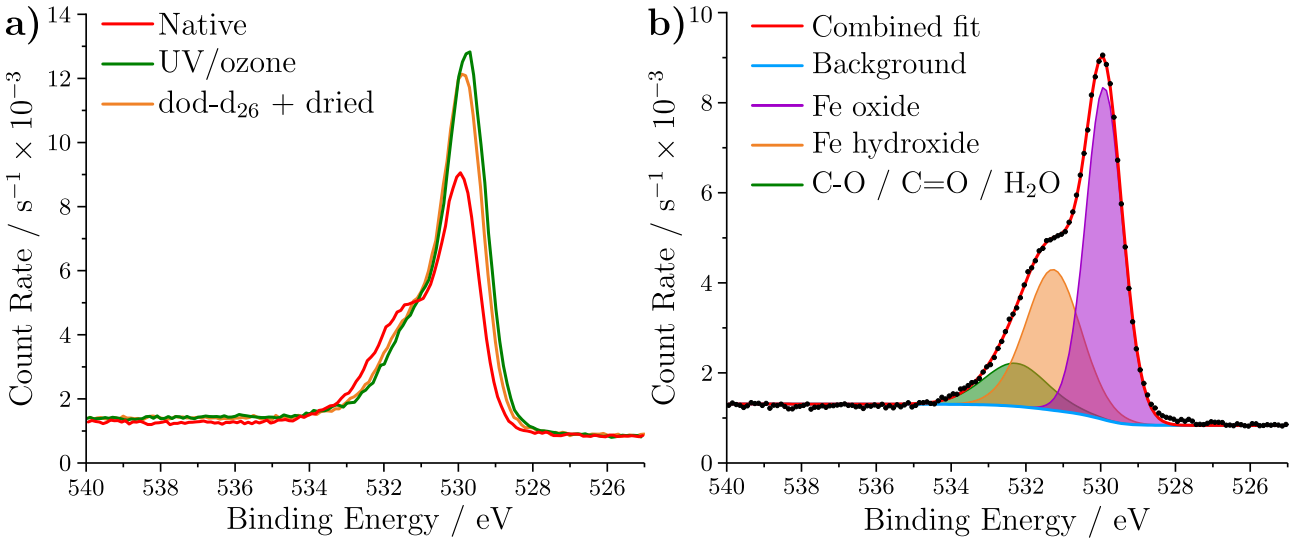

Figure 3.8: **a)** Overlaid XPS spectra of O 1s region of the substrate in the native state, after a 20 minute UV/ozone clean, and after being exposed to dodecane-d_{26} and then dried. **b)** Fits to the O 1s region of the native substrate using a Shirley background.

account for the different species present at the interface as two peaks led to a poor fit, and four peaks led to insignificant peak areas. The inferred parameter values from the fitting and MC error analysis are shown in Table 3.3. There is a clear increase in the relative amount of the iron oxide species following UV/ozone treatment. As mentioned previously, it is expected that this increase arises most significantly from the loss of carbonaceous material at the interface, and not the chemical transformation of one species into iron oxide. However, the confidence intervals overlap for the peaks attributed to the iron hydroxide and carbonaceous oxygen species between the different states and as such, it is not immediately clear which species has decreased upon cleaning. It is evident from the C 1s analysis that oxygen containing carbonaceous material is removed from the interface from UV/ozone treatment. However, it is also possible that iron hydroxides are chemically altered by UV/ozone, especially if Fe(II) hydroxides are present which could be oxidised by the ozone. Consequently, it is suggested that the loss of oxygen-containing carbonaceous species is a significant factor in the reduction of signal intensity at $BE \sim 532$ eV. However, it is not known if this change arises solely from the loss of these species, or if it also arises from the loss of iron hydroxides and/or adsorbed water.

There is also a small shift in the binding energy of the overall peak envelope between the states, which is most apparent when comparing the lower binding energy side of the peaks and the peak maxima. Shifts in binding energy are often attributed to surface charging, where charge build up leads to shifts towards higher BE. The reason for these shifts is not clear as surface charging may be expected to affect the other spectra, but the C 1s and Fe 2p spectra appear to align relatively well between the different states. As the fits were allowed to vary in BE and width, the peak area and relative amounts are not affected by the shift. However, the precise BE of all three peaks should be viewed as tentative.

Table 3.3: Median and 95 % confidence interval values for the peak parameters resulting from the MC fitting procedure to the O 1s data. CO is used to represent carbonaceous material containing oxygen.

State	Species	BE / eV	Width (FWHM) / eV	Area / eV $s^{-1} \times 10^{-3}$	Relative Amount / %
Native	FeO_x	$529.9^{+0.0}_{-0.0}$	$1.2^{+0.0}_{-0.0}$	$9.4^{+0.5}_{-0.6}$	55^{+3}_{-3}
	FeO_xH_y	$531.3^{+0.1}_{-0.1}$	$1.7^{+0.3}_{-0.2}$	$5.9^{+1.9}_{-1.2}$	34^{+11}_{-8}
	CO/H_2O	$532.3^{+0.6}_{-0.1}$	$1.9^{+0.1}_{-0.5}$	$2.0^{+0.8}_{-1.6}$	12^{+5}_{-9}
UV/ozone	FeO_x	$529.7^{+0.0}_{-0.0}$	$1.2^{+0.0}_{-0.0}$	$14.7^{+0.5}_{-0.9}$	69^{+3}_{-4}
	FeO_xH_y	$531.1^{+0.0}_{-0.0}$	$1.7^{+0.2}_{-0.2}$	$6.0^{+1.0}_{-0.7}$	28^{+5}_{-3}
	CO/H_2O	$533.0^{+0.3}_{-0.5}$	$2.0^{+0.0}_{-0.7}$	$0.7^{+0.4}_{-0.4}$	3^{+2}_{-2}
dod-d_{26}	FeO_x	$529.8^{+0.0}_{-0.0}$	$1.2^{+0.0}_{-0.0}$	$12.8^{+1.0}_{-0.5}$	63^{+5}_{-2}
	FeO_xH_y	$531.1^{+0.1}_{-0.1}$	$2.0^{+0.0}_{-0.3}$	$7.2^{+0.3}_{-1.6}$	35^{+1}_{-8}
	CO/H_2O	$533.0^{+0.5}_{-0.8}$	$2.0^{+0.0}_{-1.0}$	$0.3^{+0.6}_{-0.2}$	2^{+3}_{-1}

Iron

The Fe 2p spectra collected in the three different states are shown in Figure 3.9a. The four distinct peaks labelled by 1–4 are attributed to Fe(0) $2p_{3/2}$, Fe(II)/Fe(III) $2p_{3/2}$, Fe(0) $2p_{1/2}$ and Fe(II)/Fe(III) $2p_{1/2}$ respectively. Known standards of Fe(III) and Fe(II) oxides have been reported to have chemical shifts in the $2p_{3/2}$ region of 711 and 710 eV respectively.[166,170,171] The partial removal of adventitious carbon has increased the signal strength for the iron oxide states that are held deeper within the sample than the adventitious material, as seen with the O 1s spectra. However, the metallic Fe(0) $2p_{3/2}$ peak appears to retain the same signal strength before and after UV/ozone cleaning, while the Fe(0) $2p_{1/2}$ peak intensity increases. The approximate constant signal strength of the former peak suggests that some metallic iron is oxidised to either Fe(II) or Fe(III) states with UV/ozone treatment. The Fe(0) $2p_{1/2}$ peak is also expected to remain at a similar intensity, but the peak is expected to overlap with Fe(III) satellite peaks that are reported to have an apparent binding energy of 719 eV.[170,171] Therefore, the apparent increase in signal strength of the Fe(0) $2p_{1/2}$ species is suggested to arise through an increase in the satellite intensity upon cleaning.

The data were only fit in the Fe $2p_{3/2}$ region as the Shirley background did not behave homogeneously between the Native and UV/ozone states as shown in Figure 3.9b. The reason for this is not known, but it is reported that Shirley backgrounds are best applied to small regions of interest.[172] If the data were fit with respect to the range 700–740 eV, the change to the peak area of the different iron species upon cleaning would have a large amount of error due to the difference in background. The fit to the data collected in the native state is shown in Figure 3.9c, where the metallic iron peak, Fe(0) $2p_{3/2}$, has been modelled using an asymmetric line shape as described elsewhere.[138] In order to separate the two oxidation states,

Table 3.4: Median and 95 % confidence interval values for the peak parameters resulting from the MC fitting procedure to the Fe $2p_{3/2}$ data.

State	Species	BE / eV	Width (FWHM) / eV	Area / eV $s^{-1} \times 10^{-3}$	Relative Amount / %
Native	Fe(0) $2p_{3/2}$	$706.6^{+0.0}_{-0.0}$	$1.0^{+0.0}_{-0.0}$	$5.3^{+0.2}_{-0.2}$	31^{+2}_{-2}
	Fe(II) $2p_{3/2}$	$710.1^{+0.1}_{-0.1}$	$2.5^{+0.5}_{-0.2}$	$3.4^{+4.5}_{-0.5}$	20^{+27}_{-3}
	Fe(III) $2p_{3/2}$	$711.0^{+1.1}_{-0.0}$	$4.1^{+0.3}_{-0.4}$	$8.4^{+0.6}_{-3.7}$	49^{+3}_{-22}
UV/ozone	Fe(0) $2p_{3/2}$	$706.7^{+0.0}_{-0.0}$	$1.0^{+0.0}_{-0.0}$	$5.2^{+0.2}_{-0.3}$	24^{+1}_{-1}
	Fe(II) $2p_{3/2}$	$710.2^{+0.0}_{-0.0}$	$1.8^{+0.2}_{-0.1}$	$4.1^{+0.9}_{-0.8}$	19^{+4}_{-3}
	Fe(III) $2p_{3/2}$	$711.3^{+0.1}_{-0.1}$	$3.7^{+0.1}_{-0.1}$	$12.5^{+0.9}_{-0.8}$	58^{+4}_{-4}
dod-d_{26}	Fe(0) $2p_{3/2}$	$706.5^{+0.0}_{-0.0}$	$1.0^{+0.1}_{-0.0}$	$4.8^{+0.3}_{-0.3}$	23^{+1}_{-2}
	Fe(II) $2p_{3/2}$	$710.1^{+0.0}_{-0.0}$	$1.6^{+0.2}_{-0.2}$	$3.0^{+1.0}_{-0.6}$	15^{+4}_{-2}
	Fe(III) $2p_{3/2}$	$711.0^{+0.1}_{-0.1}$	$3.7^{+0.2}_{-0.1}$	$13.1^{+0.8}_{-0.9}$	63^{+4}_{-5}

it was necessary to introduce a constraint on the BE of the Fe(III) species, where the fitted BE could not assume values below 711.0 eV. The resulting parameter distributions from the MC analysis are shown in Table 3.4. The widths of the Fe(III) species are quite broad, which is expected to arise from the multiplet splitting that is represented by a single peaks in this case. The 1D histograms in Figure 3.9d show where the bulk of the posterior distribution lies for the peak areas of both the Fe(II) $2p_{3/2}$ and Fe(III) $2p_{3/2}$ peaks in the XPS spectrum of the native substrate. The 2D histogram of both areas show a strong anti-correlation between the parameters, which suggests that the two peaks are not particularly well-defined. As such, the correlation is likely to be a factor in the uncertainty for both peak areas. There is a clear decrease in the relative amount of Fe(0) at the interface after UV/ozone treatment. This is aligned with a slight increase in the relative amount of Fe(III). Any change to the amount of Fe(II) species is not determined from the fit but it is expected that any Fe(II) present could be oxidised to Fe(III) species, and that Fe(0) could be oxidised to Fe(II) or Fe(III) species. Therefore, it is perhaps not surprising to see an approximately stable amount of Fe(II).

3.3.2 X-ray reflectometry

An iron-coated Si substrate was characterised in air by XRR using the PANalytical X'Pert in order to assess the layered structure of the sample and to assess the homogeneity across the substrate's surface. The substrate was loaded into the analysis chamber and following an alignment procedure at the centre of the substrate, a specular θ scan was collected over a range of 0.133–8.006°, resulting in a Q range of 0.022–1.135 $Å^{-1}$. The scan was conducted with a θ step size of 0.016°, and at each angle the reflected intensity was measured for 80 seconds. The normalised data are shown in Figure 3.10a alongside two fits to the data. These were conducted using two different multilayer slab models that included a SiO_2 layer, an Fe layer and either

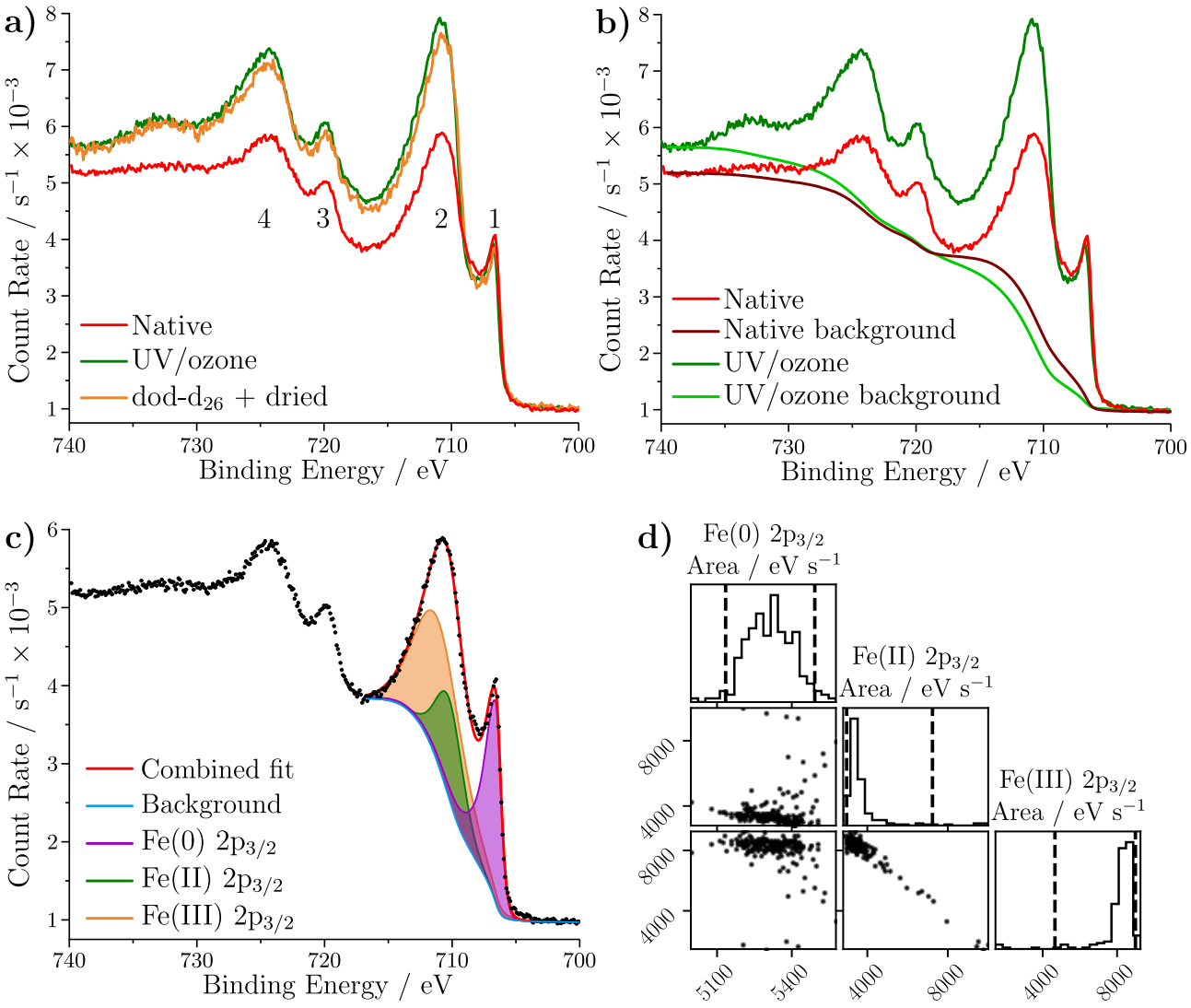

Figure 3.9: **a)** Overlaid XPS spectra of Fe 2p region of the substrate in the native state, after a 20 minute UV/ozone clean, and after being exposed to dodecane-d_{26} and then dried. **b)** Shirley backgrounds for the full Fe 2p region (700–740 eV) for the native and UV/ozone states. **c)** Fits to the Fe $2p_{3/2}$ region of the native substrate. **d)** A corner plot of the areas of the three modelled peaks in the Fe $2p_{3/2}$ region.

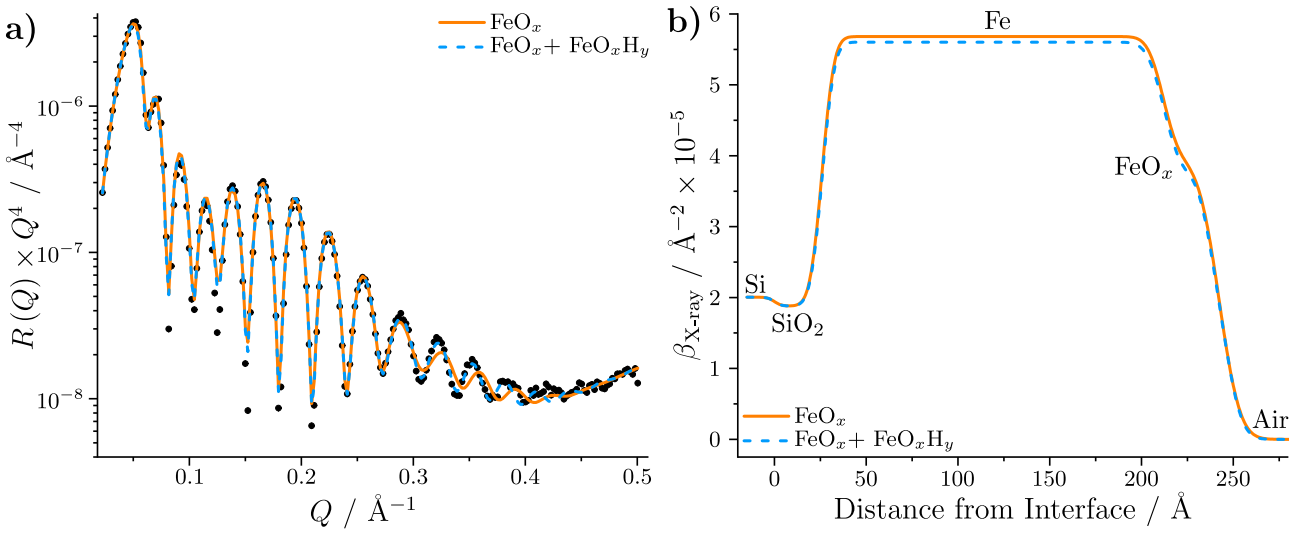

Figure 3.10: **a)** XRR profile measured from the centre of an iron-coated silicon substrate. The reflectivity is modified by a factor of Q^4 to aid comparison. The two fits shown are the median profiles from the parameter distributions. The error bars are approximately the same size as the data points. **b)** The median $\beta_{\text{X-ray}}$ profile following the modelling procedure.

a singular iron oxide layer or an iron oxide layer and an iron hydroxide layer on the outer surface of the substrate. These layers were modelled between infinite air and Si regions, as the length scales of both are too large to be resolved by reflectometry. It should be noted that the roughness of the Si substrate was not allowed to vary during the fit as meaningful inference could not be made from the fit. A nominal Si roughness value of 3 Å was held constant as the substrates were purchased with a roughness of 3 Å before sputter coating. Similarly the SiO_2 $\beta_{\text{X-ray}}$ was held constant with a value that relates to an amorphous SiO_2 layer. The fits to the data are constructed with the median parameter values from the bootstrap uncertainty estimation routine, which are shown in Table 3.5.

While the fit conducted with the iron hydroxide layer describes the data more appropriately at $Q = 0.3$–0.4 Å^{-1}, there are more parameters to model the data because of the additional layer. Therefore, the models must be assessed on the ability to fit the data and the inferred parameter values, where, if some parameter values seem non-physical, the model should be treated with more caution. The inferred distribution of the iron hydroxide thickness is within error of the iron hydroxide roughness and generally, when a layer's roughness is greater than half the layer's thickness, this translates to a poorly defined layer. As such, the iron hydroxide layer is not visible in the resulting $\beta_{\text{X-ray}}$ profile as shown in Figure 3.10b. This is unsurprising as, while it is possible iron hydroxide is present at the very edge of the interface, it is likely to only be a few Å thick and thus, not likely to appear as a slab-like layer. In effect, the iron hydroxide layer can be viewed as providing a different roughness between the iron oxide and air layers. Therefore, despite the better fit for the model with the iron hydroxide, the iron oxide model appears the most consistent without over-fitting the data.

The fit suggests that the density of the iron layer is $7.6^{+0.1}_{-0.3}$ g cm^{-3}, which is lower than the bulk density at 7.9 g cm^{-3}. This is possibly because the iron film is very thin, and as such does

Table 3.5: Median and 95 % confidence interval values for the layer parameters following the bootstrap fitting routine to the XRR data of an iron-coated silicon substrate collected in air. Those parameters without sub- and superscripts were held constant.

Model	Layer	$\beta_{\text{X-ray}}$ / $\text{Å}^{-2} \times 10^{-6}$	Thickness / Å	Roughness / Å
FeO_x	Si	20.1	∞	3
	SiO_2	18.8	$26.0^{+1.2}_{-1.9}$	$5.2^{+0.1}_{-0.2}$
	Fe	$57.0^{+1.1}_{-2.5}$	185^{+0}_{-1}	$6.7^{+0.5}_{-0.5}$
	FeO_x	$39.5^{+2.2}_{-2.4}$	$30.4^{+0.6}_{-0.5}$	$8.9^{+0.3}_{-0.4}$
FeO_x+ FeO_xH_y	Si	20.1	∞	3
	SiO_2	18.8	$26.1^{+1.4}_{-1.2}$	$5.2^{+0.1}_{-0.1}$
	Fe	$56.2^{+1.6}_{-1.8}$	186^{+0}_{-1}	$6.7^{+0.5}_{-0.5}$
	FeO_x	$37.3^{+3.1}_{-2.2}$	$22.7^{+5.6}_{-0.2}$	$4.9^{+9.3}_{-0.8}$
	FeO_xH_y	$28.8^{+13.9}_{-2.9}$	$10.1^{+0.4}_{-7.8}$	$7.5^{+1.7}_{-0.5}$

not portray the same characteristics as bulk iron. The $\beta_{\text{X-ray}}$ of iron oxide is similar to that of the most common iron oxides: α-Fe_2O_3, γ-Fe_2O_3 and Fe_3O_4 which have $\beta_{\text{X-ray}} = 41.3$, 38.2 and 40.5 $\text{Å}^{-2} \times 10^{-6}$ respectively at $\lambda = 1.54$ Å. As such, the XRR data do not reveal which particular iron oxide species are present.

The substrate was then aligned at three different positions that were spaced 5 mm apart across the substrate surface, and the specular reflectivity profiles were collected using a θ scan of 0.133–3.163°, resulting in a Q range of 0.022–0.450 Å^{-1}. The three reflectivity profiles are shown in Figure 3.11a, where the Kiessig fringes appear to have approximately the same spacing, suggesting that the thickness of the iron and iron oxide layer is consistent across the substrate. However, some variation in the amplitude in the fringes is noted; a difference in amplitude is not trivially assignable when a sample contains multiple layers but is usually related to differences in $\beta_{\text{X-ray}}$ contrast between the probed areas on the surface. Therefore, the data were modelled in an attempt to quantify the difference between the profiles, and the best fits are shown in the lower part of Figure 3.11a. The resulting $\beta_{\text{X-ray}}$ profiles from the three fits are shown in Figure 3.11b, which shows variation in the $\beta_{\text{X-ray}}$ for iron and iron oxide. This arises due to a difference in density across the interface, and small differences in the thicknesses and roughnesses. The substrate appears to be consistent over the footprint's measured here and thus are thought to be suitable for NR.

3.3.3 Neutron reflectometry

Due to the restricted access to ISIS during the CoVID-19 pandemic, some of the experiments presented below were conducted by Dr Fin Allen and Dr Becky Welbourn, ISIS, UK. In these cases, the experiments were planned and remotely led by the author. The sections that con-

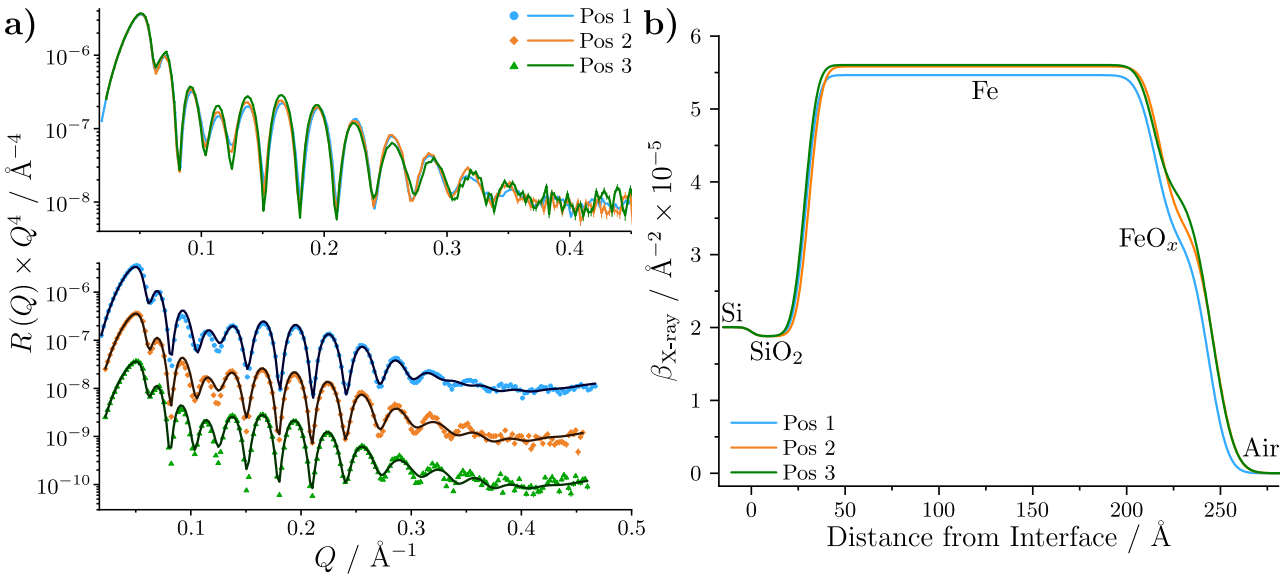

Figure 3.11: **a)** The modified X-ray reflectivity measured at three different positions across the substrate surface, spaced 5 mm apart, are compared in the upper plot. The data are plotted with linear interpolation lines to guide the eye. The panel below shows the best fits to the three datasets, where two datasets are successively offset by 10^{-1} in the modified reflectivity axis. **b)** The $\beta_{\text{X-ray}}$ profiles from the best fits to the data collected at the three different positions.

tain work collected in collaboration are highlighted. All following analysis has been conducted individually.

Iron-coated silicon substrates were characterised in solid-liquid cells by NR on INTER using two solvent contrasts of neat dodecane-d_{26} and neat dodecane-h_{26} before any surfactant was exposed to the interface. A schematic of the principal of NR with solid-liquid cells is shown in Figure 3.12a, where the incident neutron beam is brought in through the bulk silicon of the substrate at an angle of θ_i. An image of a complete solid-liquid cell on the INTER sample environment is shown in Figure 3.12b, and is representative of the solid-liquid cells used within this work. These datasets were collected to verify the suitability of the substrate and the cleanliness of the interface before conducting any experiments. Additionally, they serve as a blank comparison for qualitative interpretation of data collected with GMO. An example dataset collected at 25 °C is shown in Figure 3.13a. Both contrasts were measured at three angles of 0.7°, 1.2° and 2.3°, which were then stitched together to form a composite dataset for each contrast. The λ distribution was $\sim$ 2–17 Å, resulting in a Q range of 0.009–0.335 Å^{-1}. The dQ/Q resolution had a standard deviation of 2 %. This dataset was collected by Fin and Becky with the same substrate as the XRR dataset in subsection 3.3.2, although it should be noted that nine months had passed between the XRR and NR measurements. It is not expected that the substrate will have altered drastically in this time as it was kept under vacuum in a desiccator, and appeared to be in the same condition (not severely corroded). Before the measurements, the substrate was placed in a UV/ozone cleaner for 20 minutes in an effort to remove pre-adsorbed atmospheric contaminants.

The critical edge in the contrast collected with dodecane-d_{26} is located at $\sim$ 0.0143 Å^{-1}, relating

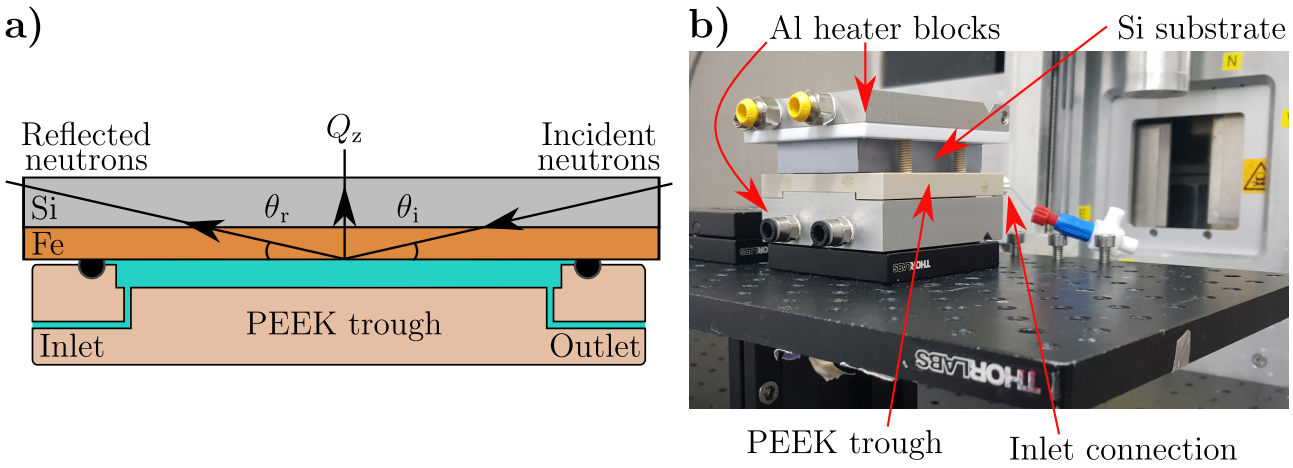

Figure 3.12: **a)** Schematic depicting the principal of NR with an iron-coated silicon substrate in a solid-liquid cell. A liquid sample can be flowed into the reservoir that sits between the substrate and the PEEK trough. The reservoir is sealed through use of an O-ring. **b)** A complete solid-liquid cell on the sample environment table on the INTER reflectometer at ISIS. The aluminium heater blocks can be connected to a water bath for temperature control.

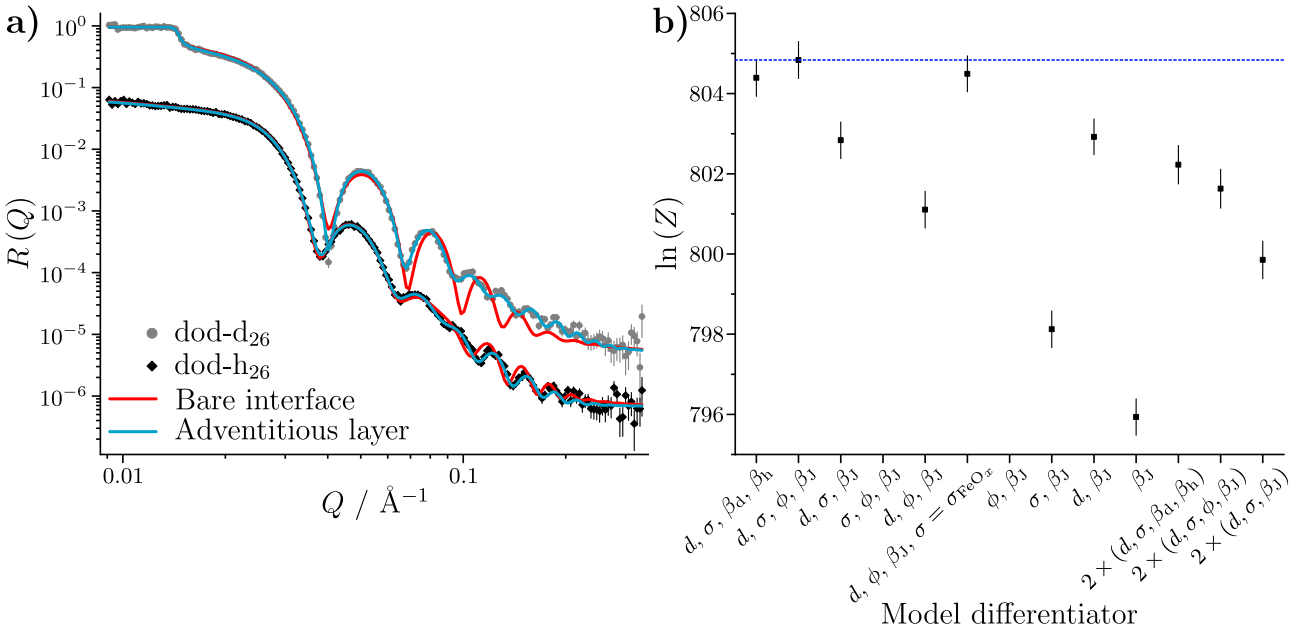

Figure 3.13: **a)** Neutron reflectivity from an iron-coated silicon substrate against dodecane-d$_{26}$ and dodecane-h$_{26}$. The dodecane-h$_{26}$ contrast is offset by a factor of 10^{-1} in the $R(Q)$ axis for clarity. The two solid lines are the simulated reflectivity for two models described in the main text. **b)** The nested sampling results for 11 different models, where the blue dotted line shows the highest evidence. The model that is described with $\sigma = \sigma_{\mathrm{FeO}_x}$ had the roughness of the adventitious layer constrained to that of the iron oxide layer. The three models at the very right of the figure have two adventitious layers.

to an approximate solvent deuteration of 92 %. This is 6 % lower than the quoted deuteration of dodecane-d_{26} from the supplier. As the dodecane-h_{26} contrast was collected first, it is believed some residual dodecane-h_{26} remained within the liquid trough when exchanging for dodecane-d_{26}, reducing the Q value for the critical edge.

The data were initially modelled in GenX using a multilayer slab model that was based on the model used to fit the XRR data in subsection 3.3.2. A global fit to both contrasts was then conducted and the best fit achieved with this model is shown as the red simulated reflectivity profile in Figure 3.13a. This model is referred to as the bare interface model. The fit does not suitably match the dodecane-d_{26} contrast but fairly represents the data collected with dodecane-h_{26}. The poor fit suggests that a component, such as an additional layer, is missing in the model and the difference in contrast suggests that the component has a low β_{n}. To test this hypothesis, an initial fit with an additional layer between the iron oxide and dodecane layers was run, resulting in a markedly improved fit quality. This fit is shown as the blue simulated reflectivity profile and is referred to as the adventitious layer model. The fitted β_{n} and thickness of the additional layer was best fit with values of -0.1×10^{-6} Å^{-2} and 11 Å. These values suggest a very thin layer that is either comprised of low density material or material of low scattering length. As the substrate is exposed to the atmosphere, this interfacial layer is likely to be only comprised of simple organic elements such as C, H, N and O. This is further supported by the absence of other elements in the XPS and XRR studies.

Other NR and XRR studies have reported comparable films at interfaces with high and low interfacial energies, which are suggested to arise from solvent depletion and/or gas present at the interface.[173–176] Impurities within solvents and solutes are also suggested to be able to form similar layers at solid-liquid interfaces.[177,178] Possible contaminants at the iron oxide-dodecane interface are suggested to be gaseous molecules introduced from the atmosphere prior to sealing the substrate in the solid-liquid cell or polar contaminants which are native within the solvent, such as dissolved water.

As the nature of the adventitious layer is not known, nested sampling was conducted in order to find the most suitable model to fit the data. The models tested in the nested sampling study were constrained further than the initial fits above; the β_{m} of the iron layer was fitted as a function of the iron magnetic moment, μ, and β_{n}, as shown in Equation 3.4.

$$\beta_{\mathrm{m}} = \mu \times \frac{\beta_{\mathrm{n}}}{b} \times C \tag{3.4}$$

Here, μ has units of Bohr magneton, μ_{B}, b is the bound coherent scattering length of iron, 9.45×10^{-5} Å, and C is a constant of 2.699×10^{-5} Å μ_{B}^{-1}. This method constrains the β_{m} so that it cannot assume non-physical values with respect to the magnetic moment and the density of iron. This method was not used for fitting the β_{m} of the iron oxide layer as the precise stoichiometric formula for this layer is not known.

For some models the adventitious layer was also constrained with a solvation parameter, where

the layer is assumed to contain a volume of dodecane, quantified by a volume fraction, ϕ, while the remaining volume is occupied by another material that comprises the adventitious layer. In general, this results in a solvated layer with a modified scattering length density, $\beta_{\mathrm{n}}^{\mathrm{solv}}$, which can be described by a linear combination of the β_{n} for the solvent and the material at the interface weighted by ϕ:

$$\beta_{\mathrm{n}}^{\mathrm{solv}} = \phi \times \beta_{\mathrm{n}}^{\mathrm{dod}} + (1 - \phi) \times \beta_{\mathrm{n}}^{\mathrm{ads}} \,. \tag{3.5}$$

Here, $\beta_{\mathrm{n}}^{\mathrm{dod}}$ and $\beta_{\mathrm{n}}^{\mathrm{ads}}$ are the scattering length densities of the dodecane and adsorbate layer respectively. For the nested sampling, the scattering length density of the adventitious layer is written as β_{J}, defining the joint adventitious layer scattering length density for both solvent contrasts. This constraint allows the separation of the adventitious scattering length density from any solvent that has penetrated into the layer, assuming that the different solvents penetrate the solvated layer to the same extent. If a model was not constructed with a solvation parameter, then two separate scattering length densities were assigned to the adventitious material that represent the scattering length density in dodecane-d_{26}, β_{d}, and in dodecane-h_{26}, β_{h}.

A full description of the initial parameter values and priors are given in Table A2. The nested sampling results for 11 different models are shown in Figure 3.13b. These models do not represent the only models that could be used to fit the data, as this number is very large, if not infinite, but do represent a reasonable limited search for a suitable model. Care was taken to ensure consistent parameter priors between the models, as this can affect the determined evidence. As a comparison, the bare interface model was found to have a $\ln(Z) = -177.0 \pm 0.5$.

The evidence for three models where two adventitious layers are simulated at the interface were investigated. The models had the same parameters for both adventitious layers. These models were found to have lower evidences than the singular adventitious layer counterparts with the same parameters. It is possible that some combination of parameters may have a greater evidence than the model found to have the greatest evidence. However, due to the large number of parameter combinations when investigating models with two interfacial layers, the time required to run the nested sampling of each model increases significantly; hence, testing the whole set of possible parameter combinations is not feasible.

The model with the greatest evidence was then used to infer the posterior distribution using an MCMC scheme. The median fits and resulting β_{++} profiles for both contrasts following the MCMC sampling are shown in Figure 3.14 and the fitted parameter distributions are shown in Table 3.6. There is a clear decrease in β_{n} across the iron oxide-dodecane-d_{26} interface, where the posterior distribution conveys a high degree of certainty to the presence of a layer with a total $\beta_{\mathrm{n}} \leq 2$ after accounting for the modelled solvation. Contrastingly, the small, almost non-existent difference in β_{n} of the adventitious layer and the dodecane-h_{26} suggest that the adventitious layer cannot be probed using hydrogenated solvent. This accounts for the

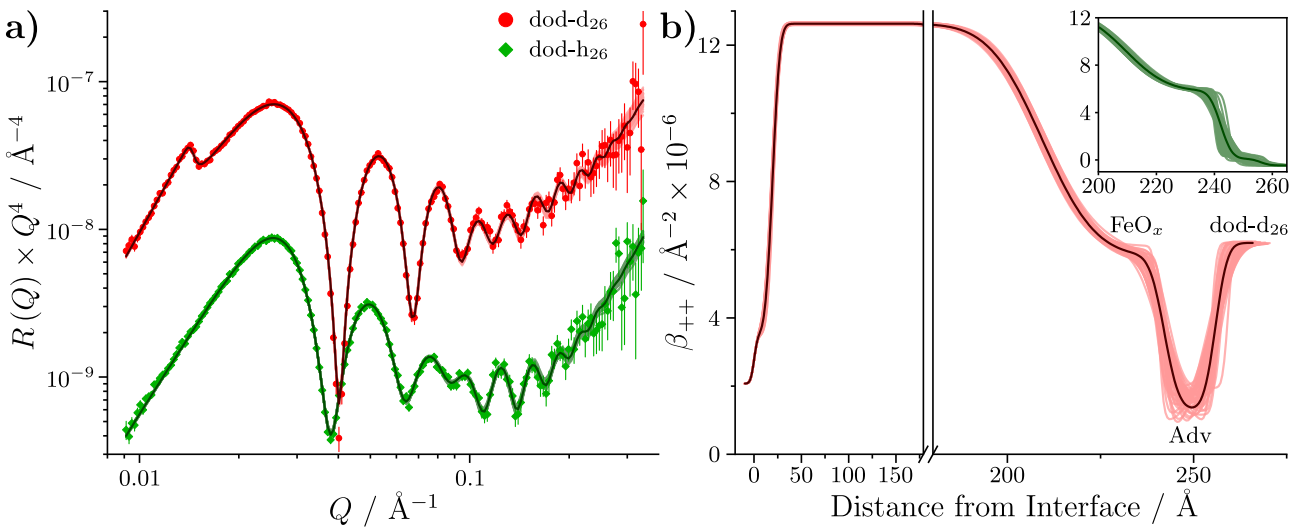

Figure 3.14: **a)** Reflectivity collected with dodecane-d_{26} and dodecane-h_{26} against an iron-coated silicon substrate. The dark lines are the median profiles, and the shaded bands are comprised of 50 random samples from the posterior distribution. The reflectivity is modified by a factor of Q^4 for comparison and the dodecane-h_{26} contrast is offset by 10^{-1} in the modified reflectivity axis. **b)** The median β_{++} profile for the dodecane-d_{26} contrast. The shaded band shows 50 random samples from the posterior distribution. Here, Adv represents the adventitious layer. The inset shows the median β_{++} profile for the dodecane-h_{26} contrast.

observing only a minor variation between the 'bare interface' and 'adventitious layer' models in Figure 3.13a. If the adventitious layer is composed of adsorbed gaseous species or water as discussed above, the inferred thickness distribution suggests a multilayer structure as these molecules span $\lesssim$ 3 Å along their longest axis. An example structure that would fit this description are island-like assemblies of adsorbed material across the interface, with solvent occupying regions between the adsorbate, accounting for the inferred distribution of solvation. However, the thickness distribution could also be consistent with the adsorption of shorter-chain molecules that have polar functionalities, facilitating the adsorption at the iron oxide-dodecane interface. As the dodecane was used as-received, it is possible that impurities that are distilled out with dodecane in the industrial production process remain dissolved in the solvent.

The inferred β_m of the iron oxide suggests that the film contains only a small proportion of magnetic iron oxides such as magnetite or maghemite. The fitted β_n for the iron oxide layer is lower than the nominal β_n for hematite, magnetite and maghemite at 7.20×10^{-6} Å^{-2}, 6.95×10^{-6} Å^{-2} and 6.67×10^{-6} Å^{-2} respectively. The lower β_n could suggest the presence of iron hydroxides which typically have lower atomic densities, and hence lower scattering length densities, than the iron oxides mentioned above.[179] Another possibility is that the iron oxide layer is somewhat porous, with the adventitious layer adsorbing into the pores.

To test the hypothesis that the adventitious layer could be comprised of water adsorbed from the dodecane solvent, three further solvent contrasts were collected using a fresh iron-coated silicon substrate in a solid-liquid cell. The three solvent contrasts were as follows: dodecane-d_{26} stirred over 1 ml of D_2O, dodecane-d_{26} stirred over 1 ml of H_2O and dodecane-h_{26} stirred over

Table 3.6: Median and 95 % confidence interval values for the parameters following the MCMC fit to the reflectivity collected with the iron-coated silicon substrate against neat dodecane-d_{26} / dodecane-h_{26}. The minimum number of independent samples was estimated to be 56090, allowing those parameters with standard deviations ≤ 1.20 to be reported to 2 decimal places. Those parameters with standard deviations > 1.20 are reported to one decimal place.

Layer	β_n / $Å^{-2} \times 10^{-6}$	β_m / $Å^{-2} \times 10^{-6}$	Thickness / Å	Roughness / Å	Solvation / %
Si	2.07	-	∞	3	-
SiO_2	3.47	-	$19.48^{+1.54}_{-1.66}$	$6.08^{+1.02}_{-1.23}$	-
Fe	$7.88^{+0.07}_{-0.07}$	$4.75^{+0.06}_{-0.05}$	$189.86^{+0.67}_{-0.86}$	$11.33^{+0.88}_{-1.16}$	-
FeO_x	$5.71^{+0.16}_{-0.14}$	$0.10^{+0.17}_{-0.09}$	$32.77^{+1.27}_{-1.06}$	$3.1^{+2.4}_{-2.0}$	-
Adv	$0.22^{+0.57}_{-0.72}$	-	$13.73^{+2.14}_{-2.10}$	$2.54^{+2.69}_{-1.47}$	$18.1^{+9.2}_{-15.2}$

1 ml of D_2O. By vigorously stirring the solvent over water for a period of two weeks prior to the experiment, it was expected that the water within the dodecane would have been replaced with the excess D_2O or H_2O in the sample vial. The mixture was allowed to separate out and care was taken to only flow the lighter dodecane fraction into the solid-liquid cell. These contrasts were measured using the same instrumental set-up as the contrasts above, and were measured by Fin and Becky in the following order: dodecane-d_{26}-D_2O, dodecane-h_{26}-D_2O and dodecane-d_{26}-H_2O.

The reflectivity measured with the two dodecane-d_{26} contrasts are shown in Figure 3.15a. The similar fringe spacing suggests that the thickness of the adventitious layer remains approximately the same between the contrasts. The small difference in fringe amplitude at higher Q could imply that the contrast over the interface is changing. This could either be assigned to the difference in water contrast, or to the difference in solvent β_n, which is indicated by the difference in Q_c. Although a small difference in solvent β_n is not expected to change the fringe amplitude significantly, a greater proportion of ^1H in the solvent may increase the background signal. This may contribute to greater fringe amplitudes at high Q.

The reflectivity measured with all three contrasts are shown in Figure 3.15b. The data are compared to the median fits following an MCMC fitting routine. The data were fit with the model that had the highest evidence in a nested sampling study, as shown in Figure 3.15c. Here, the models with β_J share the same scattering length density for the adventitious layer, while those with sub- and superscripts separate the adventitious layer scattering length densities depending on the water and solvent contrast respectively. Additionally, an inequality constraint was used to constrain the roughness of the SiO_2 layer to be at least half that of the SiO_2 thickness. The initial values and priors for the nested sampling study are shown in Table A3. The β_{++} profile following the MCMC procedure is shown in Figure 3.15d and the results from the fit are shown in Table 3.7. Note that the β_{++} of the $Adv_d^{H_2O}$ layer does not reach the inferred β_n value as stated in Table 3.7. This is due to the roughness of iron oxide, σ_{FeO_x},

Table 3.7: Median and 95 % confidence interval values for the inferred parameters from the MCMC fit to the iron-coated silicon substrate against dodecane-d_{26}/dodecane-h_{26} that was stirred with D_2O or H_2O. The minimum number of independent samples was estimated to be 10618, allowing those parameters with standard deviations ≤ 0.52 to be reported to 2 decimal places. Those parameters with standard deviations > 0.52 are reported to one decimal place.

Layer	β_n / $Å^{-2} \times 10^{-6}$	β_m / $Å^{-2} \times 10^{-6}$	Thickness / Å	Roughness / Å	Solvation / %
Si	2.07	-	∞	3	-
SiO_2	3.47	-	$19.85^{+0.48}_{-0.50}$	$9.87^{+0.24}_{-0.26}$	-
Fe	$7.68^{+0.04}_{-0.04}$	$4.49^{+0.03}_{-0.03}$	$208.33^{+0.64}_{-0.70}$	$15.21^{+0.71}_{-0.81}$	-
FeO_x	$5.80^{+0.09}_{-0.09}$	$0.10^{+0.12}_{-0.10}$	$37.1^{+1.6}_{-1.4}$	$4.6^{+1.4}_{-3.2}$	-
$Adv_J^{D_2O}$	$0.34^{+0.87}_{-0.84}$	-	$11.5^{+2.1}_{-1.8}$	$2.9^{+2.3}_{-1.8}$	$18.0^{+9.1}_{-15.7}$
$Adv_d^{H_2O}$	$1.13^{+0.86}_{-1.00}$				-

and the adventitious layer, σ_{Adv}, which are both modelled as error functions to describe the variation of β_{++} from one material to the next. The error functions have a midpoint where the scattering length density is the average β_{++} of both materials, and the variation in β_{++} extends from the midpoint into the β_{++} of the adjacent layer by approximately twice the roughness. The thickness of a layer relates to the distance between the midpoints of the two error functions. Hence, when the thickness of the interfacial layer is less than $2\sigma_{FeO_x} + 2\sigma_{Adv}$, the β_{++} of the profile will not reach the inferred value of the layer. This is true for all layers, but mostly affects those that are thin.

The difference between the two dodecane-d_{26} contrasts is easiest to interpret via the β_{++} profile, where the difference between the posterior distributions is negligible compared to the uncertainty. This suggests that stirring D_2O/H_2O over dodecane has no significant impact on the β_n of the adventitious layer. Additionally, the inferred parameters for the dodecane-h_{26} contrast suggest that little or no D_2O is contained within the adventitious layer. Coupled with the similarity between the parameters of these contrasts with those measured without water, the data strongly suggest that water does not significantly comprise the adventitious layer. This further implies that the dodecane does not contain impurities which could both adsorb at the iron oxide-interface and partition into the water in significant proportion.

The above finding does not rule out the possibility that dodecane contains impurities that could adsorb at the iron oxide-dodecane interface which are insoluble in water. To test if water-insoluble impurities remain at the interface after exposure to water, a fresh iron-coated silicon substrate was characterised against neat dodecane-d_{26} in a solid-liquid cell at 25 °C. After, the substrate was removed and completely dried with a N_2 stream. The solid-liquid cell was then washed with $\sim$ 10 ml of D_2O by pipetting D_2O over the surface before drying under a N_2 stream and setting aside. The solid-liquid cell was then washed with ethanol in a sonicator, dried and washed again in ultra-pure water in a sonicator. The solid-liquid cell was then dried

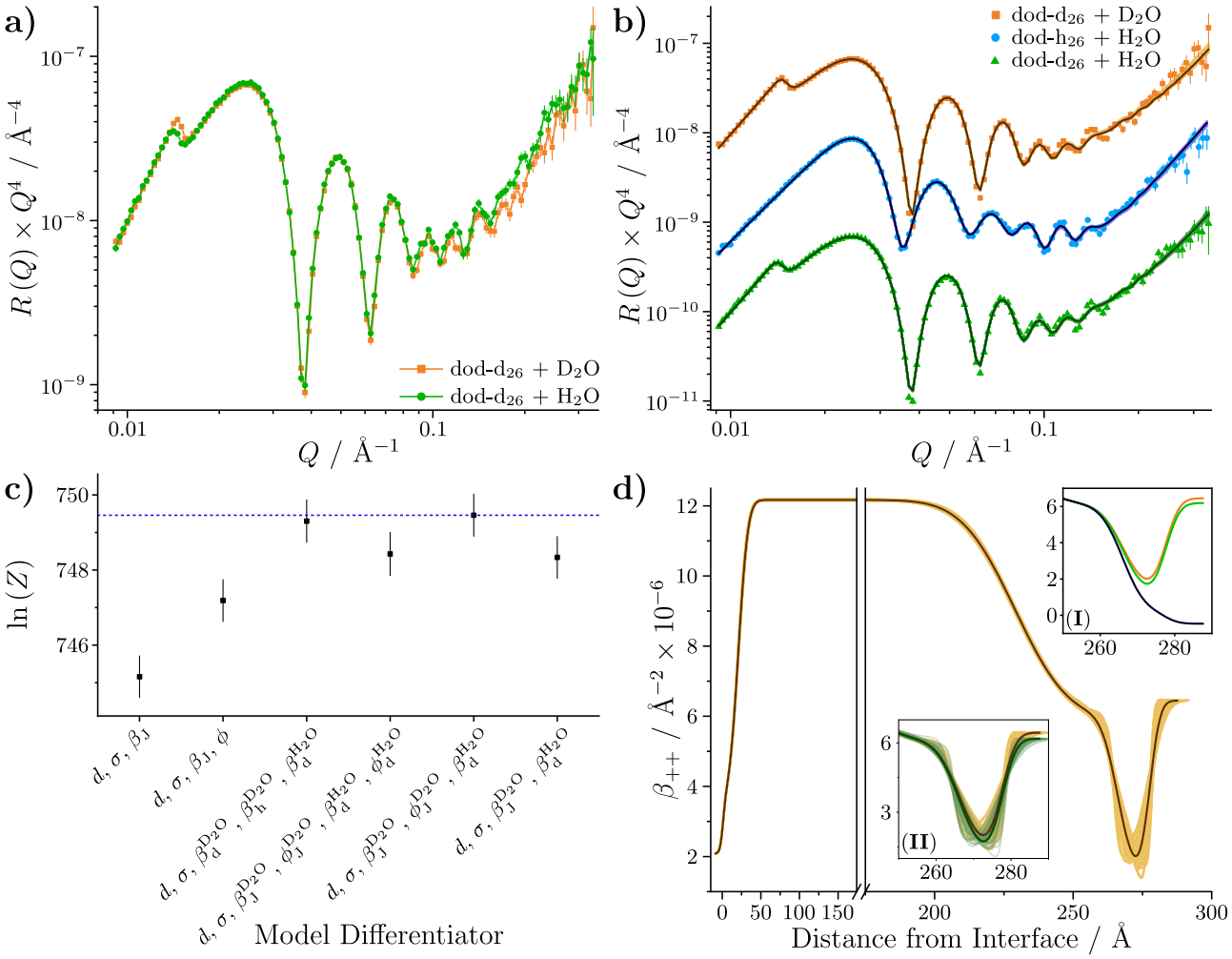

Figure 3.15: **a)** Reflectivity collected with dodecane-d_{26} stirred with either 1 ml of D_2O or H_2O against an iron-coated silicon substrate. The reflectivity has been modified by a factor of Q^4. The lines between data are linear interpolation lines to guide the eye. **b)** Reflectivity for all three contrasts of water stirred over dodecane. The dark lines show the median fits from the MCMC procedure. The shaded band shows 50 random samples from the posterior distribution. The data are offset by a factor of 10^{-1} in the modified reflectivity axis. **c)** Comparison of evidences for a selected number of models. The model differentiators relate to the adventitious layer parameters. The blue dashed line highlights the model with the greatest evidence. **d)** The β_{++} profile of the dodecane-d_{26} stirred over 1 ml of D_2O contrast resulting from the MCMC procedure. The dark line shows the median β_{++} profile while the bands show 50 random samples from the posterior distribution. The inset labelled with (**I**) shows the median profiles for the all three contrasts with the same general colours for the data in **b)**. The inset labelled with (**II**) shows a sub-sample of the β_{++} posterior distribution for the dodecane-d_{26}/D_2O and dodecane-d_{26}/H_2O contrasts.

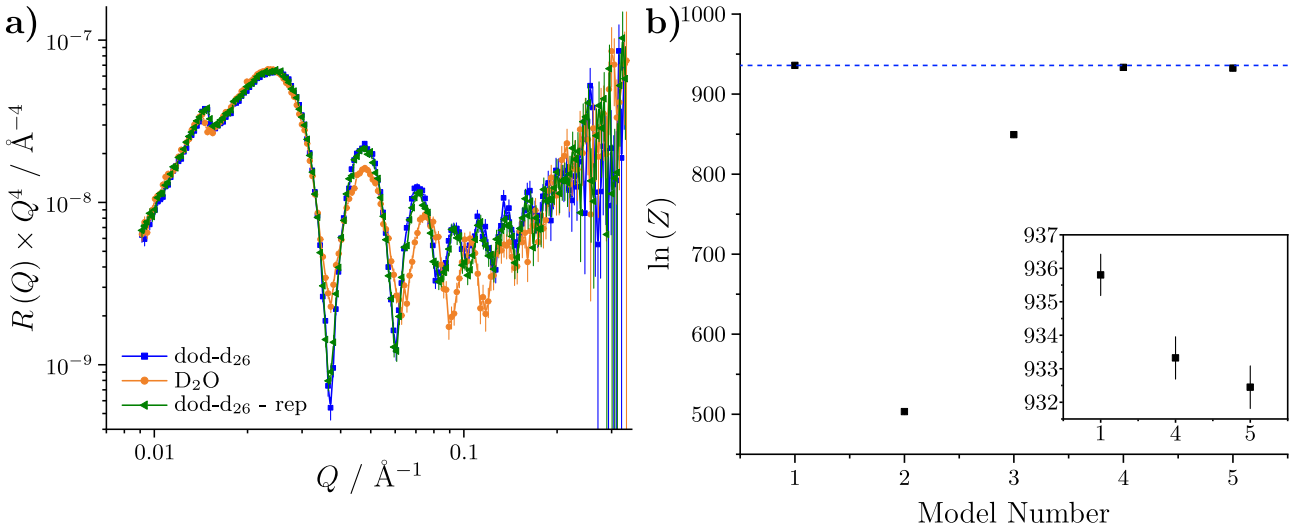

Figure 3.16: **a)** Comparison of the reflectivity from an iron-coated silicon substrate against dodecane-d_{26}, D_2O and a repeat (rep) of dodecane-d_{26} after exposure to D_2O. The reflectivity has been modified by a factor of Q^4 to aid comparison. **b)** Evidences for the five different models considered to describe the data. The inset compares the top three models.

before re-assembling the cell with D_2O against the substrate at 25 °C. The reflectivity was measured and then the cell was deconstructed before being reconstructed with dodecane-d_{26} following the reverse of the above washing steps. The reflectivity was then measured with this second contrast of dodecane-d_{26} at the same temperature. The collected data are compared in Figure 3.16a.

There is a clear shift in the Kiessig fringe spacing and amplitude between the D_2O and dodecane-d_{26} contrasts, indicating that the total thickness and contrast across the interface is substantially different. As the difference in nominal β_n of D_2O and dodecane-d_{26} is $\leq 0.4 \times 10^{-6}$ Å^{-2}, and experimentally appears to be even lower, the difference in the fringe amplitude is not expected to be due to variation in the solvent β_n. Nested sampling was conducted on five different models to ascertain the best model to fit the data. Each model is referred to by a number from 1–5. Model 1 includes an adventitious layer for the dodecane-d_{26} contrasts but not for the D_2O contrast. The iron oxide roughness is shared between all three contrasts. Model 2 includes an adventitious layer for the D_2O layer which has the same properties as that in the dodecane-d_{26} contrasts. Model 3 is similar to Model 1 but does not share the same iron oxide roughness between the dodecane-d_{26} and D_2O contrasts. Model 4 and 5 include adventitious layers for the D_2O contrast that do not share the same properties as those in the dodecane-d_{26} contrasts. Model 4 shares the iron oxide roughness between the all three contrasts while model 5 makes a distinction between the iron oxide roughness in D_2O from that in dodecane-d_{26}. The initial parameter values and priors are shown in Table A4, and the results are compared in Figure 3.16b.

As Model 1 has the greatest evidence, it was chosen to use this model when fitting the data via MCMC. The resulting fits can be seen in Figure 3.17a and the β_{++} profiles are shown in Figure 3.17b. There is a significant difference between the β_{++} profiles of the dodecane and D_2O

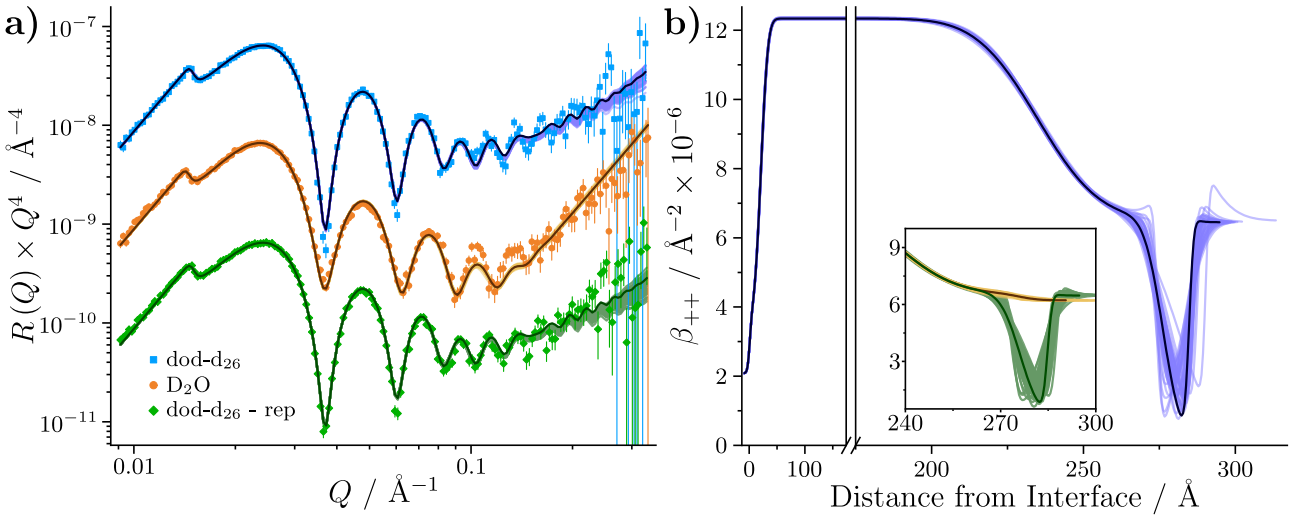

Figure 3.17: **a)** Fits to the data collected with an iron-coated silicon substrate against dodecane-d_{26}, D_2O and a repeat (rep) of dodecane-d_{26} after exposure to D_2O. The reflectivity has been modified by a factor of Q^4 and offset by 10^{-1} between datasets to aid comparison. **b)** The up-spin scattering length density profile for the initial dodecane-d_{26} contrast. The inset compares the β_{++} profiles for the D_2O contrast and the repeated dodecane-d_{26} contrast after exposure to D_2O.

Table 3.8: Median and 95 % confidence interval values for the inferred parameters from the MCMC fit to the iron-coated silicon substrate in neat dodecane-d_{26} and D_2O. The minimum number of independent samples was estimated to be 25289, allowing those parameters with standard deviations ≤ 0.81 to be reported to 2 decimal places. Those parameters with standard deviations > 0.81 are reported to one decimal place.

Layer	β_n / Å$^{-2} \times 10^{-6}$	β_m / Å$^{-2} \times 10^{-6}$	Thickness / Å	Roughness / Å
Si	2.07	-	∞	3
SiO_2	3.47	-	$20.08^{+0.49}_{-0.44}$	$9.97^{+0.23}_{-0.22}$
Fe	$7.69^{+0.08}_{-0.08}$	$4.65^{+0.08}_{-0.09}$	$213.98^{+0.76}_{-0.72}$	$15.97^{+1.06}_{-1.01}$
FeO_x	$6.19^{+0.12}_{-0.12}$	$0.35^{+0.15}_{-0.17}$	$41.2^{+3.1}_{-2.4}$	$4.8^{+3.9}_{-3.4}$
Adv	$0.09^{+1.49}_{-0.61}$	-	$8.6^{+2.7}_{-0.9}$	$2.1^{+2.9}_{-1.0}$

contrasts at the iron oxide interface, where an adventitious layer with a $\beta_{++} < 3 \times 10^{-6}$ Å^{-2} is required to suitably model the dodecane contrasts. There is some discrepancy between the data and the model which is most apparent in the D_2O contrast. This suggests that a different, unconsidered model may fit the data more suitably. However, the reasonable agreement between the data and model suggests that the region of low β_{++} is not present at the iron oxide-water interface. The inferred parameter values are shown in Table 3.8.

The thickness of an interfacial layer between hexadecane and a Si substrate coated with octadecyl-trichlorosilane (OTS) was found to be lower than that formed between a chemically cleaned Si substrate and hexadecane.[180] This was regarded as solvent depletion, which was amplified at interfaces between materials of high and low surface energy. The surface cov-

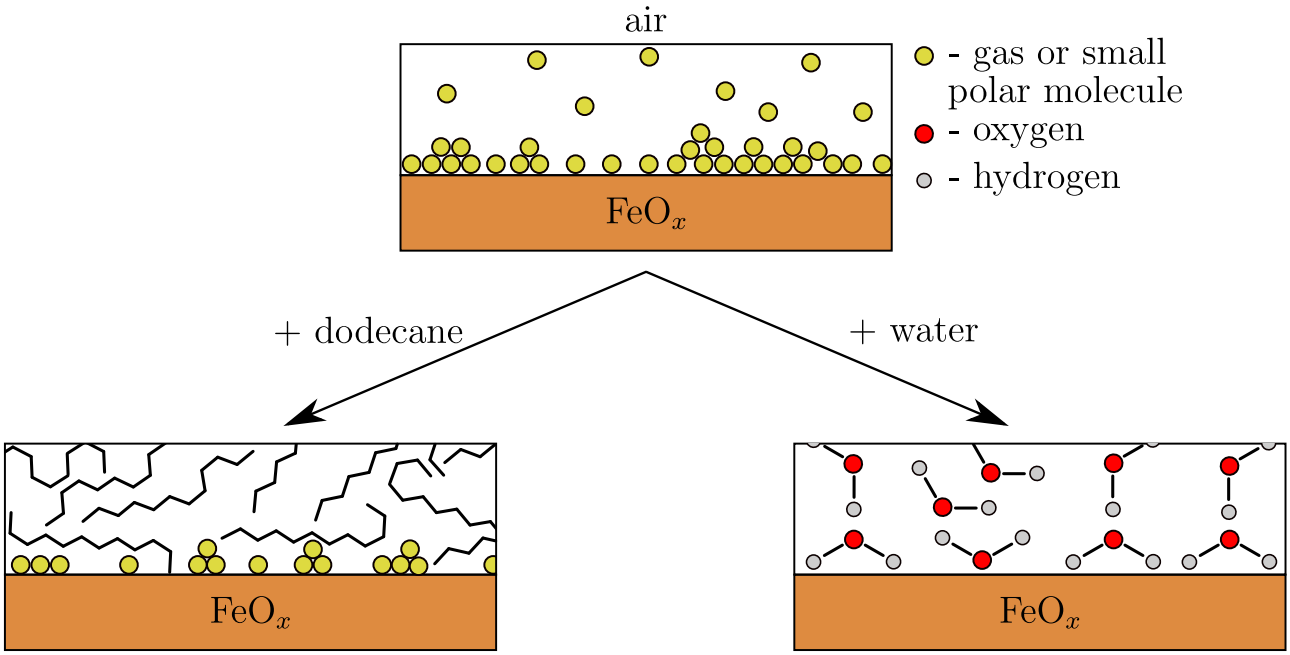

Figure 3.18: Depiction of the iron oxide surface under dodecane, water or air. The representations are not to scale. Water is expected to adsorb through hydrogen bonds to hydroxy (from iron hydroxide) and O^{2-} moieties at the iron oxide interface.

erage of nanoscopic (10-400 nm) air bubbles at the interface between D_2O and a OTS-coated Si substrate has been estimated to be 10 %, which was argued to support the solvent depletion theory.[181] However, the technique could not resolve air bubbles smaller than 10 nm, and hence, the proportion of these air bubbles could be greater. Furthermore, it is possible that surface coverage of adsorbed gas bubbles is dependant on the particular solvent and surface, which could mean that the iron oxide-dodecane interface may contain a different proportion of gas. The solubility of N_2, a proxy for the atmospheric composition, in dodecane is 0.00123 mol of N_2 per mol of dodecane, which is a factor of $\sim$ 100 greater than that in water.[182] This relates to a volume of nitrogen in 1 ml of dodecane that is a factor of $\sim$ 8 greater than the volume of nitrogen in 1 ml of water. As such, it would appear inconsistent for D_2O to solubilise the adsorbed gas while dodecane cannot. Therefore, it is suggested that the loss of the adventitious layer in D_2O is due to the ability of water to wet the high energy surface of iron oxide, while the hydrophobic dodecane does not wet the iron oxide surface. By assuming the adventitious layer is $\sim$ 10 Å thick and is homogeneous across the whole 55 $\times$ 55 mm^2 surface, the total volume of adventitious material can be estimated to be $\sim$ 3 nl. For a one 1 ml solution of D_2O, the volume of dissolved nitrogen is $\sim$ 15 µl using the above solubility of nitrogen in water; this is a factor of 5×10^3 greater than the estimated volume of the adventitious layer. As such, it is suggested that the adsorbed gas is displaced by the D_2O and solubilised within the bulk aqueous phase. When using dodecane, it is thought that residual adsorbed gas, present at the interface before exposure to dodecane, remains at the interface where it occupies regions of space that are depleted of solvent. In doing so, it screens the dodecane from the hydrophilic surface of iron oxide. Schematics of the interface under air, dodecane and D_2O are shown in Figure 3.18.

3.4 Conclusion

GMO was found to form oblate spheroid reverse micelles in dodecane at 20 mM, with average major and minor axes of $26.10^{+0.03}_{-0.03}$ and $13.72^{+0.04}_{-0.04}$ Å. It was also shown that at $W = 5$, water can be solubilised within the aggregates of GMO in dodecane, swelling the reverse micelles' volume by $\sim$ 25 %. Through pendant drop tensiometry a CMC of $2.1 \pm 0.1 \times 10^{-3}$ mol dm^{-3} was determined. It is expected that some aggregates will exist in solution before this concentration as the onset of micellisation is less sharp in non-polar solvents compared to aqueous solutions. Both monomeric and aggregated GMO are thought to exist dynamically in the bulk solution at concentrations above the CMC.

The iron oxide surface provided by iron-coated silicon substrates was determined to be mostly comprised of iron (III) oxide via XPS. Further analysis of the substrates with XRR and NR showed that the iron oxide layer is between 30–40 Å thick, and the weak magnetic character of the layer suggests that the most abundant phase is hematite. NR revealed the presence of a low scattering length density layer at the iron oxide-dodecane interface, which appears to be of variable thickness between 8–16 Å thick. Experiments with dodecane stirred over water showed little difference to the interfacial film, while the reflectivity collected with D_2O indicates the film is not present under aqueous solution. It is postulated that this layer arises from pre-adsorbed gases prior to the introduction of liquid samples. These gases remain adsorbed at the iron oxide surface when a non-polar liquid is placed against the substrate, but are displaced in aqueous solution due to the greater wettability of the surface with water. It is thought that removing this layer would require ultra-high vacuum conditions, which may lead to issues when studying liquid samples.

Chapter 4

Adsorption of glycerol monooleate at the iron oxide-dodecane interface

4.1 Background

Glycerol monooleate is the mono ester of oleic acid and glycerol. The friction reduction offered by GMO in hydrocarbon solutions has been studied using bench top tribometer tests and is comparable to solutions formed with oleic acid.[183–185] Alongside offering friction reduction comparable to fatty acids, it is an attractive OFM due to its benign nature and relative abundance of starting materials used in its synthesis. Furthermore, the corrosive ability of the ester towards metallic surfaces is thought to be lower compared to the parent fatty acid. Similar friction behaviour has been reported from simulations of GMO and oleic acid adsorbed at perfectly flat iron oxide surfaces sliding under boundary lubrication conditions.[52] However, GMO was found to have a marginally greater performance when compared to oleic acid at the same packing densities. This was postulated to arise from a greater number of hydrogen bonds between adjacent adsorbed GMO molecules, which inhibits solvent penetration and hence, leads to more defined slip planes in comparison to oleic acid.

If both additives self-assemble to form monolayers, similar packing densities may be expected for oleic acid and GMO as they share the same alkyl chain, which is thought to dictate the surface excess of the adsorbate. However, the adsorption strengths of GMO and oleic acid appear to be of differing magnitudes. Evidence of oleic acid chemisorption has been provided by polarised NR, where a substantial amount of oleic acid remained adsorbed at the iron oxide-dodecane interface after washing the interface with additional neat solvent.[45] On the other hand, quartz crystal microbalance (QCM) results show that while GMO adsorbs at stainless steels from hexadecane solution, almost all of the GMO at a comparable concentration (0.5 wt%) can be washed off with additional neat solvent.[49] This indicates that the vast majority of the GMO is physisorbed at the surface. The QCM results also show that it takes on the order of 10^3 s to form a complete GMO layer at steel surfaces. Therefore, considering the high shear

and wearing environments found in boundary lubrication, it is quite surprising that sufficient GMO remains adsorbed at the interface to offer similar friction modification to oleic acid.

Further information on the adsorption and self-assembly of GMO at iron oxide surfaces under static conditions can offer insight into the behaviour of the OFM under harsher conditions. In this chapter the adsorption of GMO at the iron oxide-dodecane interface is studied as a function of concentration and temperature via depletion isotherms. The thickness and surface excess of GMO adsorbed at the iron oxide-dodecane interface are studied with NR as a function of concentration and temperature. In addition, the film structure of adsorbed GMO in the presence of water is investigated with NR. The GMO and dodecane used in this chapter were the same as used in Chapter 3.

4.2 Depletion isotherms

FTIR was used to determine the GMO concentration due to the strong IR adsorption in the region of 1665-1800 cm^{-1} from the ester carbonyl. Standards of a known GMO concentration were prepared in triplicate and the spectra collected using a blank dodecane standard to remove additional IR adsorption from the solvent. Prior to the measurements the solutions were heated to $\sim$ 30 °C in order to hinder the precipitation of GMO in the cell. The data were baseline corrected by subtracting a linear function between 1665–1800 cm^{-1}, scaling them to the same baseline as shown in Figure 4.1a. The adsorption in this region relates to the vibrational excitation of the carbonyl stretch mode, where the peaks with adsorption maxima at $\sim$ 1728 and 1749 cm^{-1} are assigned to the hydrogen-bonded carbonyl of GMO and the non-interacting carbonyl of GMO respectively.[186] The total peak area within this region was determined by integration and is plotted as a function of the GMO concentration in Figure 4.1b. The estimated error in the concentration of GMO is represented by error bars with a magnitude calculated through the propagation of weighing error. The data were fit using orthogonal regression to take the uncertainty in the GMO concentration into account.

Depletion isotherms were then conducted. The GMO solutions were stirred over $\sim$ 0.5 g of α-Fe_2O_3 (hematite) powder for at least five hours in order to ensure equilibrium. Throughout the duration of the agitation period, the mixtures were held at four different temperatures of 30, 45, 60 and 70 °C in a water bath. Hematite (Puratronic, 99.995 %) was purchased from Alfa Aesar, and was chosen as the representative iron oxide as, according to the iron oxide phase diagram, it is the most thermodynamically stable iron oxide at room temperature.[187] Furthermore, it is very weakly ferromagnetic at the temperatures probed here, giving rise to a negligible magnetic moment, unlike ferrimagnetic magnetite (Fe_3O_4) and maghemite (γ-Fe_2O_3).[179] The advantage of the weak magnetic interaction is that mixing the powder into the sample solutions using magnetic stirrer fleas will proceed unhindered. The initial concentrations of GMO were in the range of 0.8–5 mM and the surface area of the α-Fe_2O_3 powder was found to be 11.8 ± 0.1 m^2 g^{-1} by N_2 BET sorption analysis, conducted at the Department of Materials Science & Metallurgy, University of Cambridge, by Zlatko Saracevic. After separation of the powder and

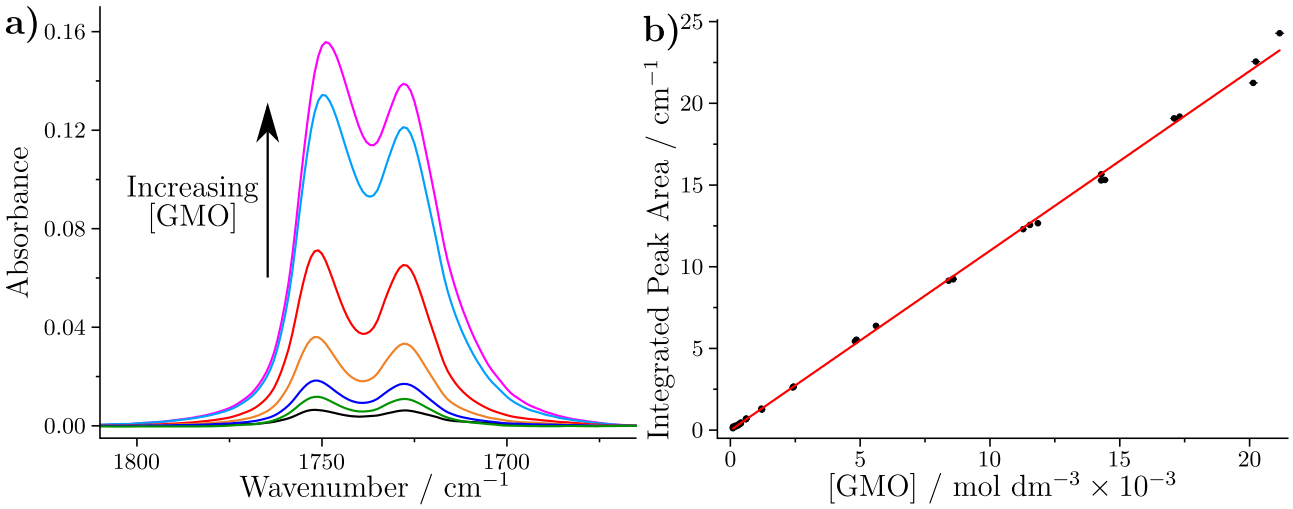

Figure 4.1: **a)** The carbonyl region of the GMO IR spectrum. The spectra are collected at increasing GMO concentration, and were baseline-subtracted. **b)** The integrated peak area as a function of the GMO concentration. The error bars in the GMO concentration are shown but are obscured by the data points. The red line shows the best linear fit to the data.

Table 4.1: The surface excess, area per molecule, and Langmuir equilibrium constant inferred from the Langmuir isotherm fit to the GMO depletion isotherm data at the four different temperatures.

Temperature / °C	Γ_m / mol m^{-2} × 10^{-6}	A_{PM}/ Å^2	K_L / mol dm^{-3} × 10^2
30	4.15 ± 0.09	40.0 ± 0.9	63.1 ± 9.9
45	3.43 ± 0.09	48.4 ± 1.3	50.6 ± 8.6
60	3.13 ± 0.08	53.1 ± 1.4	57.0 ± 10.8
70	2.13 ± 0.09	77.8 ± 3.2	52.9 ± 15.2

solution, the samples were warmed to ~ 30 °C and then loaded into the PIKE IR transmission cell. The carbonyl peak area was determined in the same way as the standards, enabling the equilibrium concentration of GMO to be determined. The surface excess, Γ, is then calculated as:

$$\Gamma = \frac{V_s \left([\text{GMO}]_i - [\text{GMO}]_{eq} \right)}{m \times S} \tag{4.1}$$

where $[\text{GMO}]_i$ and $[\text{GMO}]_{eq}$ are the initial and equilibrium concentration of GMO respectively, V_s is the initial volume of the solution, m is the mass of the added hematite powder and S is the surface area per unit mass of the hematite powder. The surface excess as a function of $[\text{GMO}]_{eq}$ for four temperatures is shown in Figure 4.2a. The data was found to be well described by the Langmuir isotherm model, as shown by the dark lines in Figure 4.2a. The inferred maximum surface excess, Γ_m, and the Langmuir equilibrium constant, K_L, for each temperature are shown in Table 4.1.

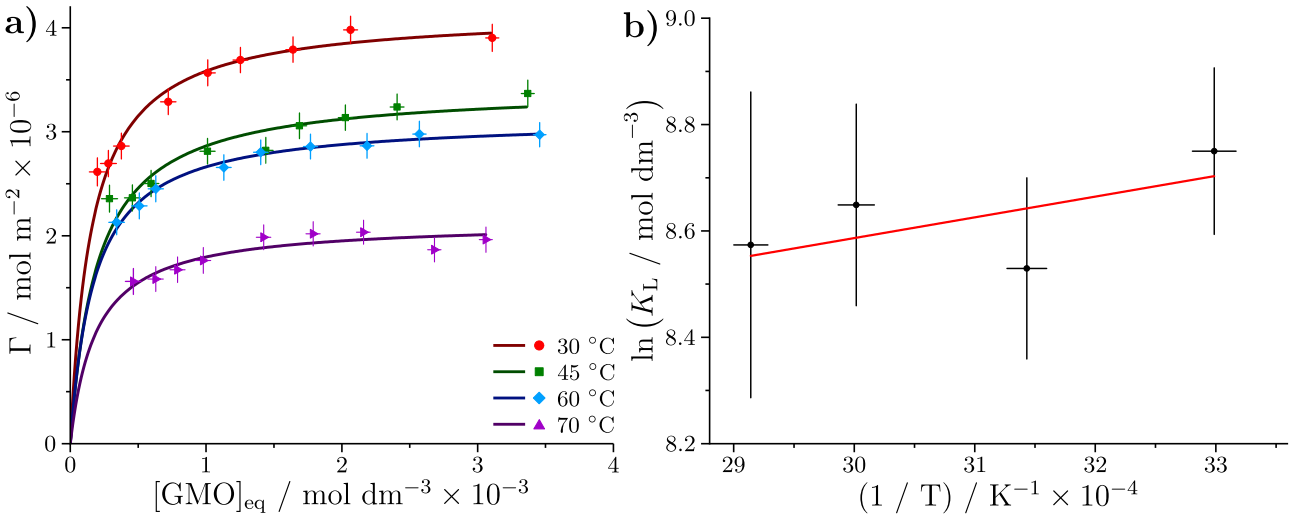

Figure 4.2: **a)** The depletion isotherm results for the four temperatures. The fits shown are the best fits of the Langmuir isotherm, which was conducted via orthogonal regression. **b)** A Van't Hoff plot constructed using the inferred K_L for each Langmuir isotherm.

As the Langmuir isotherm assumes that the adsorbate adopts a monolayer structure, the area per molecule at each temperature can be calculated following Equation 3.1. These are shown in Table 4.1 for each temperature. The precise surface of the hematite powder is not known, but hematite exhibits basal parting, which is similar to cleavage, along the hexagonal (0001) face due to the twinning of hematite domains.[188] The unit cell that describes the positions of the Fe^{3+} species on this face has a length of 5 Å.[189] Hence, if every Fe^{3+} ion were occupied by a singular GMO molecule, this would lead to an A_{PM} of 25 Å^2; therefore, it appears that occupied sites are more dispersed than the available Fe^{3+} species. It is not known if Fe^{3+} or O^{2-} species are the terminal groups on the outer of the iron oxide as it has been suggested that when oxygen pressures are $> 1 \times 10^{-3}$ mbar, such as in atmospheric conditions, the outer layer can be O^{2-} terminated.[190] In this case, the average separation of the oxygen species is 2 Å, leading to the same conclusion if Fe^{3+} is at the interface.[191] It is possible that other faces of the hematite structure could be exposed, where the separation between active adsorption sites is different; as such, the above arguments only serve as a simple approximation. Furthermore, it is likely that the surface is not ideal and planar, with defects and surface restructuring increasing the surface energy of particular sites, and potentially hindering adsorption at other potential sites. Despite these caveats, the similar A_{PM} to that determined at the dodecane-water interface suggests that the underlying structure of the iron oxide is less significant than the ability of the GMO molecules to pack together at the interface.

The area per molecule at 30 °C also agrees reasonably well with the reported A_{PM} for oleic acid, which was found to be 45 ± 2 Å^2 at ambient room temperature.[45] It may be expected that GMO has a lower area per molecule due to the greater number of hydrogen bonding sites within the GMO chemical structure; however, the similar A_{PM}s suggest any difference in hydrogen bonding has little effect on the surface excess. The cited work also compares the area per molecule of oleic acid to that of stearic and linoleic acid, which share the same polar head

group but differences in the alkyl chain. The former has no double bond, and was found to have a lower A_{PM} of 28 ± 2 Å^2, while linoleic acid, which has an additional double bond compared to oleic acid, was found to have a greater A_{PM} of 92 ± 2 Å^2. These findings are consistent with the suggestion that the packing of the alkyl chain dictates the area per molecule.

The increasing A_{PM} with temperature can be attributed to the greater thermal energy, which induces greater disorder in the adsorbed film. This leads to weaker intermolecular interactions between the adsorbate and thus, less ideal packing of the GMO molecules. The equilibrium constant of a chemical reaction is related to the standard Gibbs energy change, ΔG°, as shown in Equation 4.2.

$$\Delta G^\circ = -RT \ln K_{\mathrm{L}} \tag{4.2}$$

The standard Gibbs energy change can be written in terms of the standard enthalpy change, ΔH°, and the standard entropy change, ΔS° as shown in Equation 4.3.

$$\Delta G^\circ = \Delta H^\circ - T\Delta S^\circ \tag{4.3}$$

Therefore, a series of Langmuir equilibrium constants collected over specific temperatures can be used to calculate the enthalpy and entropy change upon adsorption of GMO by constructing a Van't Hoff plot, which is shown in Figure 4.2b. The error in the temperature was estimated to have a standard deviation of ± 1.7 K. The large error in the natural logarithm of K_{L} arises from the lack of data points at lower concentrations, where the equilibrium constant determines the initial increase in surface excess. By fitting the data to a linear model, an intercept, c, and gradient, m, can be determined which are related to the standard entropy and enthalpy of adsorption, where $c = \Delta S^\circ/R$ and $m = -\Delta H^\circ/R$. Subsequently, it was determined that $\Delta H^\circ = -3.2 \pm 5.6$ kJ mol^{-1} and $\Delta S^\circ = +61.7 \pm 17.7$ J K^{-1} mol^{-1}.

The determined enthalpy of adsorption suggests GMO adsorbs weakly at the iron oxide-dodecane interface via physisorption. It is expected that the adsorption occurs via intermolecular forces, such as hydrogen bonding and dispersion interactions between the GMO and iron oxide surface. Palmitic acid has been reported to have a greater heat of adsorption, where $\Delta H^\circ = -35 \pm 5$ kJ mol^{-1}, which was suggested to arise from a mixture of physisorption and chemisorption of the carboxylic acid. The latter leads to the formation of carboxlyates with the iron oxide surface.[47] It has been suggested that GMO is hydrolysed to form oleic acid either in the bulk solution or at the interface.[21] However, if the enthalpy of adsorption of palmitic acid and oleic acid are similar, which as they share the same head group appears feasible, the weak enthalpy of adsorption of GMO suggests that the majority of GMO does not hydrolyse. Hexadecylamine was reported to have an enthalpy of adsorption more consistent with physisorption with $\Delta H^\circ = -19 \pm 5$ kJ mol^{-1}. It is possible that the NH_2 terminal group can hydrogen bond to the iron oxide surface, and potentially interact through the lone pair of the nitrogen towards the iron cations. The potential for multiple interactions between the small terminal head group

and the iron oxide surfaces may account for the greater magnitude of enthalpy change compared to GMO.

The positive entropy change could be interpreted as an increase in the disorder of the system upon GMO adsorption. This may appear as contradictory to adsorption if considering a perfectly clean interface with a solution of monomeric GMO solely interacting with the solvent prior to adsorption. However, it could be reasoned that a positive entropy change results from the displacement of adsorbed gas molecules from the iron oxide surface upon adsorption of GMO. This can be expected to increase the number of accessible states for the gas molecules when in solution. Furthermore, it is known that some GMO is held within aggregates prior to adsorption, which is thought to lower the number of accessible states associated with translation, rotation and conformation compared to an ideal solution of monomeric GMO. This will lead to a lower entropy of the solution prior to adsorption.

Assuming ΔH° and ΔS° do not change with temperature, the standard Gibbs free energy change is calculated to become more negative with temperature, implying the spontaneous adsorption of GMO is more favourable at higher temperatures. However, the decreasing surface excess and decreasing values of K_L with temperature suggest the opposite, and hence, that the entropy change is not positive. It is thought that the inaccuracy between the data and theory arises from the small number of data points in the Van't Hoff analysis, which in addition, are noisy. As c is determined via a large extrapolation of the data, it is possible that noise in the four data points has skewed the value of c, and hence led to the inaccurate determination of ΔS°. It may be possible to decrease the error by determining K_L at more temperatures, and by collecting more data points at lower equilibrium concentrations of GMO. The latter may require a different quantification technique as the limit of detection with the FTIR transmission cell was $\sim 1 \times 10^{-4}$ mol dm^{-3} as dictated by the signal-to-noise ratio. The suggestion that the value of ΔS° is erroneous is supported by the lower values of ΔS° calculated for palmitic acid and hexadecylamine at the iron oxide-dodecane interface, which were found to have $\Delta S^\circ = -19 \pm 20$ J K^{-1} mol^{-1} and $\Delta S^\circ = +15 \pm 20$ J K^{-1} mol^{-1} respectively.[47] The surface excess of these molecules also decreases with temperature, suggesting that the entropy of adsorption is negative; this appears consistent with the reported values when considering the associated uncertainty.

4.3 Neutron reflectometry

Similar to the characterisation of the substrates via NR, some of the experiments presented below were conducted by Fin and Becky. These experiments were planned and remotely led by the author. The sections that contain work collected in collaboration are highlighted. All of the following analysis has been conducted individually.

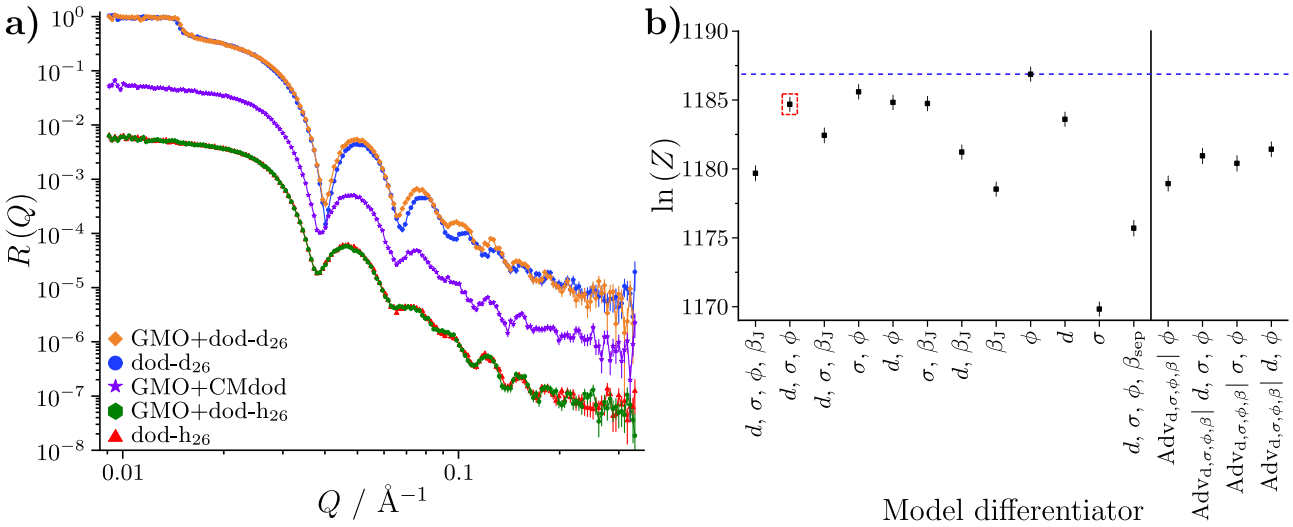

Figure 4.3: **a)** Reflectivity of the 20 mM GMO-dodecane systems. The datasets collected with CMdod and dodecane-h_{26} are offset by 10^{-1} and 10^{-2} in the reflectivity axis. Lines between data points are interpolations to guide the eye. **b)** The natural logarithm of the evidences for the models considered plausible to describe the 20 mM GMO-dodecane reflectivity profiles. The data point in the red square is the model with the greatest evidence when fitting the GMO thickness and roughness along with a parameter that influences the β_n of the GMO layer.

4.3.1 Adsorption as a function of bulk concentration

Three solutions of GMO in dodecane were prepared at 20 mM, each with a different volumetric mixture of dodecane-h_{26}/d_{26}: 100:0, 65:35 and 0:100 dodecane-h_{26}:dodecane-d_{26}, where the 65:35 contrast is referred to as CMdod. The solution in neat dodecane-d_{26} was flowed into a solid-liquid cell against a 55 × 55 × 10 mm iron-coated silicon substrate and the cell was equilibrated at 25 °C before alignment on the INTER reflectometer. The reflectivity was collected using neutron wavelengths of ∼ 2–17 Å at three angles, where θ_i = 0.7°, 1.2° and 2.3° resulting in a Q range of ∼ 0.009–0.331 Å^{-1}. The standard deviation of the momentum transfer was such that dQ/Q = 2 %. The reflectivity with the other two contrasts were then collected by exchanging the solution in the cell in the order of CMdod and then dodecane-h_{26}. Before exchanging the solutions, the cell temperature was raised to 60 °C for at least 20 minutes to ensure equilibration before re-aligning the cell and measuring the reflectivity at the higher temperature. The data collected at 25 °C with all three solutions are shown in Figure 4.3, where the contrasts collected with dodecane-d_{26} and dodecane-h_{26} are compared to the reflectivity profiles collected with neat dodecane-d_{26} and dodecane-h_{26} against the same iron-coated silicon substrate at 25 °C prior to the introduction of GMO to the substrate. The reflectivity collected at 60 °C is discussed later. The preparation of samples and collection of the data was conducted by Fin and Becky.

There is a clear difference between the amplitude and spacing of the Kiessig fringes in the datasets collected with 20 mM GMO in dodecane-d_{26} and neat dodecane-d_{26}. The different fringe spacing implies the total thickness across the interface changes upon exposure to GMO. Similarly, the difference in the fringe amplitude suggests a change in the contrast at the interface.

Both changes are assumed to arise from the adsorption of GMO at the iron oxide-dodecane interface. The similarity between the datasets collected with dodecane-h_{26} suggests that the scattering length density of the interface is similar before and after exposure to GMO. This is expected as the contrast between dodecane-h_{26} and GMO is similar to that between dodecane-h_{26} and the adventitious layer. Furthermore, the similarity suggests that the two cycles of heating up to 60 °C and back down to 25 °C prior to the collection of the dodecane-h_{26} contrast does not affect the substrate structure. Higher temperatures, $\geq$ 80 °C, have been found to alter the structure of iron-coated silicon substrates, and it was suggested that the underlying silicon may permeate the iron film.[47]

A number of models were proposed to describe the data collected at 25 °C, where the underlying substrate structure was kept constant but the number of parameters to describe the GMO layer was altered. The evidence for the different models are shown in Figure 4.3b, and the initial parameters with the corresponding priors of the varying parameters are shown in Table A5. Surprisingly, the model with the highest evidence, as highlighted by the blue dashed line, was found when only varying the solvation parameter of the GMO layer. However, it is thought the evidence for this model, and those with only one or two varying GMO parameters, would decrease sharply as the fixed values of the other GMO parameters are altered. As the values of the GMO thickness, roughness and, to some extent, the GMO β_n are not known prior to fitting, it was chosen to ignore the models which held these parameters fixed. Therefore, the model with the greatest evidence was taken to be the one highlighted by the red dashed box. Here, the β_n of GMO is held fixed at the nominal value of 0.21×10^{-6} Å^{-2} and the solvation parameter allows the β_n to vary depending on the contrast and the solvation following Equation 3.5.

The four models shown on the farthest right of Figure 4.3b included an additional layer at the interface between the adsorbed GMO and the iron oxide layer, with $\beta_n = 0\text{–}1 \times 10^{-6}$ Å^{-2}. The evidence for these four models was estimated to test for the possibility that the adventitious layer remained as a separate differentiable layer when GMO was adsorbed at the interface. However, the lower evidence indicate that these models are, in general, less descriptive than those with one layer. Furthermore, the inferred posterior distributions of the adventitious layer thicknesses had median values $\sim$ 1 Å with roughnesses a factor of $\sim$ 4 times the thickness. In these circumstances, the additional layer is likely only modelling a minor variation to the interface between the iron oxide and the GMO layer. It is possible that the adventitious material is displaced from the interface by adsorption of GMO, but this is not resolvable with the contrast used here. Therefore, it is postulated that the GMO adsorbs at the solvent depleted region of the interface to form a composite layer with residual adventitious material.

Using the model with the highest evidence, the data were fit using an MCMC routine. The median fits to the data are shown in Figure 4.4a, and the β_{++} profile is shown in Figure 4.4b. The thickness of the GMO layer, as shown in Table 4.2, was found to be $\sim$ 8 Å greater than that found for the adventitious layer in the neat solvent contrasts, supporting the suggestion of GMO adsorption at the iron oxide-dodecane interface. The shapes of the 1D and 2D distributions

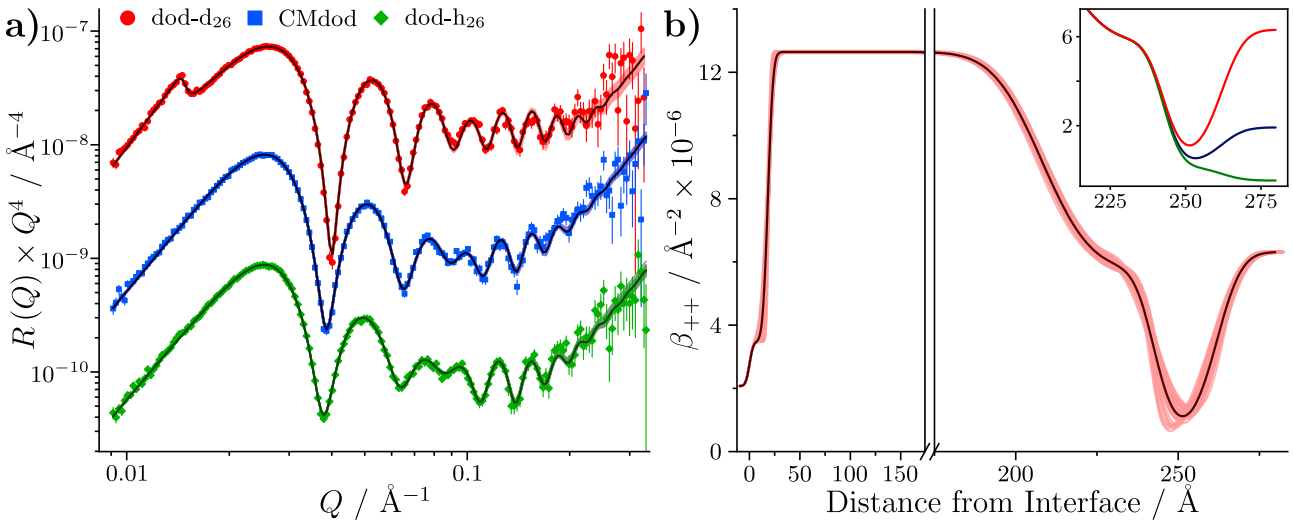

Figure 4.4: **a)** Reflectivity collected from the 20 mM GMO-dodecane contrasts. The dark lines are the median profiles, and the shaded band contains 50 random samples from the posterior distribution. The reflectivity is modified by a factor of Q^4 for comparison. **b)** The median β_{++} profile for the dodecane-d$_{26}$ contrast. The shaded band shows 50 random samples from the posterior distribution. The inset shows the median β_{++} profiles centred upon the GMO layer for all three contrasts.

Table 4.2: Median and 95 % confidence interval values for the parameters from the MCMC fit to the reflectivity collected with the 20 mM GMO-dodecane solutions at 25 °C. The minimum number of independent samples was estimated to be 44646, allowing those parameters with standard deviations ≤ 1.07 to be reported to 2 decimal places. Those parameters with standard deviations > 1.07 are reported to one decimal place.

Layer	β_n / Å$^{-2} \times 10^{-6}$	β_m / Å$^{-2} \times 10^{-6}$	Thickness / Å	Roughness / Å	Solvation / %
Si	2.07	-	∞	3	-
SiO_2	3.47	-	$18.32^{+1.25}_{-1.32}$	$9.87^{+0.24}_{-0.26}$	-
Fe	$7.91^{+0.06}_{-0.06}$	$4.73^{+0.05}_{-0.05}$	$189.73^{+0.66}_{-0.84}$	$11.92^{+0.76}_{-0.89}$	-
FeO_x	$5.64^{+0.17}_{-0.14}$	$0.11^{+0.17}_{-0.11}$	$34.50^{+0.44}_{-0.43}$	$4.80^{+2.2}_{-2.4}$	-
GMO	0.21	-	$19.39^{+1.83}_{-1.56}$	$5.98^{+1.55}_{-2.11}$	$8.6^{+8.1}_{-8.1}$

are shown in Figure B1, where a strong positive correlation between the GMO thickness and solvation is indicated by the band-like diagonal shape of the 2D histogram. This suggests that a source of the uncertainty in the GMO solvation lies in the uncertainty of the thickness parameter.

Three further measurements of GMO adsorption at the iron oxide-dodecane interface were conducted at three different GMO concentrations of 0.5, 3 and 15 mM. These experiments were conducted with a different iron-coated silicon substrate on the FIGARO neutron reflectometer at 25 °C. The neutron wavelengths were selected to be approximately 2–20 Å, and two scattering angles of $\theta = 0.65°$ and 3.20° were used, resulting in a Q range of 0.007–0.351 Å^{-1}. The standard deviation of the dQ/Q resolution was approximately 3 %. For each concentration,

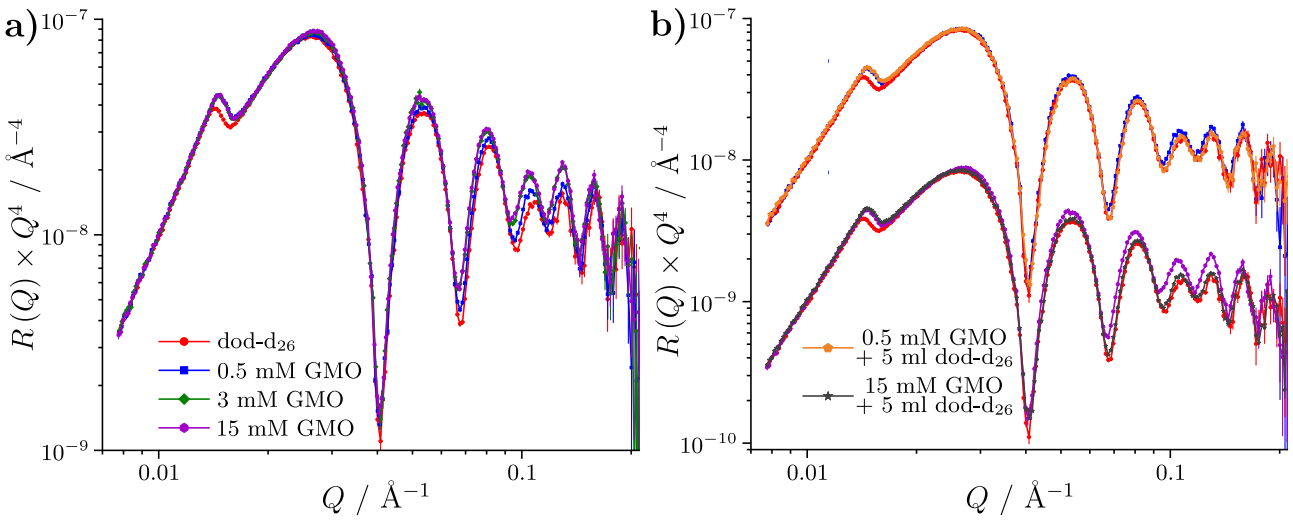

Figure 4.5: **a)** Reflectivity profiles of the GMO-dodecane systems collected with dodecane-d_{26}. The data are modified by a factor of Q^4 to aid comparison. **b)** Reflectivity profiles of the washed GMO-dodecane systems. The data collected with the 15 mM GMO solutions are offset by a factor of 10^{-1} for clarity.

three solvent contrasts were collected with approximately the same ratios as used for the 20 mM GMO-dodecane systems. The data were collected in order of ascending concentration per solvent contrast. Between each contrast, the substrates were cleaned with a 10 minute sonication in ethanol and then dodecane, followed by a 20 minute UV/ozone clean to ensure no residual GMO remained at the interface. Two additional datasets were collected after collecting the reflectivity profiles of the 0.5 and 15 mM GMO-dodecane-d_{26} systems, where an additional 5 ml of dodecane-d_{26} was passed into the solid-liquid cell before measuring the reflectivity. This was done as a qualitative check of the adsorption strength of GMO, where it can be expected that if GMO is chemisorbed at the interface, washing will not remove a significant amount from the interface. The data were then baseline subtracted in the data reduction process. The data collected with dodecane-d_{26} are shown in Figure 4.5, which are compared to the reflectivity collected with neat dodecane-d_{26} collected prior to exposure to any GMO-dodecane solutions.

The lower Q_c of the neat dodecane-d_{26} contrast is thought to arise from some residual dodecane-h_{26} remaining in the cell. The increasing difference to the Kiessig fringes as the GMO concentration increases from 0 to 0.5 to 3 mM implies the amount of GMO adsorbed at the interface increases. However, the similarity between the reflectivity of the solutions containing GMO at 3 and 15 mM suggests the amount of adsorbed GMO reaches a limit. The reflectivity collected with the washed systems appear to revert back to the reflectivity collected with neat dodecane-d_{26}. This implies that the majority of the GMO is desorbed with the additional solvent and any potential shear stress that is induced by flowing dodecane-d_{26} into the cell. Behaviour such as this is consistent with a physisorption mechanism as suggested through the depletion isotherms, and is similar to the desorption of GMO from steel-hexadecane interfaces studied using quartz crystal microbalance.[49]

The data collected with the 15 mM and 3 mM GMO-dodecane systems were fit using the same

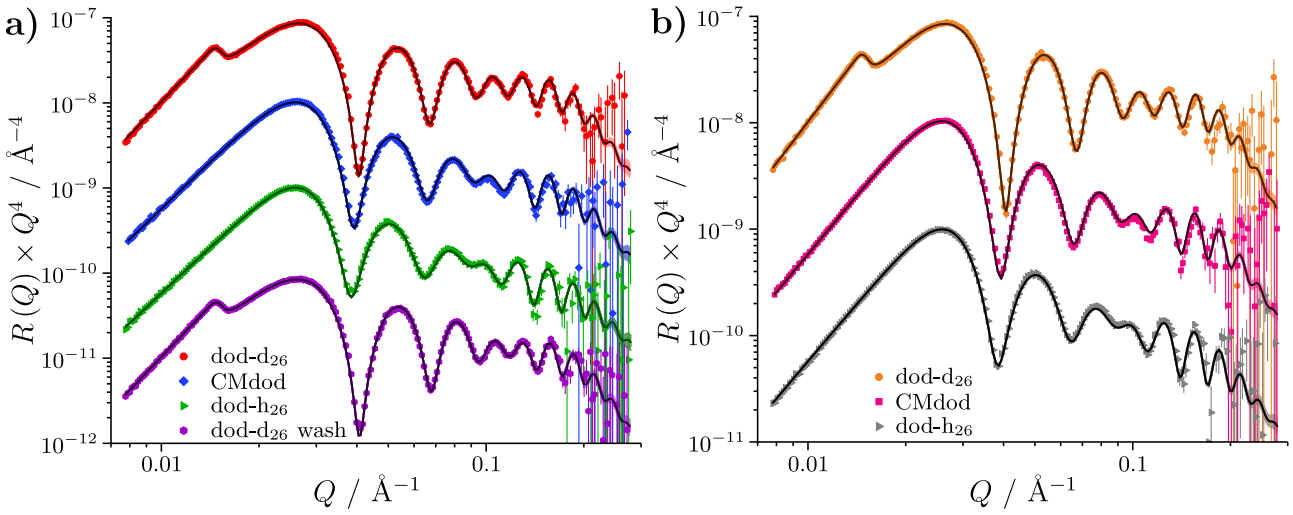

Figure 4.6: **a)** Fits to the data collected with the 15 mM GMO-dodecane solutions against the iron-coated silicon substrate. The data are offset by 10^{-1} between contrasts and are modified by a factor of Q^4 to aid comparison. **b)** The 3 mM GMO-dodecane solution equivalent to part **a)**.

model as the 20 mM system, as shown in Figure 4.4. The contrasts of the same concentrations were fit globally, including the reflectivity collected with the washed 15 mM system, which was modelled with a thickness, roughness and scattering length density. The two systems at different concentrations were fit individually. Therefore, there is a slight variation in the inferred parameters of the underlying substrate between the concentration systems. It would be more ideal to fit the three concentration systems simultaneously to constrain the parameters of the substrate, but this would drastically increase the computational time required. The resulting fits for the 15 mM system are shown in Figure 4.6a, while those to the 3 mM system are shown in Figure 4.6b. As the data were background subtracted, background parameters were not included in the fits, leading to some discrepancy around high Q. The layer parameters resulting from both fits are shown in Table 4.3.

If the adsorbed GMO forms a simple monolayer, the thickness of the GMO layers in the systems with concentrations $\geq$ 3 mM appear to be physically consistent with the expected extended length of a GMO molecule, which is 23.8 Å. If the adsorbed GMO molecules are fully extended, the angle of adsorption is estimated to be $\sim$ 45°–63° using the minimum and maximum 95 % confidence intervals for the GMO thickness from the 3, 15 and 20 mM systems. Through consideration of bond angles in GMO, the angle between the head group and the interface is calculated to be 22°–39°. This simple analysis provides an insight into a possible film structure, although it must be noted that it only considers the film to be a simple monolayer. For instance, it is most likely that gauche defects will also contribute to the difference between the inferred thickness and the extended length of GMO.

The solvation values for the 3, 15 and 20 mM GMO-dodecane systems are surprisingly low, especially for the former two. It is thought that the adsorption of GMO will decrease the apparent surface energy of the interface due to the presence of alkyl chain groups, increasing

Table 4.3: Median and 95 % confidence interval values for the inferred parameters from the MCMC fit to reflectivity collected with the 3 and 15 mM GMO-dodecane solutions against an iron-coated silicon substrate. The minimum number of independent samples was estimated to be 170858 and 71308 for the 3 and 15 mM GMO systems respectively. All the parameters had a standard deviation ≤ 2.10 and ≤ 1.36 for the 3 and 15 mM GMO systems, and hence are reported to 2 decimal places. The layers at the bottom of the table highlighted by an * are for the washed 15 mM GMO-dodecane system. The only difference for the FeO_x layer for the washed system is the roughness.

[GMO] / mol dm^{-3}	Layer	β_n / Å$^{-2} \times 10^{-6}$	β_m / Å$^{-2} \times 10^{-6}$	Thickness / Å	Roughness / Å	Solvation / %
3	Si	2.07	-	∞	3	-
	SiO_2	3.47	-	$11.53^{+0.59}_{-0.39}$	$5.57^{+0.19}_{-0.27}$	-
	Fe	$8.02^{+0.00}_{-0.00}$	$5.04^{+0.00}_{-0.00}$	$189.06^{+0.26}_{-0.33}$	$9.45^{+0.33}_{-0.41}$	-
	FeO_x	$6.30^{+0.06}_{-0.05}$	$0.06^{+0.07}_{-0.05}$	$31.79^{+0.15}_{-0.15}$	$4.83^{+0.36}_{-0.35}$	-
	GMO	0.21	-	$17.08^{+0.18}_{-0.17}$	$7.53^{+0.19}_{-0.19}$	$0.01^{+0.06}_{-0.01}$
15	Si	2.07	-	∞	3	-
	SiO_2	3.47	-	$18.32^{+1.25}_{-1.32}$	$4.94^{+0.41}_{-0.40}$	-
	Fe	$8.02^{+0.00}_{-0.00}$	$5.04^{+0.00}_{-0.00}$	$188.65^{+0.27}_{-0.27}$	$9.27^{+0.38}_{-0.40}$	-
	FeO_x	$6.38^{+0.05}_{-0.05}$	$0.15^{+0.06}_{-0.06}$	$31.70^{+0.14}_{-0.14}$	$5.29^{+0.35}_{-0.35}$	-
	GMO	0.21	-	$17.77^{+0.17}_{-0.17}$	$7.77^{+0.19}_{-0.19}$	$0.02^{+0.08}_{-0.02}$
15*	FeO_x^*	$6.38^{+0.05}_{-0.05}$	$0.15^{+0.06}_{-0.06}$	$31.70^{+0.14}_{-0.14}$	$5.92^{+0.50}_{-0.47}$	-
	GMO*	$0.79^{+0.25}_{-0.13}$	-	$14.80^{+0.67}_{-0.35}$	$7.17^{+0.21}_{-0.57}$	-

the attraction forces between the interface and dodecane. As a result, dodecane is expected to partially interdigitate into the GMO layer, forming dispersion interactions between the alkyl chains. The extent of solvent interdigitation also depends on the available volume between the adsorbate molecules, where liquid-like films tend to have greater solvations. As the solvation parameter is mostly determined by the dodecane-d_{26} contrast, it is possible that the fixed value of the GMO β_n overestimates the density of interfacial GMO, skewing the inferred solvation to lower values. This would also be the case if adventitious material remains at the interface after the adsorption of GMO and if the combined β_n of the interfacial layer is lower than 0.21×10^{-6} Å^{-2}. Whilst residual adventitious material has not been resolved from interfacial GMO, the similar reflectivity for the neat dodecane-d_{26} system and the washed interface after exposure to the 15 mM GMO-dodecane-d_{26} system suggests that the amount of adventitious material is similar between these two states. Assuming the adventitious material is not introduced to the interface via the solvent, this implies that the adventitious material is not significantly desorbed upon adsorption of GMO. Consequently, it is not possible to gauge if the GMO films are liquid- or solid-like from the inferred solvations.

The surface excess of the GMO for each fit can be calculated following Equation 4.4, assuming

Table 4.4: Median and 95 % confidence interval values for the derived surface excess and area per molecule for GMO at the iron oxide-dodecane interface at bulk GMO concentrations of 3, 15 and 20 mM.

[GMO] / mol dm^{-3}	Γ / mol m$^{-2} \times 10^{-6}$	A_{PM} / Å^2
3	$4.50^{+0.05}_{-0.04}$	$36.86^{+0.36}_{-0.39}$
15	$4.69^{+0.05}_{-0.05}$	$35.43^{+0.35}_{-0.34}$
20	$4.68^{+0.13}_{-0.13}$	$35.51^{+0.99}_{-0.97}$

that the layer is comprised solely of GMO and solvent.

$$\Gamma = \frac{d \times \beta_{\mathrm{n}} \times (1 - \phi)}{b \times N_{\mathrm{A}}} \tag{4.4}$$

Here, ϕ is the volume fraction of the solvent in the GMO layer. The calculated Γ and A_{PM} for each concentration measured on INTER and FIGARO are shown in Table 4.4. The calculated surface excesses of the 3 mM and 15 mM GMO-dodecane systems agree well with the 20 mM system. Furthermore, they also agree reasonably with the value determined via the depletion isotherm technique, although they are slightly greater. It is thought that two factors give rise to the greater surface excess. The first relates to the presence of adventitious material at the interface, where it is thought to skew the determined surface excess to greater values as NR cannot resolve GMO from the adventitious material. The second factor relates to the calculation of Γ, which does not include the effect of surface roughness.[46] Therefore, the amount of adsorbate per unit surface area is potentially overestimated.

The data collected with 0.5 mM GMO-dodecane solutions were not fit using the same model, as the reflectivity indicates that the interface was not saturated. Therefore, a nested sampling study was conducted to find a suitable model to describe the data and the results are shown in Figure 4.7. The initial values and priors for each parameter are shown in Table A6. The GMO layer formed in the 0.5 mM system was described by a scattering length density and/or a solvation alongside thickness and roughness parameters. Similar to the 15 mM system, the dataset collected after washing the 0.5 mM dodecane-d_{26} contrast was modelled simultaneously with the reflectivity collected with the 0.5 mM system. The interfacial film in the washed dataset was modelled either as a separate layer with a thickness, roughness and a scattering length density, or was forced to be the same as the GMO layer formed in the 0.5 mM systems.

Following the nested sampling, the data were fit with the highest model evidence and the resulting fits are compared in Figure 4.8a. The up-spin scattering length density profiles are presented in Figure 4.8b. The β_{++} profile prior to and after washing the surface with additional dodecane-d_{26} is also compared. The minor difference between these profiles suggest that while GMO adsorbs at the interface, the scattering length density and the thickness of the interfacial film are remarkably similar with or without GMO. The latter could imply the adoption of small

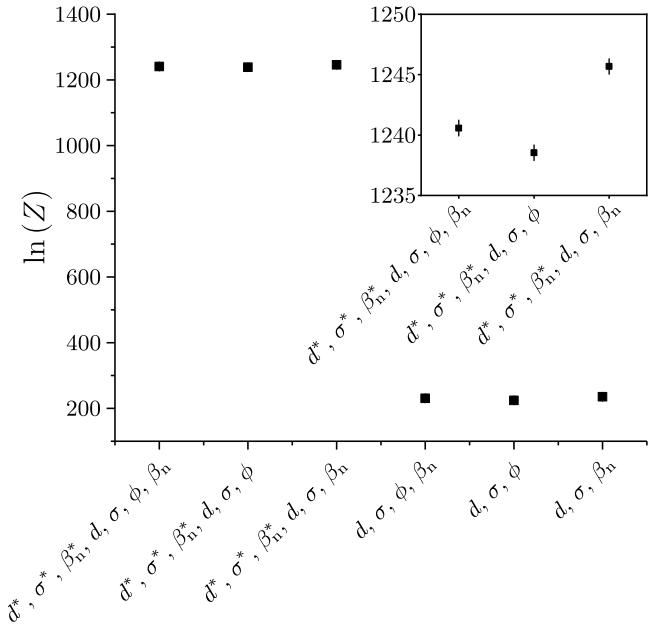

Figure 4.7: Nested sampling results for the models considered to describe the reflectivity with the 0.5 mM GMO-dodecane systems. The parameters marked with * describe the separate interfacial film modelled for the washed 0.5 mM GMO data.

angles from the interface when adsorbed with a low surface excess.

A surface excess was calculated by re-fitting the data with a separate model, where the GMO β_n was held constant at 0.21×10^{-6} Å^{-2} and the solvation allowed to vary. The determined surface excess was $4.0^{+0.0}_{-0.1} \times 10^{-6}$ mol m^{-2}. Compared to the depletion isotherm at 30 °C, the surface excess determined by NR is greater by approximately 0.8×10^{-6} mol m^{-2} or 25 %. This is greater than the difference between the surface excess determined via NR at 15 or 20 mM and the maximum surface excess, Γ_m, determined via the depletion isotherm at 30 °C. As the interface is not saturated with GMO, it is thought that the greater surface excess arises from the presence of adventitious material at the interface as discussed previously. However, in this case the adsorbed amount of GMO is even lower, increasing the difference between the NR and the depletion isotherm results.

Neutron reflectometry with partially deuterated glycerol monooleate

The calculation of the GMO angle of adsorption relies on assuming a monolayer structure. By using partially deuterated GMO (dGMO), see Figure 4.9, a significant neutron refractive index boundary can be formed at the interface between the head and the deuterated tail group, if the adsorbed dGMO adopts a monolayer-like structure. Therefore, by modelling the data with specific orientations, the structure of the adsorbate layer can be inferred.

Partially deuterated GMO was prepared by Dr James Tellam, ISIS, UK, and was estimated by ^{1}H nuclear magnetic resonance (NMR) spectroscopy to have a deuteration percentage of $\sim$ 90 % in the tail region. This was dissolved in dodecane at 0.5 mM and 20 mM, where three solvent contrasts were prepared with 100 % dodecane-d_{26}, 100 % dodecane-h_{26} and CMdod.

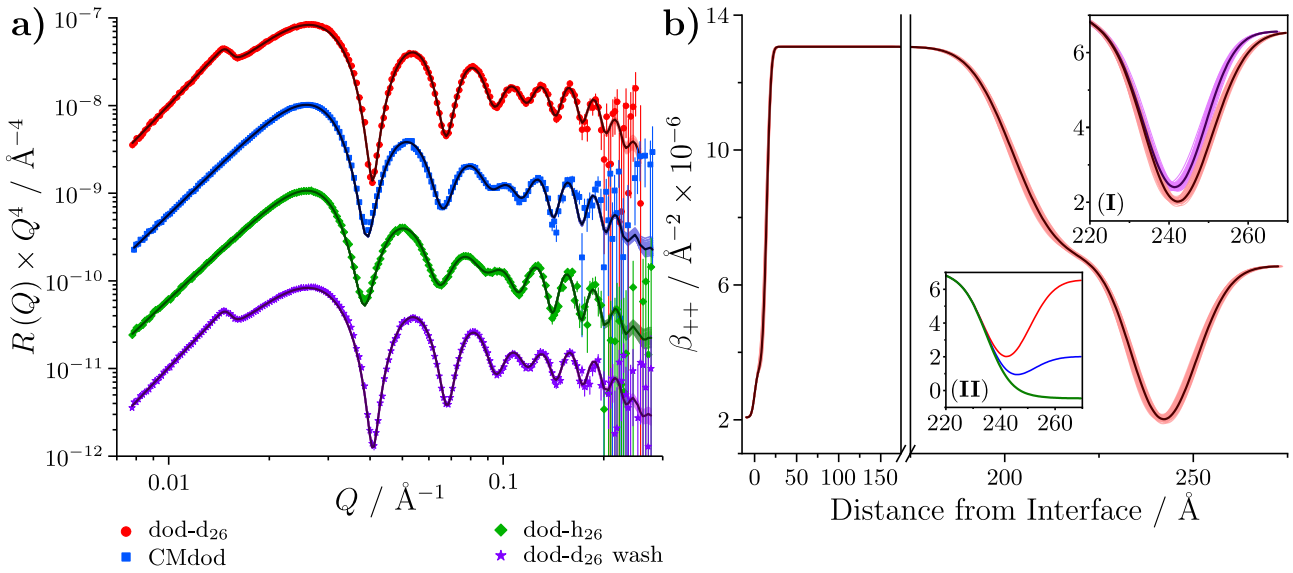

Figure 4.8: **a)** Fits to the data collected with the 0.5 mM GMO-dodecane solutions against an iron-coated silicon substrate. The data are modified by a factor of Q^4 and offset by 10^{-1} sequentially to aid comparison. **b)** The median up-spin scattering length density profile of the dodecane-d$_{26}$ contrast of the 0.5 mM GMO-dodecane system. The inset labelled (**I**) compares 50 random samples from the posterior distribution of the 0.5 mM GMO-dodecane-d$_{26}$ contrast against that of the washed system. The inset labelled (**II**) compares the median scattering length density profiles of the three 0.5 mM GMO-dodecane contrasts. The colours follow the same general trend as part **a)**.

Table 4.5: Median and 95 % confidence interval values for the inferred parameters from the MCMC fit to the reflectivity collected with the 0.5 mM GMO-dodecane solutions against an iron-coated silicon substrate. The minimum number of independent samples was estimated to be 27353. All the parameters had a standard deviation < 0.84 and hence are reported to 2 decimal places. The GMO layer highlighted by the * represents the interfacial layer after washing with the additional neat dodecane-d$_{26}$ aliquot.

Layer	β_n / Å$^{-2} \times 10^{-6}$	β_m / Å$^{-2} \times 10^{-6}$	Thickness / Å	Roughness / Å
Si	2.07	-	∞	3
SiO_2	3.47	-	$14.40^{+0.85}_{-1.07}$	$4.03^{+0.41}_{-0.40}$
Fe	$8.02^{+0.00}_{-0.00}$	$5.04^{+0.00}_{-0.00}$	$187.73^{+0.25}_{-0.25}$	$9.01^{+0.39}_{-0.43}$
FeO_x	$6.38^{+0.06}_{-0.05}$	$0.40^{+0.06}_{-0.06}$	$32.65^{+0.53}_{-0.51}$	$6.82^{+0.54}_{-0.58}$
GMO	$-0.09^{+0.33}_{-0.35}$	-	$14.64^{+0.71}_{-0.70}$	$7.69^{+0.32}_{-0.30}$
GMO*	$0.35^{+0.30}_{-0.30}$	-	$13.08^{+0.62}_{-0.59}$	$6.47^{+0.31}_{-0.30}$

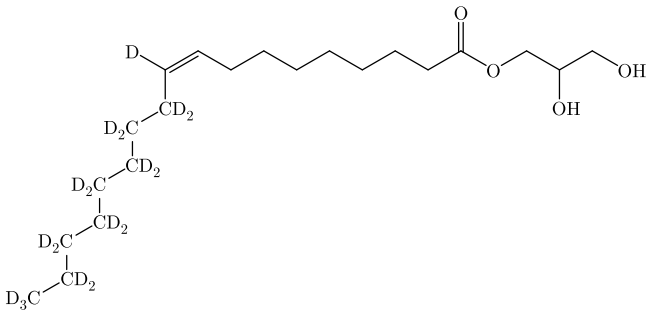

Figure 4.9: The structure of the partially deuterated GMO (dGMO) used in this work.

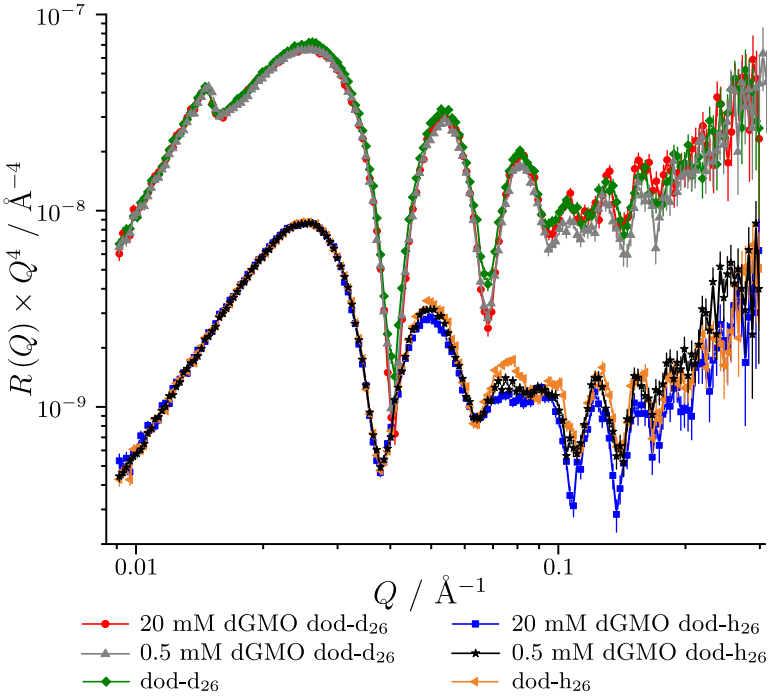

Figure 4.10: Modified reflectivity of the 0.5 and 20 mM dGMO systems compared against dodecane-d_{26} and dodecane-h_{26} contrasts of the same substrate. Reflectivity of the contrasts collected with dodecane-h_{26} have been offset by 10^{-1} for clarity. The lines are interpolations to guide the eye.

The reflectivity was measured on INTER with the same instrument settings as used in the collection of the reflectivity of the 20 mM GMO-dodecane system. The reflectivity of the 0.5 mM dGMO-dodecane system was measured first in a solid-liquid cell with the following contrast order: dodecane-h_{26}, CMdod and dodecane-d_{26}. After, the reflectivity of the 20 mM system was collected in the same order. The reflectivity collected with the 0.5 mM and 20 mM systems in 100 % dodecane-d_{26} and 100 % dodecane-h_{26} are shown in Figure 4.10. The increasing fringe amplitude in both contrasts with dGMO concentration arises from a greater contrast between the iron oxide, the interfacial film and the dodecane. The change in the dodecane-d_{26} contrast is thought to arise from an increasing number of hydrogenated head groups at the interface, thus lowering β_n between the iron oxide and solvent. Contrastingly, the difference between the dodecane-h_{26} systems is thought to result from the increasing concentration of deuterated tail groups at the interface.

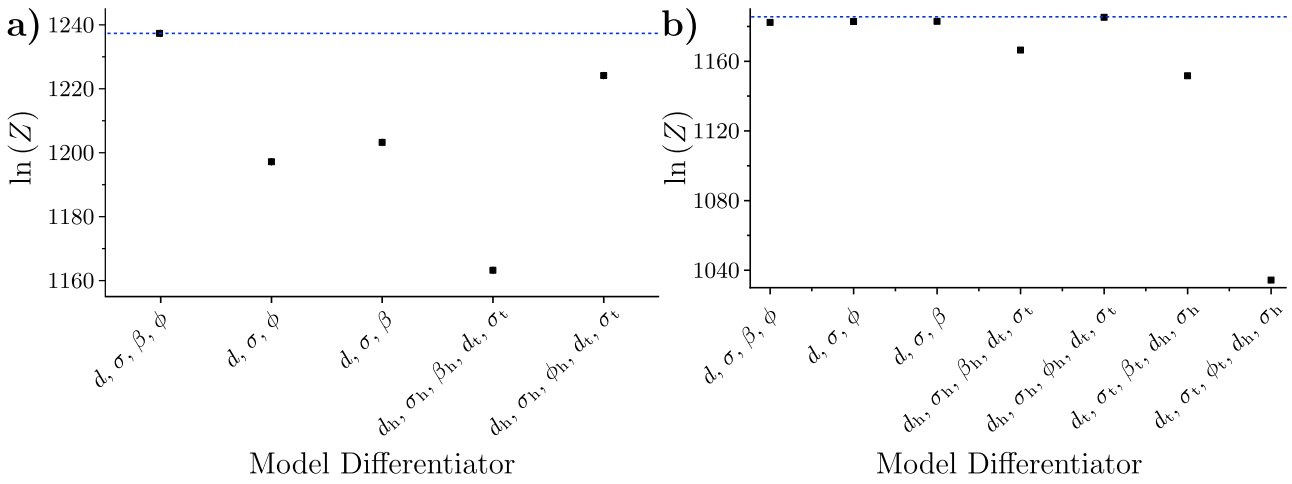

Figure 4.11: **a)** Estimated evidences for the models used to describe the 0.5 mM dGMO data. The blue dashed line shows the highest evidence determined. **b)** Estimated evidences for a number of candidate models to represent the 20 mM dGMO data.

A nested sampling study was conducted on both systems to find a suitable combination of layer parameters to adequately model the data. Three models were proposed where the adsorbed dGMO was described by one layer, with an average $\beta_{\mathrm{n}} \sim 3.2\times10^{-6}$ Å^{-2}. These models represent a layer with no orientation, where the molecules are adsorbed with the head group equally likely to face the solvent as to face the iron oxide surface. Other models were considered where the dGMO molecules are adsorbed at the interface either with their heads groups adsorbed at the interface and their alkyl tails extending into the solvent, or vice versa in the case of the 20 mM dGMO system. Additionally, for the two layer models, the surface excesses of the head and tail groups were constrained together so that the number of each matched. This was achieved by constraining either the solvation or scattering length density of the outer layer to a function of the other parameters by equating the surface excesses of the head and tail groups together. For example, in the model where the head group solvation, ϕ_{h}, was allowed to fit, the tail group solvation, ϕ_{t} was constrained so that:

$$\phi_{\mathrm{t}} = \frac{d_{\mathrm{h}}\,\beta_{\mathrm{h}}\,\phi_{\mathrm{h}}\,b_{\mathrm{t}}}{d_{\mathrm{t}}\,\beta_{\mathrm{t}}\,b_{\mathrm{h}}} \tag{4.5}$$

where the subscripts, h and t, describe the head or tail layer to which the parameters belong. The scattering lengths, b_{h} and b_{t}, are 2.07×10^{-4} and 1.80×10^{-3} Å respectively. Further to Equation 4.5, ϕ_{t} was limited to a range between zero and one to avoid non-physical parameter values. A similar technique has been used to characterise the adsorbed structure of partially deuterated material at air-liquid interfaces.[118,192] The initial values and priors for each parameter are shown in Table A7 and the results from the nested sampling are shown in Figure 4.11.

The model with the greatest evidence for the 0.5 mM system is a one layer system, suggesting that the orientation of the adsorbed GMO is not well defined. This model was used to fit the data using an MCMC scheme, and the resulting fit and β_{++} profile are both shown in Fig-

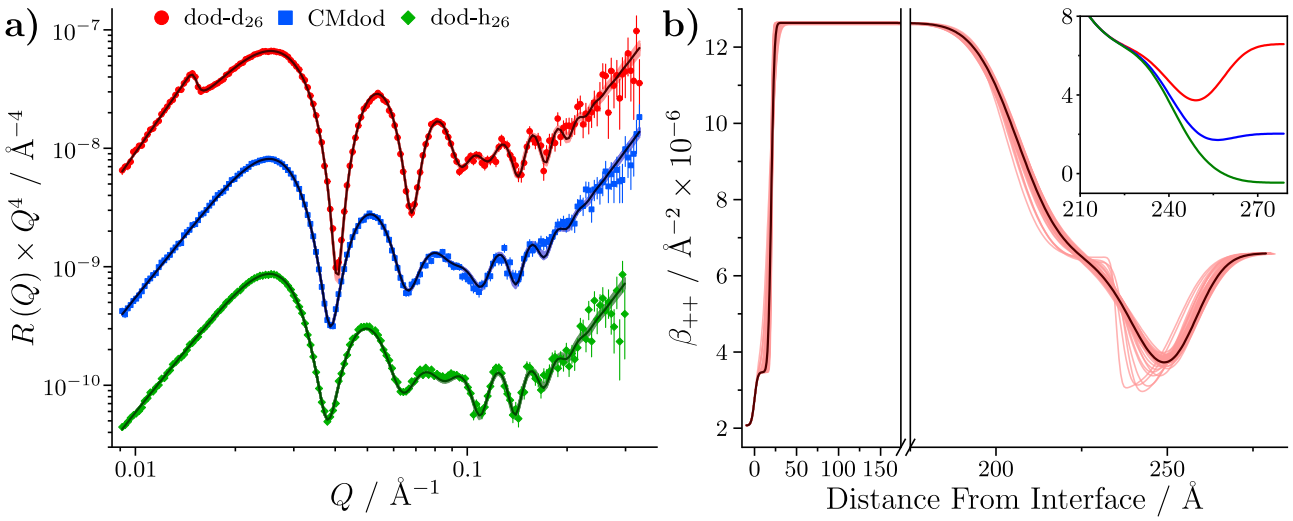

Figure 4.12: **a)** Comparison of fits to the reflectivity collected with the three contrasts of 0.5 mM dGMO in dodecane. The reflectivity is modified by a factor of Q^4. The CMdod and dodecane-h_{26} contrasts are offset by factors of 10^{-1} in reflectivity. **b)** Median spin-up scattering length density profile for the contrast collected with dodecane-d_{26}. The light band shows 50 random samples from the posterior distribution. The inset compares the median β_{++} profiles for all three contrasts at the iron oxide-dodecane interface.

Table 4.6: Median and 95 % confidence interval parameter values for the 0.5 mM dGMO-dodecane solutions against an iron-coated silicon substrate. The minimum number of independent samples was estimated to be 9044, allowing those parameters with standard deviations ≤ 0.48 to be reported to 2 decimal places. Those parameters with standard deviations > 0.48 are reported to one decimal place.

Layer	β_n / Å$^{-2} \times 10^{-6}$	β_m / Å$^{-2} \times 10^{-6}$	Thickness / Å	Roughness / Å	Solvation / %
Si	2.07	-	∞	3	-
SiO_2	3.47	-	$19.9^{+1.4}_{-2.3}$	$3.0^{+3.3}_{-1.8}$	-
Fe	$8.01^{+0.01}_{-0.03}$	$4.62^{+0.03}_{-0.02}$	$186.44^{+0.35}_{-0.37}$	$10.2^{+0.6}_{-1.9}$	-
FeO_x	$6.41^{+0.11}_{-0.10}$	$0.01^{+0.04}_{-0.01}$	$34.9^{+1.0}_{-2.6}$	$8.8^{+1.4}_{-7.0}$	-
dGMO	$0.6^{+1.4}_{-0.6}$	-	$16.0^{+2.0}_{-1.4}$	$7.2^{+1.0}_{-1.8}$	31^{+7}_{-14}

ure 4.12. Despite the large uncertainty around the iron oxide roughness, the inferred parameter values shown in Table 4.6 are similar to those collected with 0.5 mM hydrogenated GMO in dodecane. As the β_n of the dGMO is expected to be $\sim 3.2 \times 10^{-6}$ Å^{-2}, the low value of the inferred scattering length density supports the previous suggestion that adventitious material remains at the interface at low bulk concentrations of GMO. Similarly, the inferred thickness values support the suggestion that GMO adsorbs at greater angles from the normal at lower concentrations.

The model with the greatest evidence for the 20 mM dGMO-dodecane system is the monolayer model which follows Equation 4.5 where β_h and β_t were held constant. A model where the scattering length density and solvation of both head and tail group were fit simultaneously was

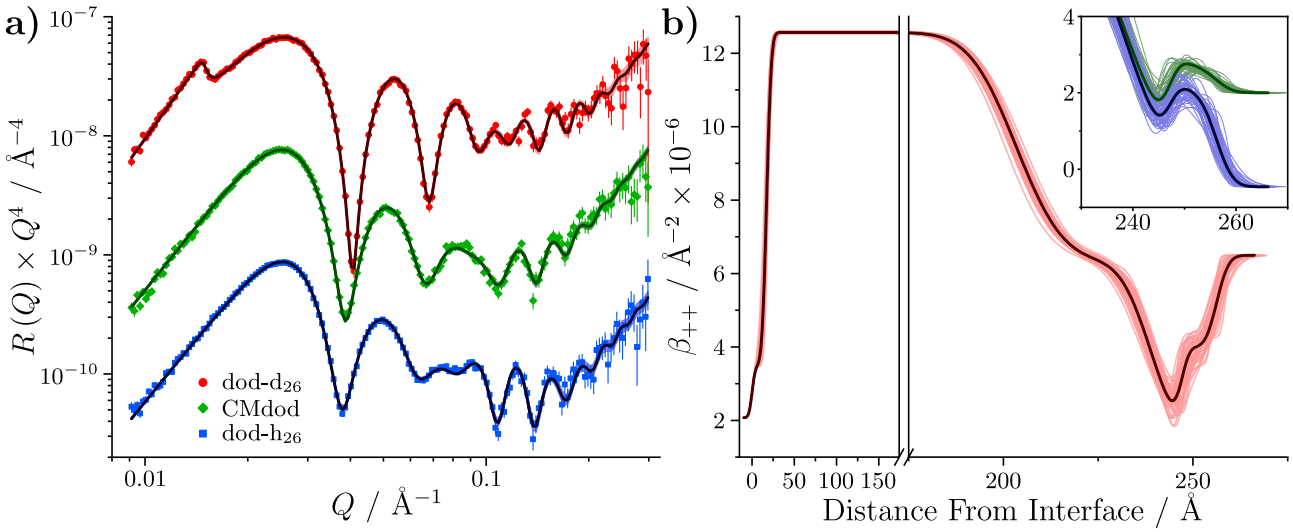

Figure 4.13: **a)** Comparison of fits to the reflectivity collected with the three contrasts of 20 mM dGMO in dodecane. The reflectivity is modified by a factor of Q^4. The CMdod and dodecane-h_{26} contrasts are offset by factors of 10^{-1} in reflectivity. **b)** Median spin-up scattering length density profile for the contrast collected with dodecane-d_{26}. The light band shows 50 random samples from the posterior distribution. The inset shows the analogous profiles for the CMdod and dodecane-h_{26} contrasts focussed on the dGMO layer.

Table 4.7: Median and 95 % confidence interval parameter values for the 20 mM dGMO-dodecane solutions against an iron-coated silicon substrate. The minimum number of independent samples was estimated to be 76853, allowing those parameters with standard deviations ≤ 1.07 to be reported to 2 decimal places. Those parameters with standard deviations > 1.07 are reported to one decimal place.

Layer	β_n / Å$^{-2} \times 10^{-6}$	β_m / Å$^{-2} \times 10^{-6}$	Thickness / Å	Roughness / Å	Solvation / %
Si	2.07	-	∞	3	-
SiO_2	3.47	-	$17.22^{+1.60}_{-2.19}$	$4.37^{+0.99}_{-1.02}$	-
Fe	$7.87^{+0.05}_{-0.05}$	$4.70^{+0.04}_{-0.04}$	$186.18^{+0.52}_{-0.55}$	$9.80^{+0.78}_{-0.94}$	-
FeO_x	$6.22^{+0.13}_{-0.12}$	$0.11^{+0.11}_{-0.10}$	$35.48^{+0.36}_{-0.36}$	$6.25^{+1.10}_{-1.32}$	-
$dGMO_h$	0.33	-	$8.17^{+0.85}_{-0.82}$	$1.78^{+1.85}_{-0.75}$	$18.04^{+9.13}_{-10.61}$
$dGMO_t$	2.88	-	$9.17^{+1.71}_{-2.21}$	$2.50^{+1.74}_{-1.42}$	$27.3^{+11.2}_{-21.9}$

proposed. However, the posterior distribution did not return feasible β_h and β_t values when allowed to vary. Therefore, the model shown with the greatest evidence was used to fit the data following an MCMC routine, where the fits and resulting β_{++} profile are shown in Figure 4.13. The inferred parameter distributions are shown in Table 4.7.

The combined thickness of the head and tail group is $17.3^{+1.4}_{-1.7}$ Å, which agrees reasonably with the thicknesses measured with hydrogenated GMO. Additionally, the fitted thickness of the head and tail group are consistent with the maximum extended lengths of both regions, 16.8 and 10.8 Å, respectively. Assuming the dGMO is fully extended, the thickness of the head group suggests the angle between the head group and the interface is 26°–32°. This range

agrees with the angles inferred from the data collected with hydrogenated GMO. By taking the smallest angle between the head group and the tail group to be 130.5°, the projection of the tail group in the normal direction from the interface can be estimated to be 10.7 to 10.4 Å. These values are in the upper region of the inferred tail thickness distribution, and so this simple model, which does not include the possible shortening effects of gauche defects, appears to be consistent with the inferred dGMO structure.

Calculating the surface excess of dGMO is not as trivial as shown in Equation 4.4 for a standard block layer. This is due to modelling the interfacial layer as separate head and tail groups, where either thickness is approximately half that of the complete GMO layer. As such, the calculated surface excesses are lower than expected by the same factor. However, a combined surface excess can be calculated if a combined solvation, ϕ_{comb}, is defined. In this case, it was defined as

$$\phi_{\mathrm{comb}} = \left(\frac{n_{\mathrm{h}}}{n_{\mathrm{tot}}}\right)\phi_{\mathrm{h}} + \left(1 - \frac{n_{\mathrm{h}}}{n_{\mathrm{tot}}}\right)\phi_{\mathrm{t}}, \tag{4.6}$$

where $n_{\mathrm{h}} = 14$ and $n_{\mathrm{tot}} = 23$, which are the number of backbone (non-branched C and O) atoms in the head group and the whole GMO molecule respectively. This method was used to take into account the different lengths of the tail and head group. Hence, it was calculated that $\phi_{\mathrm{comb}} = 21.1^{+5.2}_{-6.0}$ %. Using the combined thickness calculated above and β_{n} of the whole dGMO molecule, the combined surface excess was calculated to be $3.6^{+0.3}_{-0.2} \times 10^{-6}$ mol m^{-2} and the corresponding area per molecule was calculated as $A_{\mathrm{PM}} = 46.0^{+3.0}_{-3.5}$ Å^2. These values align with the depletion isotherm results but imply a significantly lower amount of adsorbed dGMO when compared to the values determined via NR with hydrogenated GMO.

As the overall thickness value is approximately the same between these datasets, the lower surface excess mostly arises from the greater solvation of the adsorbed dGMO layer. The values imply a less dense adsorbate layer than those determined with hydrogenated GMO, and are similar to solvation values reported for other OFMs at similar bulk concentrations.[45,46] As the contrast between the solvent and the deuterated tail region of the monolayer is less affected by the presence of any adventitious material remaining at the interface, it is possible that the solvation values are more accurate. Furthermore, as the reflectivity collected with dodecane-h_{26} has greater contrast with the deuterated tail while the dodecane-d_{26} contrast retains a high level of information on the state of the hydrogenated head group, it is postulated that the combined datasets contain more information regarding the solvation state of the interfacial layer than those contrasts with hydrogenated GMO. This is not proven here, but it would be possible to investigate the optimal contrasts for parameter inference for future studies following a methodology laid out elsewhere.[193]

Another possibility that could account for the lower surface excess is the presence of other impurity molecules. For example, the analogous glycerol ester with two alkyl chains is known to be surface active, and is feasibly formed through the esterification reaction of glycerol and

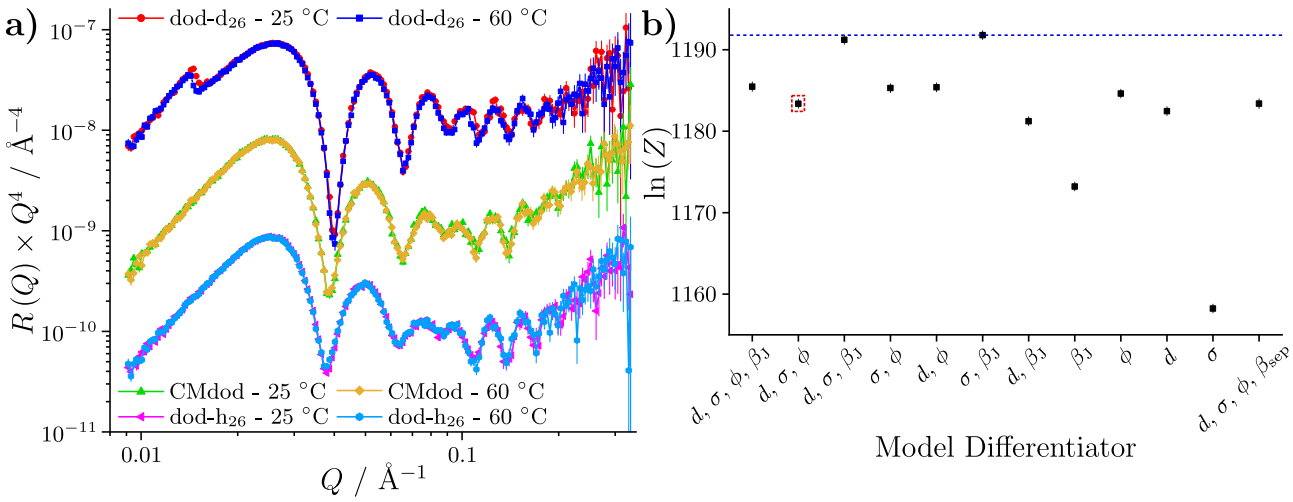

Figure 4.14: **a)** Comparison of the reflectivity from the 20 mM GMO-dodecane system against an iron-coated silicon substrate at 25 and 60 °C. The modified reflectivity has been offset by factors of 10^{-1} to aid comparison. Lines between data points are interpolations. **b)** Nested sampling results for a selection of models considered. The model used in the following fit is highlighted by the red dashed box.

oleic acid, which was used in the synthesis. If adsorbed at the interface, the greater volume occupied by the additional alkyl chain group will translate to a greater area per molecule, and hence lower surface excess.

4.3.2 Film structure at elevated temperature

The reflectivity collected on INTER with the three contrasts of the 20 mM GMO-dodecane system at 60 °C is compared to the data collected at 25 °C in Figure 4.14a. The similarity between the datasets agree with the previous suggestion that the small temperature swing does not affect the underlying substrate structure, and furthermore, suggests that the GMO layer is similar at the two temperatures. The greatest difference between the profiles is the location of the critical edge in the dodecane-d_{26} contrasts. The difference in Q_c is 3–6 $\times 10^{-4}$ Å^{-1}, which, assuming that the density of silicon is unchanged with temperature, relates to a 3–5 % decrease in the density of dodecane-d_{26} when going from 25 to 60 °C. This range arises from the uncertainty over the precise location of the critical edge due to the low number of points around the discontinuity. The reported decrease in density is 1–2 % for dodecane-h_{26} for the same temperature transition. It is expected that the density variation with temperature is approximately the same between these isotopologues, and therefore the calculated density difference agrees reasonably. It is possible that evaporation occurred over the course of the measurement, leading to greater amounts of air against the substrate. However, the flat reflectivity above the critical edge suggests that this has not occurred to a significant extent, since patches of air can be diagnosed by a negative gradient in the reflectivity above the critical edge. This is caused by the incoherent addition of reflectivity arising from the parts of the substrate coated in dodecane and those parts held against air.

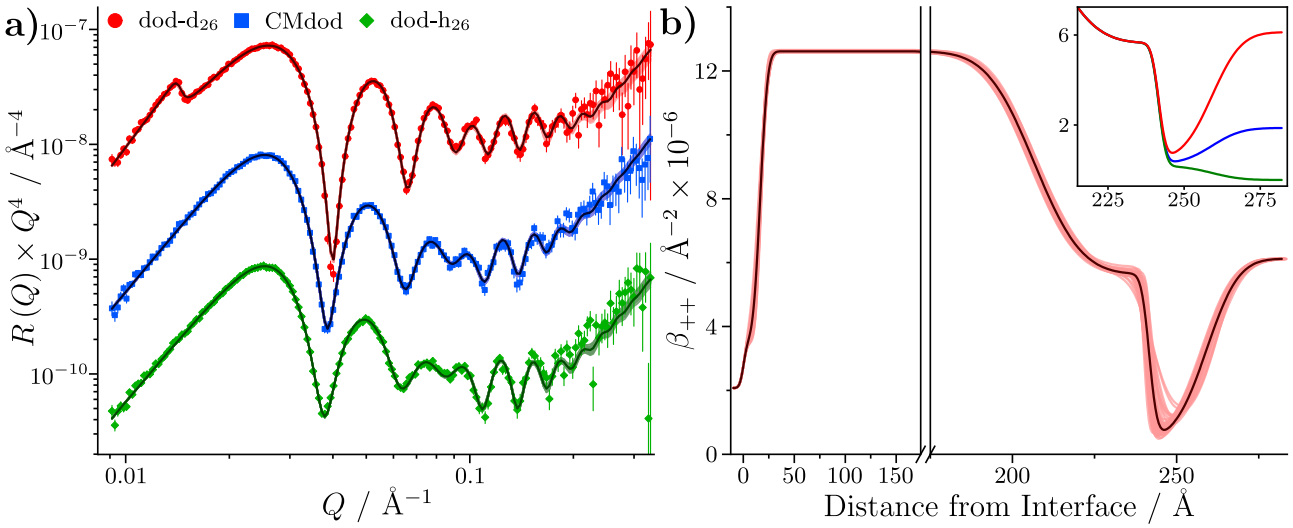

Figure 4.15: **a)** Median fits to the reflectivity collected at 60 °C. The shaded bands show 50 random samples from the posterior distribution. The contrasts are offset by 10^{-1} for clarity. **b)** The median β_{++} profile for the contrast collected with dodecane-d_{26} at 60 °C. The shaded band represents 50 random samples from the posterior distribution. The inset shows the median fits for all three contrasts focused on the iron oxide-dodecane interface.

A nested sampling study was conducted using a similar set of models as used for modelling the 25 °C data. The starting values and priors for each parameter are the same as those used for modelling the 25 °C data, and are shown Table A5. The model with highest evidence was one where not all the parameters that characterise a layer were fit. In this case, the thickness was fixed to 20 Å, and hence, no information regarding the uncertainty in the thickness could be inferred.

The models with at least three parameters are considered to represent the layer completely. Hence, the model with greatest evidence is considered to be the one where d, σ and β_J were fit. However, in this case $\beta_J = 0.8^{+0.2}_{-0.2} \times 10^{-6}$ Å^{-2}, which, if assuming a change in density is the only reason for the increase in β_n, would relate to a minimum increase of the GMO density by ~ 3 fold. It is not expected that an increase in temperature would lead to such a dramatic increase in density. Therefore, the upper limit of β_J was restricted to 0.3×10^{-6} Å^{-2}, which translates to an increase in density by a factor of ~ 1.5. The estimated evidence was found to reduce so that $\ln(Z) = 1184.0 \pm 0.3$. Similarly, for the model where β_J and ϕ are fit, when restricting $\beta_J \leq 0.4 \times 10^{-6}$ Å^{-2}, the evidence was reduced so that $\ln(Z) = 1181.3 \pm 0.5$.

Despite the higher evidence for the model where d, σ and β_J were fit, and its restricted variant, the model highlighted by the red dashed box, where $\ln(Z) = 1183.4 \pm 0.5$, was chosen to fit the data. This decision was made as the β_J of GMO is physically believable when fixed at 0.21×10^{-6} Å^{-2}. Furthermore, this model is more easily compared to the data collected at 25 °C as the relationship between the scattering length and number density still hold, and hence a comparable surface excess can be defined. The fit following the MCMC routine is compared to the data in Figure 4.15a, and the resulting β_{++} profile is shown in Figure 4.15b. The inferred parameter values are shown in Table 4.8 and the corner plot is shown in Figure B2.

Table 4.8: Median and 95 % confidence interval values for the inferred parameters from the MCMC fit to the reflectivity collected with the 20 mM GMO-dodecane solutions against an iron-coated silicon substrate at 60 °C. The minimum number of independent samples was estimated to be 108011, allowing those parameters with standard deviations ≤ 1.67 to be reported to 2 decimal places. Those parameters with standard deviations > 1.67 are reported to one decimal place.

Layer	β_n / $Å^{-2} \times 10^{-6}$	β_m / $Å^{-2} \times 10^{-6}$	Thickness / Å	Roughness / Å	Solvation / %
Si	2.07	-	∞	3	-
SiO_2	3.47	-	$16.54^{+1.35}_{-1.52}$	$5.61^{+0.89}_{-1.08}$	-
Fe	$7.94^{+0.06}_{-0.06}$	$4.68^{+0.04}_{-0.04}$	$190.01^{+0.48}_{-0.65}$	$11.38^{+0.67}_{-0.90}$	-
FeO_x	$5.58^{+0.12}_{-0.10}$	$0.04^{+0.11}_{-0.04}$	$35.05^{+0.36}_{-0.35}$	$1.93^{+1.84}_{-0.89}$	-
GMO	0.21	-	$17.48^{+1.72}_{-0.89}$	$7.63^{+0.94}_{-1.58}$	$4.2^{+9.7}_{-4.1}$

The inferred thickness and solvation are very similar to those determined from the reflectivity collected at 25 °C, suggesting that that structure of GMO is unperturbed by the increase in temperature. Consequently, the calculated surface excess and area per molecule are very similar to those calculated at 25 °C, where $\Gamma = 4.41^{+0.13}_{-0.12} \times 10^{-6}$ mol m^{-2} and $A_{PM} = 37.67^{+1.05}_{-1.09}$ Å^2. The calculated surface excess and area per molecule do not align with those calculated at 60 °C from the depletion isotherms. The reason for the discrepancy is not known but a few potential reasons are discussed below.

Following a solubility study where GMO-dodecane solutions (0.5–50 mM) remained visibly clear for an hour at 60 °C, it is not expected that significant precipitation of GMO would occur in either experiment. Furthermore, precipitation in the isotherm study would lead to a greater apparent surface excess following centrifugation; for NR, any precipitate would collect on the unprobed PEEK-dodecane interface which should not affect the GMO structure at the iron oxide-dodecane interface aside from lowering the bulk concentration of GMO. However, it is possible that the interfacial GMO structure formed in the NR experiments at 25 °C requires a long period of time to reach equilibrium when raised to 60 °C. This is contrasted in the depletion isotherm experiments, where the iron oxide surface was introduced to the GMO-dodecane solutions at 60 °C. If the GMO structure formed at 25 °C is solid-like, the temperature may not be great enough to melt the interfacial layer as has been found for monolayers of alkanes adsorbed on graphite surfaces.[194] The freezing point for a small film of GMO physisorbed on graphite powder has also been reported to be approximately 30 °C above the bulk freezing point, which may suggest the melting point of adsorbed GMO films is delayed to higher temperatures compared to the bulk GMO melting point of 35 °C.[195]

It is also possible that the comparable surface excess to that inferred from the reflectivity collected at 25 °C is caused by the presence of adventitious material at the interface. As the difference in surface excess between the 0.5 mM and 20 mM systems is only $\sim 0.7 \times 10^{-6}$

mol m^{-2} at 25 °C, it is expected that the temperature-induced desorption of GMO leads to a similar small difference between the apparent surface excesses at 25 and 60 °C. Another possible explanation is that the iron oxide surface area changed between the measurements of the depletion isotherm. However, the samples were prepared within a day of each other so if such a change were to occur, it would be minimal. Finally, it is noted that the comparison between the depletion isotherm and NR results relies on a large extrapolation of the data from from 3 mM to 20 mM. As such, it is possible that the surface excess continues to rise with concentration at 60 °C.

4.3.3 Adsorption in the presence of water

Water is a contaminant in engine oils that can be emulsified by polar chemicals. As the contents of the oil oxidise with age, the overall polarity of the oil increases, thereby increasing the solubility of water within the oil.[196] Following simulations that suggest water co-adsorbs with GMO at the mica-heptane interface[163], the adsorption of GMO in the presence of water at iron oxide-dodecane interfaces was investigated using NR. The contrast difference between H_2O and D_2O enables the differentiation of adsorbed water from GMO. Four solutions of GMO-water-dodecane were prepared at a GMO concentration of 20 mM, where the water-to-surfactant ratio, W, was fixed at 5 for all four solutions. Two solutions were prepared with dodecane-d_{26}, while the other two solutions were prepared with dodecane-h_{26} and CMdod. For the two solutions prepared with dodecane-d_{26}, one contained 100 % H_2O, and the other contained 100 % D_2O. The CMdod contrast contained H_2O, while the dodecane-h_{26} contrast contained 100 % D_2O.

The solutions were injected into a solid-liquid cell containing an iron-coated silicon substrate equilibrated at 25 °C in the order of dodecane-d_{26}+H_2O, dodecane-d_{26}+D_2O, CMdod+H_2O and finally dodecane-h_{26}+D_2O, where the subsequent reflectivity from each system was measured sequentially. The reflectivity was measured on INTER with the same instrumental set-up as discussed previously, although the standard deviation dQ/Q resolution was 3 %. Between the contrasts, the cell was heated to 60 °C and the reflectivity was measured in order to ascertain the change of the GMO interfacial structure with temperature. The sample preparation and collection of the reflectivity was conducted by Fin and Becky. The resulting reflectivity profiles for the dodecane-d_{26} and dodecane-h_{26} systems at 25 °C are shown in Figure 4.16a, and they are compared to the profiles collected with dodecane-d_{26} and dodecane-h_{26} with D_2O stirred over them, as shown in Figure 3.15.

The differences between the fringe amplitudes of the dodecane-d_{26} solutions relate to a change in the contrast at the interface, where the difference between the neat solvent and the GMO-D_2O contrast appears similar to that seen with dry GMO-dodecane solutions. As D_2O has a similar β_n to dodecane-d_{26}, the difference in fringe amplitude is attributed to the adsorption of GMO at the interface. However, the greater fringe amplitude for the GMO-H_2O contrast implies that water is also adsorbed as there appears to be a greater contrast between the

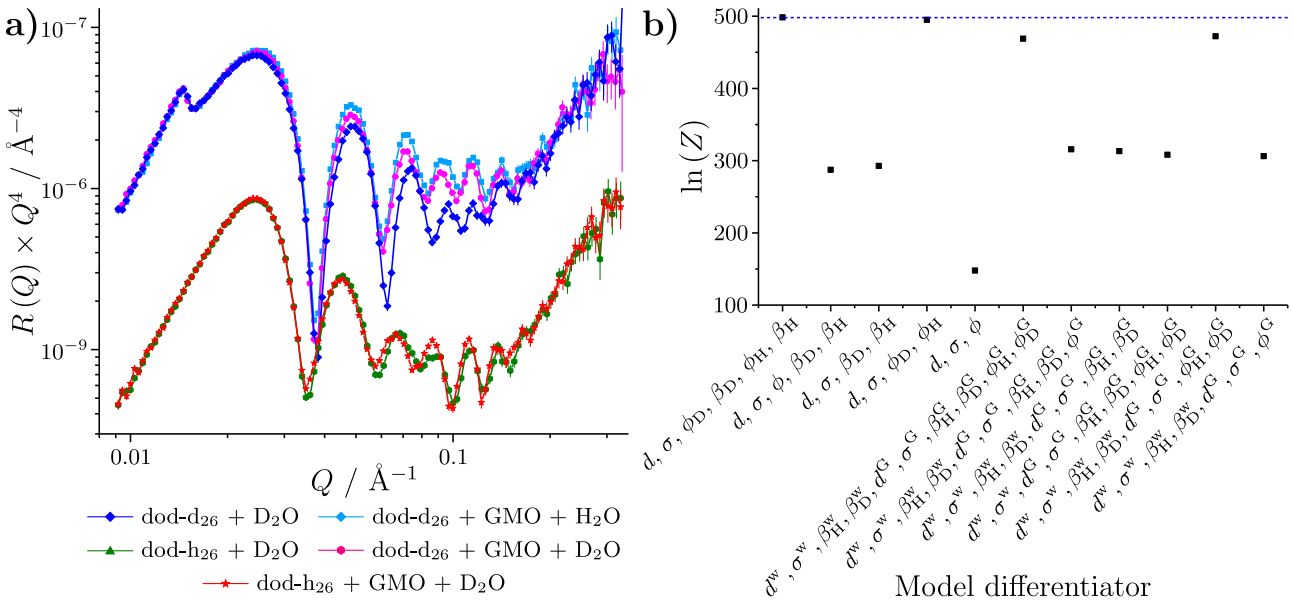

Figure 4.16: **a)** Comparison of the reflectivity data collected with the GMO-water-dodecane systems bar the CMdod contrast at 25° C. The data are modified by a factor of Q^4 to aid comparison. The contrasts collected with dodecane-h$_{26}$ are offset by 10^{-1} in reflectivity for clarity. **b)** The nested sampling results for the data collected at 25 °C. The estimated uncertainty in the nautral logarithm of the evidence is obscured by the data points. Those parameters without subscripts are shared across the D_2O/H_2O containing layers.

solvent and the adsorbate when H_2O is present rather than D_2O. This is further supported by the difference between the dodecane-h$_{26}$ contrasts, which is attributed to the adsorption of D_2O at the interface as the adsorption of GMO was observed to not significantly alter the measured reflectivity with this solvent contrast (see Figure 4.3). Therefore, the differences in the reflectivity are attributed to the co-adsorption of GMO and water.

It was considered that the co-adsorption of GMO and water could lead to the formation of two structures: a combined singular layer of water and GMO, or a discernible bilayer with a water-rich region adsorbed directly at the iron-oxide interface and a GMO-rich region adsorbed on the outer region of the interfacial layer. As such, a limited nested sampling survey was conducted to find a model that best described the data. Together with thickness and roughness parameters, the GMO layers were considered to be described by two separate nuclear scattering length densities, β_D and β_H, to account for the difference in β_n of D_2O and H_2O, which were potentially contained within an adsorbed GMO layer. Furthermore, different combinations of solvation parameters were tested, where ϕ_D and ϕ_H relate to separate solvations for the contrasts collected with either D_2O or H_2O, and ϕ relates to a joint solvation between all contrasts. The water-rich layer was also modelled with separate scattering length densities, β_D^w and β_H^w, for D_2O and H_2O, alongside thickness and roughness parameters.

A number of inequality constraints were also required to ensure the parameters maintained physical meaning. The β_H parameter of GMO layers were constrained so that $\beta_H \leq \beta_D$. The roughness of the water-rich layer was also constrained so that $\sigma^w \leq d^w/2$ and the SiO_2 roughness was similarly constrained so that the thickness was at least double the roughness.

The initial parameter values and priors for the parameters are shown in Table A8 and the model evidence results are shown in Figure 4.16b. The parameters of the bilayer models have either a superscript w or G to signify if they belong to the water or GMO layers respectively.

The model with the highest evidence, where $\ln(Z) = 498.3 \pm 0.6$, only had one interfacial layer with separate β_n and solvations for the layer containing GMO and either D_2O or H_2O. However, with this model it was found that $\beta_H = 1.2^{+0.2}_{-0.3} \times 10^{-6}$ Å^{-2} which matches the scattering length density of the GMO-D_2O layer. It is clear that this value is not physically consistent with the nominal β_n values of H_2O and GMO, as this value should be at least less than the GMO β_n if H_2O is contained within the layer. Therefore, this model was re-run where the upper bound of β_H was reduced from 6 to 0.21×10^{-6} Å^2; this resulted in a lower model evidence, where $\ln(Z) = 483.3 \pm 0.6$, which is lower than the evidence for the second highest model in Figure 4.16b, where $\ln(Z) = 494.8 \pm 0.6$. This model had the scattering length densities of GMO fixed at 0.21×10^{-6} Å^2, and only the solvations of the layers were allowed to vary. This is less ideal than fitting β_H and β_D as the difference in β_n between the layers containing H_2O and D_2O will not arise solely from different solvations. However, as the solvation values were not known prior to fitting, this model was chosen to fit the data using the MCMC routine. The resulting fits and β_{++} profiles are shown in Figure 4.17, while the inferred parameter values are shown in Table 4.9. The posterior distribution is visualised in Figure B3.

The solvation values of the GMO-water layers are markedly different, which is most likely a result of the different water content of the layer. As such, the solvation values do not represent the solvation of the layer but act as effective parameters that control the differing β_n of the GMO-H_2O and GMO-D_2O layers. Some difference in solvation between the layers may be expected; as discussed previously, the ability of dodecane to solvate the layer is due to attractive dispersion forces with alkyl tail groups. The inclusion of water into the GMO layer would be expected to decrease the solvating ability of dodecane due to the increased polar content of the layer, which will favour stronger dipolar interactions, such as hydrogen bonds, with other polar molecules. The absolute nature of these interactions will depend on the structure of the GMO-water layer, as the orientation of alkyl chain groups will dictate the available hydrophobic interface for which the dodecane can interact with. It is known that D_2O and H_2O have different physical properties, such as density, and also form marginally different structures due to the isotopic variation, where D_2O is thought to form hydrogen bonds that are 4 % longer than H_2O.[197] These differences have been attributed to structural variation arising in systems containing water upon isotopic variation, such as protein systems[198], nanoparticles[199], and surfactant aggregation[200,201]. Therefore, it is possible that there is an isotopic effect on the structure of the GMO-water layer.

The clear difference between the β_{++} of the interfacial layer between the GMO-water systems in dodecane-d_{26} shows that at 25 °C, the GMO and water co-adsorb to form a mixed layer, where the combined scattering length density for GMO-D_2O is discernible from the GMO-H_2O layer. The thickness of the GMO-water layer does not appear to be swelled significantly in

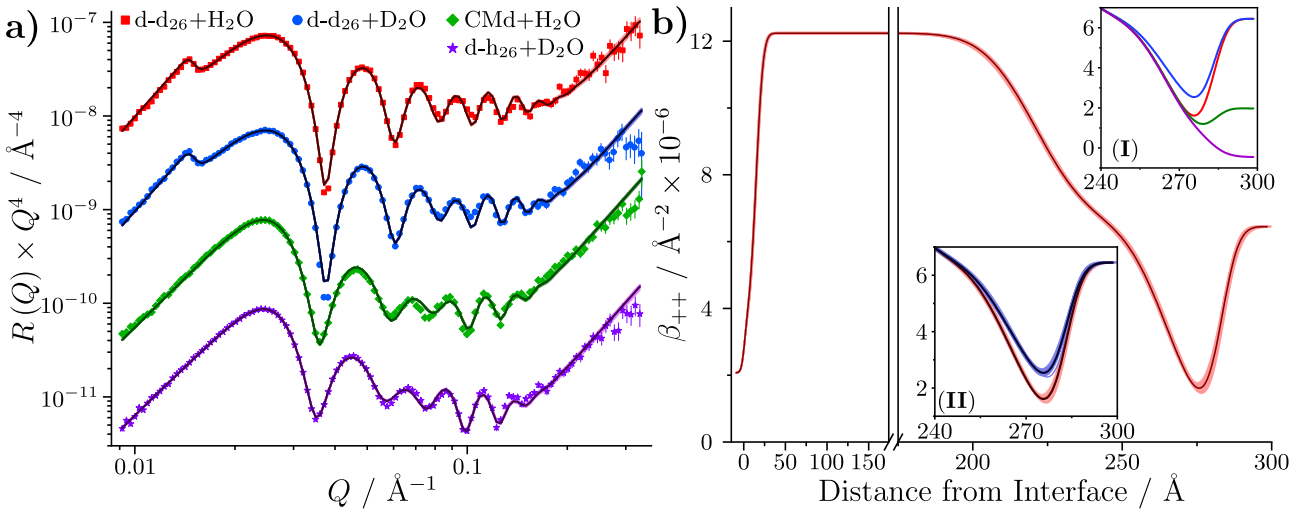

Figure 4.17: **a)** Fits to the data collected with the GMO-water-dodecane systems at 25 °C. The dark lines show the median fits to the data, while the bands show 50 random samples from the posterior distribution. The data are modified by a factor of Q^4 to aid comparison, and are sequentially offset by a factor of 10^{-1}. **b)** The spin-up scattering length density profile of the contrast collected with dodecane-d_{26} and H_2O. The inset labelled (**I**) shows the median profiles for all four contrasts focused on the iron oxide/GMO/dodecane layers. The inset (**II**) compares the posterior distribution for the GMO-H_2O and GMO-D_2O systems in dodecane-d_{26}.

Table 4.9: Median and 95 % confidence interval parameter values for the GMO-water-dodecane solutions against an iron-coated silicon substrate at 25 °C. The thickness and roughness for the GMO-water systems were shared for the two different layers. The minimum number of independent samples was estimated to be 92253, allowing all parameters to be reported to 2 decimal places as every parameter standard deviation was with standard deviations ≤ 1.54.

Layer	β_n / Å$^{-2} \times 10^{-6}$	β_m / Å$^{-2} \times 10^{-6}$	Thickness / Å	Roughness / Å	Solvation / %
Si	2.07	-	∞	3	-
SiO_2	3.47	-	$14.02^{+0.83}_{-0.63}$	$6.78^{+0.30}_{-0.36}$	-
Fe	$7.83^{+0.03}_{-0.03}$	$4.41^{+0.03}_{-0.03}$	$206.41^{+0.52}_{-0.50}$	$13.97^{+0.65}_{-0.65}$	-
FeO_x	$6.21^{+0.08}_{-0.08}$	$0.32^{+0.08}_{-0.08}$	$43.97^{+0.30}_{-0.31}$	$11.12^{+0.59}_{-0.59}$	-
GMO/D_2O	0.21	-	$18.06^{+0.34}_{-0.33}$	$4.55^{+0.46}_{-0.50}$	$19.28^{+1.56}_{-1.49}$
GMO/H_2O	0.21	-			$0.22^{+0.91}_{-0.21}$

comparison to the 20 mM GMO system measured without additional water. Therefore, as the layer volume is similar, this suggests that water occupies regions of space that contain GMO in the dry systems, translating to less adsorbed GMO.

The reflectivity collected at 60 °C is compared to the data collected at 25 °C in Figure 4.18. The data collected with D_2O show a greater difference with temperature. The change to the amplitude of the fringes suggests that the contrast between the solvent, the interfacial layer and the iron oxide varies with temperature. The small shifts in the fringes suggest that the thickness of the interface remains similar. The difference in the critical edge, Q_c, of the contrasts collected

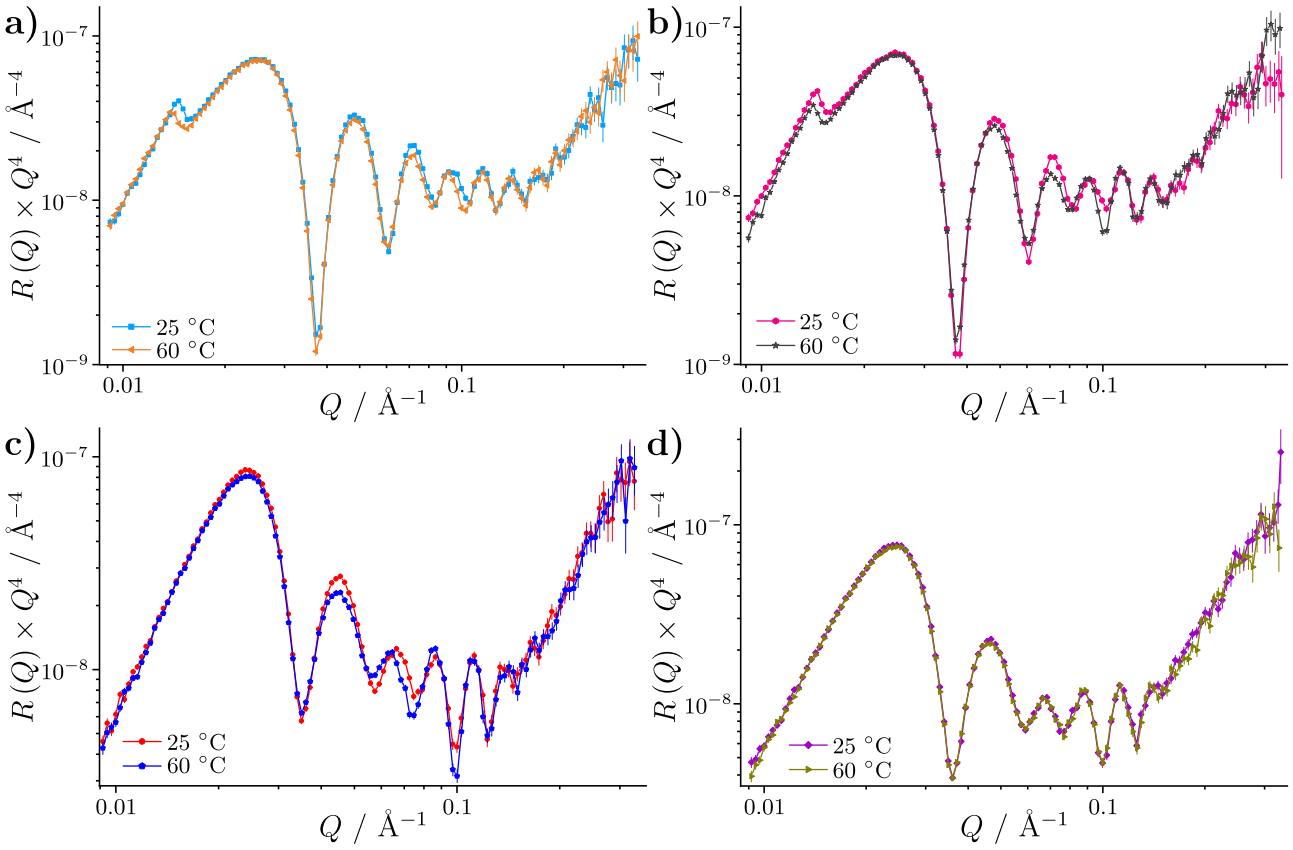

Figure 4.18: Comparison of reflectivity collected with the GMO-water-dodecane systems at 25 and 60 °C. The data shown are: **a)** - GMO-H_2O-dodecane-d_{26}, **b)** - GMO-D_2O-dodecane-d_{26}, **c)** - GMO-D_2O-dodecane-h_{26}, **d)** - GMO-H_2O-CMdod. The lines between the data are interpolations.

with dodecane-d_{26} is $\sim 4 \times 10^{-4}$ Å^{-1}, and is consistent with that arising between the GMO-dodecane systems at 25 and 60 °C. The similarity between the CMdod profiles arises from the similar β_n of CMdod and the GMO-H_2O layer, and hence, these contrasts are sensitive only to the structure of sputtered layers. The similarity between the temperatures further supports the suggestion that raising the temperature to 60 °C does not influence the substrate structure.

A nested sampling study that considered the same models as the 25 °C study was conducted. The results are shown in Figure 4.19, where the parameter descriptions are the same as the 25 °C data. These results were collected using the same constraints and priors as discussed for the lower temperature data. The model with the greatest evidence, where $\ln(Z) = 776.1 \pm 0.7$, was found to have $\beta_H^G = 1.4^{+0.2}_{-0.3} \times 10^{-6}$ Å^{-2} which is greater than β_n for GMO and H_2O, and thus, is not physically meaningful. Therefore, the model with the second highest evidence was used to fit the data. Similar to the model used to fit the data collected at 25 °C, this has a fixed β_H^G value of 0.21×10^{-6} Å^{-2}, and relies on the solvation parameter to account for any difference in scattering length density of the GMO layer. The median fits are compared to the data in Figure 4.20a, and the resulting β_{++} profiles are shown in Figure 4.20b.

The inferred parameter values are shown in Table 4.10 and a visual overview of the correlation between parameters is shown in Figure B4. The scattering length density of the D_2O-rich

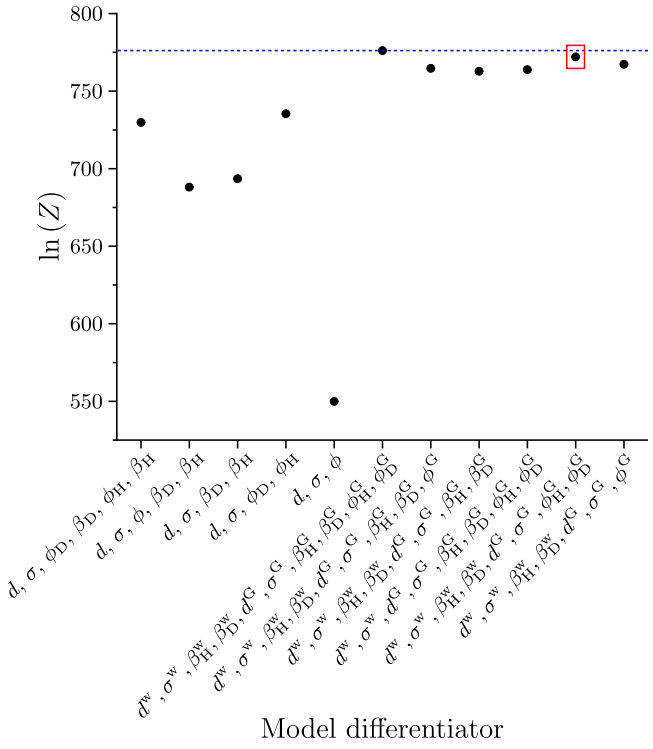

Figure 4.19: Results from the nested sampling study of the reflectivity collected with the GMO-water-dodecane systems at 60 °C. The uncertainties in the estimated evidence values are obscured by the data points. The model with highest evidence is highlighted by the dashed blue line. The red box shows the model used to model the data in the MCMC fit.

layer suggests that it likely contains GMO and adventitious material as the β_n would otherwise be closer to the nominal value of 6.37×10^{-6} Å^{-2}. It is also possible that dodecane is held within this layer, but as a solvation parameter was not included in the model, the inferred scattering length density accounts for any solvent. Due to the wide uncertainty in the H_2O-rich β_n and small contrast between H_2O and GMO or adventitious material, little can be discussed regarding the inferred β_n. The solvation of the GMO layer appears to be equivalent within error across the H_2O and D_2O contrasts, suggesting that the isotopic effect from any residual water within this region of the interface is minimal. Additionally, the values of ϕ suggest that the GMO-rich portion of the film is less dense than the GMO layer formed at the same GMO concentration but without additional water.

The difference in the scattering length densities around the iron oxide-dodecane interface due to the presence of D_2O or H_2O is compared in Figure 4.20c and Figure 4.20d. A significant difference between the inferred posterior distributions of the iron oxide-water interface is indicated by the white space between the β_{++} profiles, where the contrasts containing D_2O have a greater scattering length density over the iron oxide-water interface. When comparing the dodecane-d_{26} contrasts, the similar β_{++} of the GMO-rich layer on the outer of the interfacial layer suggests that little water is contained within this region. While the scattering length densities of this layer were not fit, if the values were lower than the inferred value in the fit, then the solvation value of the GMO layer of the H_2O contrasts would be lower.

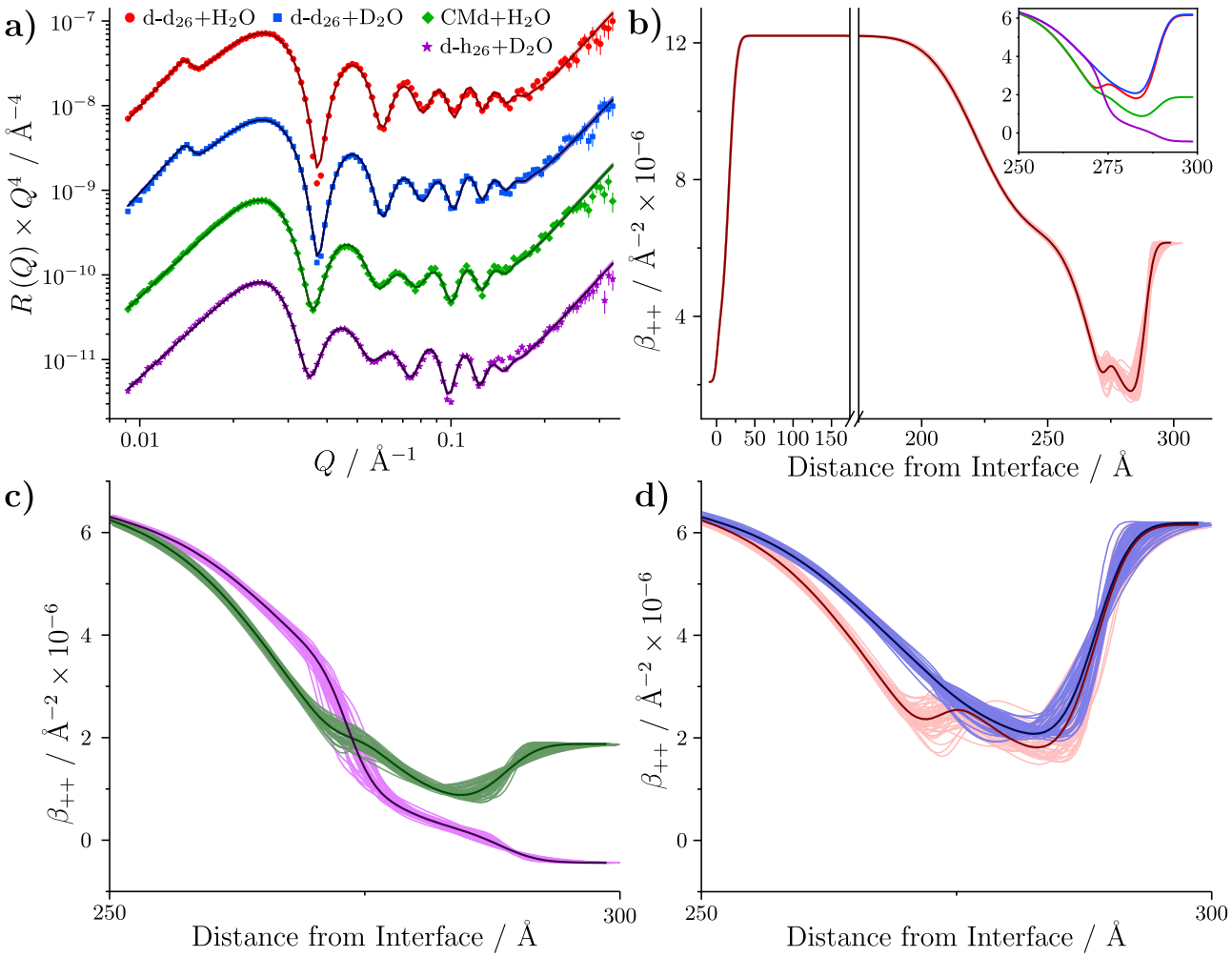

Figure 4.20: **a)** Median fits to the data collected at 60 °C. **b)** Median up-spin scattering length density profile of the GMO-H_2O-dodecane-d_{26} system at 60 °C. The inset shows the median fits for the four contrast systems. **c)** Comparison of the median β_{++} profiles and 50 random samples from the posterior distribution for the CMdod and dodecane-h_{26} contrasts. **d)** Comparison of the median β_{++} profiles and 50 random samples from the posterior distribution from the dodecane-d_{26} contrasts.

The significance of the small inflexion between the H_2O and GMO layer in the dodecane-d_{26} contrast is difficult to assess, as the uncertainty around this region of the β_{++} profile is of similar magnitude to the inflexion. However, it is thought that this arises as a result of the iron oxide roughness extending over the length of the water layer. In the region of inflexion, it is postulated that the number density of H_2O declines faster than that of iron oxide, leading to a small rise in scattering length density as the available volume is increasingly occupied by GMO or dodecane-d_{26} which have greater β_ns than H_2O. This effect is a function of the density of all materials present, the iron oxide topography and the distribution of water across the interface; for instance, it may be possible that water preferentially collects in the channels or pores of the iron oxide, leading to an inhomogeneity of water thickness across the iron oxide. This would lead to a more rapid decline of water density at the tips of the iron oxide asperities.

A schematic of the interface that is consistent with the β_{++} profiles is presented in Figure 4.21. The water is primarily adsorbed at the iron oxide surface, forming a water-rich region. As

Table 4.10: Median and 95 % confidence interval parameter values for the GMO-water-dodecane solutions against an iron-coated silicon substrate at 60 °C. The layers labelled 'water' and 'GMO' represent the water-rich and GMO-rich layers. The minimum number of independent samples was estimated to be 14718, allowing those parameters with standard deviations ≤ 0.61 to be reported to 2 decimal places. Those parameters with standard deviations > 0.61 are reported to one decimal place. Parameters marked by either * or † differentiate the layers containing D_2O or H_2O.

Layer	β_n / $Å^{-2} \times 10^{-6}$	β_m / $Å^{-2} \times 10^{-6}$	Thickness / Å	Roughness / Å	Solvation / %
Si	2.07	-	∞	3	-
SiO_2	3.47	-	$15.54^{+0.66}_{-0.63}$	$7.61^{+0.29}_{-0.36}$	-
Fe	$7.78^{+0.03}_{-0.03}$	$4.43^{+0.03}_{-0.03}$	$205.30^{+0.48}_{-0.48}$	$14.95^{+0.65}_{-0.66}$	-
FeO_x	$6.06^{+0.07}_{-0.07}$	$0.20^{+0.07}_{-0.07}$	$46.38^{+0.50}_{-0.52}$	$9.49^{+0.87}_{+0.77}$	-
Water	$^{*}1.83^{+0.34}_{-0.41}$ $^{\dagger} -0.19^{+0.19}_{-0.33}$	-	$5.3^{+1.9}_{-1.8}$	$1.92^{+1.09}_{-0.86}$	-
GMO	0.21	-	$15.3^{+1.7}_{-2.4}$	$2.7^{+2.9}_{-1.7}$	$^{*}25.6^{+5.1}_{-11.9}$ $^{\dagger}19.2^{+9.3}_{-12.4}$

the vertical displacement from the beginning of the iron oxide surface increases, the number of water molecules begins to increase as the total volume of the iron oxide decreases as a consequence of the roughness. In the presence of H_2O, this leads to the rapid decrease in β_{++} as the distance from the interface increases, whereas with D_2O, a slower β_{++} variation with distance is observed. This continues until the very thin nature of the water layer means that the number of water molecules begins to decrease towards the GMO layer. In the case of the dodecane-d_{26}+H_2O contrast, this leads to the scattering length density rising very slightly. Beyond this region, the tips of the iron oxide asperities are reached and the volume fraction of iron oxide becomes zero. As the GMO alkyl chains extend out from these asperities, the β_{++} reaches a minimum, after which the increasing presence of solvent molecules begins to increase β_{++}. While the schematic shows the GMO adsorbed at the iron oxide surfaces for simplicity, it is possible that GMO could also adsorb at the water-dodecane interface.

Another method for modelling the continuous nature of the interface might be a spline method, which allows a free form nature of the scattering length density with a set of knots. One particular example is the piecewise cubic hermite interpolating polynomial (PCHIP), which has recently been used to study the volume fraction profile of polymer brushes.[202] The drawback of this method is the significant increase in time required to model the data.

4.3.4 Comparison with molecular dynamics simulations

Through collaboration with Dr Rui Apòstolo and Professor Philip Camp at the School of Chemistry, University of Edinburgh, the experimental results presented previously were compared to

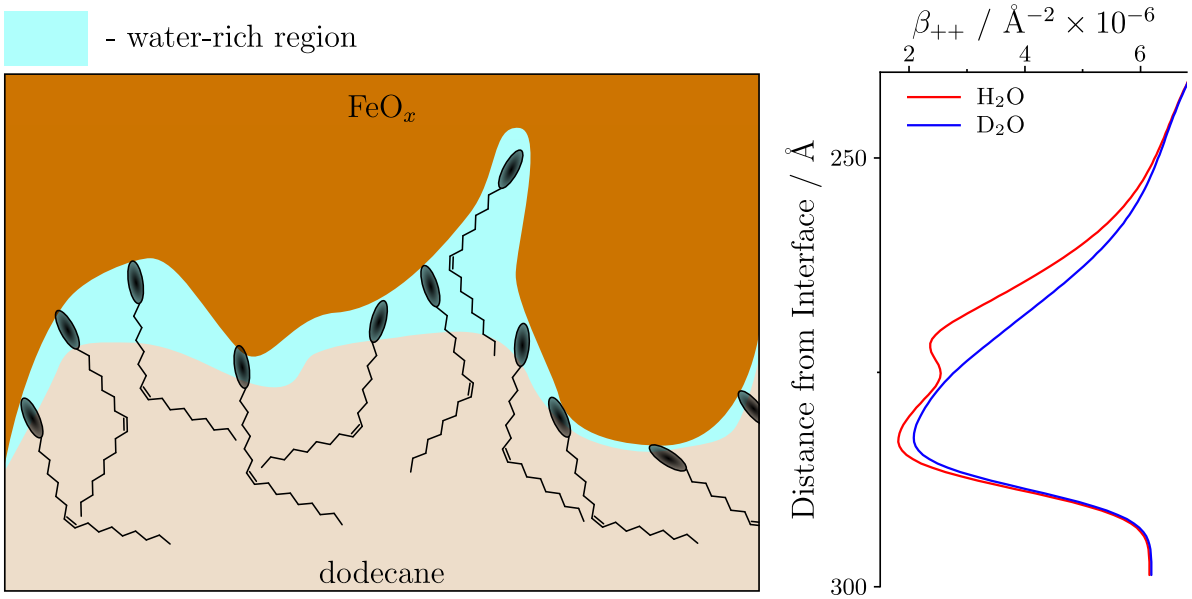

Figure 4.21: Schematic depicting the interface of the iron-coated Si substrate against the GMO-water-dodecane systems at 60 °C. The two dodecane-d_{26} β_{++} profiles are shown at the side as an aide to how the scattering length changes over the interface. The schematic is not drawn to scale and nor is the drawn roughness Gaussian as assumed by the Croce-Névot factor.

all-atom molecular dynamics simulations of these systems. These simulations were conducted by Rui, who provided the average scattering length density profiles and images. The author conducted the data processing in order to compare the density profiles with our experimental results, which are presented here. Analysis was conducted individually without input from collaborators.

The full details of the all-atom molecular dynamics (MD) simulations are not given here, but a brief description of the simulations is given to describe the system conditions. As the number of atoms used within simulations increases the computational time, these simulations were limited to the iron oxide-dodecane interface and do not include the Si substrate or the Fe and SiO_2 layers as used in the NR experiments. Two perfectly flat hematite surfaces (50 × 55 Å^2) were confined under a pressure of 1 atmosphere with a volume of dodecane and GMO molecules between the surfaces. The distance between the iron oxide surfaces was 80 Å, which enables the middle of the system to behave as bulk solvent. The concentration of GMO in dodecane was 1.3 M, which is greater than those studied experimentally, but the concentration of GMO near to the interface can be expected to be greater than the bulk concentration. This concentration was found to relate to an adsorbate area per molecule of 32 Å^2. The simulation ran an equilibration step of 160 ps to dissipate excess energy from the initial confinement stage and lower the temperature of the system to 30 °C. The equilibrated system was then run for 16 ns at constant temperature and pressure.

A snapshot of the system in its final state after the simulation is shown in Figure 4.22. It is difficult to determine the precise structure of the adsorbate through the image, but it does appear that a significant proportion of the GMO oxygen atoms are adsorbed $\gtrsim$ 8 Å from the iron oxide. This distance is greater than expected if the GMO formed a conventional monolayer,

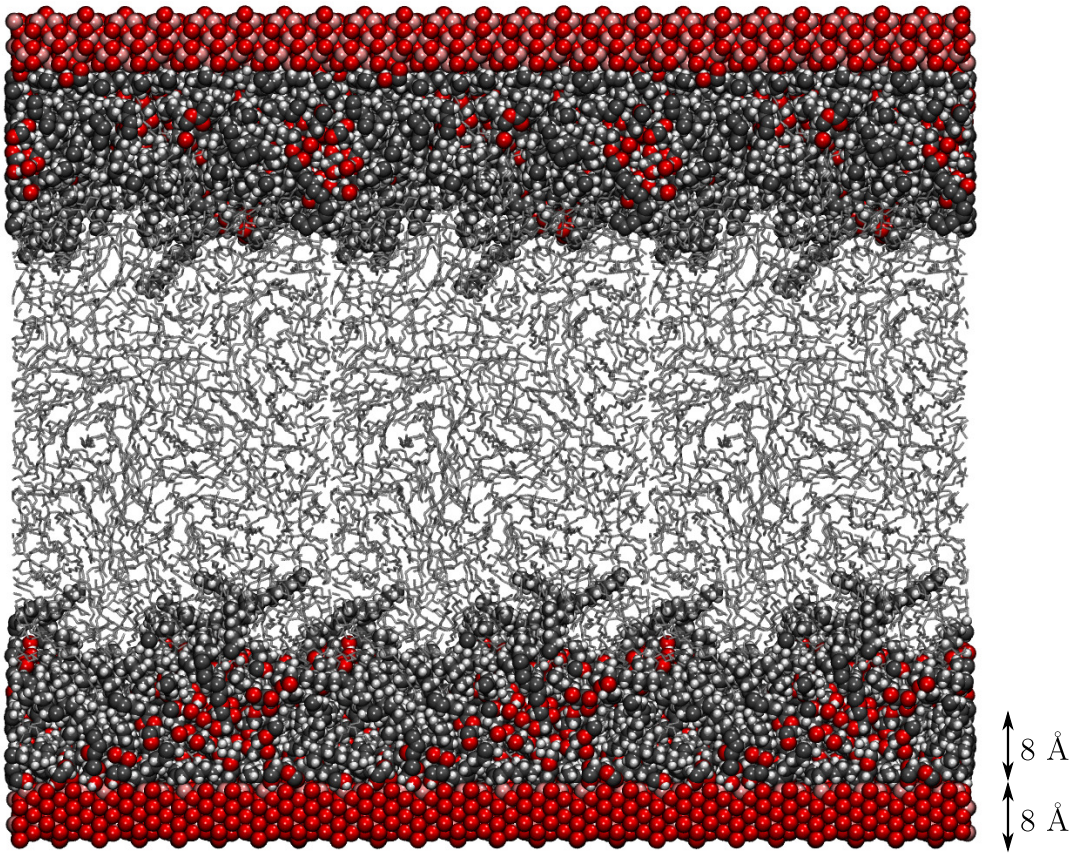

Figure 4.22: The snapshot of the iron oxide, dodecane and GMO system at the end of the simulation. The iron oxide and GMO are shown in space-filling representation, where hydrogen is highlighted as white, oxygen as red, carbon as grey and pink as iron. The dodecane is represented in a stick model for clarity.

where the polar head groups are adsorbed at the surface. For example, the carbonyl oxygen atom is estimated to be $\sim$ 6 Å from the H in the terminal OH group of GMO if the molecule is fully extended. This would translate to a similar distance from the iron oxide surface if the terminal OH group was the interacting functionality with the iron oxide surface at the normal angle. Other arrangements of the polar functionalities at the iron oxide surfaces reduce the distance between the iron oxide surface and the ester oxygen. Two monolayer scenarios are depicted in Figure 4.23a. Therefore, the simulated structure suggests that agglomeration between neighbouring GMO molecules is a significant factor in determining the adsorbate structure.

Scattering length density profiles of the iron oxide, dodecane, and GMO compounds were calculated by Rui, who counted every atom in 0.5 Å slices in the normal direction over the interface. The number density of each element could then be calculated, which was then multiplied by the elemental coherent scattering length to give the scattering length density as a function of distance. As the simulation contained two surfaces, the scattering length densities from both interfaces were calculated and averaged. The total and individual β_n profiles of the GMO, iron oxide and dodecane are shown in Figure 4.23b. The dodecane was simulated as dodecane-h_{26} but was assumed to be 100 % deuterated in the calculation of the β_n profile.

The β_n fluctuations close to the iron oxide surface are due to the ordering of GMO and dodecane.

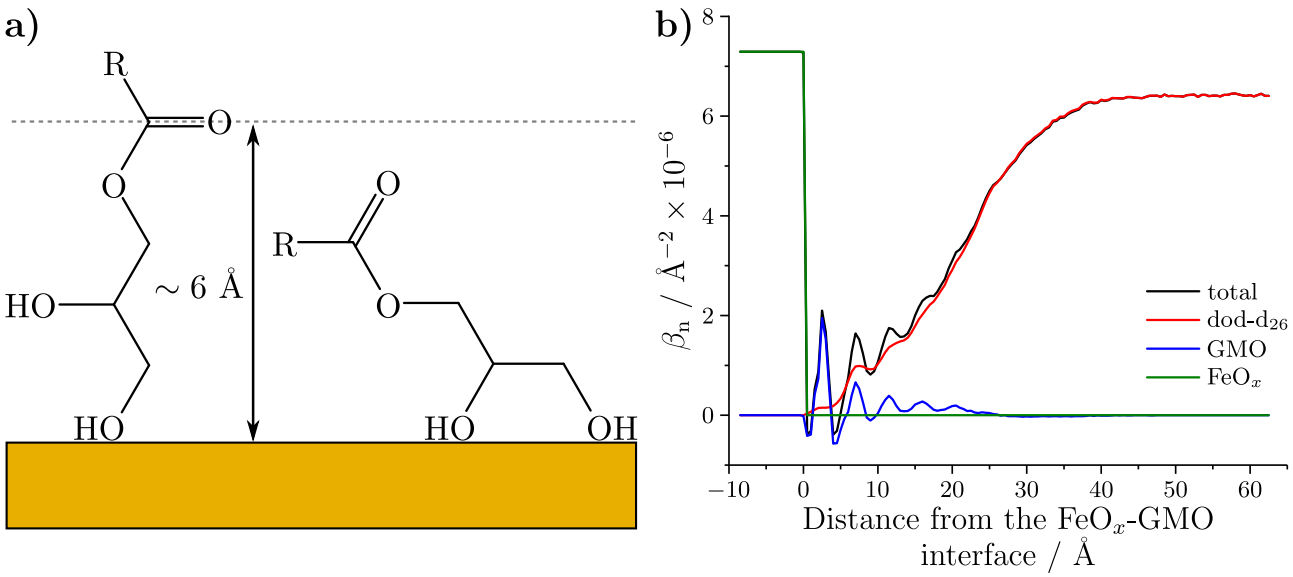

Figure 4.23: **a)** Distances between the iron oxide surface and two possible orientations that could be adopted if GMO adsorbs as a monolayer. **b)** The average nuclear scattering length density profiles, which are centred on the iron oxide-dodecane interface.

It is likely that the negative troughs in the GMO profile arise from slices containing a large number of hydrogen atoms, and those that have a higher β_n contain a greater number of oxygen or carbon. Ordering along the normal direction at the iron oxide surface can be expected as the gain in free energy through molecular interactions, or any chemical reactions, between GMO and iron oxide will be maximised when the GMO adopts a preferred orientation. The conventional theory suggests that the favoured orientation is with the GMO head group adsorbed at the surface so that the polar functionalities can interact with the iron oxide surface. As suggested above, the interactions between adjacent adsorbate molecules may also influence the structure of the adsorbed GMO, and hence influence the ordering in the normal direction. These interactions are typically weak but as the enthalpy of adsorption is also weak, as indicated by the depletion isotherms, they are expected to be of similar magnitude. Therefore, the van der Waals forces between the adjacent adsorbate molecules is expected to be a significant factor in determining the overall film structure. The roughness of the iron oxide interface as used in the experiments will smear any β_n fluctuations, arising from the ordering of GMO and dodecane, over the length scale of the roughness. The wavelength of the fluctuations is ~ 5 Å, which is around the limit of the resolvable length scale via NR. Therefore, the sharp characteristics of these fluctuations are less significant than the average trend of β_n.

In order to compare the reflectivity arising from the simulated system to the data collected experimentally, the scattering length density profile in Figure 4.23b had to be stitched onto the median β_n and β_m of the Fe layer inferred from the MCMC fit in order to capture the roughness between Fe and FeO$_x$. This was achieved using the following steps: initially, the position closest to the iron-iron oxide interface at which the iron scattering length densities were stable was identified. The portion of the β profiles between this position and the iron oxide-dodecane interface was then extracted. Next, the position at which the nuclear scattering length density

reaches the median FeO_x β_n inferred from the MCMC fit was identified. Beyond this position, the iron oxide β_n and β_m were set to the median values from the fit. In effect, this creates a sharp iron oxide interface as seen in the MD simulations, but one that is scaled to match the layer parameters from the fit with the correct roughness modelled between the iron and iron oxide. The scattering length density profile from the MD simulations could then be stitched onto the iron oxide surface. However, before stitching, the solvent β_n was scaled to match the inferred or fixed β_n from the fit for the three solvent contrasts. This was necessary as the solvent β_n was calculated assuming the dodecane had a 100 % D content, and does not correspond to the solvent β_n as used in the experiments. The scaling was achieved by multiplying the average scattering length density of the last 10 Å in the MD derived β_n profile by the median solvent β_n from the fit.

The composite scattering length density profile was then modelled as separate layers, each with a thickness of 0.5 Å and a roughness of 0.01 Å. Additionally, the Si substrate with the SiO_2 and Fe layers were modelled underneath the composite scattering length density profile. These layers had the median parameter values inferred from the MCMC fit. However, the thickness of the iron was adjusted so that the total thickness in the composite scattering length density and the iron layer was the same length as the median iron thickness from the fit. The simulated reflectivity for all three contrasts with the composite scattering length density is shown Figure 4.24a.

The reasonable fit suggests that the structure formed in the MD simulation is consistent with the experimental data. The final composite MD β_{++} profile is compared to the inferred β_{++} from the MCMC fit in Figure 4.24b. The two profiles share a remarkably similar β_{++} trend around the iron oxide-dodecane interface, which leads to the good fit. This suggests that the MD-derived structure is consistent with the experimental data, implying the experimental structure is not restricted to a monolayer. The sharpness of the iron oxide-dodecane interface may be expected to cause some discrepancy between the fit and the data; the contrast collected with dodecane-h_{26} is the most sensitive towards the characteristics of the iron oxide surface, while being moderately insensitive to the adsorbate film. Therefore, the good fit to the dodecane-h_{26} data suggests that the iron oxide sharpness does not significantly influence the simulated reflectivity, although it may be factor in the slightly greater fringe amplitudes observed at $Q > 0.08$ Å^{-1}. One area that may merit more investigation is how the presence of adsorbed gases, thought to comprise the adventitious layer, alters the structure of the adsorbed GMO film and how that compares to the NR data.

As the MD simulations provide atomistic detail, a well-matched comparison between the simulated structure and the data collected with dGMO would provide a greater level of detail on the structure of the dGMO adsorbate film than that inferred from fitting the experimental data. Therefore, Rui calculated the scattering length density profile from the same system but with the GMO tails deuterated. Using the same method as outlined above to scale and then stitch the MD-derived β_n profile onto the inferred substrate structure, the simulated reflectivity was

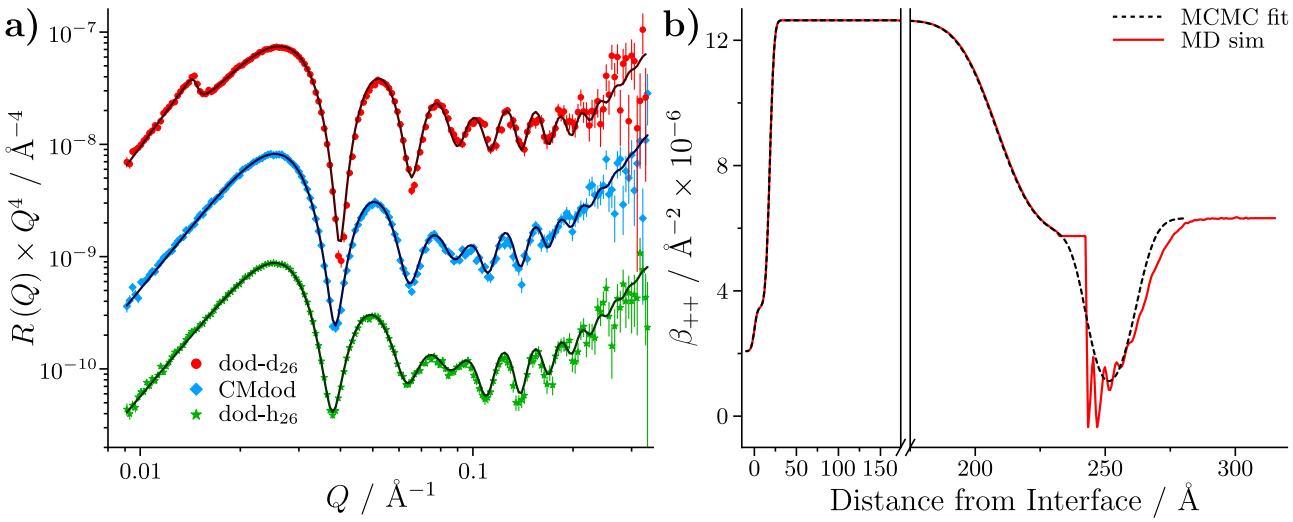

Figure 4.24: **a)** The modified reflectivity collected with an iron-coated silicon substrate against 20 mM GMO in three H/D contrasts of dodecane. The dark lines are the simulated reflectivity from the stitched MD β_n and β_m profile. The reflectivity data are sequentially by 10^{-1} for clarity. **b)** Comparison of the β_{++} profiles for the dodecane-d_{26} system from the MCMC fit and from the MD simulation.

compared to the data as shown in Figure 4.25a. In general, the fit quality is worse than for the hydrogenated GMO system, and the quality of the fit for the dodecane-d_{26} system is much poorer than the fit for the other two solvent contrasts. This implies that the structure of the adsorbed material with a low scattering length, such as the hydrogenated polar head group, does not match with the experimental system. As a result, it is expected that the deuterated tail group structure will not be consistent between simulation and experiment; this may account for the slightly smaller discrepancy noted in the CMdod contrast, which has limited sensitivity to the tail group. By inspecting Figure 4.25b, it appears that the overall scattering length density profiles are not consistent. It appears that the same scattering length densities for the GMO-dodecane interface are ~ 8 Å apart, implying that the inferred dGMO thickness is smaller than the MD-derived structure.

It is possible that the discrepancy between the structure formed by dGMO arises from a different adsorbate structure in comparison to the hydrogenated GMO. This is supported by the lower surface excess for dGMO compared to GMO at the same bulk concentration as determined via NR. One reason for this could the presence of other compounds in the experimental system such as the diester of glycerol and oleic acid as discussed previously.

Finally, a comparison between the experimental reflectivity arising from the GMO-water-dodecane systems and the equivalent simulated *in silico* is presented. The systems containing water were simulated in the same manner as the GMO-dodecane systems with the same concentration of GMO but with a fixed water content, where $W = 5$, as used in the experimental systems. The water was simulated as H_2O but two scattering length density profiles were determined, where one was calculated to contain 100 % H_2O and the other was assumed to contain 100 % D_2O. A snapshot of the final system is shown in Figure 4.26, where water molecules can

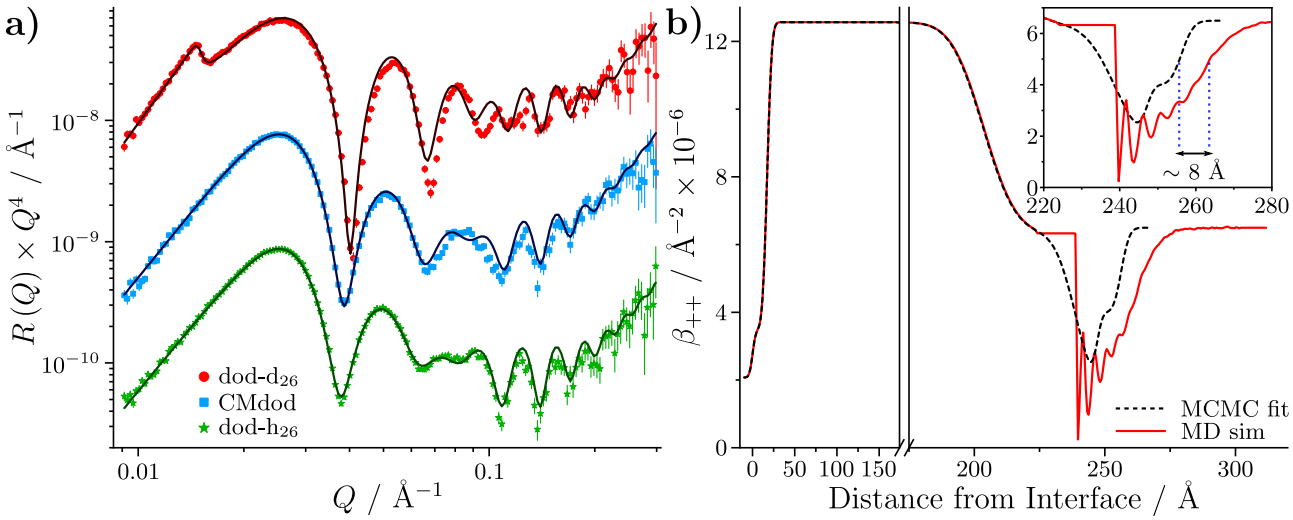

Figure 4.25: **a)** The modified reflectivity collected with the 20 mM dGMO-dodecane solutions against an iron-coated silicon substrate with three H/D contrasts of dodecane. The dark lines are the simulated reflectivity from the stitched MD scattering length density profile. **b)** Comparison of the dodecane-d$_{26}$ β_{++} profiles from the MCMC fit and from the MD simulation. The inset shows the approximate 8 Å difference between the β_{++} profiles.

be seen both adsorbed directly at the surface and held within the GMO film, with some distance to the iron oxide surface. These environments are particularly clear in the D_2O β_n profile calculated from the final system, as shown in Figure 4.27. Similar to the water-free system, some GMO oxygens can be seen in the snapshot at a distance from the interface that is greater than expected for a simple monolayer. It is thought that these oxygens will form hydrogen bonds with the water molecules within the GMO film. The β_n profile for GMO displays less fluctuations than in the profile for the dry GMO systems, suggesting that water reduces the surface ordering of GMO molecules.

Following the same method, the scattering length densities were scaled and stitched onto the inferred iron-iron oxide interface, and simulated with the underlying median Si, SiO_2 and Fe layers inferred from the fit to the data collected at 25 °C. The comparison of the experimental and simulated reflectivity is shown in Figure 4.28a. The scattering length density profiles of the dodecane-d$_{26}$+H_2O systems are compared in Figure 4.28b.

In general, the fits to the data are poor. The CMdod contrast is the least sensitive to the interfacial layer, but is sensitive to the iron and iron oxide layers. Therefore, it is suggested that the one source of discrepancy between simulation and reflectivity is due to the ideal nature of the iron oxide surface in the simulation. The experimental iron oxide surface was found to have a roughness of $11.12^{+0.59}_{-0.59}$ Å as shown in Table 4.9. This translates to an approximate 45 Å region of the interface where the variation of the iron oxide scattering length density is not appropriately accounted for in the simulated system. This distance is estimated by multiplying the roughness by four to calculate the distance over which the error function varies from the β_{++} of the iron oxide to that of the interfacial layer. It is expected that this will lead to a mismatch in the dodecane-h$_{26}$ contrast, and a smaller misfit in the dodecane-d$_{26}$ contrast. As

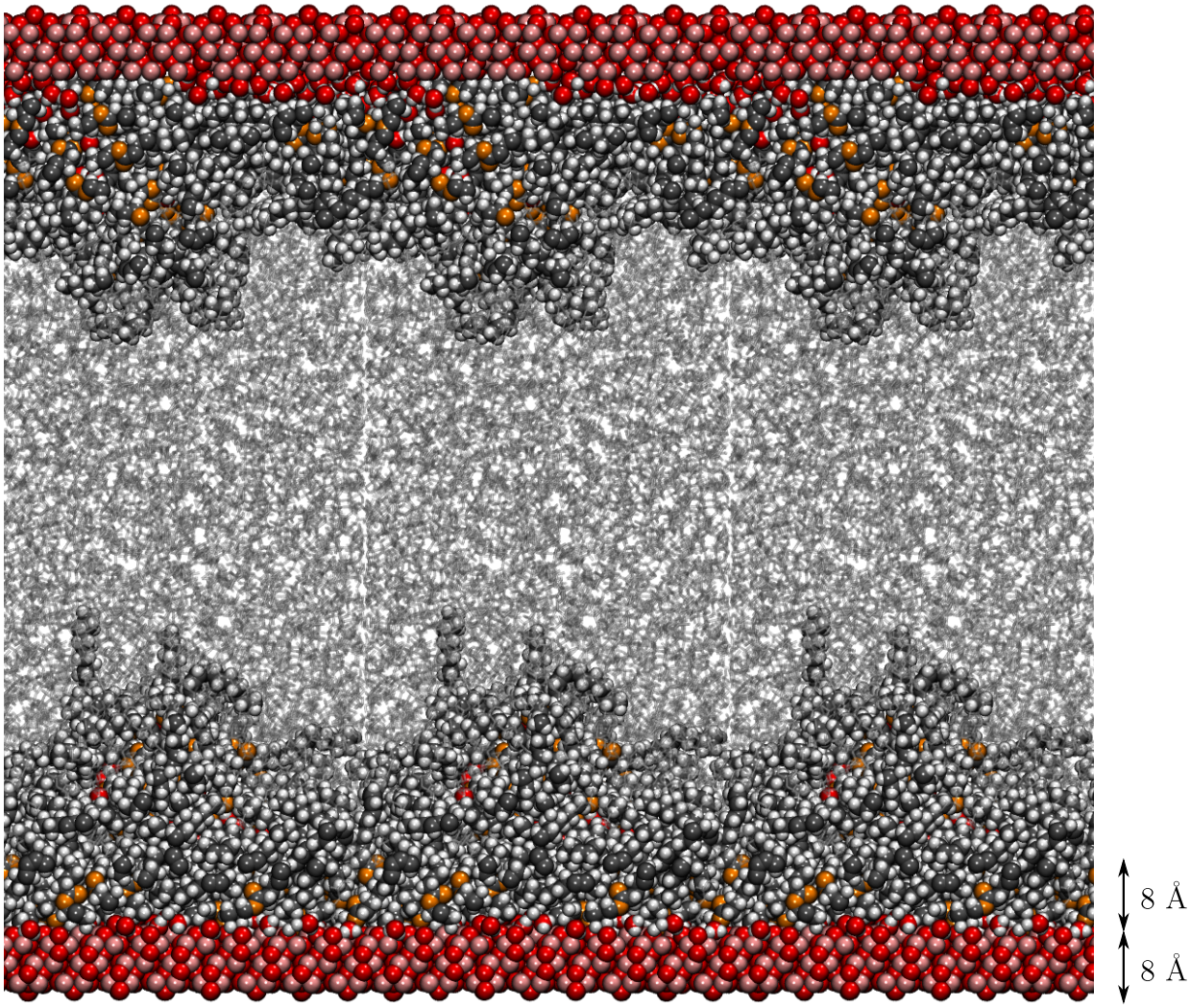

Figure 4.26: Snapshot of the GMO-water-dodecane system simulated between two perfectly flat iron oxide surfaces. The GMO, water and surfaces are shown in space-filling representation, where hydrogen is highlighted as white, oxygen from water or the iron oxide as red, oxygen within GMO is orange, carbon as grey and pink as iron. The dodecane is shown in a stick representation for clarity.

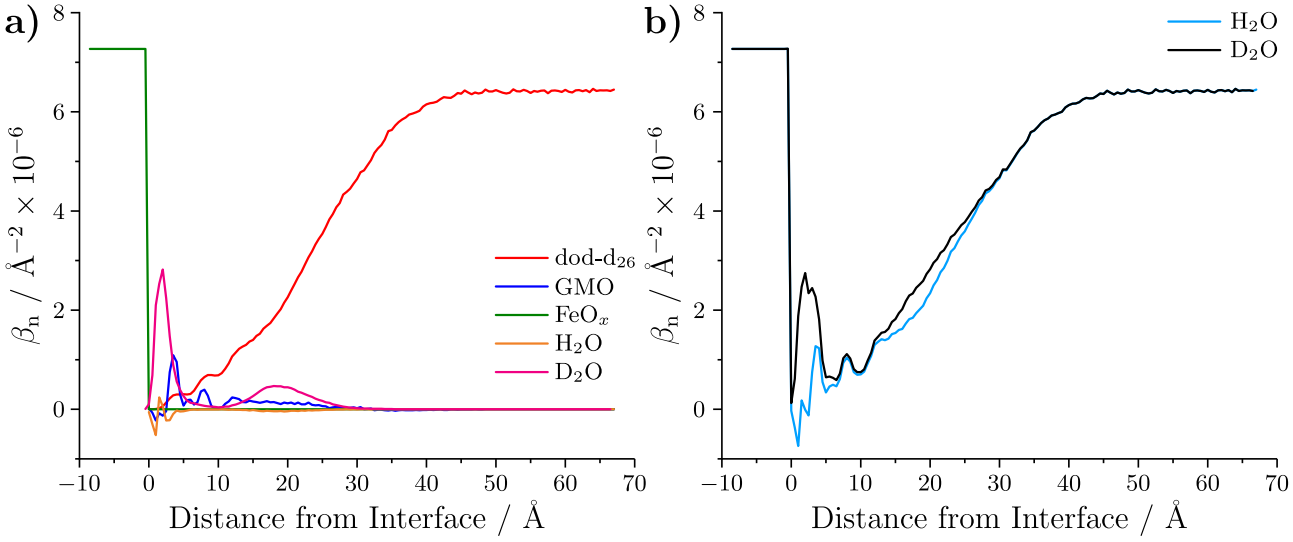

Figure 4.27: **a)** The scattering length density of each material as a function of distance over the interface. **b)** The total scattering length density profile for the H_2O and D_2O contrasts.

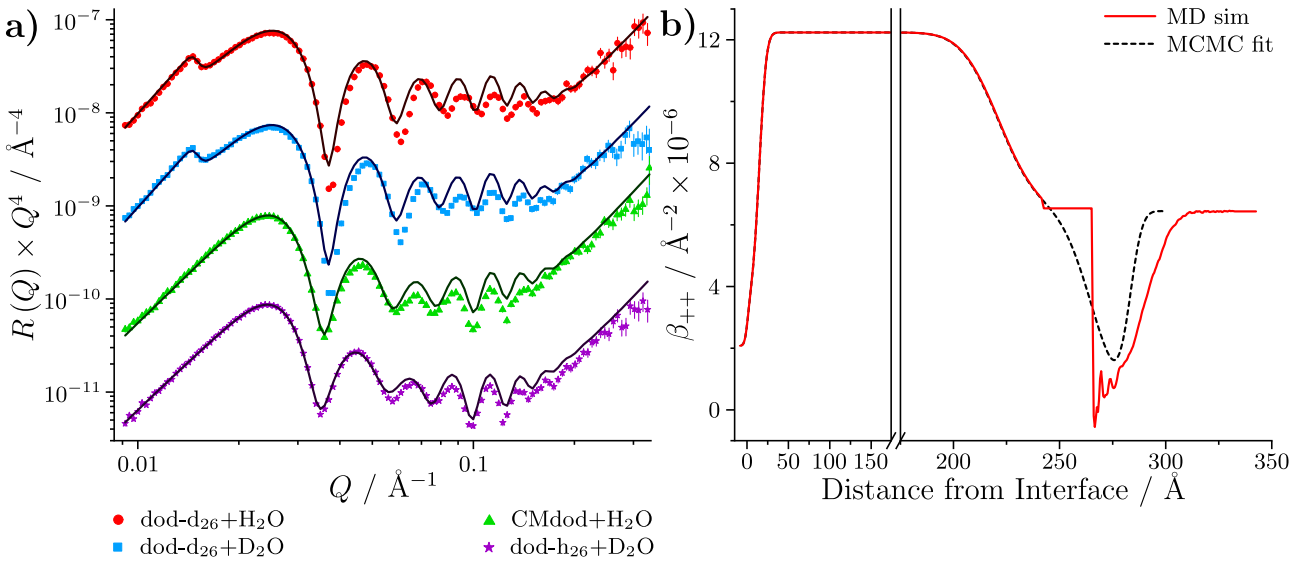

Figure 4.28: **a)** The modified reflectivity collected with the GMO-water-dodecane solutions against an iron-coated silicon substrate at 25 °C. The dark lines are the simulated reflectivity from the stitched MD scattering length density profile. **b)** Comparison of the dodecane-d$_{26}$ β_{++} profiles from the MCMC fit and from the MD simulation.

the other contrasts are more sensitive to both the water and GMO, these differences in the scattering length density will compound. It is suggested that some roughness of iron oxide can be tolerated when comparing experimental data to the simulated system, such as that seen in the system without additional water with hydrogenated GMO. However, ensuring that the roughness of the substrate is minimised will lead to better comparisons between experimental data and simulation.

The dodecane-d$_{26}$ contrasts are mostly sensitive to the interfacial region, which appears to be thinner and less dense in the experimental system. This discrepancy may arise from a differing surface excess of GMO as it was assumed to remain the same as the dry systems. There is also a possible mismatch in the location of the water within in the interfacial film as the water was inferred to be mixed throughout the layer. However, as the models in the nested sampling study only investigated the extremes of the continuum of where water molecules could be located within the interfacial film, it is not possible to confirm this.

4.4 Conclusion

The Langmuir-like adsorption of GMO, determined through depletion isotherms, suggests the formation of monolayer films at the iron oxide-dodecane interface. The thickness of the adsorbate film at 25 °C was determined to be between 17–19 Å for concentrations > 3 mM, which aligns with the suggestion of a monolayer film. However, comparison between the structures simulated via MD and the reflectivity suggests that more complex structures than a monolayer are also consistent with the data. Whilst the reflectivity collected with dGMO at 20 mM was found to be best modelled as a monolayer, the difference between the surface excesses

determined for the 20 mM systems with dGMO and hydrogenated GMO casts doubt over the similarity of the structure adsorbed at the interface in both systems. This is supported by the poor comparison between the experimental data and the simulated reflectivity from the MD derived dGMO β_n profile. Additionally, it is noted that the nested sampling was only conducted on a simple monolayer model, where all molecules are in the same orientation; it may be that a model which contains a proportion of adsorbed monomers and a proportion of adsorbed aggregates, which is more representative of the MD structure, has a greater Bayesian evidence. Some caution should be applied to the direct comparison of the MD structure and the measured reflectivity, as the MD simulations did not account for the presence of adsorbed gases and the surface excess used to determine the starting GMO concentration was greater than any of determined surface excess presented here.

Above 3 mM, the surface excess does not appear to increase, suggesting that the interface becomes saturated at higher concentrations. The similar surface excesses between the depletion isotherm and pendant drop tensiometry indicates that the self-assembled structure under equilibrium is determined by packing of the molecules and not the nature of the interface. Specifically, this is thought to be controlled by the alkyl chain group, where the non-linear nature of the *cis* double bond dictates the maximum packing density. This is supported by the similar area per molecule for GMO and oleic acid. At concentrations below 3 mM, the interfacial film is $\sim$ 2 Å thinner. Through comparison to the depletion isotherms, a lower thickness and surface excess may be expected. However, it is thought the interfacial film is also comprised of residual pre-adsorbed gas, which would lead to an inaccurate determination of the surface excess. The presence of this material within the interfacial film is not resolvable due to the low β_n of GMO and adsorbed gas.

The temperature-dependant behaviour of the isotherms suggest that GMO physisorbs at the iron oxide-dodecane interface, where $\Delta H^\circ = -3.2 \pm 5.6$ kJ mol^{-1}. This is supported by the removal of GMO when the interface is washed with 5 ml of additional solvent, as determined via NR. The adsorption is thought to be facilitated through hydrogen bonding or dipolar interactions of the polar head group with the iron oxide surface, and appears to be weaker than the adsorbing interactions of fatty amines and acids at the iron oxide-dodecane interface. It is possible that the enthalpy of adsorption is greater when the interface is completely void of adsorbed gas, as the GMO will not be screened from the hydrophilic surface. Similarly, the packing of GMO at the interface may be more efficient without additional molecules present. However, the surface excess determined by pendant drop tensiometry indicates the packing at the iron oxide-dodecane interface is not significantly affected by the adsorbate gas, as it is not expected that gas molecules would collect at the water-dodecane interface formed in the pendant drop tensiometry experiments. It is noted that the systems studied here will represent engine conditions more-so than systems controlled so that adsorbed gases are not present.

The depletion isotherms show that less GMO adsorbs at the iron oxide-dodecane interface at higher temperatures. The NR results collected at 60 °C do not align with these findings, where

the film thickness and surface excess are only marginally different from those found at 25 °C. Two explanations were suggested, where either the adsorbed GMO at 25 °C is solid-like and metastable with respect to temperature change, or the adsorbed gas leads to similar apparent surface excesses between temperatures. The former is thought to be a kinetic effect and thus, it would be possible to probe by simply exposing the interface to the solution at 60 °C. If a frozen, solid-like layer of GMO can exist at temperatures above the bulk melting point, this may have implications for friction reduction at elevated temperatures.

Solubilised water was shown to co-adsorb with GMO at the iron oxide-dodecane interface: it was indicated via nested sampling that water is dispersed within the interfacial film at 25 °C. Upon raising the temperature to 60 °C, the reflectivity was found to alter suggesting a rearrangement of the interfacial film. Nested sampling indicated a water-rich layer adsorbed directly at the iron oxide surface with a GMO-rich region adsorbed on the outer of the interface. The change with temperature suggests that the layer formed when co-adsorbed with water is not solid-like. This qualitatively matches the density profile determined via MD simulation, where the ordering of GMO appeared to be lower in the presence of water. A meaningful comparison between the experimental and simulated reflectivity could not be made due to the large mismatch of the iron oxide roughness. It is suggested that future comparisons would benefit from the use of smoother substrates; additionally, it maybe possible that some iron oxide roughness can be incorporated into the simulation without vastly increasing the computational time required to complete the process.

Chapter 5

Adsorption of glycerol monooleate at the iron oxide-dodecane interface under shear

This chapter contains work published in Armstrong, A. *et al.* Towards a neutron and X-ray reflectometry environment for the study of solid-liquid interfaces under shear, *Sci. Rep.*, **11**, 9713; 10.1038/s41598-021-89189-1 (2021).

5.1 Background

Shear rates in combustion engines have been estimated to reach up to 10^8 s^{-1}.[203] It is known that shear applied to solid-liquid interfaces can alter the structure and behaviour of interfaical soft-matter films; for example, shear can distort the equilibrium structures of adsorbate films formed under static conditions, where peripheral adsorbate layers in a multi-layer structure can be disordered and/or removed.[204,205] Greater shear rates have also been shown to lower the surface excess of surface-active materials.[206] Molecular dynamics simulations suggest that the self-assembly of GMO is also influenced by shear, where GMO was found to adsorb at the mica-heptane interface as aggregates and partially flatten when under shear.[152] Other simulations have suggested that shear can also increase the surface excess of GMO adsorbed at the iron oxide-squalene interface compared to static conditions.[153]

The majority of the techniques used for *in-situ* characterisation of OFMs and other similar molecules have been conducted in nanotribology studies, such as AFM and surface-force apparatus, where the probed areas of the adsorbate film are typically between square nm[207,208] to square µm[51,71] respectively. As a result, the interfacial film is only subject to shear in localised regions of the interface so that the average structure remains unperturbed, inhibiting long range rearrangements. Some studies have used tribometers specialised for optical interferometry[74,76] or sum-frequency generation[209], so that the interface under boundary lubrication conditions can

be probed. However, in the case of the former, it is not possible to resolve adsorbate structure from residual bulk oil remaining in the contact, and for the latter, it is not possible to obtain the thickness of the interfacial structure. Furthermore, due to the poor penetration of optical light, these studies have been limited to probing adsorbate films at surfaces of transparent quartz, which has a different chemical nature to steel or iron oxide surfaces.

Due to the sub-nm resolution of NR and XRR, both techniques can provide detailed information of layered structures. As the probed sample area extends from μm^2 to mm^2, both techniques can examine the average structure of surface films on a macroscopic scale. NR typically requires a greater sample area compared to XRR because the flux of neutron sources is lower than those available at synchrotrons. Despite this, NR is generally preferred for the study of buried solid-liquid interfaces as the penetration depth of neutrons is significantly greater. Consequently, the number of documented shear cells designed for the study of solid-liquid interfaces with XRR is smaller.[205,210]

Closed-loop flow cells are perhaps the most user friendly NR sample environments for the study of interfaces under applied shear. These have been used to study shear-induced surfactant behaviour at the Si-water interface.[211,212] Whilst shear rates have been reported to reach up to 5.5×10^4 s^{-1} in Poiseuille shear cells[213], it is difficult to control the range of accessible shear rates, which are also non-trivial to define; often, numerical simulations are used to predict shear rates in these cells. Furthermore, it is not possible to study the elastic and loss moduli of adsorbed samples. Cone and plate rheometers have been fitted onto NR environments to meet these needs, enabling the application of oscillatory and steady shear to solid-liquid interfaces.[204,214]

The effect of applied loads on adsorbate structure can be studied through the use of NR confinement cells. Here, the main principle is to move a surface towards the interface of interest and to apply a pressure. This has been achieved by either the actuation of a solid surface towards the interface or by the expansion of an inflatable elastic material against the interface.[215–217] While the former technique is complicated in terms of ensuring both surfaces remain parallel over the areas required for NR, shear is perhaps more trivial to apply at the interface with this type of confinement. Steady shear rates of up to 20 s^{-1} and oscillatory shear rates up to 10^4 s^{-1} are reported in confinement cells.[218]

This chapter details the NR and XRR experiments conducted with the tribometer. Due to the wear induced on the reflectometry substrates, as detailed in Chapter 2, the tribometer was used in non-contact mode to inhibit any change to the substrate structure during experimentation. The pressures and shear rates afforded by the tribometer in non-contact mode are limited by the entrainment velocity and roller-substrate gap. Therefore, these experiments were conducted under the hydrodynamic lubrication regime, where shear rates are much lower than those found in the boundary lubrication regime. While the achievable shear rates were low in comparison to those typically found in contacts under boundary lubrication, these experiments have facilitated the development of the theory behind reflectivity arising from a roller-substrate

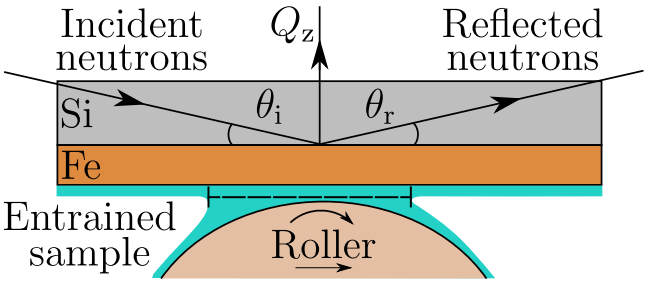

Figure 5.1: The principal of neutron reflectometry with the tribometer in non-contact mode. The incident neutron beam illuminates an area that is greater than the meniscus region above the roller. The meniscus held above the roller is outlined by the dashed bracket in the schematic.

geometry. Furthermore, it also presented an opportunity to characterise any potential differences on the self-assembly of GMO at the iron oxide-dodecane interface at lower shear rates. A full description of the models used to infer the *in-situ* adsorbed GMO structure whilst under shear at the iron oxide-dodecane interface is presented and discussed.

5.2 Neutron reflectometry

A schematic of the NR environment provided by the tribometer is shown in Figure 5.1. The experiments presented were conducted on INTER, where the wavelength distribution was $\lambda \sim$ 2–17 Å. Two incident angles of 0.7° and 2.3° were used to collect the full Q range of $\sim$ 0.009–0.300 Å^{-1}. The standard deviation of the dQ/Q resolution was 2 %. The neutron guide slits were set to give a footprint of approximately 40.7 mm along the interface, which can be estimated to have a trapezoid intensity distribution with a 25.4 mm region of homogeneous intensity at the centre.

The iron-coated silicon substrates were cleaned by UV-ozone (20 min) before use. The tribometer roller and oil bath were washed with *n*-dodecane-h_{26} and dried with a N_2 stream before any sample solution was added to the tribometer oil bath. The temperature of the oil bath and substrate were kept constant at 25 °C during the experiments. The reduced data were fit in GenX by minimising χ^2 (see Equation 2.53) and the 95 % confidence intervals were estimated using the bootstrap resampling routine.

5.2.1 Characterisation of the iron oxide-dodecane interface under shear

An iron-coated silicon substrate was loaded into the tribometer, and the roller-substrate gap was calibrated at 200 µm. The tribometer was loaded with 10 ml of dodecane-d_{26} and the neutron beam was aligned at the substrate-air interface. The solution was then entrained onto the substrate at two maximum shear rates of 7.0 $\times$ 10^2 s^{-1} and 3.6 $\times$ 10^3 s^{-1} using horizontal roller velocities of 1.1 $\times$ 10^{-3} m s^{-1} and 1.8 $\times$ 10^{-3} m s^{-1} and surface velocities of 1.4 $\times$ 10^{-1} m s^{-1} and 7.2 $\times$ 10^{-1} m s^{-1}. The shear rates are calculated as the ratio of the roller surface

velocity to the minimum roller-gap separation. The reflected intensity of neutrons was then measured for at least 1.25 hours. The widths of the resulting menisci appeared to be consistent with those in Figure 2.23 and the regions held outside of the menisci remained visibly wetted by the solution. The variation in the distance between the substrate and the roller within the 20 mm meniscus width is estimated to range from 200 to 2290 µm for the data collected at 3.6×10^3 s^{-1}. This results in a range of shear rates from 0.3–3.6×10^3 s^{-1} assuming the flow remains parallel to the substrate over the meniscus. However, it is likely that the fluid will have a larger vertical velocity component at the extremities of the meniscus due to the curvature of the roller, and thus this range of shear rates only serves as an approximation.

The NR profiles are shown in Figure 5.2a. The critical edge is located at $Q = 0.0144$ Å^{-1} for both profiles, corresponding to approximately 96 % solvent deuteration and is comparable to that found in solid-liquid cells. The total reflection observed at $Q < 0.0144$ Å^{-1} suggests that dodecane-d_{26} completely wets the area illuminated by the neutron beam as any area within the footprint that remained dry would contribute a non-zero gradient to the region of total reflection. The lower shear rate data have significant differences between the first fringe minima, at $Q \sim 0.04$ Å^{-1}, for the two scattering angles; this is not reproduced at the higher shear rate. Therefore, the data were not stitched together in the usual manner, such as with solid-liquid cell data.

Figure 5.2b shows the NR profiles collected with another iron-coated silicon substrate with a 0.06:0.94 dodecane-d_{26}:dodecane-h_{26} volumetric mixture entrained against the surface at the same shear rates with the same calibrated gap and roller velocities. The solvent mixture is referred to as ACdod and has an overall $\beta_n = 0 \times 10^{-6}$ Å^{-2}. The data were collected with $\theta_i = 0.8°$ and 2.3°, where the slightly higher first angle was chosen to give better counting statistics around the first fringe minima. There appears to be no significant difference between the data collected at the two scattering angles, and nor is there any visible change with shear rate. It is not expected that the different first angle should cause the variation in reflectivity between the two solvent contrasts. The difference between the data collected with dodecane-d_{26} shows that the interface changes with shear rate. The lack of difference when using ACdod implies that shear alters the structure of a low β_n material at the interface. The model used to describe these data is laid out in the following paragraphs.

As the footprint of the beam along the interface is greater than the width of the meniscus at both shear rates, the measured reflectivity is expected to contain a fractional contribution from the interface that is not contained in the meniscus. The total reflectivity, R_{tot}, can be modelled using Equation 5.1.

$$R_{tot} = R_S \times \bar{\gamma} + R_{NS} \times (1 - \bar{\gamma}) \tag{5.1}$$

Here, R_{tot} is the weighted linear combination of reflectivity arising from the region held within the meniscus, R_S, and the region held outside of the meniscus, R_{NS}. The weighting factor, $\bar{\gamma}$, is referred to as the average weighted shear fraction, and is the ratio of the meniscus width

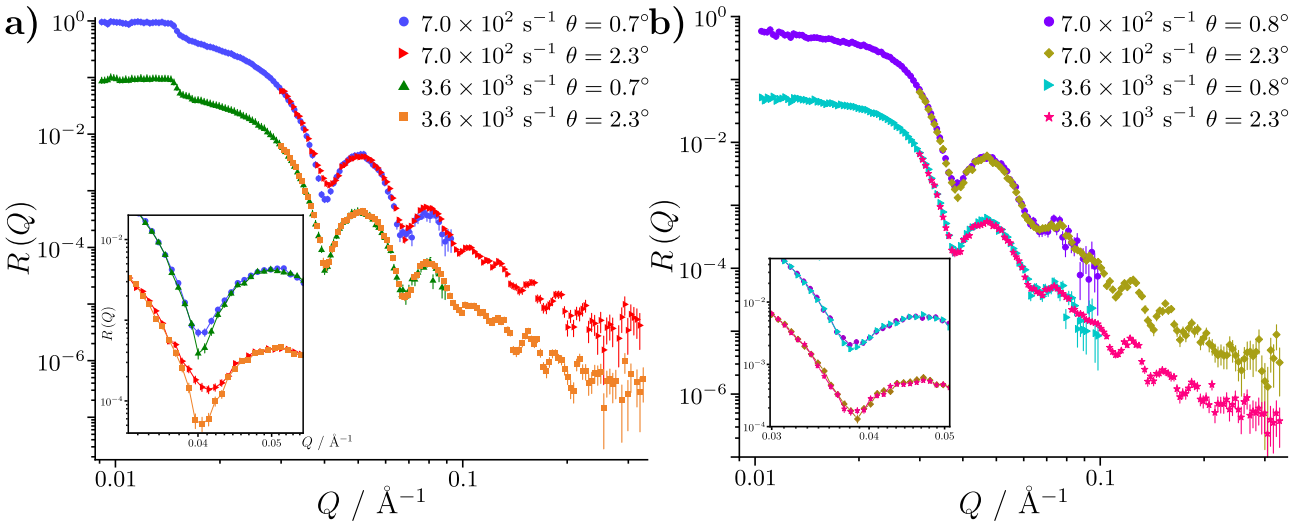

Figure 5.2: **a)** NR data for dodecane-d_{26} entrained against an iron-coated silicon substrate at 7.0×10^2 s^{-1} and 3.6×10^3 s^{-1}. The data collected at 3.6×10^3 s^{-1} are offset by 10^{-1} in the vertical axis. The inset compares the two shear rates for each angle, where the data collected at $\theta = 2.3°$ are offset by 10^{-1} in the vertical axis. The lines between data points are linear interpolations to guide the eye. **b)** NR data collected with a different iron-coated silicon substrate against ACdod at the same shear rates as **a)**. The format of the plot follows the same as part **a)**.

within the footprint of the neutron beam to the total footprint of the beam, all weighted by the relative intensity of the footprint. The value of $\bar{\gamma}$ at different shear rates can be determined following the procedure outlined in Figure 5.3.

The calculation of $\bar{\gamma}$ does not account for the parabolic neutron trajectory under the effect of gravity. However, the true location of the footprint can be approximated following the method set out by Gutfreund *et al.*.[219] The position where a neutron of a specific λ hits the sample, x_s, is given as $x_s = x_0 - (y_0/k)^{1/2}$. Here, k is an inverse length defined as $k = g/(2v_n^2)$, where g is the gravitational acceleration and v_n is the neutron velocity. The variables x_0 and y_0 are defined as

$$x_0 = \frac{y_1 - y_2 + k\left(x_1^2 - x_2^2\right)}{2k\left(x_1 - x_2\right)} \text{ and}$$
$$y_0 = y_2 + k\left(x_2 - x_0\right)^2, \tag{5.2}$$

where x_1, x_2, y_1 and y_2 are the horizontal and vertical distances from the sample to the collimating slits 1 and 2. The distance between the slits is 1894 mm and the distance from the center of the sample to Slit 2 is 411 mm at an angle of 2.3°, so that $x_1 = 2303$ mm, $x_2 = 411$ mm, $y_1 = 93$ mm and $y_2 = 16$ mm. Therefore, the maximum horizontal shift towards the collimating slits is ~ 2.1 mm when $\lambda = 17$ Å. Using this value, the maximum difference to the shear fraction is approximated to be 1.3 % at a shear rate of 7.0×10^2 s^{-1}. However, the difference quickly falls away to < 1 % when $\lambda \leq 15$ Å. At the higher shear rate, the difference in the shear fraction decreases to 0.8 % at $\lambda = 17$ Å. Therefore, the shift due to gravitational droop is deemed negligible and does not need to be included in the calculation. It is suggested

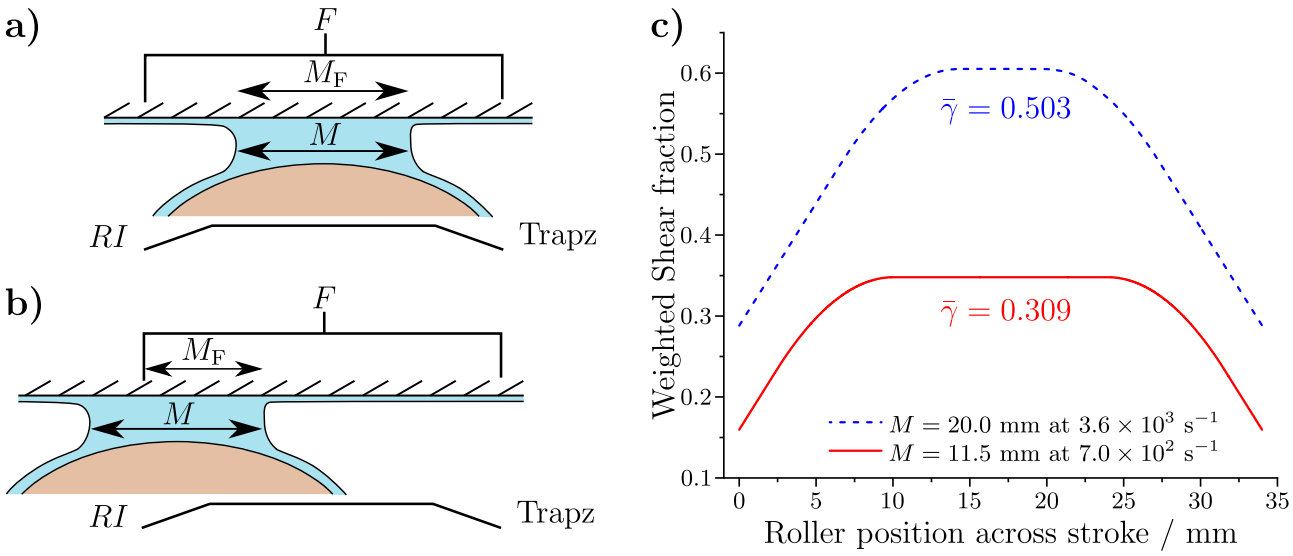

Figure 5.3: **a)** Schematic of the roller centred in the middle of the beam footprint, F. The meniscus width, M, lies completely within F and hence the meniscus width within the footprint, M_F, is equal to M. Below the schematic, the relative intensity (RI) between 0 and 1 is shown by the trapezoid distribution. To calculate the shear fraction at all positions across the footprint, the ratio, M_F/F, must be weighted by the total intensity within F. **b)** This schematic represents the scenario when the roller has moved some distance across its stroke. Some of the meniscus width lies outside of the footprint, leading to $M_F \neq M$. Therefore, the shear fraction is reduced from its maximum value of M/F. **c)** The weighted shear fraction, γ, as a function of roller position across the stroke for meniscus widths of 20.0 mm and 11.5 mm. The centre of the roller stroke is 17 mm. As the roller reciprocates across the interface many times during an experiment, the average of the weighted shear fraction, $\bar{\gamma}$, is required. The value of $\bar{\gamma}$ is shown for both shear rates.

that gravitational effects should be taken into consideration when using neutron wavelengths $\geq$ 20 Å, where the trapezoid distribution of intensity will become increasingly smeared over the footprint with increasing λ.

Both R_{NS} and R_S of Equation 5.1 account for the reflectivity arising over the immediate Si interface which includes the sputtered and adsorbed thin films. However, it is thought that R_{NS} contains a further reflectivity contribution which results from neutrons propagating over the dodecane film that wets the substrate when not held in the meniscus. Upon reaching the dodecane-air interface, the neutrons are either reflected towards the detector or transmitted into air. Reflectivity arising over thicker films on the micrometer length scale has been reported previously, and this process is depicted in Figure 5.4a.[220,221] The total reflectivity for the non-sheared portion of the interface is given as

$$R_{NS} = R_1 + \frac{(1 - R_1)^2 R_2 e^{-\mu L}}{1 - R_1 R_2 e^{-\mu L}} . \tag{5.3}$$

Here, R_1 is the reflectivity from the immediate Si interface and R_2 is the reflectivity from the dodecane-air interface. The neutron path length within the dodecane layer, L, is defined as $L = 2d/\sin\theta_t$, where θ_t is the angle of transmittance and d is the film thickness of the dodecane

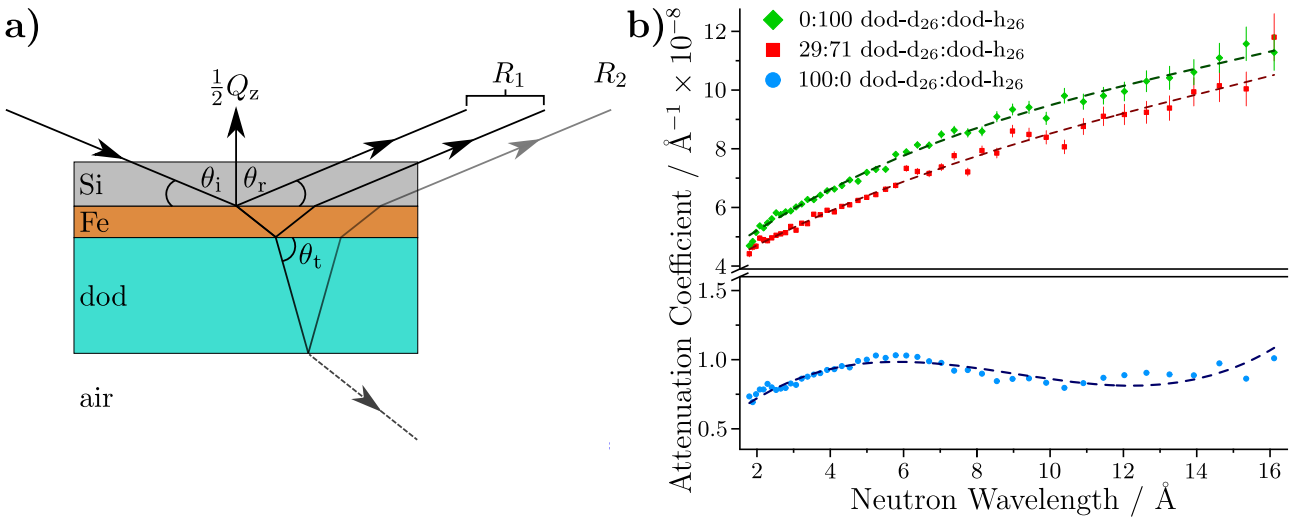

Figure 5.4: **a)** Schematic of thick film reflectivity from the non-sheared portion of the interface. R_1 is the reflectivity term that accounts for reflection from the immediate Si interface. Neutrons transmitted over the immediate interface will propagate through dodecane at an angle θ_t before being either reflected or transmitted at the dodecane-air interface. R_2 is the reflectivity term that accounts for reflection from the dodecane-air interface. **b)** Neutron attenuation coefficients for three dodecane contrasts measured on ZOOM, ISIS, UK.

layer. The attenuation coefficient of dodecane, μ, is wavelength dependant and is also sensitive to the H/D content. To determine μ for some of the contrasts used in this work, three volumetric mixtures of dodecane-d_{26}:dodecane-h_{26} (100:0, 29:71 and 0:100) were measured on the ZOOM instrument at ISIS, UK, by Dr Diego Alba Venero. The increased attenuation when the H content of the dodecane increases arises from the greater incoherent scattering of H compared to D. As μ is wavelength dependant, the data were fit with third order polynomials in order to use the fitted coefficients when modelling the NR data; the attenuation data and polynomial fits are shown in Figure 5.4b.

Equation 5.3 accounts for multiple reflections across the thick dodecane film and any resulting attenuation of the neutron beam over this layer. It also assumes that the thickness of the wetting dodecane layer is greater than the coherence length of the neutron beam in the vertical direction. This length is specific to each individual experiment as it is defined by the slit settings used, but is approximated to be < 2 µm for a comparable ToF instrument at the ILL.[221] Therefore, it is expected that the coherence length on INTER is approximately on the same length scale. As the dodecane layer is visibly thick, Kiessig fringes will not arise from the thick dodecane layer due to the smearing effect of the Q resolution. This is expected to be the case for a film with a thickness $\gtrsim 2$ µm, and is not dependant on the vertical coherence length. The reflected intensity measured from the sheared portion of the interface, R_S, is assumed to arise solely from the immediate interface. This assumption is used as it is not expected that significant specular reflection occurs from the dodecane-PEEK interface due to the angle of reflection adopted when striking the roller. Additionally, as discussed in Chapter 2, the roller has an RMS roughness of 1.6 µm which will further diminish the intensity of specular reflection from the roller.

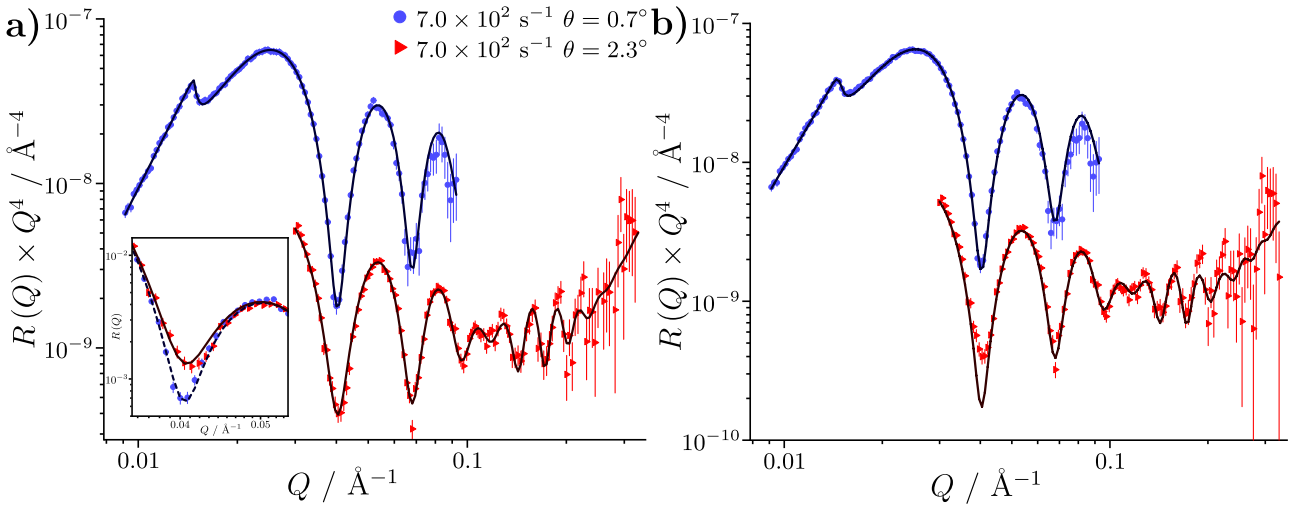

Figure 5.5: **a)** The best fit, shown by the dark lines, to the NR data collected with dodecane-d_{26} entrained against an iron-coated silicon substrate at 7.0×10^2 s^{-1}. The reflectivity has been modified by a Q^4 factor to aid comparison. The data collected at $\theta = 2.3°$ are offset by 10^{-1} in the vertical axis. The inset compares the fit to the unadjusted reflectivity at the first fringe minimum. **b)** The best fit to the data without accounting for the R_2 term.

The difference between the reflectivity of the two angles collected at the lower shear rate with dodecane-d_{26} is thought to arise from the different values of L and μ at $Q \sim 0.04$ Å^{-1}. These variables will also be different for the ACdod contrast; however, the reflectivity from the dodecane-air interface is nullified as there is no significant β_n contrast between ACdod and air. This leads to the predominance of R_1 when using ACdod, and hence, no difference between the two scattering angles is observed.

The model defined above was coupled with a conventional multilayer slab model to describe the reflectivity from the thin films present on the substrate surface. The best fit to the data collected at 7.0×10^2 s^{-1} with neat dodecane-d_{26} is shown by the black line in Figure 5.5a. The average thickness of the residual dodecane layer which remains on the substrate when not sheared was fit with values of 112^{+85}_{-23} µm, where the roughness of the dodecane-air interface was modelled to be 3 Å. This roughness is not considered to be an accurate value but serves as an upper bound when calculating the thickness of the wetting dodecane, as a greater roughness will reduce the reflected intensity from the dodecane-air interface. Therefore, the apparent thickness of the dodecane required to suitably attenuate the beam is expected to be thinner than the above distribution. The inferred distributions of the other layer parameters from the bootstrap analysis are shown in Table 5.1. The best fit achieved without modelling the additional R_2 reflection is shown in Figure 5.5b, where the fringe minimum for the second angle is not suitably modelled.

Similar to the data collected in solid-liquid cells, an adventitious layer was required to suitably model the data. To account for possible variation in the adsorbed structure under the two flow environments, separate adventitious layers were modelled for the R_S and R_{NS} contributions which represent the average surface layer structure whilst sheared and non-sheared. The pa-

Table 5.1: Fitted layer parameters for dodecane-d_{26} entrained against an iron-coated silicon substrate at 7.0×10^2 s^{-1}. The central parameter values are the median values obtained from the bootstrap routine, with the 95 % confidence intervals reported in the sub- and superscripts. Those values without uncertainties were held constant. * – parameters used to model the sheared layer. † – parameters used to model the non-sheared layer.

Layer	β_n / Å$^{-2} \times 10^{-6}$	β_m / Å$^{-2} \times 10^{-6}$	Thickness / Å	Roughness / Å
Si	2.07	-	∞	3.0
SiO_2	3.47	-	$6.4^{+6.5}_{-5.4}$	$4.9^{+1.3}_{-1.4}$
Fe	$7.7^{+0.1}_{-0.1}$	$4.7^{+0.1}_{-0.1}$	186^{+2}_{-2}	$5.3^{+2.9}_{-2.6}$
FeO_x	$6.1^{+0.5}_{-0.7}$	$1.3^{+0.0}_{-0.7}$	$32.6^{+4.6}_{-4.5}$	$8.6^{+3.6}_{-4.5}$
*Adv	$1.4^{+3.9}_{-1.9}$	-	$16.3^{+12.3}_{-12.3}$	$7.5^{+5.5}_{-4.1}$
†Adv	$1.6^{+3.1}_{-2.2}$	-	$12.8^{+13.2}_{-6.3}$	$7.7^{+5.0}_{-4.1}$

rameter values and uncertainties for the sheared and non-sheared adventitious layers are similar with wide uncertainties. Consequently, the effects of shear on the structure of the adventitious layer are not clear. A possible factor that contributes to the wide uncertainty is correlation between layer parameters. Another factor could be the effect of shear itself; for example, the confidence intervals for the sheared layer parameters are marginally wider, which could suggest a greater variation in the structure of the adventitious layer when sheared. However, the fit is less influenced by the parameters of the sheared layer due to the lower weighting of the R_S contribution at 7.0×10^2 s^{-1}. As a result, the parameters of the sheared layer can vary more widely whilst remaining consistent with the data. With this in mind, it would appear that the adventitious layers are equivalent within error.

The thickness of the adventitious layers are also consistent with those reported in the solid-liquid cells. This would imply that shear at 7.0×10^2 s^{-1} has little effect on the structure of the adventitious layer. This contrasts the reported contraction of $\sim$ 1–7 Å for an equivalent layer at the silicon-hexadecane interface when sheared at 500 s^{-1} using a cone-plate rheometer.[180] The uncertainties achieved in the cited work are reported to be much smaller than those here; therefore, it is possible that a similar contraction occurs, but the sensitivity to the sheared portion of the interface is such that any change appears equivalent within error.

The model used to fit the data collected at 7.0×10^2 s^{-1} does not reproduce the sharp fringe minima in the reflectivity collected with dodecane-d_{26} at 3.6×10^3 s^{-1} as shown in Figure 5.6a. Here, the data was fit using an average thickness of 200 µm for the residual dodecane wetting layer in the non-sheared region. This value represents the upper bound used in the fitting of the 7.0×10^2 s^{-1} data and the minimum roller-substrate gap. The quality of the fit is satisfactory for the data collected at $\theta = 0.7°$. However, a discrepancy between the fit and collected data at $\theta = 2.3°$ is apparent in the first fringe minima. The sharper fringe is thought to result from reduced specular reflection from the dodecane-air interface at higher roller angular velocities.

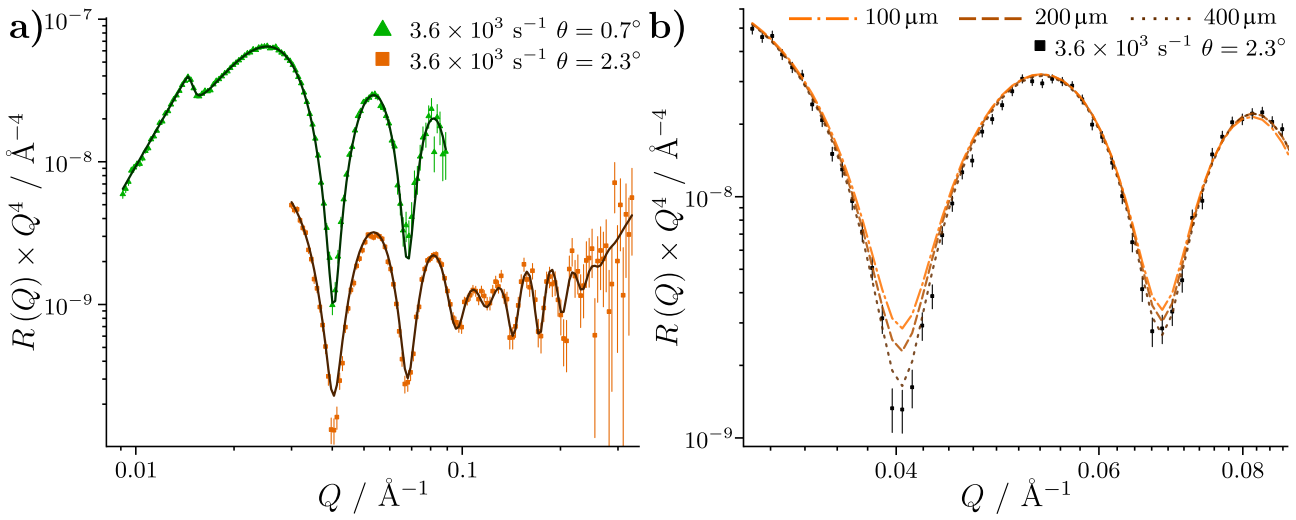

Figure 5.6: **a)** Best fit to the data collected with dodecane-d_{26} entrained against an iron-coated silicon substrate at 3.6×10^3 s^{-1}. The fit was modelled with a residual dodecane thickness of 200 µm. The data collected at $\theta = 2.3°$ is offset by 10^{-1} in the vertical axis. **b)** Comparison of three fits to the first two fringe minima of the data collected at $\theta = 2.3°$. The fits used three residual dodecane layer thickness that are listed in the key.

This could be caused by increased attenuation over a thickened wetting dodecane layer and/or from a significant roughening of the interface. The former case has been calculated to require the dodecane layer to thicken substantially, approximately to 400 µm, to produce the sharper fringe minima. This is shown in Figure 5.6b. While some thickening is expected with greater angular velocities, this scale of thickening would be visible and has not been observed.

It has been observed that higher roller angular velocities lead to roughening of the wetting layer, where visible waviness is present for the whole stroke length of the tribometer roller. Images comparing the roughness of the wetting layer at 7.0×10^2 s^{-1} and 3.6×10^3 s^{-1} are shown in Figure 5.7. Here, three images are presented which show the reflection of a screw on the far-side of the tribometer from the mirrored surface of the substrate. One of the images has been captured with a dry substrate without the roller moving, while the other images have been captured with entrained dodecane on the substrate surface using roller surface velocities of 1.4×10^{-1} m s^{-1} and 7.2×10^{-1} m s^{-1} and a roller horizontal velocity of 1.8×10^{-3} m s^{-1}. These velocities correspond to maximum shear rates of 7.0×10^2 s^{-1} and 3.6×10^3 s^{-1}. When the substrate is dry, an undistorted and focused image is formed. When entraining dodecane onto the substrate, the reflection must propagate through the wetting layer of dodecane before reaching the camera. If the surface of the wetting layer is not mirror-like, distortions will be apparent in the captured image. There is little difference between the images captured with the dry substrate and with the dodecane entrained at 7.0×10^2 s^{-1}, suggesting that the dodecane-air interface is reasonably smooth. However, in comparison to the former two images, the image captured at 3.6×10^3 s^{-1} shows significant distortion. The texture of the dodecane-air interface has been visualised by focussing the camera onto the substrate, where substantial waviness is visible across the entire substrate.

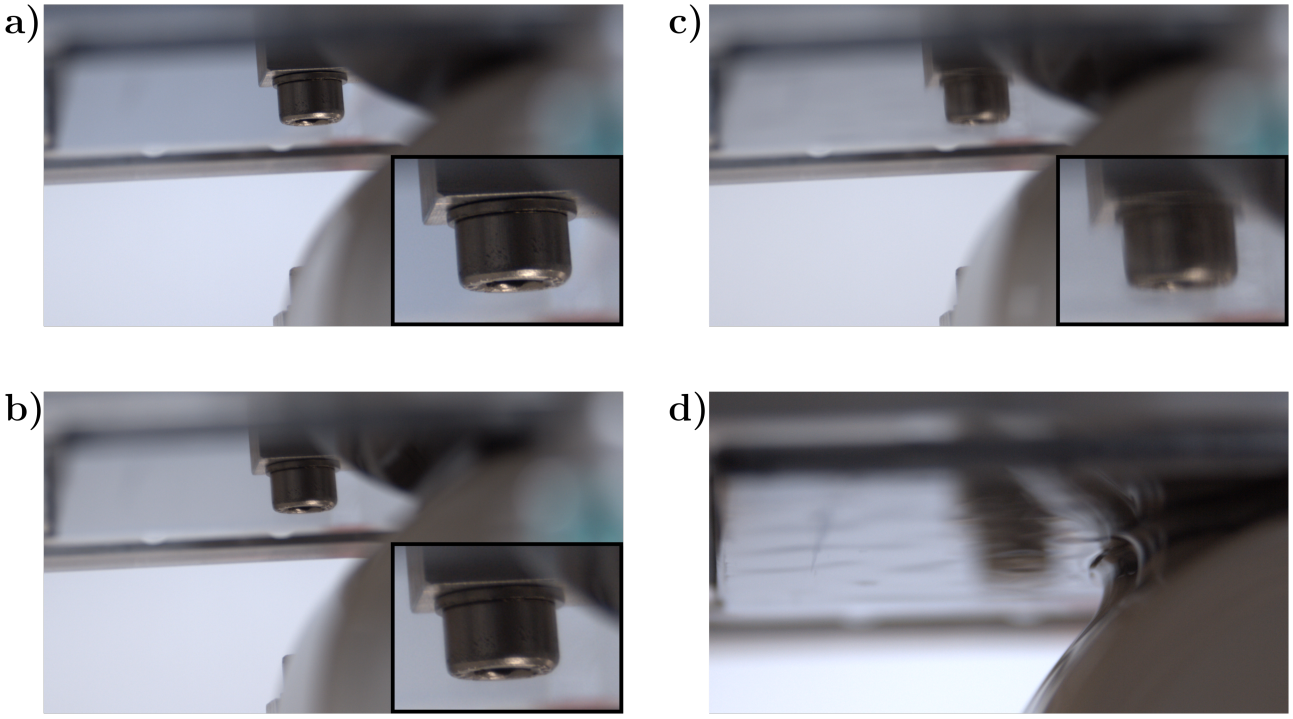

Figure 5.7: **a)** Image captured with a dry substrate. The screw shown in the reflection from the substrate is the focus point. The inset is a magnified view of the screw. **b)** Image captured with the substrate wetted with dodecane, where the dodecane is entrained onto the surface at 7.0×10^2 s^{-1}. **c)** Image captured with the substrate wetted with dodecane. The dodecane is entrained onto the surface at 3.6×10^3 s^{-1}. **d)** Image captured at 3.6×10^3 s^{-1}, but with focus shifted to the substrate. Clear undulations are seen on the dodecane surface across the substrate.

As macroscopic roughness is visible at 3.6×10^{-3} s^{-1}, it is suggested that the reflection from the dodecane-air interface will be reduced, potentially so much that R_2 becomes negligible. This would lead to the reduction of Equation 5.3 to the R_1 term. However, the average roughness of the layer is not known, and therefore the combinations of dodecane roughness and thickness that could describe the reflectivity are very large. It would be possible to constrain the fit if the thickness or roughness could be determined via other techniques. However, due to the geometry of the tribometer, experimental determination of these values is a particularly difficult challenge.

Figure 5.8 shows the fit to the data collected with ACdod at both shear rates, with the best fit values shown in Table C1. Only one adventitious layer was modelled as the purpose of the fit was to show that the reflectivity can be suitably simulated with a model that is consistent with Equation 5.3. As such, the modelled layer represents the average structure across the interface. This approach is validated due to the poor contrast between the adventitious layer and the solvent, leading to little extractable information. Therefore, it serves little purpose to model two adventitious layers. A bootstrap analysis of the parameter values was not conducted for these reasons.

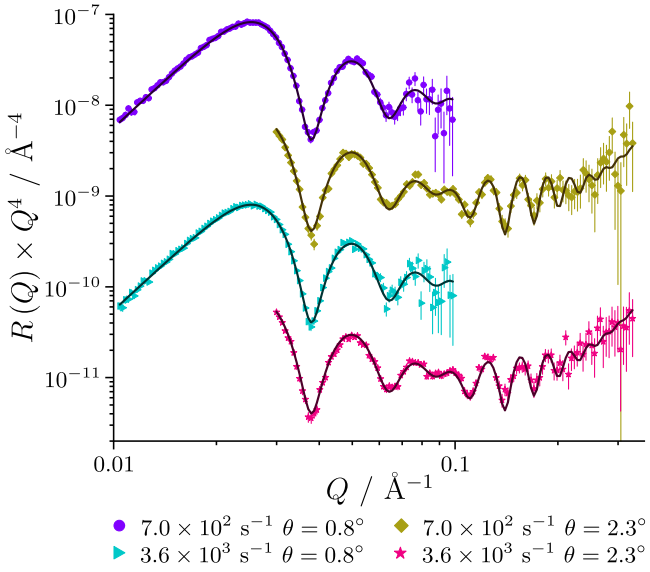

Figure 5.8: Best fits to the data collected with ACdod at 7.0×10^2 s^{-1} and 3.6×10^3 s^{-1}. The data are modified by a factor of Q^4 and are offset by 10^{-1} for clarity.

GMO at the iron oxide-dodecane interface under shear

Two dodecane solutions containing GMO (20 mM) were entrained against an iron-coated silicon substrate at 7.0×10^2 s^{-1} and their NR profiles were collected. The shear rate was achieved using a horizontal velocity of 1.8×10^{-3} m s^{-1} and a roller surface velocity of 1.4×10^{-1} m s^{-1}. One of the GMO solutions was made with 100 % dodecane-d_{26} and the other solution was made with a 29:71 volumetric mixture of dodecane-d_{26}:dodecane-h_{26}, referred to as CMdod. Figure 5.9a compares the reflectivity measured at 7.0×10^2 s^{-1} with neat dodecane-d_{26} to the reflectivity measured with the 20 mM solution of GMO in dodecane-d_{26}. While the substrates used for the collection of these profiles are not the same, the properties of the underlying substrate layers were found to be similar. Therefore, it is expected that the shift in the Kiessig fringes between the datasets is due to the adsorption of GMO at the iron oxide-dodecane interface and not differences between the two coated substrates.

The two solvent contrasts of the GMO-dodecane system were globally fit using the same model used to fit the neat dodecane-d_{26} contrast at 7.0×10^2 s^{-1}. The adsorbed GMO was represented by two layers to account for possible variation with shear. The best fit to the data and the median β_{++} profile from the parameter distributions are shown in Figure 5.9b and Figure 5.9c respectively. The parameter distributions from the fit are shown in Table 5.2. The film thickness of the residual dodecane layer was found to be 104^{+71}_{-33} µm.

The inferred thickness for the sheared and non-sheared GMO layers appear to be equivalent within error, where the distribution is wider for the sheared layer. It is expected that, in a similar manner to the adventitious layer, the lower sensitivity towards the sheared portion of the interface leads to the greater uncertainty. Due to the large uncertainty, the thickness values are equivalent within error to that inferred for the layer formed with the 20 mM GMO-dodecane solutions in solid-liquid cells under static conditions. However, it is noted that the distributions

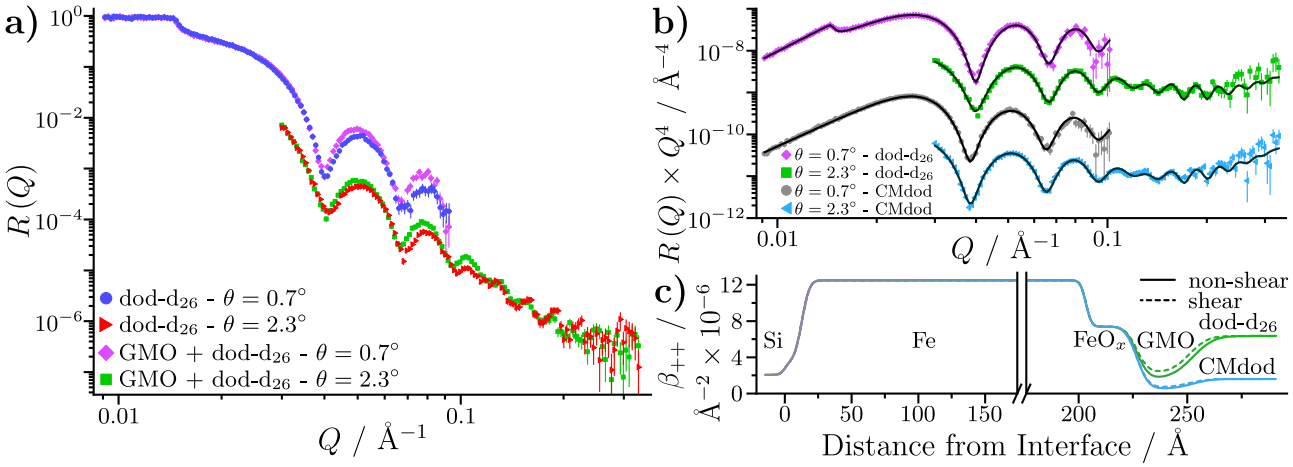

Figure 5.9: **a)** Comparison of NR data for dodecane-d_{26} with and without GMO entrained against iron-coated silicon substrates at 7.0×10^2 s^{-1}. Data collected at $\theta = 2.3°$ are offset by 10^{-1} in the vertical axis. **b)** NR data for 20 mM GMO in dodecane-d_{26} and CMdod entrained against an iron-coated silicon substrate at 7.0×10^2 s^{-1}. The reflectivity has been modified by a Q^4 factor to aid comparison. Data are offset in the vertical axis for clarity. **c)** β_{++} profiles for the GMO-dodecane systems. A small SiO_2 layer was modelled between the Si and Fe layer but is not labelled for clarity.

Table 5.2: Fitted layer parameters for the GMO-dodecane solutions entrained against an iron-coated silicon substrate at 7.0×10^2 s^{-1}. The central parameter values are the median values obtained from the bootstrap routine, with the 95 % confidence intervals reported in the sub- and superscripts. Those values without uncertainties were held constant. * – parameters used to model the sheared layer. † – parameters used to model the non-sheared layer.

Layer	β_n / Å^{-2} × 10^{-6}	β_m / Å^{-2} × 10^{-6}	Thickness / Å	Roughness / Å	Solvation / %
Si	2.07	-	∞	3.0	-
SiO_2	3.47	-	$12.7^{+2.9}_{-7.4}$	$4.6^{+1.9}_{-3.6}$	-
Fe	$7.9^{+0.1}_{-0.1}$	$4.6^{+0.1}_{-0.1}$	191^{+1}_{-2}	$2.1^{+4.4}_{-1.1}$	-
FeO_x	$6.9^{+0.3}_{-0.3}$	$0.5^{+0.3}_{-0.3}$	$23.3^{+0.8}_{-0.8}$	$4.3^{+4.8}_{-2.3}$	-
*GMO	0.21	-	$24.3^{+9.9}_{-10.2}$	$6.7^{+3.3}_{-4.7}$	$35.2^{+45.3}_{-35.2}$
†GMO	0.21	-	$25.8^{+4.4}_{-5.2}$	$7.7^{+2.3}_{-5.7}$	$24.5^{+21.6}_{-22.4}$

are centred around values that are $\sim$ 5 Å greater than the static counterparts. Similarly, the solvation distributions have wider uncertainties and are centred around higher values than found for the interfacial layer formed with 20 mM GMO in dodecane under static conditions. These higher values could imply the formation of structures that are thicker and more solvated than a monolayer, such as adsorbed reverse micelles, which have been reported from molecular dynamic simulations for GMO adsorbed at hematite and mica surfaces in non-aqueous solvents.[152,153,163] However, as the parameter distributions are not resolved from one another, strong conclusions cannot be made about the structure of GMO from the data presented here.

It is also possible that the variation arises from the formation of a range of adsorbed structures when under different shear environments, as the tribometer does not provide a homogeneous sheared environment. If a complex structure is formed, it is possible that the GMO layer does not completely relax during the time taken to traverse the interface ($\sim$ 18 s). Interfacial polymer micelles have been reported to relax over the time scale of hours, although GMO, and its surface aggregates, are much smaller structures in comparison.[222]

5.2.2 Reflectivity with deuterated base oil

In general, base oils have a greater viscosity than dodecane, which when forced through a converging gap will generate greater hydrodynamic pressures as predicted by lubrication theory.[7] These pressures could be used to support a light applied load across the contact while avoiding wear. In this section, the neutron reflectivity from an iron-coated silicon substrate with base oil, Yubase-4, entrained against the surface was measured with a calibrated gap of 200 µm. This was conducted to assess the reflectivity in relation to dodecane, and any potential effects caused by the greater viscosity of the base oil.

Yubase-4 is a synthetic base oil with a long chain aliphatic structure, termed polyalphaolefin, and is comprised of carbon and hydrogen, leading to a similar β_n compared to dodecane-h_{26}. Therefore, deuterated Yubase-4 is required for contrast with the dodecane-air interface and any interfacial film adsorbed at the iron oxide surface. Partially deuterated Yubase-4 was prepared by Colin Willis, Infineum UK, to a deuteration of $\sim$ 85 % as estimated by ^{1}H NMR. A 10 ml sample of deuterated Yubase-4 was entrained at two different shear rates of 7.0×10^2 and 3.6×10^3 s^{-1} using roller surface velocities of 1.4×10^{-1} m s^{-1} and 7.2×10^{-1} m s^{-1} and a horizontal roller velocity of 1.8×10^{-3} m s^{-1}. The NR data was collected on INTER, with λ = 2–17 Å and θ = 0.7° and 2.3°, resulting in a Q range of 0.009–0.300 Å^{-1}. The standard deviation of the dQ/Q resolution was 2 %. The individual angle data are compared in Figure 5.10a, where the overlap between the fringes appears consistent for both shear rates. Therefore, it was deemed acceptable to stitch the data together to form composite datasets. The datasets collected at the different shear rates are directly compared in Figure 5.10b. Here, the reflectivity is comparable, indicating that shear has not altered the state of the interface.

The origin of the improved fringe minima overlap with deuterated Yubase-4 is not known, although some possible reasons are suggested that could account for improved overlap. In

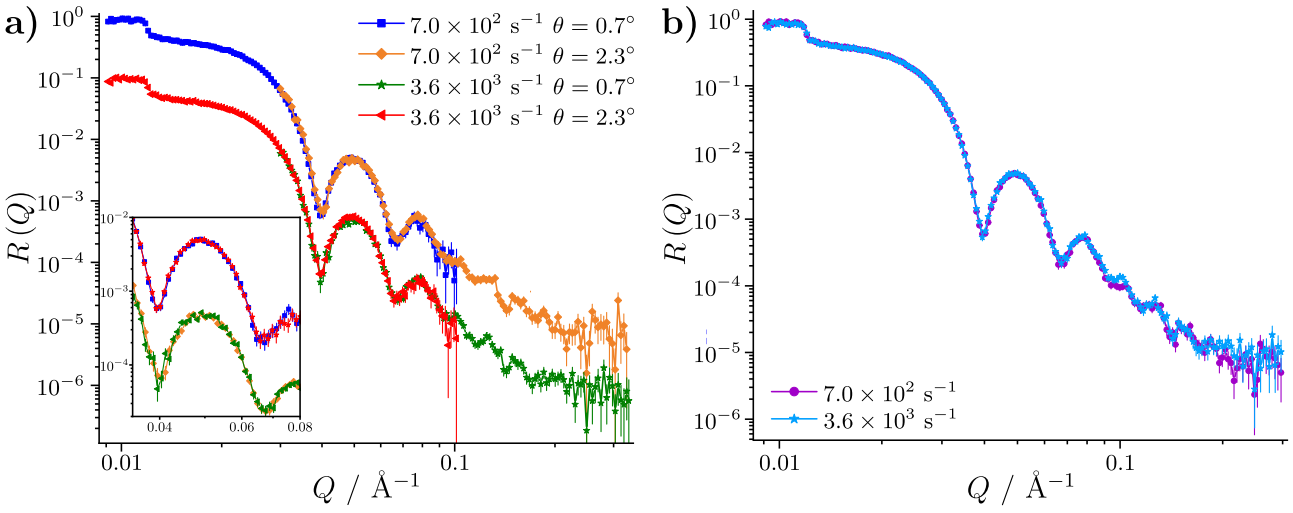

Figure 5.10: **a)** Comparison of single angle NR data collected with partially deuterated Yubase-4 against an iron-coated silicon substrate. Data collected at 3.6×10^3 s^{-1} are offset by 10^{-1}. The inset compares the data collected at the same angle but at different shear rates. The data collected at $\theta = 2.3°$ are offset by 10^{-1}. **b)** Stitched NR profiles of the single angle data shown in **a)** overlaid.

Table 5.3: Comparison of the physical properties of dodecane-d_{26} and Yubase-4 at 25 °C, where γ is the surface tension, η is the dynamic viscosity and ρ is the density.

Substance	γ / mN m^{-1}	η / mPa s	ρ / g cm^{-3}
dodecane-d_{26}	24.9[223]	1.38[146,147]	0.86
Yubase-4	30.6	22.1	0.83

comparison to dodecane, the greater viscosity will lead to an increased amount of oil lifted into the meniscus. As the surface tension and density of dodecane-d_{26} and Yubase-4 are of comparable magnitude, as shown in Table 5.3, the drainage via the formation of droplets from the inverted surface is expected to be similar. Therefore, as the amount of entrained oil onto the substrate is larger in comparison to dodecane, the thickness of the residual wetting layer can be expected to be greater. It is possible that the roughness or waviness of the wetting layer is also greater as a result of the inhomogeneity of the thicker film. Finally, the greater hydrogen content of the partially deuterated Yubase-4 may also improve fringe overlap as the attenuation coefficient will be greater than the dodecane attenuation coefficient. This will reduce the R_2 contribution in the total reflectivity, which is thought to give rise to the different fringe minima with dodecane-d_{26} at the lower shear rate.

Figure 5.11a shows two images of a ribbing instability that formed on the surface of the roller at the higher shear rate, which was not apparent on the roller at the lower shear rate. It is possible to see light through the meniscus in the second image, which could arise from air channels adjacent to fingers of Yubase-4 flowing across the surface. However, in this case the instabilities would have to be smaller than the 200 µm gap, and any spreading of the oil on the substrate would have to be negligible. Furthermore, as the reflectivity appears equivalent

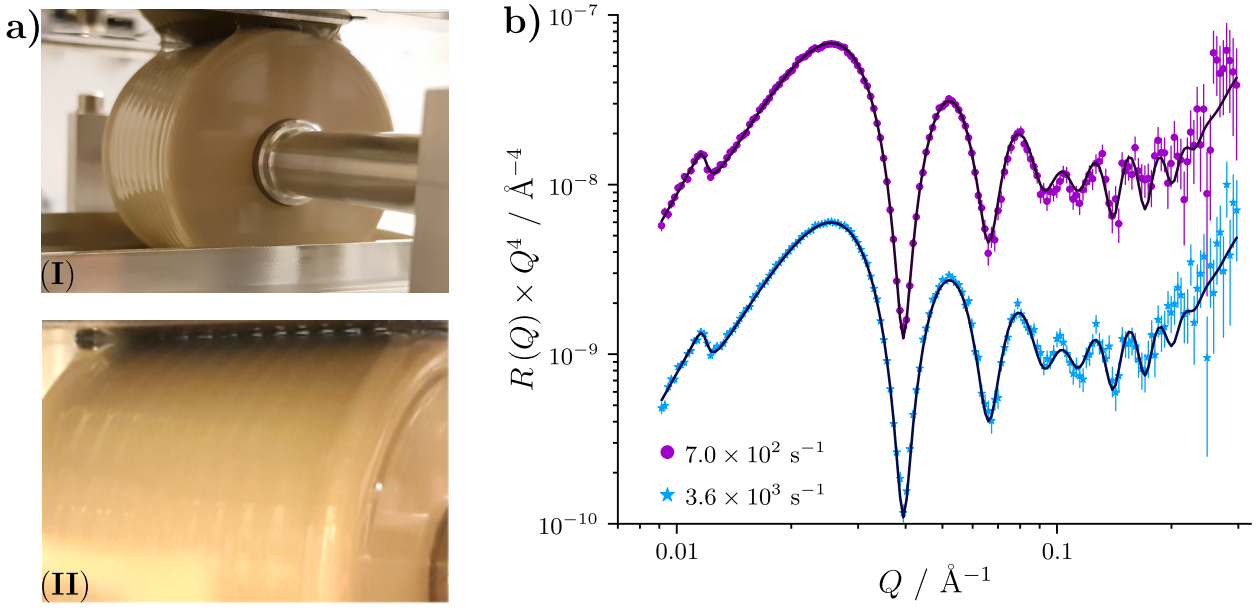

Figure 5.11: **a)** Two images of the ribbing instability on the roller (**I**) and between the roller and substrate (**II**). **b)** Comparison of the fitted model to the reflectivity. The higher shear rate data is offset by 10^{-1} in the modified reflectivity axis for clarity.

between the uniform and ribbed states, it is not expected that significant channels of air are formed against the surface. Instead it is thought that the wave-like characteristics of the instability lead to sinusoidal positions of the three-phase contact line, where the Yubase-4 separates from the substrate surface. If the length over which the light has to travel through the meniscus is marginally greater at some locations due to the protruding fingers of Yubase-4, a lower intensity of light may be expected to propagate through them.

Alongside the uniform behaviour of the meniscus at low shear rate with Yubase-4, the instability is not observed at any accessible shear rate with dodecane. It is known that ribbing occurs at a critical value of the capillary number, C_a, for the plate-roll geometry when the roller is held in a stationary position while rotating.[224] The capillary number is defined as

$$C_\mathrm{a} = \frac{\eta V}{\gamma}, \tag{5.4}$$

where V is the velocity of the fluid, which is assumed to be the roller surface velocity. Viscous forces have been suggested to destabilise the meniscus formed on the outlet of the roller, while the surface tension acts to minimise the instability.[225] Therefore, if the viscosity and fluid velocity are great enough, the instabilities are formed.

Following Figure 8 in the cited work[226], the onset of ribbing is thought to occur with $C_\mathrm{a} \sim$ 0.06–0.2 for the plate-roll geometry as used in this experiment. Here, $h_0/R = 4 \times 10^{-3}$, where h_0 is the minimum roller-substrate separation, 0.2 mm, and R is the radius of the roller, 25 mm. This suggests that a uniform meniscus should be formed for dodecane at both shear rates, where $C_\mathrm{a} \sim 0.01$ and 0.04 for the low and high shear rate. On the other hand, ribbing is predicted for the higher shear rate with Yubase-4, where $C_\mathrm{a} \sim 0.52$, but the lower shear

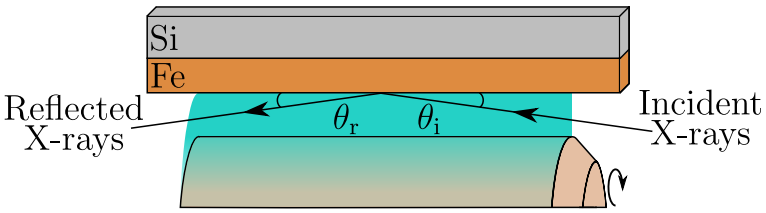

Figure 5.12: Schematic of XRR setup with tribometer. The incident X-ray beam strikes the dodecane-substrate interface at θ_i.

rate sits within the transition region as $C_a \sim 0.10$. Tests later showed that the transition between the uniform and ribbed meniscus occurs around a surface velocity of 0.16 m s^{-1}, where $C_a = 0.12$. The transition boundary from the cited work was suggested to be only taken as an approximate guide, as the ribbing instability is also dependant on the dynamic contact angle of the downstream meniscus.[226] This is a property of both the liquid and of the solid surface, and as the iron oxide surface and Yubase-4 used here will have different surface energies to those used in the literature, it is possible that the critical values of C_a at which the onset of ribbing occurs are different.

The stitched data were fit in GenX without accounting for additional reflection from the air-Yubase-4 interface. Furthermore, the modelled interface was not split into the sheared and non-sheared portions as in Equation 5.1, as the meniscus widths were not determined with Yubase-4. As such, the modelled adventitious layer represents the average structure of the layer under shear and when not under shear. The best fit is shown in Figure 5.11b and the best fit parameters are shown in Table C2. The acceptable fit suggests that deuterated base oil can be used to simplify the analysis of the reflectivity, and that an adventitious layer is present under Yubase-4. The ribbing instability appears not to alter the reflectivity of the system at the shear rates studied; however, it is postulated that the flow within the meniscus when ribbed contains a significant velocity component in the direction along the roller than when the meniscus is uniform, thereby altering the shear applied to the interface.

5.3 X-ray reflectometry

Similar to the NR experiments, the tribometer was operated in non-contact mode in an attempt to minimise wear on the substrate surface. However, as the X-ray beam width is < 1 mm, the whole beam footprint can fall completely within the meniscus region. Therefore, the roller was only set to rotate in one horizontal position. The same cleaning procedures as used in the NR experiments for the substrate and tribometer components were carried out prior to use. In addition, the tribometer was held at 25 °C during use. A schematic showing the basic principal for the XRR experiments with the tribometer is shown in Figure 5.12.

XRR experiments with the tribometer were conducted on I07. The photon energy was 25.0 keV, corresponding to a wavelength of 0.496 Å. A range of scattering angles, $\theta = 0.092$–$1.140°$,

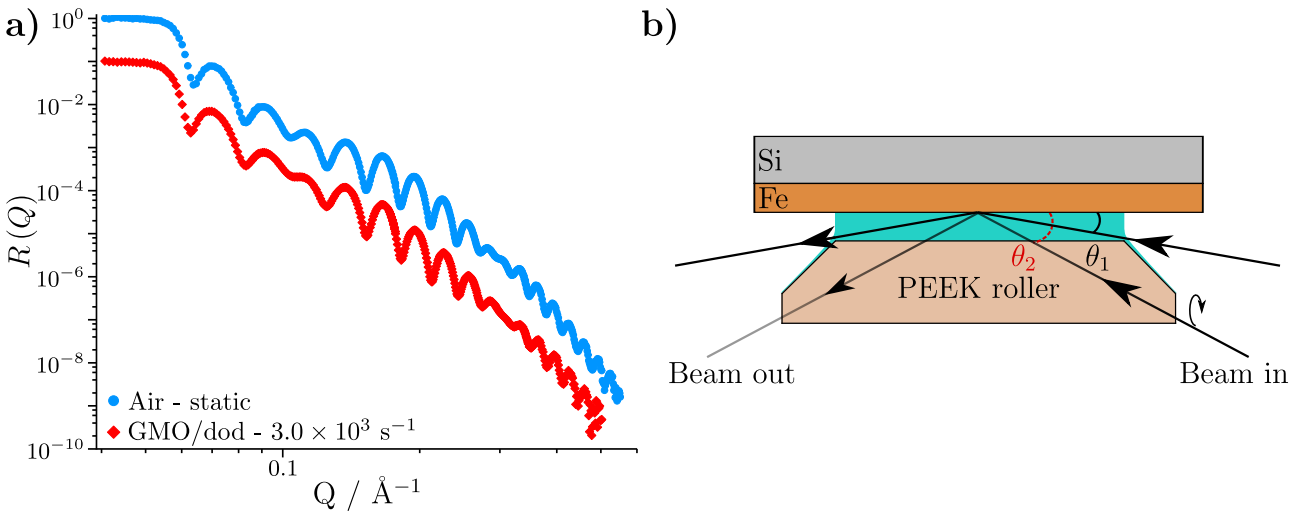

Figure 5.13: **a)** XRR data collected from an iron-coated silicon substrate in air and with a 20 mM GMO dodecane-h_{26} solution entrained against the surface at 3.0×10^{3} s^{-1}. The data collected with the entrained solution has been offset by 10^{-1} in the vertical axis. Error bars have been removed for clarity. **b)** Comparison of the X-ray beam path depending on the scattering angles used. θ_1 depicts the beam path at low scattering angles, where the beam propagates through dodecane before and after reflection at the interface. θ_2 shows the approximate beam path at greater incident angles, where the X-ray propagates through the PEEK roller and then through dodecane before and after reflection.

were used to provide a Q range of 0.041–0.504 $Å^{-1}$. The reflected intensity was measured with a Pilatus 100K 2D detector with a count time of one second per scattering angle. The 2θ angular resolution was 0.01°, resulting in a momentum transfer standard deviation resolution, dQ, of 2.2×10^{-3} $Å^{-1}$. At low θ the sample was over-illuminated by the X-ray beam, which had a full width at half maximum vertical height of approximately 100 µm.

The collected data were reduced with the RodAn package in DAWN, where a region-of-interest with an area of 7 × 7 pixels was used to define the specular reflection.[227] Linear background subtraction was performed using two adjacent areas of 5 × 5 pixels to define the background intensity. The data were also corrected for any over-illumination at low θ. The reduced data were then fit using GenX by minimising the FOM in Equation 2.79, which was then used to estimate parameter confidence intervals through the bootstrap resampling routine.

An iron-coated silicon substrate was loaded into the tribometer and the beam aligned at the iron oxide-air interface. The XRR profile was subsequently measured in air while the roller was in the lowered position so as to reduce interference effects with the X-ray beam. Afterwards, the tribometer oil bath was loaded with a 20 mM solution of GMO in dodecane-h_{26} and the roller was positioned 200 µm from the substrate surface. The beam was then re-aligned to correct for any movement of the interface during the tribometer set up, and care was taken to align the beam down the centre of the roller. The roller was set to a surface velocity of 6.0×10^{-1} m s^{-1} whilst held in a horizontal position, resulting in a shear rate of 3.0×10^{3} s^{-1}. The reduced data for the contrasts against air and the 20 mM GMO-dodecane solution are shown in Figure 5.13a.

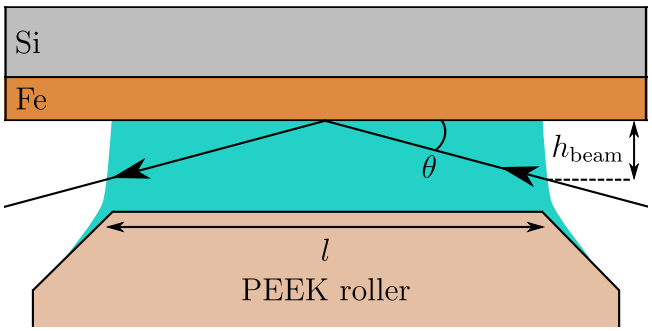

Figure 5.14: X-ray beam path at low scattering angles. Not drawn to scale.

The model used to fit the dataset collected with GMO includes a transmission scale factor to account for the attenuation of the X-ray beam before and after reflection at the substrate. Similar factors have been used with other sample environments to correct for X-ray transmission.[228] As the roller is positioned close to the substrate surface, the beam will propagate through dodecane at low θ and through PEEK and dodecane at higher θ as depicted in Figure 5.13b. As the beam propagates through both materials the beam is attenuated, resulting in a reduced intensity of coherent scatter falling on the detector. At low θ any angle change upon refraction at the air-dodecane interface is negligible as it is less than 2×10^{-7} degrees. In the case of a 200 µm gap, the influence of any meniscus curvature is also negligible as the maximum deviation of intensity is less than the measured reflectivity error.

At higher θ the X-ray beam propagates through the PEEK roller and then through dodecane, both before and after reflection. The X-ray beam initially strikes the 45° chamfered edge of the roller, where the refractive angle follows Snell's law. The beam is then refracted at the horizontal PEEK-dodecane interface and propagates towards the substrate through dodecane. After reflection, the X-ray beam propagates in the direction of the detector through dodecane and PEEK with a similar path to the incident beam. The intensity at the detector is calculated using the path lengths and the pre-determined linear attenuation coefficients of dodecane and PEEK which are 0.205 cm^{-1} and 0.388 cm^{-1} respectively.[120] The transmission scale factor was not included when modelling the data collected with the substrate in air as the roller was far from the surface and did not cross the beam path. The calculation of the path lengths and the overall X-ray attenuation factor is detailed in the following sections.

Determination of path lengths in dodecane and the PEEK roller

The path followed by the center of the beam at low θ values is depicted in Figure 5.14. Here, the X-ray beam strikes the air-dodecane interface at a vertical distance from the substrate surface, h_{beam}, which is calculated as

$$h_{\text{beam}} = \frac{l}{2} \tan\theta \,. \tag{5.5}$$

Here, the width of the upper roller surface, l, is 40.4 mm. The X-ray beam then propagates through dodecane which attenuates the beam before being reflected at the substrate-dodecane

interface towards the detector. The attenuation is dependant on the path length within the dodecane, P_{dod}, which can be determined via

$$P_{\text{dod}} = 2\frac{h_{\text{beam}}}{\sin\theta}\,. \tag{5.6}$$

As the change in angle is less than 2×10^{-7} degrees when refracted at the air-dodecane interface, the path length before and after reflection are considered to be equivalent.

At greater θ values the X-ray beam propagates through the PEEK roller, as shown in Figure 5.15a. This process occurs when h_{beam} is greater than the roller-substrate gap, h_{gap}. The X-ray beam will strike the air-PEEK interface at the chamfered edge of the roller at a vertical distance from the substrate, h_{PEEK}. This can be related to h_{beam} and an additional height contribution from the chamfered edge, h_{edge}, as shown in Equation 5.7. In the case of the experiment presented, the X-ray beam does not strike the roller at the flat surface below the chamfered edge as this would only occur at $\theta > 2.72°$.

$$h_{\text{PEEK}} = h_{\text{beam}} + h_{\text{edge}} \tag{5.7}$$

As shown in Figure 5.15b, h_{edge}, can be calculated as $h_{\text{edge}} = c_1 \sin\theta_{\text{air}}$, where c_1 is the longest side of the triangle formed with sides a_1 and b_1. The law of cosines can be used to calculate c_1 using a_1, b_1 and α_1, which are given as:

$$a_1 = \tan(45°) \times (h_{\text{beam}} - h_{\text{gap}})\,,$$

$$\alpha_1 = 45° - \sin\theta_{\text{air}}\,, \tag{5.8}$$

$$\text{and } b_1 = a_1\frac{\sin\theta_{\text{air}}}{\sin\alpha_1}\,.$$

Following the determination of h_{PEEK} the path length of the incident beam within the PEEK, $P_{\text{in-PEEK}}$, can be calculated following Equation 5.9. This is depicted in Figure 5.15c.

$$P_{\text{in-PEEK}} = \frac{h_{\text{PEEK}} - h_{\text{gap}}}{\sin\theta_{\text{PEEK}}} \tag{5.9}$$

Here, $\sin\theta_{\text{PEEK}}$ is the angle adopted upon refraction at the air-PEEK interface which can be calculated through Snell's law. Similarly, the angle adopted upon refraction at the PEEK-dodecane interface, $\sin\theta_{\text{dod}}$, can be calculated via the same principle. The refracted angle θ_{dod} is the final angle at which the beam will impinge on the surface. The total path length in dodecane, P_{dod}, before and after reflection is

$$P_{\text{dod}} = 2\frac{h_{\text{gap}}}{\sin\theta_{\text{dod}}}\,. \tag{5.10}$$

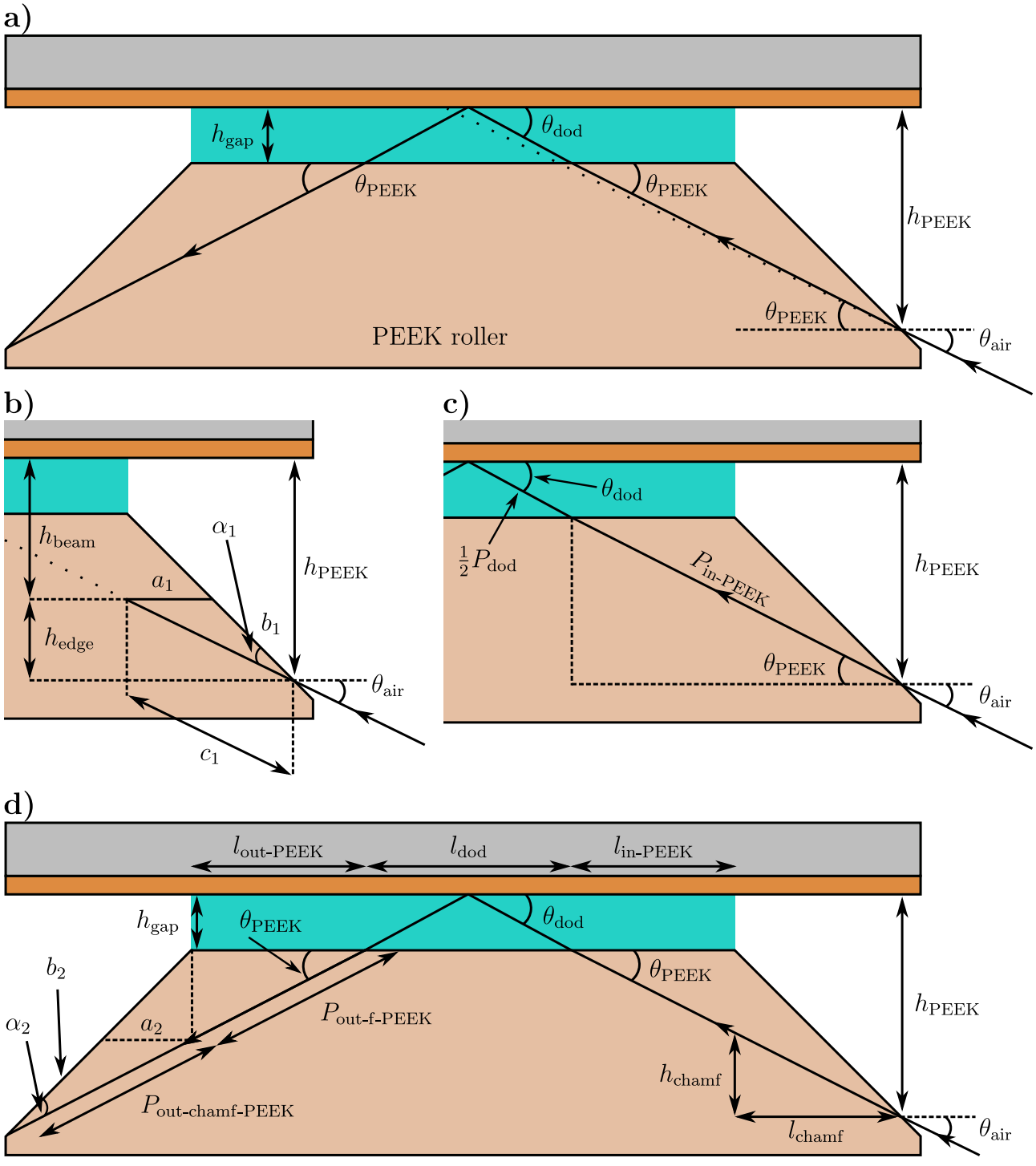

Figure 5.15: **a)** The X-ray beam propagates through PEEK and dodecane before and after reflection at the substrate. The non-dashed ray shows the approximate beam path. **b)** Zoomed-in perspective of the chamfered edge, where h_{edge} and the length c_1 are depicted. **c)** The path lengths $P_{\text{in-PEEK}}$ and P_{dod} can be calculated with θ_{PEEK} and θ_{dod}. **d)** Distances used to calculate the path length of the X-ray beam in PEEK after reflection.

The path length through the PEEK after reflection can be calculated by considering the horizontal lengths from the flat upper surface of the roller as shown in Figure 5.15d. The horizontal length $l_{\text{out-PEEK}}$ is calculated as

$$l_{\text{out-PEEK}} = l - (l_{\text{in-PEEK}} + l_{\text{dod}}) \,, \tag{5.11}$$

where

$$l_{\text{dod}} = 2\frac{h_{\text{gap}}}{\tan\theta_{\text{dod}}} \,, \tag{5.12}$$

$$l_{\text{in-PEEK}} = \frac{h_{\text{PEEK}} - h_{\text{chamf}}}{\tan\theta_{\text{PEEK}}} \,, \tag{5.13}$$

and $h_{\text{chamf}} = \tan\theta_{\text{PEEK}} \times l_{\text{chamf}}$. The term l_{chamf} is given by $l_{\text{chamf}} = \sqrt{c_1^2 - h_{\text{edge}}^2}$. Finally $P_{\text{out-PEEK}}$ can be calculated as shown in Equation 5.14.

$$P_{\text{out-f-PEEK}} = \frac{l_{\text{out-PEEK}}}{\cos\theta_{\text{PEEK}}} \tag{5.14}$$

The small remaining path length in the chamfer of the roller, $P_{\text{out-chamf-PEEK}}$, can be calculated using the law of cosines using the variables a_2, b_2 and α_2 that are given as:

$$a_2 = \tan(45^\circ) \times \sqrt{P_{\text{out-f-PEEK}}^2 - l_{\text{out-PEEK}}^2} \,,$$

$$\alpha_2 = 45^\circ - \sin\theta_{\text{PEEK}} \,, \tag{5.15}$$

$$\text{and } b_2 = a_2\frac{\sin\theta_{\text{PEEK}}}{\sin\alpha_2} \,.$$

The total path length in dodecane and PEEK is then given by the sum of $P_{\text{in-PEEK}}$, P_{dod}, $P_{\text{out-f-PEEK}}$ and $P_{\text{out-chamf-PEEK}}$.

Determination of the X-ray attenuation scale factor

The incident beam has a Gaussian distribution, $G(x)$, with a full width at half maximum amplitude of 100 µm. In this work, the full width of the beam has been estimated to be ± 3 standard deviations, σ. At $\theta \leq 0.240^\circ$, $Q \leq 0.106$ Å^{-1}, the footprint of the beam is greater than the length of the substrate, l_{s}, at 55 mm. Therefore, the width of the beam that falls on the substrate is given by $x_{\text{w}} = \sin\theta \times l_{\text{s}}/2$. At these low angles, all of the beam that falls on the substrate propagates through the dodecane meniscus, as depicted in Figure 5.16. The path length within the dodecane meniscus is given by Equation 5.3 and is equal for all distances from the center of the beam that fall onto the substrate. The total intensity of the beam that

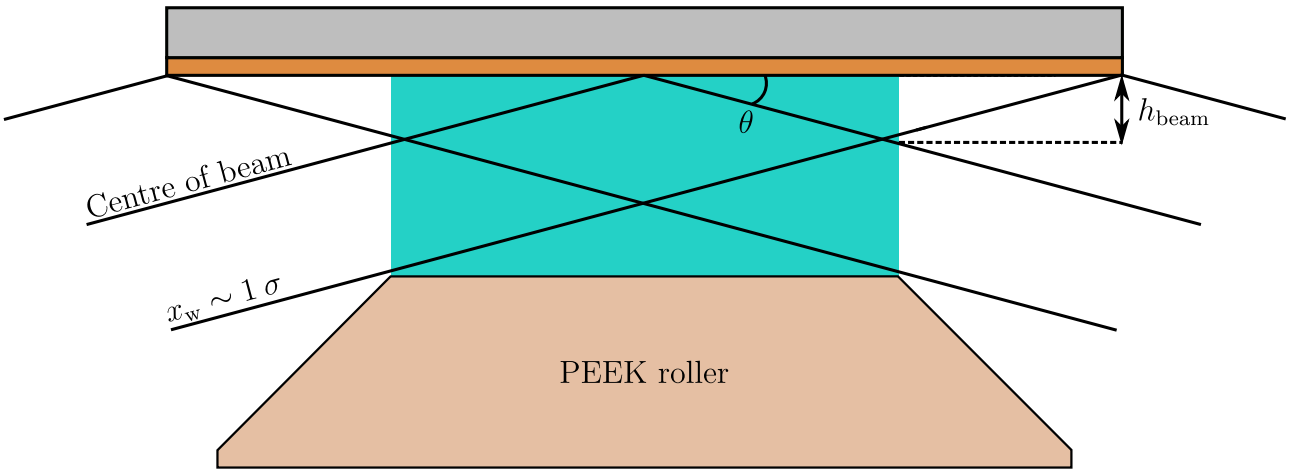

Figure 5.16: Schematic of the X-ray beam footprint on the substrate at $\theta = 0.092°$. The width of the beam that falls on the substrate is approximately $\pm$ 1 σ from the beam center. Not drawn to scale.

reflects from the substrate is

$$I_{\mathrm{s}} = \int_{-x_{\mathrm{w}}}^{+x_{\mathrm{w}}} G\,(x)\,\mathrm{d}x\,. \tag{5.16}$$

The data reduction carried out in DAWN corrected for the footprint effect, and hence I_{s} can be normalised by itself to obtain a footprint corrected normalised intensity, I_{n}. The total transmitted intensity, I_{tot}, is then given by

$$I_{\mathrm{tot}} = I_{\mathrm{n}} e^{-\mu_{\mathrm{dod}} P_{\mathrm{dod}}}\,, \tag{5.17}$$

where μ_{dod} is the X-ray attenuation coefficient in dodecane. As the data reduction also normalised the whole reflectivity profile to the first reflectivity data point (an approximation to scale the reflectivity to unity), the relative footprint-corrected transmission is calculated by dividing I_{tot} at each Q value by I_{tot} at $Q = 0.041$ Å^{-1}. While Figure 5.16 shows a dry area either side of the dodecane meniscus, in reality these areas are coated in dodecane but are not contained within the meniscus. As an approximation, it is assumed that no attenuation via dodecane occurs outside of the meniscus. It is further assumed that any reflection in this area is equivalent to the reflection in the meniscus. The full width of the beam falls within the meniscus at $\theta \geq 0.362°$.

In the range $0.242° \leq \theta \leq 0.566°$, $0.107 \leq Q \leq 0.250$ Å^{-1}, the outer portion of the beam that hits the substrate propagates through the PEEK roller either before or after reflection while the central portion of the beam propagates purely through dodecane. The path length adopted by the beam that propagates purely through dodecane is given by Equation 5.3. For the outer portion of the beam, the path lengths in PEEK and dodecane are a function of the distance from the centre of the beam and are also a function of the scattering angle. The beam width at which X-rays begin to propagate through PEEK instead of dodecane, x_{PEEK}, can be calculated for each θ as $x_{\mathrm{PEEK}} = \cos\theta\,(h_{\mathrm{gap}} - h_{\mathrm{beam}})$. For a given angle, the path lengths in PEEK

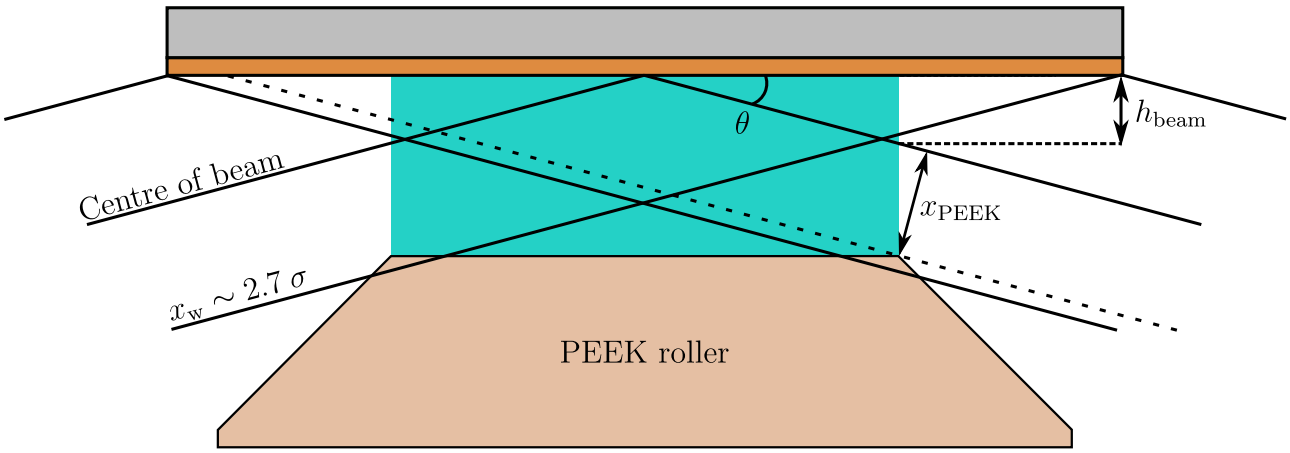

Figure 5.17: Schematic of the X-ray beam footprint on the substrate at $\theta = 0.242°$. The width of the beam that falls on the substrate is approximately $\pm$ 2.7 σ from the beam center. When $\theta > 0.262°$ the full width of the beam falls on the substrate. Not drawn to scale.

and dodecane were approximated by splitting the distance between x_{w} and x_{PEEK} in to 10000 individual points. For each individual point the path length in both materials was calculated, and then the attenuation coefficient for each point was calculated. The same methodology can be applied to the part of the beam that propagates through dodecane before propagating through PEEK. The attenuation coefficients for every part of the Gaussian beam were then used to modulate the beam profile that hits the substrate. Finally, the relative footprint-corrected transmission can be calculated by integrating the modulated Gaussian profiles and then following the normalisations outlined above.

In the range $0.568° \leq \theta \leq 0.928°$, $0.251 \leq Q \leq 0.410$ Å^{-1}, the central part of the beam passes through the PEEK roller and then through dodecane before reflection at the substrate as shown in Figure 5.18. Following reflection, the beam then propagates back through dodecane and PEEK towards the detector. This portion of the beam is small at $\theta = 0.568°$ and is almost all of the Gaussian beam by $\theta = 0.928°$. The outer portion of the beam propagates through the PEEK roller either before or after reflection. The total intensity in this range is given in the same way in the range $0.242° \leq \theta \leq 0.566°$.

Finally, in the range $0.932° \leq \theta \leq 1.140°$, $0.412 \leq Q \leq 0.504$ Å^{-1}, all of the beam propagates through the PEEK roller and dodecane before and after reflection. The total intensity in this range is then the attenuated normalised intensity following this path. Figure 5.19a shows the transmission scale factor calculated as a function of Q, where it is approximately unity at low Q due to the normalisations discussed above. At higher Q, the scale factor decreases as a larger fraction of the beam propagates through the PEEK roller. The gradient of the transmission scale factor becomes less negative at $Q \sim 0.35$ Å^{-1}. This is because the gradient of the average path length in PEEK, as followed by the portion of the beam that propagates through PEEK and dodecane before and after reflection, decreases as a function of Q as shown in Figure 5.19b. The modelled reflection in GenX was multiplied by the scale factor at each point in Q in order to account for the attenuation.

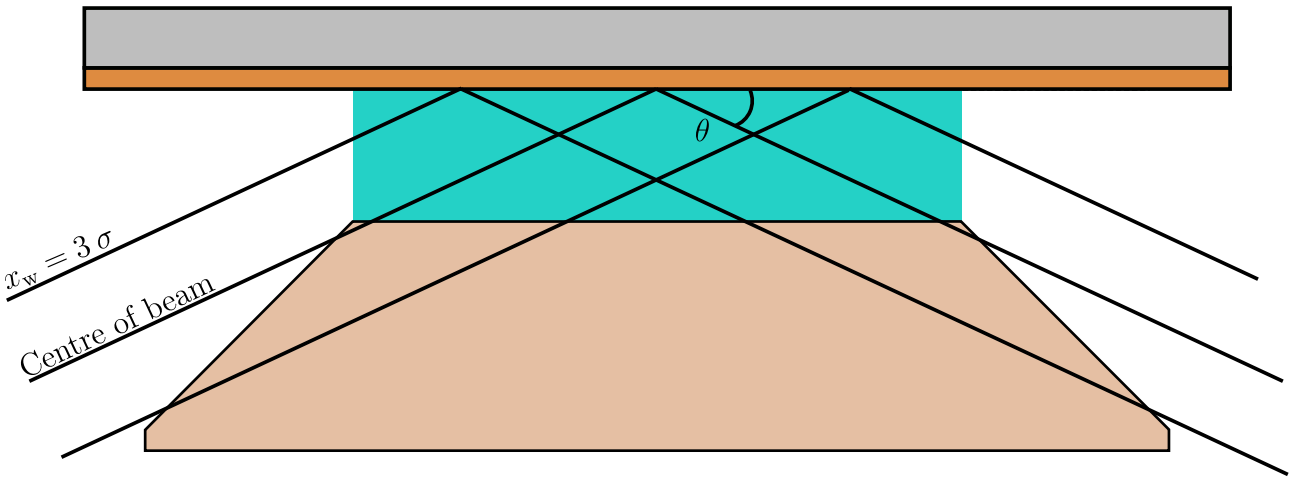

Figure 5.18: Schematic of the X-ray beam footprint on the substrate at $\theta = 0.568°$. The width of the beam that falls on the meniscus of the substrate is now $\pm$ 3 σ. Not drawn to scale.

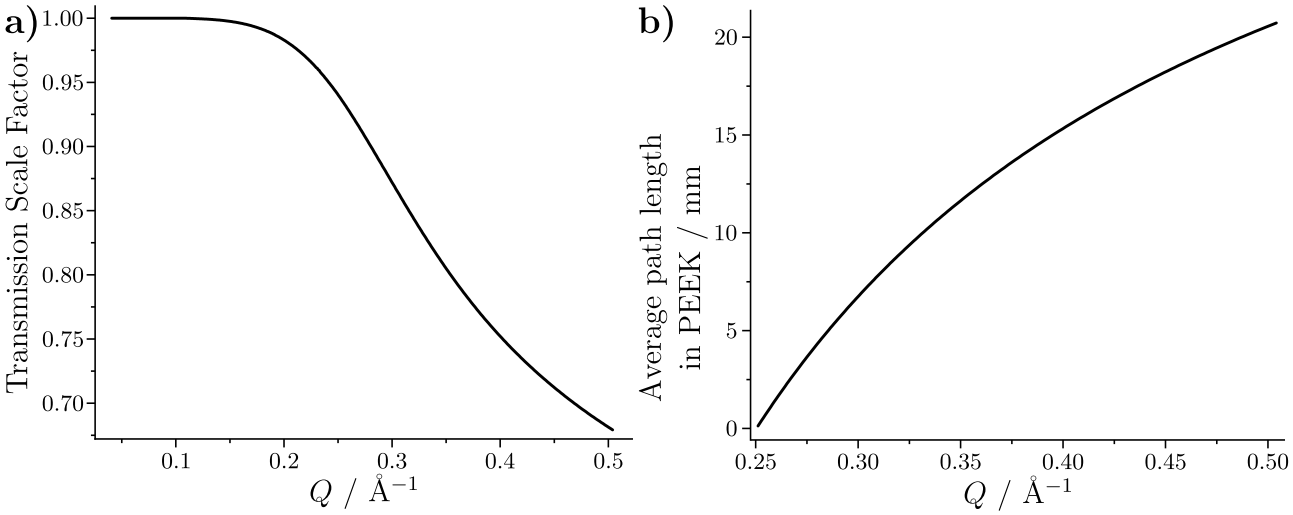

Figure 5.19: **a)** The transmission scale factor calculated for each Q point in the XRR data for the 20 mM GMO-dodecane system at 3.0×10^3 s^{-1}. **b)** The average path length in PEEK of the portion of the beam that propagates through PEEK and dodecane before and after reflection as a function of Q.

Reflection at the PEEK-dodecane interface for the incident and reflected beam has also been considered. In the limiting case of a perfectly flat interface, the maximum reflection is estimated to be 2×10^{-5}. Therefore, to a reasonable approximation, the reflection from the PEEK-dodecane interface can be treated as negligible. It should be noted that the roller's roughness will reduce the transmitted intensity in the specular direction and increase the off-specular intensity, which was not accounted for here.

5.3.1 Fitting the data

It was necessary to include a θ-offset in the model to provide an adequate fit to the data collected under shear with the 20 mM GMO-dodecane system. The best fit achieved without the θ-offset is shown in Figure 5.20a, where the critical edge is not modelled satisfactorily. By inspecting the alignment scans conducted before the reflection measurements, as shown in Figure 5.20b, it

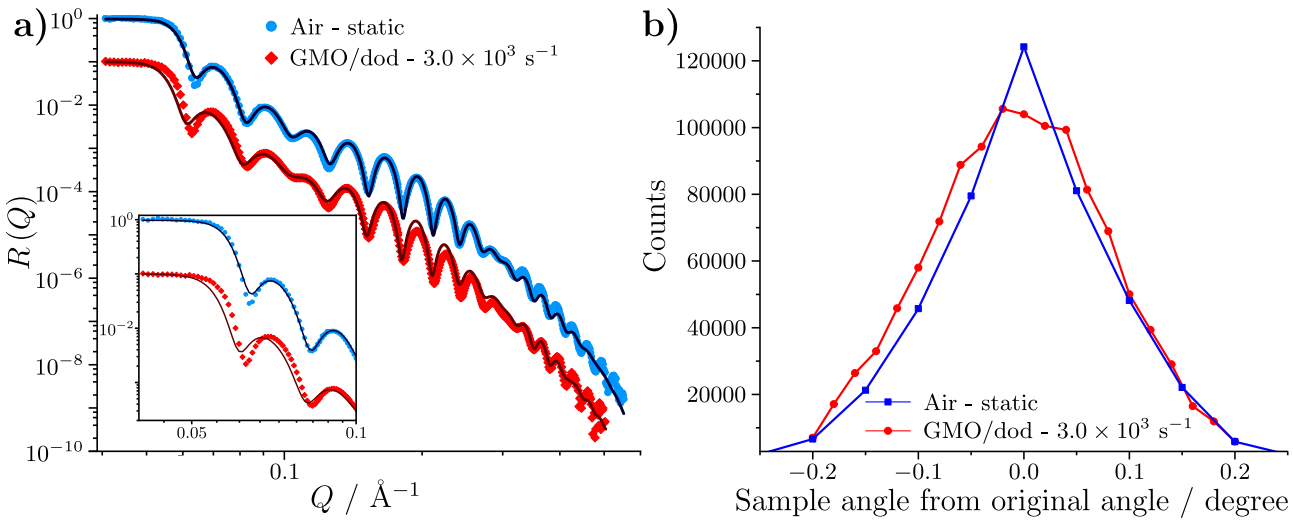

Figure 5.20: **a)** The best fit to the XRR collected with the 20 mM GMO-dodecane solution at 3.0×10^{-3} s^{-1} without including a θ-offset. The inset shows the reflectivity around the critical edge. **b)** Alignment scans for the sample angle which defines the θ-offset. These scans were conducted statically before the reflection measurements were taken. For the air scan, the roller was not near to the surface, while for the scan before the GMO-dodecane system, the roller was positioned 200 µm from the substrate surface.

is possible to justify the use of the θ-offset parameter. The alignment scans were recorded while rocking the sample along the path of the beam to find the angle at which the sample lay flat with respect to the beam. Ideally the scan should result in a sharp symmetric peak as seen in the scan conducted before the reflection measurement in air. The center of the peak can then be chosen as the sample angle to use in the reflection measurements. However, in the case of the alignment scan before the measurement with the entrained GMO-dodecane solution, a poorly defined peak was found. As the peak and peak maximum are asymmetric about the centre of the scan, the center-of-mass of the peak is likely to be at a negative angle relative to the original angle before the start of the scan procedure. It is suggested that the center-of-mass is approximately $-0.01°$ from the angle at the center of the scan. However, the sample angle used in the reflection experiment with the GMO-dodecane solution was the central angle covered in the scan. Therefore, the calculated θ value for each angle is most likely to be an overestimate of the true angle, and hence by including the θ-offset parameter the overestimated angle can be accounted for.

With the θ-offset parameter included and the transmission scale factor applied, the data were fit. The best fit is shown in Figure 5.21a and the resultant median $\beta_{\text{X-ray}}$ profile for both contrasts is shown in Figure 5.21b. The inferred parameter distributions are shown in Table 5.4. It was found that the θ-offset was $-9^{+3}_{-2} \times 10^{-3}$ degrees, suggesting that the Q values in the dodecane-GMO system are expected to be overestimates by approximately $4^{+1}_{-1} \times 10^{-3}$ Å^{-1}.

The distribution of the adsorbed GMO thickness is broader, with a lower median value, compared to the GMO thickness inferred from the NR analysis at 7.0×10^{2} s^{-1}. It is expected that the poor $\beta_{\text{X-ray}}$ contrast between the solvent and the GMO leads to the wide range of GMO

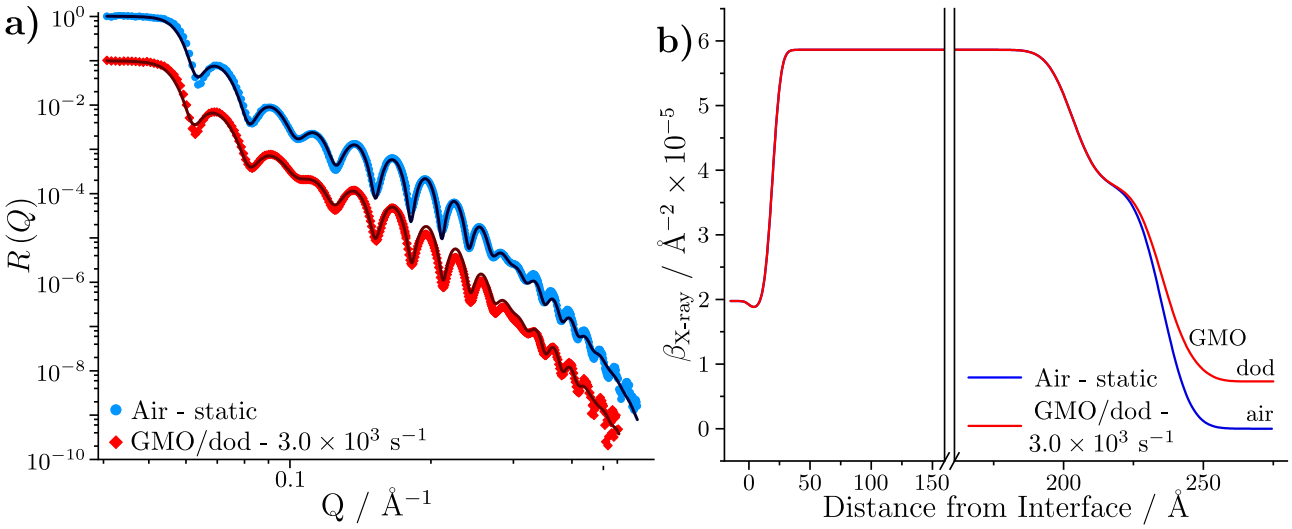

Figure 5.21: **a)** The best fit to the XRR data collected from an iron-coated silicon substrate in air and with a 20 mM GMO dodecane-h_{26} solution entrained against the substrate at 3.0×10^3 s^{-1}. The data collected with the entrained solution has been offset by 10^{-1} in the vertical axis. The solid lines show the fits to the data. Error bars have been removed for clarity. **b)** The $\beta_{\text{X-ray}}$ profile across the interface, constructed using the median parameter values.

Table 5.4: XRR fitted parameter values for the iron-coated silicon substrate in air and with a 20 mM GMO solution entrained against the substrate at 3.0×10^3 s^{-1}. The central parameter values are the median values obtained from the bootstrap routine, with the 95 % confidence intervals reported in the sub- and superscripts. Those values without uncertainties were held constant. * – layer only included in the 20 mM GMO solution model.

Layer	$\beta_{\text{X-ray}}$ / $\text{Å}^{-2} \times 10^{-6}$	Thickness / Å	Roughness / Å
Si	19.8	∞	3.0
SiO_2	18.6	$19.3^{+10.5}_{-14.1}$	$5.5^{+2.8}_{-0.2}$
Fe	$58.6^{+2.4}_{-1.2}$	184^{+1}_{-1}	$7.2^{+1.9}_{-0.5}$
FeO_x	$37.6^{+1.3}_{-1.8}$	$32.2^{+0.8}_{-0.5}$	$7.9^{+0.3}_{-2.8}$
*GMO	8.9	$15.3^{+23.0}_{-12.5}$	$4.9^{+4.5}_{-2.5}$

thicknesses that are consistent with the data. This is shown particularly well by Figure 5.21b, where the GMO layer is unresolvable from the iron oxide-dodecane interface. As a result, a comparison of the GMO structure at 7.0×10^2 s^{-1} and 3.0×10^3 s^{-1} is not appropriate, aside from noting that the fitted thickness of GMO at 7.0×10^2 s^{-1} falls within the range determined at 3.0×10^3 s^{-1}. Nevertheless, the reasonable fit shows that XRR data collected from an interface under shear with the tribometer can be interpreted.

5.4 Conclusion

The neutron reflectivity from the tribometer can be interpreted by modelling the data with a split interface, enabling the separation of the sheared and non-sheared portions of the interface. The latter is of less interest than the sheared part of the interface, and hence, gives rise to a signal that would be ideally minimised. Additionally, when the attenuation coefficient of the solvent is low, the reflectivity from the non-sheared portion of the interface is comprised of reflectivity arising from both the immediate substrate-dodecane interface and the distant dodecane-air interface. The latter signal is also of little interest when considering the structure of interfacial layers under shear, and furthermore, adds significant complexity to the model.

It was shown that if the solvent β_n matches that of air, the additional reflectivity from the dodecane-air interface is negligible; this simplifies the model somewhat, but leads to the requirement of deuterated surfactant to provide the contrast necessary to infer the structure of the interfacial layer. It may be possible to retain some contrast between solvent and adsorbate by using solvent with specific a H/D content so that the attenuation coefficient is large enough to reduce the secondary reflectivity contribution. For example, it is estimated that if μ is $\sim 5 \times 10^{-8}$ Å for a 100 µm layer with 3 Å roughness, the fringe minimum at $Q \sim 0.04$ Å^{-1} will approximately match the fringe minimum arising without the R_2 contribution. At $Q \sim 0.04$ Å^{-1} when $\theta = 0.7°$, $\lambda = 3.8$ Å so that the volumetric ratio required to achieve these attenuation coefficients would be similar to the 29:71 dodecane-d_{26}:dodecane-h_{26} contrast as shown in Figure 5.4b. However, with a high H content, the contrast between the interfacial layer and the solvent will be poor, leading to less extractable information about the interfacial layer. In this regard, using deuterated base oils that are more viscous than dodecane may assist in the reduction of the secondary reflectivity. A balance may then be struck between the thickness of the wetting layer, which is thought to be vary with viscosity, the attenuation coefficient, and the contrast between the solvent and interfacial layer. Base oils with high purities have to be used to ensure only the additive of choice adsorbs at the interface; synthetic base oils can be produced with greater purity than standard mineral base oils, although supply of deuterated base oil becomes an issue.

The effect of shear on the structure of the adsorbed GMO film was found to be unresolvable at 7.0×10^2 s^{-1} when comparing the uncertainty with respect to both GMO adsorbed in the non-sheared portion of the interface, and the GMO films formed under static conditions. The large distribution of GMO thickness values under shear that are consistent with the reflectivity

arise from the lower sensitivity to the sheared portion of the interface than compared to the non-sheared portion. The sensitivity to the sheared interface could be improved by restricting the beam footprint to fall only within the meniscus region. This would have the additional benefit of simplifying the model. However, the time required to achieve satisfactory counting error would increase significantly. It would also be possible to increase the size of the meniscus by using a roller with a greater radius, although it is estimated that in order to double the meniscus width, a roller with approximately four times the radius is required. This has the drawback of requiring larger quantities of expensive deuterated material.

Unlike the NR methodology with the tribometer, the whole XRR profile arises from the sheared interface due to the small footprint of the X-ray beam. This is a particularly attractive aspect of XRR, and coupled with the cheaper solvent requirements, it is suggested that XRR would be a very powerful technique for the *in-situ* investigation of surface active inorganic friction modifiers and anti-wear additives under shear. Compounds such as these contain electron-rich elements which would lead to greater contrast with the solvent than that between GMO and dodecane. It is suggested that the tribometer could reach greater shear rates and applied loads if the geometry was inverted, so that the substrate lay under the roller. This way, sample solutions would saturate the whole interface, reducing opportunity for lubrication starvation in the contact when attempting to load the surface lightly. Special care would have to be taken to ensure the meniscus of the dodecane does not attenuate the beam either through reflection or transmission; it is possible that X-ray transparent windows may assist in reducing these affects.

Chapter 6

Final conclusions and future work

6.1 Final conclusions

The adsorption and film structure of GMO at the iron oxide-dodecane interface under static and sheared environments has been the main focus of this thesis. Under static conditions this has been achieved through the use of depletion isotherms and NR. The depletion isotherms showed that GMO adsorbs weakly via physisorption at the iron oxide-dodecane interface. Additionally, the adsorption appears to follow the Langmuir isotherm, indicating the formation of a monolayer. In agreement with the suggestion of a monolayer, NR showed that the adsorbed film of GMO was $\sim$ 17–19 Å, which is thinner than the full length of one GMO molecule. NR also showed that GMO could be easily washed off the interface with additional solvent, further supporting the suggestion of physisorption of GMO at the iron oxide-dodecane interface. The NR data collected with the solutions of GMO in dodecane were compared to the simulated reflectivity of the GMO film structure adsorbed at the iron oxide-dodecane interface as calculated through MD simulation. The likeness of the simulated and experimental reflectivity suggest that the NR data are not only consistent with a monolayer but appear to be consistent with a monolayer-like film that contains a degree of aggregation between GMO molecules. It is suggested that through depletion isotherms and NR alone, it would be difficult to resolve the difference between a monolayer of monomers and a monolayer of aggregates, such as hemi-micelles.

Prior to the adsorption of GMO, NR showed the presence of an interfacial layer with thicknesses between 8–16 Å; this is thought to be comprised of adsorbed gas molecules that are present at the interface prior to the introduction of non-polar liquids against the substrate. If this layer is adsorbed gas, it is likely that it is present within all systems bar those under ultra-high vacuum conditions. It is also possible that this adsorbed material remains at the interface as OFMs are adsorbed, which is a prospect that does not appear to feature in the conventional OFM mechanism. It is suggested that adsorbed gas could screen OFMs from the hydrophilic functionalities of the engine surface, reducing the interaction strength between OFM and interface.

The addition of water to solutions of GMO in dodecane leads to the co-adsorption of GMO and water at the iron oxide-dodecane interface. At 25 °C, nested sampling suggested a combined layer of water and GMO was more appropriate to model the data than a water-rich region adsorbed directly at the iron oxide surface, with a GMO-rich region held on the outer of the interface. Water adsorbed at the interface but not directly at the iron oxide surface suggests that it is contained within the hydrophilic region of a GMO-water agglomerate within the monolayer-like film. In contrast to the singular combined layer at 25 °C, nested sampling suggested that the reflectivity collected at 60 °C should be modelled with separate water-rich and GMO-rich regions. The implications of this rearrangement on the adsorption of GMO and friction modification are not clear. However, in comparison to the dry system, it is thought that the systems containing water will exhibit different adsorption strengths of GMO, and will potentially interact with solvent and films on opposing surfaces differently.

The *in-situ* characterisation of the GMO film structure at the iron oxide-dodecane interface under shear was conducted with the tribometer and either NR or XRR. Special considerations were required to model datasets from both techniques. When using dodecane-d_{26} with NR, the data were modelled as the composite reflectivity from a sheared and non-sheared portion of the interface, with an additional reflectivity contribution from the dodecane-air interface in the non-sheared portion. Splitting the interface requires the width of the meniscus above the roller to be measured, and modelling the additional reflectivity requires the neutron attenuation coefficient of the solvent used. As shown, it is possible to remove the additional reflection from the dodecane-air interface by using a solvent with a β_n close to 0 $Å^{-2}$. However, this reduces the contrast between the solvent and hydrogenated adsorbate. Therefore, it would be necessary to use deuterated surfactant. It is also possible that the additional reflectivity is removed when the dodecane-air interface is roughened, which is thought to occur at greater angular velocities of the roller. This opens up the opportunity for the analysis of data collected at higher shear rates, although further work is required to confirm this.

The effect of applied shear at 7.0×10^2 s^{-1} on the structure of GMO adsorbed at the iron oxide-dodecane interface was not resolvable from either the structure of GMO formed under non-sheared portion of the interface nor the GMO structure formed under static conditions. While it is possible that the shear rate was not great enough to induce a change in the GMO film, the sensitivity to the sheared portion of the interface is roughly half that to the non-sheared portion of the interface. By increasing the area of the footprint under shear, it is thought that the technique will be able to resolve finer detail on the adsorbate structure under shear. Due to the lack of contrast between the dodecane and GMO when scattering with X-rays, the effect of shear on the GMO film structure was also not resolvable in the XRR experiments. However, the model presented here should be of direct use to future experiments with additives that contain electron-rich elements.

6.2 Future work

6.2.1 Tribometer Development

The current state of the tribometer limits the type of lubrication that can be studied with *in-situ* NR or XRR to the hydrodynamic regime. This is due to the rapid wear of the substrates under applied load, which is thought to arise from both the oscillatory movement of the roller and the uneven actuator motion when bringing the roller into contact with the substrate. While the tribometer can be successfully used in non-contact mode, the shear rate that can be applied without causing damage to the substrate is limited to $\sim 3.8 \times 10^3$ s^{-1}. Therefore, there is a large scope for improving the capabilities of the tribometer. Due to high rates of wear in the boundary lubrication regime, the tribometer coupled with reflectometry may not be suitable for studying friction modifiers under such conditions. However, the exploration of the interface under harsher conditions, such as within the elastohydrodynamic regime, is thought to be achievable due to the micron sized oil films that typically separate loaded, sliding surfaces, minimising wear. In this regime it can be expected that higher shear rates, on the order of 10^4–10^5 s^{-1} are achievable.

As stated above, one of the main goals would be to improve the maximum achievable shear rate at which the substrate remains undamaged. The maximum shear rate was estimated by taking the greatest surface velocity, 7.2×10^{-1} m s^{-1}, where the entrained oil on the roller is not sprayed by roller's angular velocity and a calibrated gap of 190 µm, which is just greater than twice the oscillation amplitude of 91 µm. An initial step towards this goal could be taken by minimising the oscillation in the roller axis. This could be achieved by replacing the bearings and bearing housings with those designed for finer rotational tolerances. Care over the selection of bearings would be necessary as those that have finer tolerances may not be suitable for using with applied loads. Additionally, moving the motor to be directly in-line with the roller shaft would remove forces, applied by the belt-drive, that pull on the bearings.

A friction measuring capability was not installed on the tribometer as the contact was limited to hydrodynamic lubrication, where the friction is dictated by the oil viscosity and is insensitive to the surface structure of the OFM. The least intrusive way of installing such a capability is thought to be through measuring the power delivered to the motor to drive the roller at set angular velocities. The power at the motor can be measured by installing a current and voltmeter in series before the motor. It would be possible to calibrate the power required to rotate the roller at a set angular velocity when not in contact, and then equate any angular velocity differential when in contact to a frictional torque. If installed with the belt drive it is expected that this would display significant noise due to the imperfect drive afforded by the belt. Therefore, it may prove beneficial to install the motor in-line with the roller to directly drive the shaft. This set up would require a tachometer to measure the angular velocity of the roller during use. Unfortunately, this geometry would not be suitable for *in-situ* XRR as the motor would sit directly in the incident beam path.

The horizontal velocity of the roller is slower than the surface velocity of the roller, limiting the accessible SRR of the tribometer to be between 1.95–2. This is an important factor for friction arising in the elastohydrodynamic regime, and hence, broadening the accessible range of SRRs would lead to a greater capability. Furthermore, increasing the maximum horizontal velocity would increase the applied shear rate. For a simple improvement, it may be possible to increase the pitch of the threaded screw that the assembly plate is pulled along by the motor. This would likely only offer a small increase in horizontal velocity; therefore, a redesign of how the tribometer assembly plates would be needed to significantly increase the velocity.

By using more viscous base oils as the solvent, it is thought that greater hydrodynamic pressures would be generated within the meniscus region. These greater pressures should be able to support applied loads, enabling the conditions found within operating engines to be more closely matched while improving the shear rate. Therefore, the exploration of the lubrication and wear with more viscous oils is required to find the critical oil properties at which loaded lubrication is supported. Similarly, inverting the geometry of the tribometer so that the substrate is held underneath the roller may reduce any potential effects of lubricant starvation. As the neutron reflectometers used in this work both have supermirrors, it should be possible to set up the instruments to reflect down from the iron oxide-dodecane interface. Similarly for XRR, the detector can be positioned so that the reflection is measured in the upward geometry.

6.2.2 Adsorption of GMO at the iron oxide-interface under static conditions

This section considers the future work for exploring the adsorption of GMO at the iron oxide-dodecane interface under static conditions. A number of techniques are considered that could bolster the findings within this thesis, and suggestions for future experiments are considered to broaden the understanding of GMO, and more generally, OFM adsorption. Of specific interest are experiments conducted under higher temperatures, which are relevant to the conditions seen within operating car engines, where the temperatures are often greater than 80 °C within the sump; even greater temperatures can be expected within the tribological contacts of the engine due to frictional heating. Further to the experiments conducted with water, the adsorption of GMO in the presence of other molecules such as other OFMs, dispersants and detergents, is of interest.

One of the simplest suggestions would be to widen the depletion isotherm study with more data points at low equilibrium concentrations of GMO. In doing so, a larger proportion of the isotherm would be probed and the uncertainty in the equilibrium constants potentially reduced, enabling a more accurate determination of the thermodynamic parameters of adsorption. Detection of lower bulk concentrations could be achieved by designing a transmission cell with a wider path length; as the path length used here was 1 mm, it would be feasible to increase the limit of quantification by a factor of 10 by increasing the path length to 10 mm. Furthermore, conducting isotherms at temperatures $\geq$ 80 °C would not only provide more data points for

the Van't Hoff analysis, but would enable the determination of the surface excess of GMO at temperatures more applicable to an operating engine environment. Depletion isotherms could also be used in the study of the co-adsorption of GMO in the presence of other molecules if the quantification technique can detect GMO separately from other additives. If FTIR is not suitable for this task, another technique that has been proven to detect bulk concentrations down to 1 mM is ^{1}H NMR spectroscopy.[229] Like FTIR, ^{1}H NMR can detect differing functionalities of molecules, but is also insensitive to deuterium so that the influence of water on the adsorption behaviour could be further studied by substituting H_2O for D_2O. Information on the GMO surface excess in the presence of water can be used to ensure the MD simulations are physically consistent.

As demonstrated, NR can be used to study the co-adsorption of GMO and water. The use of contrast can be used with other molecules, provided the co-adsorbate can be deuterated and purified as this is non-trivial for GMO. Nested sampling may then be used to infer the most likely structure for the interfacial film. If contrast between GMO and the other additive is not possible, NR can still provide information regarding the film thickness of the interfacial layer. NR or polarised NR could be further used to study the adsorption behaviour of GMO at higher temperatures as the glycol heater baths that provide the thermal energy to the solid-liquid cells can facilitate temperatures in excess of 100 °C. Preliminary tests of the substrates' resistance to greater temperatures would have to be conducted to ensure the substrates remained the same over the course of the experiment. It was suggested that adsorbed GMO exhibits desorption hysteresis as the temperature is increased from 25 to 60 °C as indicated by the NR data. Whilst a conclusive finding could not be reached with the data presented alone, further NR experiments where the interface is only exposed to GMO at 60 °C may confirm if hysteresis occurs. In this respect, an additional technique that may be able to detect the possible melting of the GMO layer is differential scanning calorimetry. This technique has been used extensively in the study of the melting behaviour of physisorbed alkane monolayers at graphite surfaces. Additionally, quartz crystal microbalance with dissipation measurement (QCM-D) could be used to study the desorption of GMO from iron oxide or steel surfaces with temperature swings. Beyond desorption behaviour, QCM-D could also provide information on the adsorption kinetics, surface excess and film thickness of GMO at iron oxide or steel surfaces over a wide temperature range.

As indicated by MD simulations, it is possible the self-assembled film of GMO displays some reverse micellar structure. If aggregates are present at the interface, one technique that could be used to detect their presence is grazing-incidence small angle neutron scattering (GISANS). This is an elastic scattering technique that is similar to SANS but a reflection geometry is used to ensure the path length within the thin interfacial film is maximised, enabling detectable scatter from a small sample volume. Analysis of the data is rather complicated compared to NR or SANS, and requires the consideration of the aggregate form and structure factors for the probed interfacial film, and the structure of the underlying substrate.[230] A complimentary real-space image of GMO adsorbed at the iron oxide-dodecane interface could be achieved using *in-situ* AFM as used previously to study OFMs adsorbed at mica-hydrocarbon interfaces.[78,207]

Here, a cantilever with an attached atomically sharp tip is submerged in solvent and probes the interface through direct contact. As the tip traverses across the surface, any fluctuations in the height of the surface are recorded via the reflection of a laser off the cantilever and into a position sensitive detector. Similarly, the viscoelasticity of the film can be probed in a so-called phase image of the film. It is possible that either of these images could highlight the presence of aggregates, where either the height or phase images can detect in-plane structure at the interface. This approach has used before to study the structure of aggregates at solid-liquid interfaces.[231,232]

6.2.3 Adsorption of GMO at the iron oxide-interface under shear

While the reflectivity collected with the tribometer can be fit successfully with the split interface model, a comparison of Bayes factors was not conducted. Comparison of the model evidences for those that take into account the split interface compared to those that do not may assist in determining if the modelled data presented herein have been over parametrised. Furthermore, if a model that does not take into account the split interface is more suitable than those that do, this indicates that either the tribometer does not provide enough sheared interface for changes with shear to be detected, or that the shear rate applied was not great enough to alter the structure of GMO. For the dodecane-d_{26} contrasts, this work will require custom python code to be written which includes reflection over multiple interfaces within the calculation. It is suggested that nested sampling should be used to appropriately model the data collected with the tribometer.

Comparisons between the reflectivity from the tribometer with reflectivity from other sample environments that can facilitate the application of shear, such as Poiseuille shear cells, may provide further useful comparisons when it comes to inferring changes to the structure of adsorbed materials. Beyond NR, other techniques that could be used to detect the *in-situ* surface excess of GMO and film thickness whilst under shear, such as QCM-D, could affirm the parameter values inferred through NR. Flow cells are commercially available for QCM-D instruments, where continual flow over the sensor can be achieved with a peristaltic pump. Calibration of the flow rates through the cell, and potentially some modification to the flow cell, would be required to match the achievable shear rates with the tribometer.

Bibliography

1. Popova, E., & Popov, V. L. The research works of Coulomb and Amontons and generalized laws of friction. *Friction* **3**, 183–190 (2015).
2. Israelachvili, J. N. *Intermolecular and surface forces* (Academic press, Cambridge, MA, USA, 2015). [Third edition]
3. Hutchings, I., & Shipway, P. *Tribology: friction and wear of engineering materials* (Butterworth-Heinemann, Oxford, 2017). [Second edition]
4. Bowden, F. P., Tabor, D., & Taylor, G. I. The area of contact between stationary and moving surfaces. *Proc. R. Soc. A.* **169**, 391–413 (1939).
5. Eder, S. J., Vernes, A., & Betz, G. On the Derjaguin offset in boundary-lubricated nanotribological systems. *Langmuir* **29**, 13760–13772 (2013).
6. Bowden, F. P., Hughes, T. P., & Desch, C. H. The friction of clean metals and the influence of adsorbed gases. The temperature coefficient of friction. *Proc. R. Soc. A.* **172**, 263–279 (1939).
7. Hamrock, B. J., Schmid, B. J., & Jacobson, B. O. *Fundamentals of fluid film lubrication* vol. 169. (CRC press, New York, USA, 2004). [Second edition]
8. Woydt, M., & Wäsche, R. The history of the Stribeck curve and ball bearing steels: The role of Adolf Martens. *Wear* **268**, 1542–1546 (2010).
9. Hersey, M. D. The laws of lubrication of horizontal journal bearings. *JSTOR* **4**, 542–552 (1914).
10. Szeri, A. Z. *Fluid film lubrication* (Cambridge University Press, Cambridge, 2010). [Second edition]
11. Holmberg, K., Andersson, P., & Erdemir, A. Global energy consumption due to friction in passenger cars. *Tribol. Int.* **47**, 221–234 (2012).
12. Wong, V. W., & Tung, S. C. Overview of automotive engine friction and reduction trends–Effects of surface, material, and lubricant-additive technologies. *Friction* **4**, 1–28 (2016).
13. Santos, N. D. S. A., Roso, V. R., & Faria, M. T. C. Review of engine journal bearing tribology in start-stop applications. *Eng. Fail. Anal.* **108**, 104344 (2020).
14. Spikes, H. Friction modifier additives. *Tribol. Lett.* **60**, 5; 10.1007/s11249-015-0589-z (2015).
15. Folkson, R. *Alternative fuels and advanced vehicle technologies for improved environmental performance: towards zero carbon transportation* (Woodhead Publishing, 2014).

16. Bhadeshia, H., & Honeycombe, R. *Steels: microstructure and properties* (Butterworth-Heinemann, Oxford, 2017). [Fourth edition]
17. Surface Roughness Modelling for Piston Ring Lubrication: Solving the Problems. In: *The Third Body Concept Interpretation of Tribological Phenomena*. Ed. by Dowson, D. *et al.* Vol. 31. Tribology Series. 527–537
18. Olsson, C.-O., & Landolt, D. Passive films on stainless steels—chemistry, structure and growth. *Electrochim. Acta* **48**, 1093–1104 (2003).
19. Qiu, J. H., & Chua, P. H. EIS and XPS study of the corrosion of carbon steel in inhibited natural seawater. *Surf. Interface Anal.* **28**, 119–122 (1999).
20. Wood, M. H., Browning, K. L., Barker, R. D., & Clarke, S. M. Using Neutron Reflectometry to Discern the Structure of Fibrinogen Adsorption at the Stainless Steel/Aqueous Interface. *J. Phys. Chem. B* **120**, 5405–5416 (2016).
21. Tang, Z., & Li, S. A review of recent developments of friction modifiers for liquid lubricants (2007–present). *Curr. Opin. Solid State Mater. Sci.* **18**, 119–139 (2014).
22. Prutton, C. F., Frey, D. R., Turnbull, D., & Dlouhy, G. Corrosion of Metals by Organic Acids in Hydrocarbon Solvents. *Ind. Eng. Chem.* **37**, 90–100 (1945).
23. Hardy, W. B., & Doubleday, I. Boundary lubrication.— The paraffin series. *Proc. R. Soc. A.* **100**, 550–574 (1922).
24. Beare, W. G., Bowden, F. P., & Lowry, T. M. Physical properties of surfaces I - Kinetic friction. *Proc. R. Soc. A.* **234**, 329–354 (1935).
25. Bowden, F. P., Leben, L., & Taylor, G. I. The friction of lubricated metals. *Proc. R. Soc. A.* **239**, 1–27 (1940).
26. Langmuir, I. Mechanical properties of monomolecular films. *J. Franklin. Inst.* **218**, 143–171 (1934).
27. Bowden, F., Gregory, J., & Tabor, D. Lubrication of metal surfaces by fatty acids. *Nature* **156**, 97–101 (1945).
28. Cook, E. L., & Hackerman, N. Adsorption of polar organic compounds on steel. *J. Phys. Chem.* **55**, 549–557 (1951).
29. Greenhill, E. B. The adsorption of long chain polar compounds from solution on metal surfaces. *Trans. Faraday Soc.* **45**, (0), 625–631 (1949).
30. Studt, P. The influence of the structure of isomeric octadecanols on their adsorption from solution on iron and their lubricating properties. *Wear* **70**, 329–334 (1981).
31. Spikes, H. A., Cameron, A., & Eley, D. D. A comparison of adsorption and boundary lubricant failure. *Proc. R. Soc. A.* **336**, 407–419 (1974).
32. Okabe, H., Masuko, M., & K, S. Dynamic Behavior of Surface-Adsorbed Molecules Under Boundary Lubrication. *ASLE Trans.* **24**, 467–473 (1981).
33. Jahanmir, S., & Beltzer, M. An adsorption model for friction in boundary lubrication. *ASLE Trans.* **29**, 423–430 (1986).
34. Godfrey, D. *STP340-EB: Symposium on Properties of Surfaces: Lubrication* (ASTM International, West Conshohocken, PA, 1963).

35. Yildirim Erbil, H. *Surface Chemistry: Of Solid and Liquid Interfaces* (John Wiley & Sons, Hoboken, NJ, 2006).
36. Tabor, D. Effect of temperature on lubricant films. *Nature* **145**, 308–308 (1940).
37. Frewing, J. J., & Taylor, G. I. The influence of temperature on boundary lubrication. *Proc. R. Soc. A.* **181**, 23–42 (1942).
38. Frewing, J. J., & Rideal, E. K. The heat of adsorption of long-chain compounds and their effect on boundary lubrication. *Proc. R. Soc. A.* **182**, 270–285 (1944).
39. Jahanmir, S. Chain length effects in boundary lubrication. *Wear* **102**, 331–349 (1985).
40. Menter, J. W., & Tabor, D. Orientation of Fatty Acid and Soap Films on Metal Surfaces. *Proc. R. Soc. A.* **204**, 514–524 (1951).
41. Sahoo, R. R., & Biswas, S. K. Frictional response of fatty acids on steel. *J. Colloid Interf. Sci.* **333**, 707–718 (2009).
42. Loehlé, S. *et al.* Mixed lubrication of steel by C18 fatty acids revisited. Part I: Toward the formation of carboxylate. *Tribol. Int.* **82**, 218–227 (2015).
43. Simič, R., & Kalin, M. Adsorption mechanisms for fatty acids on DLC and steel studied by AFM and tribological experiments. *Appl. Surf. Sci.* **283**, 460–470 (2013).
44. Gattinoni, C., Ewen, J. P., & Dini, D. Adsorption of Surfactants on α-Fe_2O_3(0001): A Density Functional Theory Study. *J. Phys. Chem. C* **122**, 20817–20826 (2018).
45. Wood, M. H. *et al.* Comparative adsorption of saturated and unsaturated fatty acids at the iron oxide/oil interface. *Langmuir* **32**, 534–540 (2016).
46. Wood, M. H. *et al.* Hexadecylamine adsorption at the iron oxide–oil interface. *Langmuir* **29**, 13735–13742 (2013).
47. Wood, M. H. Adsorption at the metal/liquid interface. University of Cambridge. (2015).
48. Nalam, P. C., Pham, A., Castillo, R. V., & Espinosa-Marzal, R. M. Adsorption Behavior and Nanotribology of Amine-Based Friction Modifiers on Steel Surfaces. *J. Phys. Chem. C* **123**, 13672–13680 (2019).
49. Zachariah, Z. *et al.* Correlation between the adsorption and the nanotribological performance of fatty acid-based organic friction modifiers on stainless steel. *Tribol. Lett.* **68**, 1–16 (2020).
50. Chen, Y. L., & Israelachvili, J. N. Effects of ambient conditions on adsorbed surfactant and polymer monolayers. *J. Phys. Chem.* **96**, 7752–7760 (1992).
51. Yoshizawa, H., Chen, Y. L., & Israelachvili, J. Fundamental mechanisms of interfacial friction. 1. Relation between adhesion and friction. *J. Phys. Chem.* **97**, 4128–4140 (1993).
52. Ewen, J. P., Gattinoni, C., Morgan, N., Spikes, H. A., & Dini, D. Nonequilibrium Molecular Dynamics Simulations of Organic Friction Modifiers Adsorbed on Iron Oxide Surfaces. *Langmuir* **32**, 4450–4463 (2016).
53. Loehlé, S. *et al.* Mixed lubrication of steel by C18 fatty acids revisited. Part II: Influence of some key parameters. *Tribol. Int.* **94**, 207–216 (2016).

54. Ewen, J. P., Restrepo, S. E., Morgan, N., & Dini, D. Nonequilibrium molecular dynamics simulations of stearic acid adsorbed on iron surfaces with nanoscale roughness. *Tribol. Int.* **107**, 264–273 (2017).
55. Barrena, E., Kopta, S., Ogletree, D. F., Charych, D. H., & Salmeron, M. Relationship between friction and molecular structure: alkylsilane lubricant films under pressure. *Phys. Rev. Lett.* **82**, 2880–2883 (1999).
56. Salmeron, M. Generation of defects in model lubricant monolayers and their contribution to energy dissipation in friction. *Tribol. Lett.* **10**, 69–79 (2001).
57. Brukman, M. J., Oncins, G., Dunbar, T. D., Boardman, L. D., & Carpick, R. W. Nanotribological Properties of Alkanephosphonic Acid Self-Assembled Monolayers on Aluminum Oxide: Effects of Fluorination and Substrate Crystallinity. *Langmuir* **22**, 3988–3998 (2006).
58. Flater, E. E., Ashurst, W. R., & Carpick, R. W. Nanotribology of Octadecyltrichlorosilane Monolayers and Silicon: Self-Mated versus Unmated Interfaces and Local Packing Density Effects. *Langmuir* **23**, 9242–9252 (2007).
59. Gao, H., Ewen, J. P., Hartkamp, R., Müser, M. H., & Dini, D. Scale-Dependent Friction–Coverage Relations and Nonlocal Dissipation in Surfactant Monolayers. *Langmuir* **37**, 2406–2418 (2021).
60. Dorinson, A. The Slow-Speed Frictional Behavior of Some Lubricant Additive Type-Substances. *ASLE Trans.* **13**, 215–224 (1970).
61. Chugg, K., & Chaudhri, M. M. Boundary lubrication and shear properties of thin solid films of dioctadecyl dimethyl ammonium chloride (TA 100). *J. Phys. D: Appl. Phys* **26**, 1993–2000 (1993).
62. Campen, S., Green, J., Lamb, G., Atkinson, D., & Spikes, H. On the increase in boundary friction with sliding speed. *Tribol. Lett.* **48**, 237–248 (2012).
63. Ingram, M., Noles, J., Watts, R., Harris, S., & Spikes, H. A. Frictional Properties of Automatic Transmission Fluids: Part II—Origins of Friction–Sliding Speed Behavior. *Tribol. Trans.* **54**, 154–167 (2010).
64. Briscoe, B. J., & Evans, D. C. B. The shear properties of Langmuir—Blodgett layers. *Proc. R. Soc. A.* **380**, 389–407 (1982).
65. Eyring, H. Viscosity, Plasticity, and Diffusion as Examples of Absolute Reaction Rates. *J. Chem. Phys* **4**, 283–291 (1936).
66. Spikes, H. Stress-augmented thermal activation: Tribology feels the force. *Friction* **6**, 1–31 (2018).
67. He, G., & Robbins, M. O. Simulations of the kinetic friction due to adsorbed surface layers. *Tribol. Trans.* **10**, 7–14 (2001).
68. Glosli, J. N., & McClelland, G. M. Molecular dynamics study of sliding friction of ordered organic monolayers. *Phys. Rev. Lett.* **70**, (13), 1960–1963 (1993).
69. Doig, M., Warrens, C. P., & Camp, P. J. Structure and Friction of Stearic Acid and Oleic Acid Films Adsorbed on Iron Oxide Surfaces in Squalane. *Langmuir* **30**, 186–195 (2014).

70. Farrow, M. R., Chremos, A., Camp, P. J., Harris, S. G., & Watts, R. F. Molecular simulations of kinetic-friction modification in nanoscale fluid layers. *Tribol. Lett.* **42**, 325–337 (2011).
71. Mazuyer, D., Cayer-Barrioz, J., Tonck, A., & Jarnias, F. Friction Dynamics of Confined Weakly Adhering Boundary Layers. *Langmuir* **24**, 3857–3866 (2008).
72. Ingram, M., Noles, J., Watts, R., Harris, S., & Spikes, H. A. Frictional Properties of Automatic Transmission Fluids: Part I—Measurement of Friction–Sliding Speed Behavior. *Tribol. Trans.* **54**, 145–153 (2010).
73. Loehle, S. *et al.* Mixed lubrication with C18 fatty acids: effect of unsaturation. *Tribol. Lett.* **53**, 319–328 (2014).
74. Glovnea, R., Forrest, A., Olver, A., & Spikes, H. Measurement of sub-nanometer lubricant films using ultra-thin film interferometry. *Tribol. Lett.* **15**, 217–230 (2003).
75. Anghel, V., Bovington, C., & Spikes, H. A. Thick-boundary-film formation by friction modifier additives. *Lubr. Sci.* **11**, 313–335 (1999).
76. Nakano, K., & Spikes, H. A. Process of boundary film formation from fatty acid solution. *Tribol. Online* **7**, 1–7 (2012).
77. Ratoi, M., Anghel, V., Bovington, C., & Spikes, H. A. Mechanisms of oiliness additives. *Tribol. Int.* **33**, 241–247 (2000).
78. Campen, S., Green, J., Lamb, G., & Spikes, H. In situ study of model organic friction modifiers using liquid cell AFM; saturated and mono-unsaturated carboxylic acids. *Tribol. Lett.* **57**, 1–20 (2015).
79. Allen, C. M., & Drauglis, E. Boundary layer lubrication: monolayer or multilayer. *Wear* **14**, 363–384 (1969).
80. Berry, J. D., Neeson, M. J., Dagastine, R. R., Chan, D. Y., & Tabor, R. F. Measurement of surface and interfacial tension using pendant drop tensiometry. *J. Colloid Interface Sci.* **454**, 226–237 (2015).
81. Hoorfar, M., & W. Neumann, A. Recent progress in Axisymmetric Drop Shape Analysis (ADSA). *Adv. Colloid Interface Sci.* **121**, 25–49 (2006).
82. Foo, K., & Hameed, B. Insights into the modeling of adsorption isotherm systems. *Chem. Eng. J.* **156**, 2–10 (2010).
83. Langmuir, I. The constitution and fundamental properties of solids and liquids. Part 1. Solids. *J. Am. Chem. Soc.* **38**, 2221–2295 (1916).
84. Poon, J., Madden, D. C., Wood, M. H., & Clarke, S. M. Characterizing surfaces of garnet and steel, and adsorption of organic additives. *Langmuir* **34**, 7726–7737 (2018).
85. Dudášová, D., Simon, S., Hemmingsen, P. V., & Sjöblom, J. Study of asphaltenes adsorption onto different minerals and clays: Part 1. Experimental adsorption with UV depletion detection. *Colloids Surf. A Physicochem. Eng. Asp.* **317**, 1–9 (2008).
86. Haghseresht, F., & Lu, G. Q. Adsorption Characteristics of Phenolic Compounds onto Coal-Reject-Derived Adsorbents. *Energy Fuels* **12**, 1100–1107 (1998).

87. Brunauer, S., Emmett, P. H., & Teller, E. Adsorption of gases in multimolecular layers. *J. Am. Chem. Soc.* **60**, 309–319 (1938).
88. Hall, C., Wales, D. S., & Keane, M. A. Copper removal from aqueous systems: biosorption by *Pseudomonas syringae*. *Sep. Sci. Technol.* **36**, 223–240 (2001).
89. Vázquez, G., González-Álvarez, J., García, A., Freire, M., & Antorrena, G. Adsorption of phenol on formaldehyde-pretreated Pinus pinaster bark: Equilibrium and kinetics. *Bioresour. Technol.* **98**, 1535–1540 (2007).
90. Daillant, J., & Gibaud, A. *X-ray and Neutron Reflectivity: Principles and Applications* (Springer, Berlin Heidelberg, 2009). [Second edition]
91. Sivia, D. *Elementary Scattering Theory: For X-ray and Neutron Users* (Oxford University Press, Oxford, 2011).
92. Penfold, J., & Thomas, R. K. The application of the specular reflection of neutrons to the study of surfaces and interfaces. *J. Condens. Matter Phys.* **2**, 1369–1412 (1990).
93. Zhou, X.-L., & Chen, S.-H. Theoretical foundation of X-ray and neutron reflectometry. *Phys. Rep.* **257**, 223–348 (1995).
94. Sears, V. F. Neutron scattering lengths and cross sections. *Neutron News* **3**, 26–37 (1992).
95. Parratt, L. G. Surface Studies of Solids by Total Reflection of X-Rays. *Phys. Rev.* **95**, 359–369 (1954).
96. Webster, J., Holt, S., & Dalgliesh, R. INTER the chemical interfaces reflectometer on target station 2 at ISIS. *Physica B Condens. Matter* **385-386**, 1164–1166 (2006).
97. Campbell, R., Wacklin, H., Sutton, I., Cubitt, R., & Fragneto, G. FIGARO: The new horizontal neutron reflectometer at the ILL. *Eur. Phys. J. Plus* **126**, 1–22 (2011).
98. Hughes, I., & Hase, T. *Measurements and their uncertainties: a practical guide to modern error analysis* (Oxford University Press, Oxford, 2010).
99. Brooks, S., Gelman, A., Jones, G., & Meng, X.-L. *Handbook of markov chain monte carlo* (CRC press, 2011).
100. MacKay, D. J. *Information theory, inference and learning algorithms* (Cambridge University Press, Cambridge, 2003).
101. Roy, V. Convergence Diagnostics for Markov Chain Monte Carlo. *Annu. Rev. Stat. Appl.* **7**, 387–412 (2020).
102. Gelman, A., & Rubin, D. B. Inference from Iterative Simulation Using Multiple Sequences. *Statist. Sci.* **7**, 457–472 (1992).
103. Gelman, A. *et al. Bayesian data analysis* (CRC press, 2013).
104. Flegal, J. M., Haran, M., & Jones, G. L. Markov chain Monte Carlo: Can we trust the third significant figure? *Statist. Sci.*, 250–260 (2008).
105. Virtanen, P. *et al.* SciPy 1.0: Fundamental Algorithms for Scientific Computing in Python. *Nat. Methods* **17**, 261–272 (2020).
106. Efron, B., & Tibshirani, R. J. *An introduction to the bootstrap* (CRC press, 1994).
107. Kass, R. E., & Raftery, A. E. Bayes factors. *J. Am. Stat. Assoc.* **90**, 773–795 (1995).

108. Sivia, D., Hamilton, W., & Smith, G. Analysis of neutron reflectivity data: maximum entropy, Bayesian spectral analysis and speckle holography. *Physica B Condens. Matter* **173**, 121–138 (1991).
109. Sivia, D., & Skilling, J. *Data analysis: a Bayesian tutorial* (OUP Oxford, Oxford, 2006).
110. Skilling, J. Nested sampling for general Bayesian computation. *Bayesian Anal.* **1**, 833–859 (2006).
111. Feroz, F., & Hobson, M. P. Multimodal nested sampling: an efficient and robust alternative to Markov Chain Monte Carlo methods for astronomical data analyses. *Mon. Not. R. Astron. Soc.* **384**, 449–463 (2008).
112. Bjorck, M., & Andersson, G. GenX: an extensible X-ray reflectivity refinement program utilizing differential evolution. *J. Appl. Crystallogr.* **40**, 1174–1178 (2007).
113. Kienzle, P.A., Krycka, J., Patel, N., & Sahin, I. Refl1D (Version 0.8.13) [Computer Software]. College Park, MD: University of Maryland., https://refl1d.readthedocs.io/en/latest/index.html, Retrieved Jan 27, 2021.
114. Vrugt, J. A. *et al.* Accelerating Markov Chain Monte Carlo Simulation by Differential Evolution with Self-Adaptive Randomized Subspace Sampling. *Int. J. Nonlinear Sci. Numer. Simul.* **10**, 273–290 (2009).
115. Nelson, A. R., & Prescott, S. W. refnx: neutron and X-ray reflectometry analysis in Python. *J. Appl. Crystallogr.* **52**, 193–200 (2019).
116. Speagle, J. S. dynesty: a dynamic nested sampling package for estimating Bayesian posteriors and evidences. *Mon. Notices Royal Astron. Soc* **493**, 3132–3158 (2020).
117. Sivia, D., David, W., Knight, K., & Gull, S. An introduction to Bayesian model selection. *Physica D* **66**, 234–242 (1993).
118. McCluskey, A. R., Cooper, J. F. K., Arnold, T., & Snow, T. A general approach to maximise information density in neutron reflectometry analysis. *Mach. Learn.: Sci. Technol.* **1**, 035002 (2020).
119. Chason, E., & Mayer, T. M. Thin film and surface characterization by specular X-ray reflectivity. *Crit. Rev. Solid State Mater. Sci.* **22**, 1–67 (1997).
120. Henke, B. L., Gullikson, E. M., & Davis, J. C. X-ray interactions: photoabsorption, scattering, transmission, and reflection at E=50-30000 eV, Z=1-92. *At. Data Nucl. Data Tables* **54**, 181–342 (1993).
121. Nicklin, C., Arnold, T., Rawle, J., & Warne, A. Diamond beamline I07: a beamline for surface and interface diffraction. *J. Synchrotron Rad.* **23**, 1245–1253 (2016).
122. Sentenac, D., Shalaginov, A. N., Fera, A., & Jeu, W. H. de. On the instrumental resolution in X-ray reflectivity experiments. *J. Appl. Crystallogr.* **33**, 130–136 (2000).
123. Singh, H. S. Y. *The SAXS Guide - Getting Acquainted with the Principles* (Anton Paar, Graz, Austria, 2017). [Fourth edition]
124. Zaccai, G., & Jacrot, B. Small angle neutron scattering. *Ann. Rev. Biophys. Bioeng.* **12**, 139–157 (1983).

125. Guinier, A., Fournet, G., & Yudowitch, K. L. *Small-angle scattering of X-rays* (Wiley New York, 1955).
126. Lindner, P., May, R., & Timmins, P. A. Upgrading of the SANS instrument D11 at the ILL. *Physica B Condens. Matter* **180-181**, 967–972 (1992).
127. Lindner, P., & Schweins, R. The D11 Small-Angle Scattering Instrument: A New Benchmark for SANS. *Neutron News* **21**, 15–18 (2010).
128. SASmodels [Computer Software], https://pypi.org/project/sasmodels/, (accessed May 18, 2021.)
129. Kienzle, P.A., Krycka, J., Patel, N., & Sahin, I. Bumps (Version 0.8.0) [Computer Software]. College Park, MD: University of Maryland., https://bumps.readthedocs.io/en/latest/, Retrieved May 18, 2021.
130. SASview [Computer Software], https://www.sasview.org/, (accessed May 18, 2021.)
131. Van der Heide, P. *X-Ray photoelectron spectroscopy: An Introduction to Principles and Practices* (John Wiley & Sons, 2011).
132. Wagner, C. D. *et al.* Empirical atomic sensitivity factors for quantitative analysis by electron spectroscopy for chemical analysis. *Surf. Interface Anal.* **3**, 211–225 (1981).
133. Stojilovic, N. Why Can't We See Hydrogen in X-ray Photoelectron Spectroscopy? *J. Chem. Educ.* **89**, 1331–1332 (2012).
134. Moulder, J. F., Stickle, W. F., Sobol, P. E., & Bomben, K. D. *Handbook of X-ray photoelectron spectroscopy* (Perkin-Elmer Corporation, USA, 1992).
135. Doniach, S., & Sunjic, M. Many-electron singularity in X-ray photoemission and X-ray line spectra from metals. *J. Phys. C: Solid State Phys.* **3**, 285 (1970).
136. Gupta, R. P., & Sen, S. K. Calculation of multiplet structure of core p-vacancy levels. *Phys. Rev. B* **10**, 71–77 (1974).
137. Gupta, R. P., & Sen, S. K. Calculation of multiplet structure of core p -vacancy levels. II. *Phys. Rev. B* **12**, 15–19 (1975).
138. Biesinger, M. C. *et al.* Resolving surface chemical states in XPS analysis of first row transition metals, oxides and hydroxides: Cr, Mn, Fe, Co and Ni. *Appl. Surf. Sci.* **257**, 2717–2730 (2011).
139. Engelhard, M. H., Baer, D. R., Herrera-Gomez, A., & Sherwood, P. M. A. Introductory guide to backgrounds in XPS spectra and their impact on determining peak intensities. *J. Vac. Sci. Technol. A* **38**, 063203 (2020).
140. Shirley, D. A. High-Resolution X-Ray Photoemission Spectrum of the Valence Bands of Gold. *Phys. Rev. B* **5**, (12), 4709–4714 (1972).
141. Tougaard, S., & Sigmund, P. Influence of elastic and inelastic scattering on energy spectra of electrons emitted from solids. *Phys. Rev. B* **25**, (7), 4452–4466 (1982).
142. Greczynski, G., & Hultman, L. X-ray photoelectron spectroscopy: Towards reliable binding energy referencing. *Prog. Mater. Sci* **107**, 100591 (2020).
143. Bhushan, B. *Modern tribology handbook* (CRC press, 2000).

144. Zhang, J., & Spikes, H. On the mechanism of ZDDP antiwear film formation. *Tribol. Lett.* **63**, 1–15 (2016).
145. Salguero, J., Vazquez-Martinez, J. M., Sol, I. D., & Batista, M. Application of Pin-On-Disc Techniques for the Study of Tribological Interferences in the Dry Machining of A92024-T3 (Al–Cu) Alloys. *Materials* **11**, (2018).
146. Liu, H., & Zhu, L. Excess Molar Volumes and Viscosities of Binary Systems of Butylcyclohexane with *n*-Alkanes (C7 to C14) at $T = 293.15$ K to 313.15 K. *J. Chem. Eng. Data* **59**, 369–375 (2014).
147. Zhang, L., Guo, Y., Xiao, J., Gong, X., & Fang, W. Density, Refractive Index, Viscosity, and Surface Tension of Binary Mixtures of *exo*-Tetrahydrodicyclopentadiene with Some *n*-Alkanes from (293.15 to 313.15) K. *J. Chem. Eng. Data* **56**, 4268–4273 (2011).
148. Yu, S.-H., Lee, K.-S., & Yook, S.-J. Film flow around a fast rotating roller. *Int. J. Heat Flow* **30**, 796–803 (2009).
149. Malone, B. An experimental investigation of roll coating phenomena. University of Leeds. (1992).
150. Bradley-Shaw, J. L., Camp, P. J., Dowding, P. J., & Lewtas, K. Glycerol Monooleate Reverse Micelles in Nonpolar Solvents: Computer Simulations and Small-Angle Neutron Scattering. *J. Phys. Chem. B* **119**, 4321–4331 (2015).
151. Shrestha, L. K., Shrestha, R. G., Abe, M., & Ariga, K. Reverse micelle microstructural transformations induced by oil and water. *Soft Matter* **7**, (21), 10017–10024 (2011).
152. Bradley-Shaw, J. L., Camp, P. J., Dowding, P. J., & Lewtas, K. Molecular dynamics simulations of glycerol monooleate confined between mica surfaces. *Langmuir* **32**, 7707–7718 (2016).
153. Tsagkaropoulou, G., Warrens, C. P., & Camp, P. J. Interactions between friction modifiers and dispersants in lubricants: the case of glycerol monooleate and polyisobutylsuccinimide-polyamine. *ACS Appl. Mater. Interfaces* **11**, 28359–28369 (2019).
154. Caravaggio, G. A., Charland, J.-P., Macdonald, P., & Graham, L. *n*-Alkane Profiles of Engine Lubricating Oil and Particulate Matter by Molecular Sieve Extraction. *Environ. Sci. Technol.* **41**, 3697–3701 (2007).
155. Zarbakhsh, A., Bowers, J., & Webster, J. R. P. A new approach for measuring neutron reflection from a liquid/liquid interface. *Meas. Sci. Technol.* **10**, 738–743 (1999).
156. Day, J. P. R., & Bain, C. D. Ellipsometric study of depletion at oil-water interfaces. *Phys. Rev. E* **76**, (4), 041601 (2007).
157. Zeppieri, S., Rodríguez, J., & López de Ramos, A. L. Interfacial Tension of Alkane + Water Systems. *J. Chem. Eng. Data* **46**, 1086–1088 (2001).
158. Myers, D. *Surfactant science and technology* (John Wiley & Sons, 2020). [Third edition]
159. Ruckenstein, E., & Nagarajan, R. Aggregation of amphiphiles in nonaqueous media. *J. Phys. Chem.* **84**, 1349–1358 (1980).
160. Smith, G. N., Brown, P., Rogers, S. E., & Eastoe, J. Evidence for a Critical Micelle Concentration of Surfactants in Hydrocarbon Solvents. *Langmuir* **29**, 3252–3258 (2013).

161. Mukherjee, I., Moulik, S. P., & Rakshit, A. K. Tensiometric determination of Gibbs surface excess and micelle point: A critical revisit. *J. Colloid Interface Sci.* **394**, 329–336 (2013).
162. Zwierzykowski, W., & Konopacka-Łyskawa, D. The interactions of saturated fatty acids at the dodecane/water interface and their sodium salts at the air/water interface. *Colloids Surf. A Physicochem. Eng. Asp.* **160**, 183–188 (1999).
163. Bradley-Shaw, J. L., Camp, P. J., Dowding, P. J., & Lewtas, K. Self-assembly and friction of glycerol monooleate and its hydrolysis products in bulk and confined non-aqueous solvents. *Phys. Chem. Chem. Phys.* **20**, 17648–17657 (2018).
164. Gengenbach, T. R., Major, G. H., Linford, M. R., & Easton, C. D. Practical guides for x-ray photoelectron spectroscopy (XPS): Interpreting the carbon 1s spectrum. *J. Vac. Sci. Technol. A* **39**, 013204 (2021).
165. Wandelt, K. Photoemission studies of adsorbed oxygen and oxide layers. *Surf. Sci. Rep.* **2**, 1–121 (1982).
166. McIntyre, N., & Zetaruk, D. X-ray photoelectron spectroscopic studies of iron oxides. *Anal. Chem.* **49**, 1521–1529 (1977).
167. Roberts, M., & Wood, P. The mechanism of the oxidation and passivation of iron by water vapour—an electron spectroscopic study. *J. Electron Spectros. Relat. Phenomena* **11**, 431–437 (1977).
168. McCafferty, E., & Wightman, J. P. Determination of the concentration of surface hydroxyl groups on metal oxide films by a quantitative XPS method. *Surf. Interface Anal.* **26**, 549–564 (1998).
169. López, G. P., Castner, D. G., & Ratner, B. D. XPS O 1s binding energies for polymers containing hydroxyl, ether, ketone and ester groups. *Surf. Interface Anal.* **17**, 267–272 (1991).
170. Yamashita, T., & Hayes, P. Analysis of XPS spectra of Fe^{2+} and Fe^{3+} ions in oxide materials. *Appl. Surf. Sci.* **254**, 2441–2449 (2008).
171. Lin, T.-C., Seshadri, G., & Kelber, J. A. A consistent method for quantitative XPS peak analysis of thin oxide films on clean polycrystalline iron surfaces. *Appl. Surf. Sci.* **119**, 83–92 (1997).
172. Tougaard, S. Practical guide to the use of backgrounds in quantitative XPS. *J. Vac. Sci. Technol. A* **39**, 011201 (2021).
173. Maccarini, M. *et al.* Density depletion at solid-liquid interfaces: a neutron reflectivity study. *Langmuir* **23**, 598–608 (2007).
174. Steitz, R. *et al.* Nanobubbles and their precursor layer at the interface of water against a hydrophobic substrate. *Langmuir* **19**, 2409–2418 (2003).
175. Doshi, D. A., Watkins, E. B., Israelachvili, J. N., & Majewski, J. Reduced water density at hydrophobic surfaces: effect of dissolved gases. *PNAS* **102**, 9458–9462 (2005).
176. Chu, M., Miller, M., & Dutta, P. Interfacial Density Profiles of Polar and Nonpolar Liquids at Hydrophobic Surfaces. *Langmuir* **36**, 906–910 (2020).

177. Scoppola, E. *et al.* Reflectometry reveals accumulation of surfactant impurities at bare oil/water interfaces. *Molecules* **24**, 4113; 10.3390/molecules24224113 (2019).
178. Seo, Y. S., & Satija, S. No intrinsic depletion layer on a polystyrene thin film at a water interface. *Langmuir* **22**, 7113–7116 (2006).
179. Cornell, R. M., & Schwertmann, U. *The Iron Oxides: Structure, Properties, Reactions, Occurrences and Uses* (Wiley-VCH, Weinheim, 2003). [Second edition]
180. Gutfreund, P. *et al.* Depletion at solid/liquid interfaces: flowing hexadecane on functionalized surfaces. *J. Chem. Phys.* **134**, 064711; 10.1063/1.3549895 (2011).
181. Gutfreund, P., Maccarini, M., Dennison, A. J., & Wolff, M. The Search for Nanobubbles by Using Specular and Off-Specular Neutron Reflectometry. *Langmuir* **32**, 9091–9096 (2016).
182. Battino, R., Rettich, T. R., & Tominaga, T. The Solubility of Nitrogen and Air in Liquids. *J. Phys. Chem. Ref. Data* **13**, 563–600 (1984).
183. Devlin, M. T. *et al.* Friction and film-formation properties of oil-soluble inorganic nanoparticles. *SAE Int. J. Fuels Lubr.* **1**, 1503–1510 (2009).
184. Jiang, S., Yuan, C., & Wong, J. S. Effectiveness of glycerol-monooleate in high-performance polymer tribo-systems. *Tribol. Int.* **155**, 106753 (2021).
185. Koshima, H., Kamano, H., Hisaeda, Y., Liu, H., & Ye, S. Analyses of the Adsorption Structures of Friction Modifiers by Means of Quantitative Structure-Property Relationship Method and Sum Frequency Generation Spectroscopy. *Tribol. Online* **5**, 165–172 (2010).
186. Murgia, S., Lampis, S., Zucca, P., Sanjust, E., & Monduzzi, M. Nucleotide Recognition and Phosphate Linkage Hydrolysis at a Lipid Cubic Interface. *J. Am. Chem. Soc.* **132**, 16176–16184 (2010).
187. Ketteler, G., Weiss, W., Ranke, W., & Schlögl, R. Bulk and surface phases of iron oxides in an oxygen and water atmosphere at low pressure. *Phys. Chem. Chem. Phys.* **3**, (6), 1114–1122 (2001).
188. Anthony, J. W., Bideaux, R. A., Bladh, K. W., & Nichols, M. C. *Handbook of Mineralogy* (Mineral Data Publishing, Tucson Arizona, 1990).
189. Shaikhutdinov, S. K., Joseph, Y., Kuhrs, C., Ranke, W., & Weiss, W. Structure and reactivity of iron oxide surfaces. *Faraday Discuss.* **114**, (0), 363–380 (1999).
190. Wang, X.-G. *et al.* The Hematite (α-Fe_2O_3) (0001) Surface: Evidence for Domains of Distinct Chemistry. *Phys. Rev. Lett.* **81**, (5), 1038–1041 (1998).
191. Parkinson, G. S. Iron oxide surfaces. *Surf. Sci. Rep.* **71**, 272–365 (2016).
192. McCluskey, A. R. *et al.* Bayesian determination of the effect of a deep eutectic solvent on the structure of lipid monolayers. *Phys. Chem. Chem. Phys.* **21**, (11), 6133–6141 (2019).
193. Heinrich, F., Kienzle, P. A., Hoogerheide, D. P., & Lösche, M. Information gain from isotopic contrast variation in neutron reflectometry on protein–membrane complex structures. *J. Appl. Crystallogr.* **53**, 800–810 (2020).

194. Castro, M. A., Clarke, S. M., Inaba, A., Arnold, T., & Thomas, R. K. Competitive Adsorption of Simple Linear Alkane Mixtures onto Graphite. *J. Phys. Chem. B* **102**, 10528–10534 (1998).
195. Li, B. L., Clarke, S. M., & Wilson, D. I. Solid monolayers of glycerides adsorbed on the surface of graphite powder. *Colloids Surf. A Physicochem. Eng. Asp.* **389**, 180–187 (2011).
196. Kurre, S. K., Garg, R., & Pandey, S. A review of biofuel generated contamination, engine oil degradation and engine wear. *Biofuels* **8**, 273–280 (2017).
197. Soper, A. K., & Benmore, C. J. Quantum Differences between Heavy and Light Water. *Phys. Rev. Lett.* **101**, 065502 (2008).
198. Goryunov, A. H/D isotope effects on protein hydration and interaction in solution. *Gen. Physiol. Biophys.* **25**, 303 (2006).
199. Kutsenko, V. *et al.* Isotope effect in heavy/light water suspensions of optically active gold nanoparticles. *Appl. Nanosci.* **9**, 957–963 (2019).
200. Whiddon, C., & Söderman, O. Unusually Large Deuterium Isotope Effects in the Phase Diagram of a Mixed Alkylglucoside Surfactant/Water System. *Langmuir* **17**, 1803–1806 (2001).
201. Bastardo, L. A., Mészáros, R., Varga, I., Gilányi, T., & Cleasson, P. M. Deuterium Isotope Effects on the Interaction between Hyperbranched Polyethylene Imine and an Anionic Surfactant. *J. Phys. Chem. B* **109**, 16196–16202 (2005).
202. Gresham, I. J. *et al.* Quantifying the robustness of the neutron reflectometry technique for structural characterization of polymer brushes. *J. Appl. Crystallogr.* **54**, (2021).
203. Taylor, R. I., & de Kraker, B. R. Shear rates in engines and implications for lubricant design. *P. I. Mech. Eng. J-J. Eng.* **231**, 1106–1116 (2017).
204. Welbourn, R. J. L., Bartholomew, F., Gutfreund, P., & Clarke, S. M. Neutron reflectometry of an anionic surfactant at the solid–liquid interface under shear. *Langmuir* **33**, 5982–5990 (2017).
205. Yu, C., Evmenenko, G., Kmetko, J., & Dutta, P. Effects of shear flow on interfacial ordering in liquids: X-ray scattering studies. *Langmuir* **19**, 9558–9561 (2003).
206. Corvis, Y., Barré, L., Jestin, J., Gummel, J., & Cousin, F. Asphaltene adsorption mechanism under shear flow probed by *in situ* neutron reflectivity measurements. *Eur. Phys. J. Spec. Top.* **213**, 295–302 (2012).
207. Campen, S., Green, J., Lamb, G., & Spikes, H. In situ study of model organic friction modifiers using liquid cell AFM: self-assembly of octadecylamine. *Tribol. Lett.* **58**, 1–15 (2015).
208. Hirayama, T. *et al.* Cross-Sectional Imaging of Boundary Lubrication Layer Formed by Fatty Acid by Means of Frequency-Modulation Atomic Force Microscopy. *Langmuir* **33**, 10492–10500 (2017).
209. Watanabe, S., Nakano, M., Miyake, K., & Sasaki, S. Analysis of the Interfacial Molecular Behavior of a Lubrication Film of n-Dodecane Containing Stearic Acid under Lubricat-

ing Conditions by Sum Frequency Generation Spectroscopy. *Langmuir* **32**, 13649–13656 (2016).

210. Qiao, Y. *et al.* An *in situ* shearing x-ray measurement system for exploring structures and dynamics at the solid–liquid interface. *Rev. Sci. Instrum.* **91**, 013908 (2020).
211. Penfold, J., Staples, E., Tucker, I., & Fragnetto, G. The effect of shear on the adsorption of non-ionic surfactants at the liquid—solid interface. *Physica B Condens. Matter* **221**, 325–330 (1996).
212. Baker, S. M. *et al.* Shear cell for the study of liquid-solid interfaces by neutron scattering. *Rev. Sci. Instrum.* **65**, 412–416 (1994).
213. Junghans, A. *et al.* Analysis of biosurfaces by neutron reflectometry: from simple to complex interfaces. *Biointerphases* **10**, 019014; 10.1116/1.4914948 (2015).
214. Wolff, M. *et al.* Combined neutron reflectometry and rheology. *J. Appl. Crystallogr.* **46**, 1729–1733 (2013).
215. Cosgrove, T., Luckham, P. F., Richardson, R. M., Webster, J. R. P., & Zarbakhsh, A. The measurement of volume fraction profiles for adsorbed polymers under compression using neutron reflectometry. *Colloids Surf., A* **86**, 103–110 (1994).
216. Cho, J. H. J. *et al.* Surface force confinement cell for neutron reflectometry studies of complex fluids under nanoconfinement. *Rev. Sci. Instrum.* **79**, 103908; 10.1063/1.3005483 (2008).
217. Vos, W. M. de *et al.* Measuring the structure of thin soft matter films under confinement: a surface-force type apparatus for neutron reflection, based on a flexible membrane approach. *Rev. Sci. Instrum.* **83**, 113903; 10.1063/1.4767238 (2012).
218. Kuhl, T. L., Smith, G. S., Israelachvili, J. N., Majewski, J., & Hamilton, W. Neutron confinement cell for investigating complex fluids. *Rev. Sci. Instrum.* **72**, 1715–1720 (2001).
219. Gutfreund, P. *et al.* Towards generalized data reduction on a chopper-based time-of-flight neutron reflectometer. *J. Appl. Cryst.* **51**, 606–615 (2018).
220. Zarbakhsh, A., Querol, A., Bowers, J., & Webster, J. R. P. Structural studies of amphiphiles adsorbed at liquid–liquid interfaces using neutron reflectometry. *Faraday Discuss.* **129**, 155–167 (2005).
221. Browning, K. L. *et al.* Specular neutron reflection at the mica/water interface - irreversible adsorption of a cationic dichain surfactant. *J. Appl. Cryst.* **47**, 1638–1646 (2014).
222. Wolff, M. *et al.* Shear Induced Relaxation of Polymer Micelles at the Solid-Liquid Interface. *Langmuir* **24**, 11331–11333 (2008).
223. Azizian, S., & Bashavard, N. Surface Tension of Dilute Solutions of Alkanes in Cyclohexanol at Different Temperatures. *J. Chem. Eng. Data* **53**, 2422–2425 (2008).
224. Savage, M. D. Cavitation in lubrication. Part 1. On boundary conditions and cavity—fluid interfaces. *J. Fluid Mech.* **80**, 743–755 (1977).
225. Pearson, J. R. A. The instability of uniform viscous flow under rollers and spreaders. *J. Fluid Mech.* **7**, 481–500 (1960).

226. Adachi, K., Tamura, T., & Nakamura, R. Coating flows in a nip region and various critical phenomena. *AIChE Journal* **34**, 456–464 (1988).
227. Basham, M. *et al.* Data analysis workbench (DAWN). *J. Synchrotron Rad.* **22**, 853–858 (2015).
228. Reich, C., Hochrein, M. B., Krause, B., & Nickel, B. A microfluidic setup for studies of solid-liquid interfaces using x-ray reflectivity and fluorescence microscopy. *Rev. Sci. Instrum.* **76**, 095103 (2005).
229. Alloway, R. M. *et al.* Adsorption of 4-*n*-Nonylphenol, Carvacrol, and Ethanol onto Iron Oxide from Nonaqueous Hydrocarbon Solvents. *Langmuir* **35**, 11662–11669 (2019).
230. Pospelov, G. *et al.* BornAgain: software for simulating and fitting grazing-incidence small-angle scattering. *J. Appl. Crystallogr.* **53**, 262–276 (2020).
231. Inoue, S., Uchihashi, T., Yamamoto, D., & Ando, T. Direct observation of surfactant aggregate behavior on a mica surface using high-speed atomic force microscopy. *Chem. Commun.* **47**, 4974–4976 (2011).
232. Schniepp, H. C., Shum, H. C., Saville, D. A., & Aksay, I. A. Surfactant Aggregates at Rough Solid-Liquid Interfaces. *J. Phys. Chem. B* **111**, 8708–8712 (2007).

Appendix A

Nested sampling priors and initial values

Throughout the presented work, all priors used were uniform with no varying probability across the bounded region. The initial parameter value is given as the central value, while the upper, $\uparrow$, and lower, $\downarrow$, bounds of the priors are specified by the superscript and subscript values respectively. For all the models listed here except the example problem, the intensity scale factor and background for each contrast had initial values and priors of $1^{\uparrow 1.2}_{\downarrow 0.8}$ and $10^{-6}\ ^{\uparrow 2\times 10^{-5}}_{\downarrow 10^{-7}}$ respectively.

Table A1: Initial parameter values and priors used in the nested sampling of the simulated data of two interfacial layers on an iron-coated silicon substrate. The surfactant layers are specified by the total of number of surfactant layers in the superscript number and the position of the surfactant from the inner-most position at 1 and outermost position at the greatest number.

Layer	β_n / $Å^{-2} \times 10^{-6}$	β_m / $Å^{-2} \times 10^{-6}$	Thickness / Å	Roughness / Å
Si	2.07	-	∞	3
SiO_2	3.47	-	$20^{\uparrow 30}_{\downarrow 1}$	$4^{\uparrow 10}_{\downarrow 1}$
Fe	$8.02^{\uparrow 8.20}_{\downarrow 7.50}$	$4.81^{\uparrow 4.94}_{\downarrow 4.27}$	$200^{\uparrow 230}_{\downarrow 170}$	$5^{\uparrow 15}_{\downarrow 1}$
FeO_x	$7.00^{\uparrow 7.20}_{\downarrow 6.00}$	$0.5^{\uparrow 1.30}_{\downarrow 0.00}$	$30^{\uparrow 20}_{\downarrow 40}$	$6^{\uparrow 15}_{\downarrow 1}$
dod-d_{26}	$6.70^{\uparrow 6.80}_{\downarrow 6.00}$	-	-	-
$surf_1^1$	$0.21^{\uparrow 6.70}_{\downarrow 0.21}$	-	$20^{\uparrow 25}_{\downarrow 15}$	$3^{\uparrow 15}_{\downarrow 1}$
$surf_1^2$	$0.21^{\uparrow 6.70}_{\downarrow 0.21}$	-	$10^{\uparrow 15}_{\downarrow 5}$	$3^{\uparrow 15}_{\downarrow 1}$
$surf_2^2$	$0.21^{\uparrow 6.70}_{\downarrow 0.21}$	-	$30^{\uparrow 35}_{\downarrow 25}$	$3^{\uparrow 15}_{\downarrow 1}$
$surf_1^3$	$0.21^{\uparrow 6.70}_{\downarrow 0.21}$	-	$5^{\uparrow 15}_{\downarrow 5}$	$3^{\uparrow 15}_{\downarrow 1}$
$surf_2^3$	$0.21^{\uparrow 6.70}_{\downarrow 0.21}$	-	$5^{\uparrow 15}_{\downarrow 5}$	$3^{\uparrow 15}_{\downarrow 1}$
$surf_3^3$	$0.21^{\uparrow 6.70}_{\downarrow 0.21}$	-	$5^{\uparrow 15}_{\downarrow 5}$	$3^{\uparrow 15}_{\downarrow 1}$
$surf_1^4$	$0.21^{\uparrow 6.70}_{\downarrow 0.21}$	-	$7.5^{\uparrow 12.5}_{\downarrow 7.5}$	$3^{\uparrow 15}_{\downarrow 1}$
$surf_2^4$	$0.21^{\uparrow 6.70}_{\downarrow 0.21}$	-	$7.5^{\uparrow 12.5}_{\downarrow 7.5}$	$3^{\uparrow 15}_{\downarrow 1}$
$surf_3^4$	$0.21^{\uparrow 6.70}_{\downarrow 0.21}$	-	$7.5^{\uparrow 12.5}_{\downarrow 7.5}$	$3^{\uparrow 15}_{\downarrow 1}$
$surf_4^4$	$0.21^{\uparrow 6.70}_{\downarrow 0.21}$	-	$7.5^{\uparrow 12.5}_{\downarrow 7.5}$	$3^{\uparrow 15}_{\downarrow 1}$

Table A2: The initial parameter values and priors used in the nested sampling of the iron-coated silicon substrate against neat dodecane-d_{26} and dodecane-h_{26} as shown in Figure 3.13.

Layer	β_n / $Å^{-2} \times 10^{-6}$	β_m / $Å^{-2} \times 10^{-6}$	Thickness / Å	Roughness / Å	Solvation / %
Si	2.07	-	∞	3	-
SiO_2	3.47	-	$15^{\uparrow 25}_{\downarrow 1}$	$4^{\uparrow 10}_{\downarrow 1}$	-
Fe	$8.02^{\uparrow 8.10}_{\downarrow 7.50}$	$4.81^{\uparrow 5.04}_{\downarrow 4.35}$	$190^{\uparrow 210}_{\downarrow 170}$	$5^{\uparrow 15}_{\downarrow 1}$	-
FeO_x	$7.00^{\uparrow 7.20}_{\downarrow 5.00}$	$0.5^{\uparrow 1.30}_{\downarrow 0.00}$	$30^{\uparrow 20}_{\downarrow 40}$	$6^{\uparrow 15}_{\downarrow 1}$	-
Adv	$0.00^{\uparrow 6.00}_{\downarrow -0.54}$	-	$10^{\uparrow 20}_{\downarrow 1}$	$7^{\uparrow 15}_{\downarrow 1}$	$0^{\uparrow 100}_{\downarrow 0}$
dod-d_{26}	$6.70^{\uparrow 6.70}_{\downarrow 5.00}$	-	-	-	-
dod-h_{26}	-0.46	-	-	-	-

Table A3: Initial parameter values and priors used in the nested sampling of the data collected with the iron-coated silicon substrate against the three contrast systems of dodecane-d_{26}/D_2O, dodecane-h_{26}/D_2O and dodecane-d_{26}/H_2O as shown in Figure 3.15c.

Layer	β_n / $Å^{-2} \times 10^{-6}$	β_m / $Å^{-2} \times 10^{-6}$	Thickness / Å	Roughness / Å	Solvation / %
Si	2.07	-	∞	3	-
SiO_2	3.47	-	$15^{\uparrow 25}_{\downarrow 1}$	$4^{\uparrow 15}_{\downarrow 1}$	-
Fe	$8.02^{\uparrow 8.10}_{\downarrow 7.50}$	$4.81^{\uparrow 5.04}_{\downarrow 4.35}$	$190^{\uparrow 230}_{\downarrow 190}$	$5^{\uparrow 20}_{\downarrow 1}$	-
FeO_x	$7.00^{\uparrow 7.20}_{\downarrow 5.00}$	$0.5^{\uparrow 1.30}_{\downarrow 0.00}$	$30^{\uparrow 20}_{\downarrow 40}$	$7^{\uparrow 15}_{\downarrow 1}$	-
Adv_J	$0.00^{\uparrow 6.00}_{\downarrow -0.54}$	-	$10^{\uparrow 20}_{\downarrow 1}$	$7^{\uparrow 15}_{\downarrow 1}$	$0^{\uparrow 100}_{\downarrow 0}$
dod-d_{26}	$6.70^{\uparrow 6.70}_{\downarrow 5.00}$	-	-	-	-
dod-h_{26}	-0.46	-	-	-	-

Table A4: Initial parameter values and priors used in the nested sampling of the data collected with the iron-coated silicon substrate against two contrasts of neat dodecane-d_{26} and one contrast of D_2O.

Layer	β_n / $Å^{-2} \times 10^{-6}$	β_m / $Å^{-2} \times 10^{-6}$	Thickness / Å	Roughness / Å
Si	2.07	-	∞	3
SiO_2	3.47	-	$15^{\uparrow 25}_{\downarrow 1}$	$4^{\uparrow 15}_{\downarrow 1}$
Fe	$8.0^{\uparrow 8.10}_{\downarrow 7.50}$	$4.8^{\uparrow 5.0}_{\downarrow 4.4}$	$190^{\uparrow 250}_{\downarrow 150}$	$5^{\uparrow 15}_{\downarrow 1}$
FeO_x	$7.00^{\uparrow 7.20}_{\downarrow 5.00}$	$0.5^{\uparrow 1.30}_{\downarrow 0.00}$	$30^{\uparrow 20}_{\downarrow 60}$	$7^{\uparrow 15}_{\downarrow 1}$
Adv	$0.0^{\uparrow 6.00}_{\downarrow -0.50}$	-	$10^{\uparrow 20}_{\downarrow 1}$	$7^{\uparrow 15}_{\downarrow 1}$
dod-d_{26}	$6.70^{\uparrow 6.70}_{\downarrow 5.00}$	-	-	-
D_2O	$6.4^{\uparrow 6.4}_{\downarrow 5.0}$	-	-	-

Table A5: Complete description of the initial parameter values and priors used in the nested sampling of the iron-coated silicon substrate against solutions of GMO in dodecane (20 mM) at 25 and 60 °C. The β_n of dodecane-h_{26} is listed twice, where * and † relate to β_n at 25 and 60 °C respectively.

Layer	β_n / $Å^{-2} \times 10^{-6}$	β_m / $Å^{-2} \times 10^{-6}$	Thickness / Å	Roughness / Å	Solvation / %
Si	2.07	-	∞	3	-
SiO_2	3.47	-	$15^{\uparrow 25}_{\downarrow 1}$	$4^{\uparrow 10}_{\downarrow 1}$	-
Fe	$8.02^{\uparrow 8.10}_{\downarrow 7.50}$	$4.81^{\uparrow 5.04}_{\downarrow 4.35}$	$190^{\uparrow 210}_{\downarrow 170}$	$5^{\uparrow 15}_{\downarrow 1}$	-
FeO_x	$7.00^{\uparrow 7.20}_{\downarrow 5.00}$	$0.5^{\uparrow 1.30}_{\downarrow 0.00}$	$30^{\uparrow 20}_{\downarrow 40}$	$6^{\uparrow 15}_{\downarrow 1}$	-
GMO	$0.21^{\uparrow 6.00}_{\downarrow -0.54}$	-	$20^{\uparrow 30}_{\downarrow 10}$	$1^{\uparrow 15}_{\downarrow 1}$	$0^{\uparrow 100}_{\downarrow 0}$
dod-d_{26}	$6.70^{\uparrow 6.70}_{\downarrow 5.00}$	-	-	-	-
dod-h_{26}	-0.46^* $-0.44^\dagger$	-	-	-	-

Table A6: Complete description of the initial parameter values and priors used in the nested sampling of the iron-coated silicon substrate against solutions of GMO in dodecane (0.5 mM) at 25 °C on the FIGARO reflectometer. The GMO layer marked with a * represents the washed interfacial film.

Layer	β_n / $Å^{-2} \times 10^{-6}$	β_m / $Å^{-2} \times 10^{-6}$	Thickness / Å	Roughness / Å	Solvation / %
Si	2.07	-	∞	3	-
SiO_2	3.47	-	$15^{\uparrow 25}_{\downarrow 1}$	$4^{\uparrow 10}_{\downarrow 1}$	-
Fe	$8.02^{\uparrow 8.02}_{\downarrow 7.50}$	$4.81^{\uparrow 5.04}_{\downarrow 4.35}$	$190^{\uparrow 210}_{\downarrow 170}$	$5^{\uparrow 15}_{\downarrow 1}$	-
FeO_x	$7.00^{\uparrow 7.20}_{\downarrow 5.00}$	$0.5^{\uparrow 1.30}_{\downarrow 0.00}$	$30^{\uparrow 20}_{\downarrow 40}$	$6^{\uparrow 15}_{\downarrow 1}$	-
GMO	$0.21^{\uparrow 6.00}_{\downarrow -0.54}$	-	$20^{\uparrow 30}_{\downarrow 10}$	$1^{\uparrow 15}_{\downarrow 1}$	$0^{\uparrow 100}_{\downarrow 0}$
GMO*	$0.00^{\uparrow 6.00}_{\downarrow -0.54}$	-	$10^{\uparrow 20}_{\downarrow 1}$	$1^{\uparrow 15}_{\downarrow 1}$	-
dod-d_{26}	$6.70^{\uparrow 6.70}_{\downarrow 5.00}$	-	-	-	-
dod-h_{26}	-0.46^*	-	-	-	-

Table A7: Complete description of the initial parameter values and priors used in the nested sampling of the iron-coated silicon substrate against solutions of dGMO in dodecane at 25 °C.

Layer	β_n / $Å^{-2} \times 10^{-6}$	β_m / $Å^{-2} \times 10^{-6}$	Thickness / Å	Roughness / Å	Solvation / %
Si	2.07	-	∞	3	-
SiO_2	3.47	-	$15^{\uparrow 25}_{\downarrow 1}$	$4^{\uparrow 10}_{\downarrow 1}$	-
Fe	$8.02^{\uparrow 8.10}_{\downarrow 7.50}$	$4.81^{\uparrow 5.04}_{\downarrow 4.35}$	$190^{\uparrow 210}_{\downarrow 170}$	$5^{\uparrow 15}_{\downarrow 1}$	-
FeO_x	$7.00^{\uparrow 7.20}_{\downarrow 5.00}$	$0.5^{\uparrow 1.30}_{\downarrow 0.00}$	$30^{\uparrow 20}_{\downarrow 40}$	$1^{\uparrow 15}_{\downarrow 1}$	-
dGMO	$0.21^{\uparrow 6.00}_{\downarrow -0.54}$	-	$20^{\uparrow 30}_{\downarrow 10}$	$1^{\uparrow 15}_{\downarrow 1}$	$0^{\uparrow 100}_{\downarrow 0}$
$dGMO_h$	0.33	-	$15^{\uparrow 18}_{\downarrow 1}$	$1^{\uparrow 7}_{\downarrow 1}$	$0^{\uparrow 100}_{\downarrow 0}$
$dGMO_t$	2.88	-	$10^{\uparrow 11}_{\downarrow 1}$	$1^{\uparrow 7}_{\downarrow 1}$	$0^{\uparrow 100}_{\downarrow 0}$
dod-d_{26}	$6.70^{\uparrow 6.70}_{\downarrow 5.00}$	-	-	-	-
dod-h_{26}	-0.46	-	-	-	-

Table A8: Complete description of the initial parameter values and priors used in the nested sampling of the iron-coated silicon substrate against solutions of the GMO-water-dodecane systems at 25 and 60 °C. The combined GMO-water layers had the same priors and initial values, and hence, are not listed individually. The layer labelled with * represents the mixed GMO-water layer for the systems where there are two interfacial layers, whereas $^\bullet$ represents the GMO-water layer for the system with one layer. The β_n of dodecane-h_{26} is listed twice, where * and † relate to β_n at 25 and 60 °C respectively. Two separate β_ns were modelled for both dodecane-d_{26} contrasts, but share the same initial and prior values so are just shown once.

Layer	β_n / $Å^{-2} \times 10^{-6}$	β_m / $Å^{-2} \times 10^{-6}$	Thickness / Å	Roughness / Å	Solvation / %
Si	2.07	-	∞	3	-
SiO_2	3.47	-	$15^{\uparrow 25}_{\downarrow 1}$	$4^{\uparrow 15}_{\downarrow 1}$	-
Fe	$8.02^{\uparrow 8.10}_{\downarrow 7.50}$	$4.81^{\uparrow 5.04}_{\downarrow 4.35}$	$190^{\uparrow 230}_{\downarrow 190}$	$5^{\uparrow 15}_{\downarrow 1}$	-
FeO_x	$7.00^{\uparrow 7.20}_{\downarrow 5.00}$	$0.5^{\uparrow 1.30}_{\downarrow 0.00}$	$30^{\uparrow 20}_{\downarrow 60}$	$1^{\uparrow 15}_{\downarrow 1}$	-
H_2O	$-0.54^{\uparrow 0.00}_{\downarrow -0.54}$	-	$1^{\uparrow 10}_{\downarrow 1}$	$7^{\uparrow 15}_{\downarrow 1}$	-
D_2O	$6.37^{\uparrow 6.37}_{\downarrow -0.00}$				
GMO-water*	$0.21^{\uparrow 6.00}_{\downarrow -0.54}$	-	$20^{\uparrow 30}_{\downarrow 10}$	$7^{\uparrow 15}_{\downarrow 1}$	$0^{\uparrow 100}_{\downarrow 0}$
GMO-water$^\bullet$	$0.21^{\uparrow 6.00}_{\downarrow -0.54}$	-	$25^{\uparrow 40}_{\downarrow 10}$	$7^{\uparrow 15}_{\downarrow 1}$	$0^{\uparrow 100}_{\downarrow 0}$
dod-d_{26}	$6.70^{\uparrow 6.70}_{\downarrow 5.00}$	-	-	-	-
dod-h_{26}	-0.46^*	-	-	-	-
	$-0.44^\dagger$				

Appendix B

Corner plots

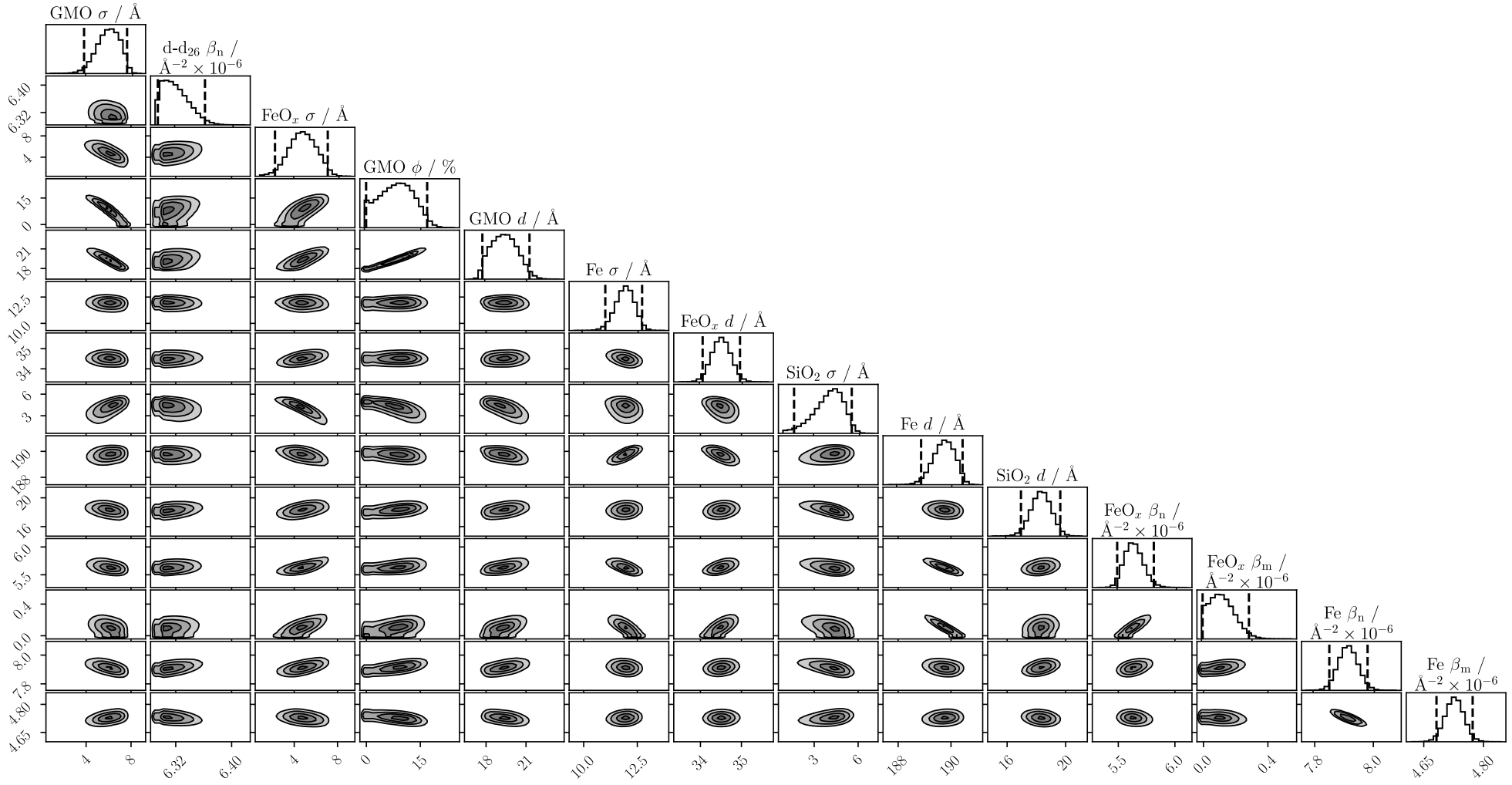

Figure B1: A corner plot of the parameter distributions following fitting the data of the 20 mM GMO-dodecane systems collected 25 °C. The intensity and background parameters are not shown for clarity.

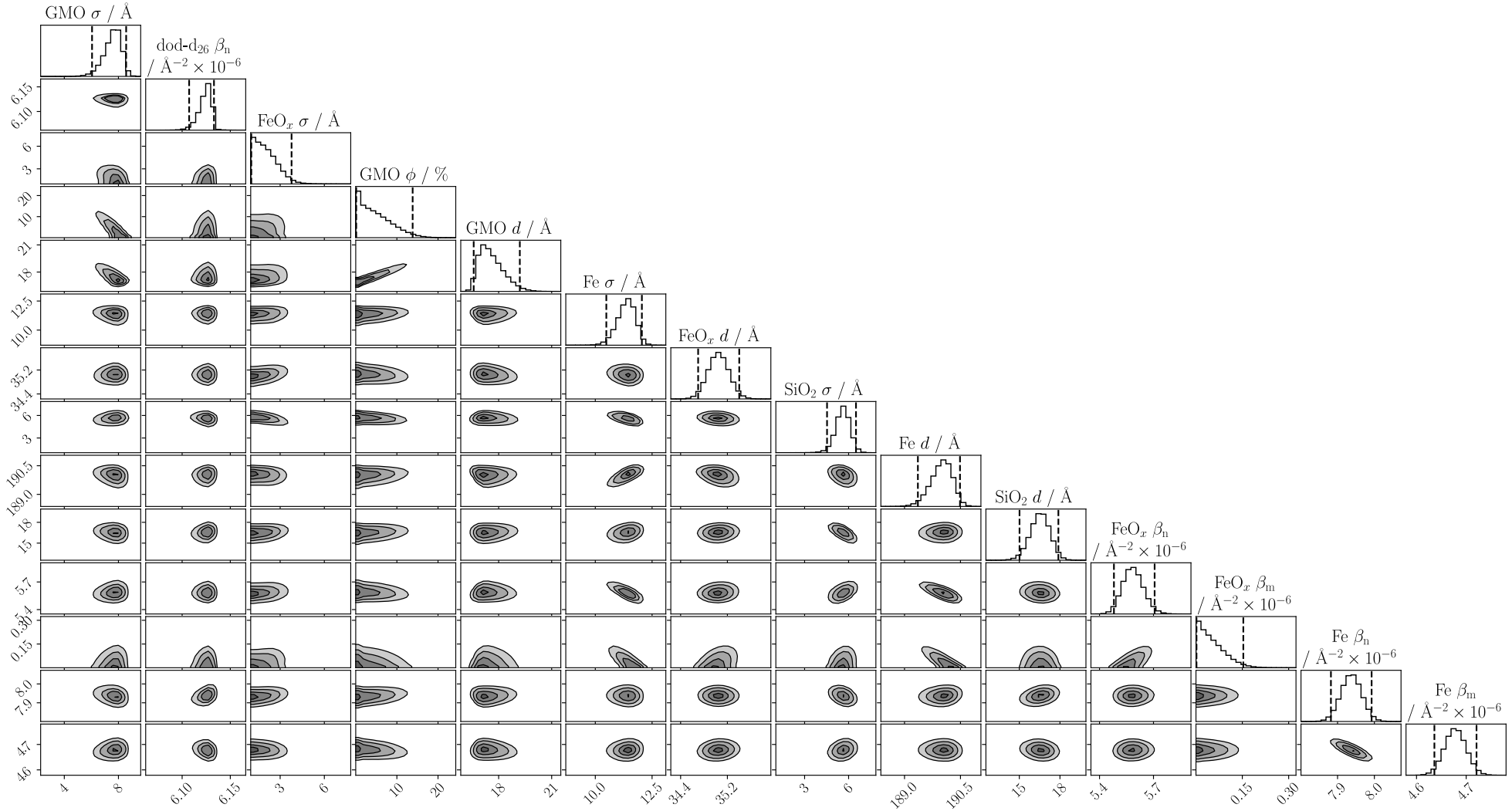

Figure B2: A corner plot of the parameter distributions following fitting the data of the 20 mM GMO-dodecane systems collected 60 °C. The intensity and background parameters are not shown for clarity.

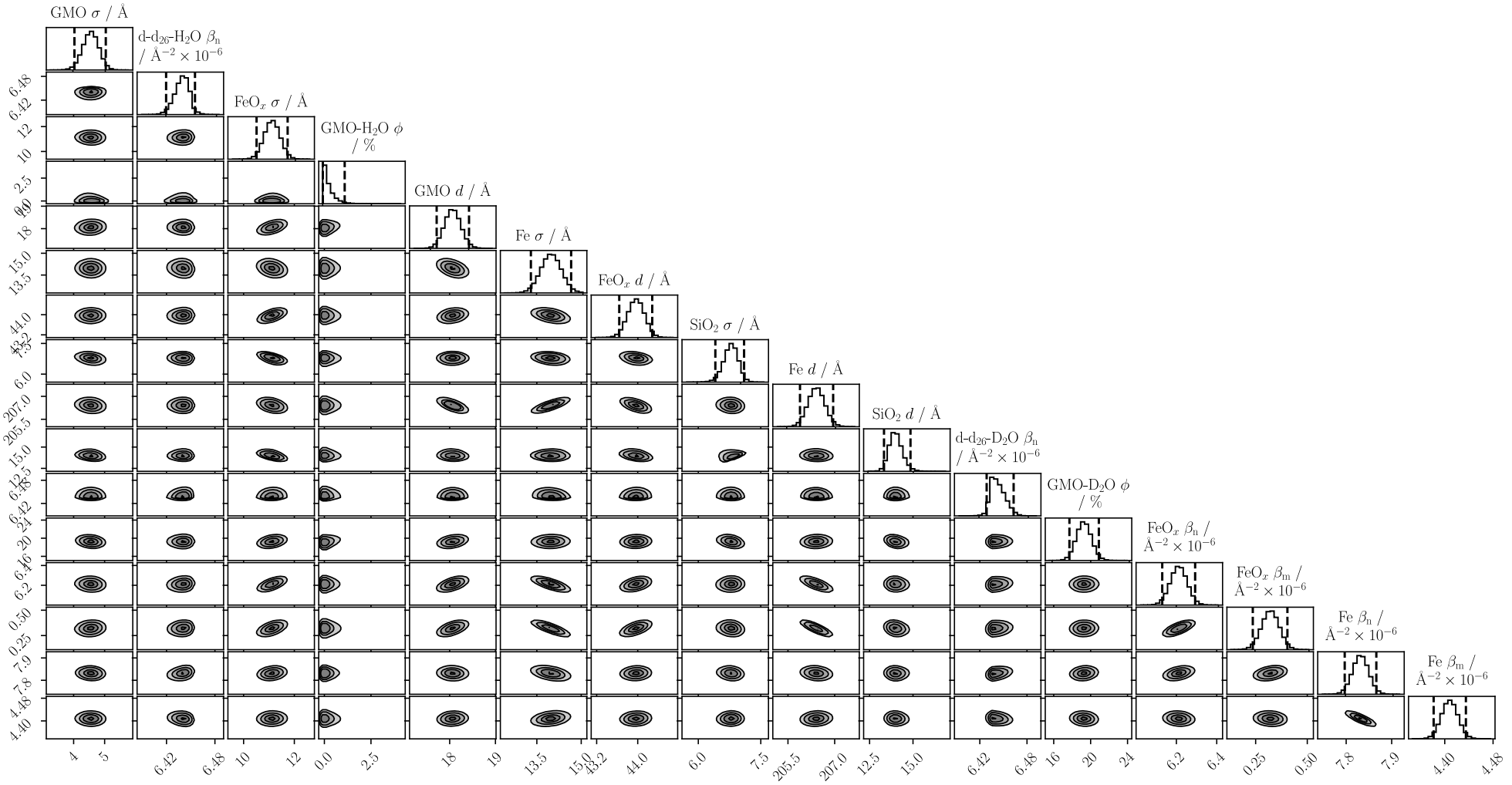

Figure B3: A corner plot showing the parameter distributions from the fit to the NR data collected at 25 °C with the GMO-water-dodecane systems. The intensity and background parameters are not shown for clarity.

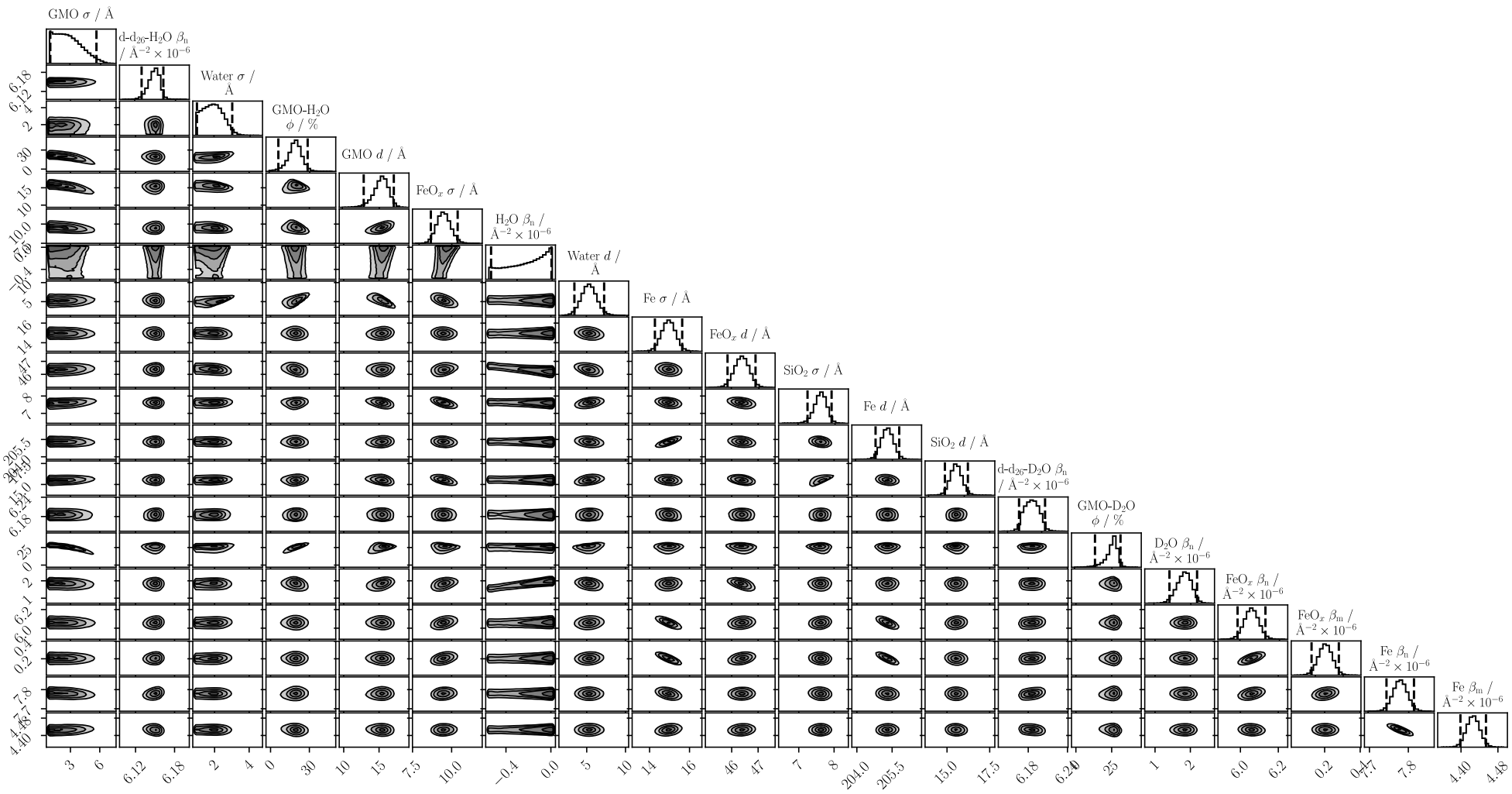

Figure B4: A corner plot showing the parameter distributions from the fit to the NR data collected at 60 °C with the GMO-water-dodecane systems. The intensity and background parameters are not shown for clarity.

Appendix C

Best fit tables

Table C1: The best fit parameter values for the ACdod contrasts collected at 7.0×10^2 s^{-1} and 3.6×10^3 s^{-1}. The intensity scale factors are 0.90 and 0.88 for the data collected at 7.0×10^2 s^{-1} and 3.6×10^3 s^{-1} respectively. The background values are 2.4×10^{-6} and 4.1×10^{-6}.

Layer	β_n / $Å^{-2} \times 10^{-6}$	β_m / $Å^{-2} \times 10^{-6}$	Thickness / Å	Roughness / Å
Si	2.07	-	∞	3
SiO_2	3.47	-	14.3	3.0
Fe	8.02	4.63	188	7.0
FeO_x	6.31	0.29	32.6	2.2
Adv	0.87	-	20.0	7.0
ACdod	0.00	-	-	-

Table C2: The best fit parameter values for the ACdod contrasts collected at 7.0×10^2 s^{-1} and 3.6×10^3 s^{-1} with the tribometer and d-Yubase-4. The intensity scale factors are 0.88 and 0.77 for the data collected at 7.0×10^2 s^{-1} and 3.6×10^3 s^{-1} respectively. The background values are 5.4×10^{-6} and 6.1×10^{-6}.

Layer	β_n / $Å^{-2} \times 10^{-6}$	β_m / $Å^{-2} \times 10^{-6}$	Thickness / Å	Roughness / Å
Si	2.07	-	∞	3
SiO_2	3.47	-	18.7	5.0
Fe	8.02	4.58	188	6.2
FeO_x	6.80	0.00	31.6	7.5
Adv	1.00	-	21.1	7.0
d-Yubase-4	4.85	-	-	-